

AD-A033 386

PRINCETON UNIV N J GAS DYNAMICS LAB
OBLIQUE SHOCK WAVE/TURBULENT BOUNDARY LAYER INTERACTIONS IN THR--ETC(U)
JUN 76 B OSKAM, I E VAS, S M BOGDONOFF F33615-75-C-3126

UNCLASSIFIED

1292

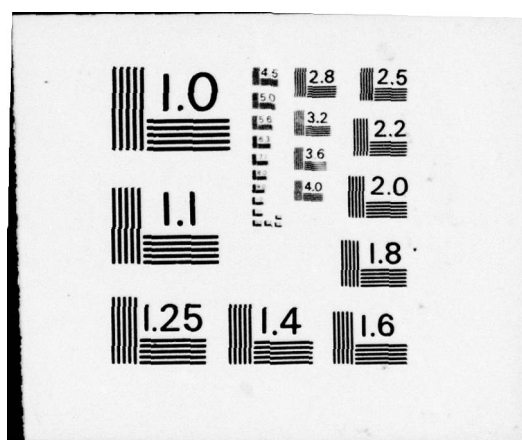
AFFDL-TR-76-48-PT-1

F/G 20/4

NL

1 of 2
ADAO33386





ADA033386

AFFDL-TR-76-48
PART I

25
DK

**OBlique SHOCK WAVE/TURBULENT BOUNDARY LAYER
INTERACTIONS IN THREE DIMENSIONS AT MACH 3
PART I**

PRINCETON UNIVERSITY

JUNE 1976



FINAL REPORT FOR THE PERIOD JUNE 1975 - JANUARY 1976

Approved for public release; distribution unlimited

AIR FORCE FLIGHT DYNAMICS LABORATORY
AIR FORCE WRIGHT AERONAUTICAL LABORATORIES
AIR FORCE SYSTEMS COMMAND
WRIGHT-PATTERSON AIR FORCE BASE, OHIO 45433

NOTICE

When Government drawings, specifications, or other data are used for any purpose other than in connection with a definitely related Government procurement operation, the United States Government thereby incurs no responsibility nor any obligation whatsoever; and the fact that the government may have formulated, furnished, or in any way supplied the said drawings, specifications, or other data, is not to be regarded by implication or otherwise as in any manner licensing the holder or any other person or corporation, or conveying any rights or permission to manufacture, use, or sell any patented invention that may in any way be related thereto.

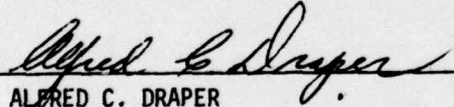
This report has been reviewed by the Information Office (OI) and is releasable to the National Technical Information Service (NTIS). At NTIS, it will be available to the general public, including foreign nations.

This report has been reviewed and is approved for publication.



RICHARD D. NEUMANN
Project Engineer

FOR THE COMMANDER



ALFRED C. DRAPER
Ast for Research & Technology
Aeromechanics Division



Copies of this report should not be returned unless return is required by security considerations, contractual obligations, or notice on a specific document.

UNCLASSIFIED

SECURITY CLASSIFICATION OF THIS PAGE (When Data Entered)

Final rept. Jun 75 -
Jan 76,

REPORT DOCUMENTATION PAGE

READ INSTRUCTIONS
BEFORE COMPLETING FORM

1. REPORT NUMBER AFFDL TR-76-48-Part-1	2. GOVT ACCESSION NO.	3. RECIPIENT'S CATALOG NUMBER
4. TITLE (and Subtitle) OBlique SHOCK WAVE/TURBULENT BOUNDARY LAYER INTERACTIONS IN THREE DIMENSIONS AT MACH 3 PART I.		5. TYPE OF REPORT & PERIOD COVERED Final Report June 1975-January 1976
7. AUTHOR(s) B. Oskam, I. E. Vas S. M. Bogdonoff		6. PERFORMING ORG. REPORT NUMBER 14 1292
9. PERFORMING ORGANIZATION NAME AND ADDRESS Princeton University Department of Aerospace & Mechanical Sciences Gas Dynamics Laboratory, Princeton, N. J. 08540		8. CONTRACT OR GRANT NUMBER(s) F33615-75-C-3126 new
11. CONTROLLING OFFICE NAME AND ADDRESS United States Air Force Air Force Systems Command Wright-Patterson AFB, Ohio 45433		10. PROGRAM ELEMENT, PROJECT, TASK AREA & WORK UNIT NUMBERS Project No. 1366
14. MONITORING AGENCY NAME & ADDRESS (if different from Controlling Office)		12. REPORT DATE 11 Jun 76
16. DISTRIBUTION STATEMENT (of this Report) Approved for public release; distribution unlimited.		13. NUMBER OF PAGES 156 12 172 p.
17. DISTRIBUTION STATEMENT (of the abstract entered in Block 20, if different from Report)		15. SECURITY CLASS. (of this report)
18. SUPPLEMENTARY NOTES		
19. KEY WORDS (Continue on reverse side if necessary and identify by block number) Three-dimensional separation Turbulent boundary layer Flow field description Surface measurements Shock wave/boundary layer interaction		
20. ABSTRACT (Continue on reverse side if necessary and identify by block number) An experimental study, thoroughly documenting the flow field and surface data resulting from the three-dimensional interaction of a shock wave, a shock generator and a high Reynolds number turbulent boundary layer, is described. Detailed surface static pressure data and heat transfer measurements are presented for 7 shock generator deflection angles ranging from 2° to 14° in 2° increments. The test conditions consist of a free stream Reynolds number per inch of 1.6 10 million, a near adiabatic wall temperature and ambient stagnation temperature.		

DD FORM
1 JAN 73 1473

EDITION OF 1 NOV 65 IS OBSOLETE

UNCLASSIFIED

SECURITY CLASSIFICATION OF THIS PAGE (When Data Entered)

next page

145770 - 88

cont

UNCLASSIFIED

SECURITY CLASSIFICATION OF THIS PAGE (When Data Entered)

→ In addition to the surface data detailed flow field surveys have been conducted of time-averaged variables including flow angularity, pitot pressure, static pressure and total temperature at 2 shock generator deflection angles of 4 and 10 degrees.

Detailed discussions of the experimental techniques are given which include a complete set of error estimates of the various types of data. Finally the data are presented in graphical form which may be used to analyse the problem under consideration.



UNCLASSIFIED

SECURITY CLASSIFICATION OF THIS PAGE (When Data Entered)

FOREWORD

This document presents a detailed experimental investigation on flow fields caused by a three-dimensional shock wave/turbulent boundary layer interaction. The study was conducted by the Gas Dynamics Laboratory, Princeton University, under Contract F33615-75-C-3126, Project No. 1366, issued by the Air Force Flight Dynamics Laboratory, Wright-Patterson Air Force Base. This final report, submitted by the authors in June 1976, describes all the work accomplished for the duration of the contract from June 1975 to January 1976.

The contract effort was directed by Mr. Richard D. Neumann, AFFDL/FXG, of the Flight Dynamics Laboratory. Mr. B. Oskam, as graduate student, was responsible for carrying out the test program, development of experimental techniques, and machine plotting and interpretation of results. Professor S. M. Bogdonoff and Dr. I. E. Vas, Co-Principal Investigators, supervised all technical efforts. The technical staff of the Gas Dynamics Laboratory provided the design, fabrication, photographic, data acquisition, mechanical, electronic and typing services.

TABLE OF CONTENTS

<u>Section</u>	<u>Page</u>
1. INTRODUCTION	1
2. EXPERIMENTAL PROGRAM	5
2.1 General Objectives	5
2.2 Test Environment	6
2.2.1. Windtunnel Facility	6
2.2.2. Test Section and Shock Generator Apparatus	8
2.2.3. Test Conditions	10
2.3 Instrumentation and Techniques	12
2.3.1. Eccentric, Rotatable System	12
2.3.2. Static Pressure Plug and Scanivalve	13
2.3.3. Heat Transfer Measurement	14
2.3.3.1. Introduction	14
2.3.3.2. Hardware	15
2.3.3.3. Test Procedures	16
2.3.4. Probe Drive Mechanism	17
2.3.5. Cobra Probes	19
2.3.5.1. Yaw Angle-Pitot Pressure Probe	19
2.3.5.2. Pitch Angle-Pitot Pressure Probe	20
2.3.6. Static Pressure Probe	21
2.3.7. Total Temperature Probes	21
2.3.8. Data Acquisition Systems	22
2.4 Estimated Uncertainties and Reduction of Data	23
2.4.1. Transducer Calibrations	23
2.4.2. Shock Generator Deflection Angles	24
2.4.3. Surface Static Pressure	26
2.4.4. Heat Transfer Studies	27
2.4.4.1. Heat Transfer Data Reduction	27
2.4.4.2. Adiabatic Wall Temperature	29
2.4.4.3. Van Driest II Skin Friction Formula	31
2.4.4.4. Heat Transfer Variation with Reynolds Number	32
2.4.4.5. Heat Transfer Data Uncertainty	33
2.4.5. Cobra Probe Surveys	33
2.4.5.1. Cobra Probe Displacement Effect	33
2.4.5.2. Cobra Probe Angle Sensitivity	34
2.4.5.3. Cobra Probe Data Uncertainties	35
2.4.6. Static Pressure Surveys	36
2.4.7. Total Temperature Surveys	38

TABLE OF CONTENTS
(cont)

<u>Section</u>	<u>Page</u>
2.4.8. Derived Flow Field Variables	40
2.5 Uniformity of Initial Boundary Layer Flow	42
2.6 Summary of Estimated Uncertainties of Data	43
2.7 Summary of Data	44
3. CONCLUDING REMARKS	48
4. FIGURES	49
5. APPENDICES A THROUGH J	
Appendix A: Surface Static Pressures	72
Appendix B: Surface Isobar Patterns	81
Appendix C: Surface Heat Transfers	88
Appendix D: Surface Heat Transfer Patterns	92
Appendix E: Yaw Angle Surveys	97
Appendix F: Pitot Pressure Surveys	112
Appendix G: Static Pressure Surveys	127
Appendix H: Total Temperature Surveys	137
Appendix I: Pitot Pressure Surveys in the Immediate Vicinity of the Shock Generator	146
Appendix J: Total Temperature Profiles in the Immediate Vicinity of the Shock Generator	150
6. REFERENCES	155

LIST OF ILLUSTRATIONS

<u>Figure No.</u>	<u>Title</u>	<u>Page</u>
1	Schematic of Experimental Configuration	49
2	Coordinate System	50
3	Photograph of Wind Tunnel Test Section	51
4	Line Drawing of Shock Generator Mechanism	52
5	Tunnel Temperature Variations with Time	53
6	Eccentric , Rotatable System	54
7	Photograph of Static Pressure Plug	55
8	Photograph of Heat Transfer Plug	56
9	Drawing of Slug Calorimeter Arrangement	57
10	Temperature-Time History of Slug Calorimeter	58
11	Photograph of Probe Drive Mechanism	59
12	Drawing of Probe Drive Mechanism	60
13	Photograph of Five Flow Field Probes	61
14	Frontal View of Yaw-Pitot Probe and Pitch-Pitot Probe	62
15	Line Drawing of Probe Tips	63
16	Photograph of Static Pressure Probe Tip	64
17	Photograph of Total Temperature Probe Supports and Thermocouple Junction	65
18	Typical Flow Chart of Data Acquisition System	66
19	Heat Transfer Versus Reynolds Number	67
20	Angle Sensitivity of Yaw Pitot Probe	68
21	Angle Sensitivity of Static Pressure Probe	69
22	Shock Generator Orientation with Respect to Tunnel Nozzle	70
23	Two-Dimensionality of Initial Boundary Layer Flow . .	71

LIST OF ILLUSTRATIONS

APPENDICES A-J

Figure No.	Title	Page
APPENDIX A		
A-1	Surface Static Pressure, $X = 4.6$ inches	72
A-2	Surface Static Pressure, $X = 5.1$ inches	73
A-3	Surface Static Pressure, $X = 5.6$ inches	74
A-4	Surface Static Pressure, $X = 7.1$ inches	75
A-5	Surface Static Pressure, $X = 7.6$ inches	76
A-6	Surface Static Pressure, $X = 8.1$ inches	77
A-7	Surface Static Pressure, $X = 8.6$ inches	78
A-8	Surface Static Pressure, $X = 9.1$ inches	79
A-9	Surface Static Pressure, $X = 9.6$ inches	80
APPENDIX B		
B-1	Surface Isobar Pattern, 2 degrees	81
B-2	Surface Isobar Pattern, 4 degrees	82
B-3	Surface Isobar Pattern, 6 degrees	83
B-4	Surface Isobar Pattern, 8 degrees	84
B-5	Surface Isobar Pattern, 10 degrees	85
B-6	Surface Isobar Pattern, 12 degrees	86
B-7	Surface Isobar Pattern, 13 degrees	87
APPENDIX C		
C-1	Surface Heat Transfer, $X = 4.6$ inches	88
C-2	Surface Heat Transfer, $X = 5.1$ inches	89
C-3	Surface Heat Transfer, $X = 7.1$ inches	90
C-4	Surface Heat Transfer, $X = 7.6$ inches	91

LIST OF ILLUSTRATIONS
(cont.)
APPENDICES A-J

Figure No.	Title	Page
APPENDIX D		
D-1	Surface Heat Transfer Pattern, 4 degrees	92
D-2	Surface Heat Transfer Pattern, 6 degrees	93
D-3	Surface Heat Transfer Pattern, 8 degrees	94
D-4	Surface Heat Transfer Pattern, 10 degrees	95
D-5	Surface Heat Transfer Pattern, 12 degrees	96
APPENDIX E		
E-1	Yaw Angle Surveys, $X = 3.56$ inches, $\alpha_G = 0^\circ$	97
E-2	Yaw Angle Surveys, $X = 7.6$ inches, $\alpha_G = 4^\circ$	98
E-3	Yaw Angle Surveys, $X = 7.6$ inches, $\alpha_G = 4^\circ$	99
E-4	Yaw Angle Surveys, $X = 7.6$ inches, $\alpha_G = 4^\circ$	100
E-5	Yaw Angle Surveys, $X = 7.6$ inches, $\alpha_G = 4^\circ$	101
E-6	Yaw Angle Surveys, $X = 7.6$ inches, $\alpha_G = 4^\circ$	102
E-7	Yaw Angle Surveys, $X = 7.1$ inches, $\alpha_G = 4^\circ$	103
E-8	Yaw Angle Surveys, $X = 7.1$ inches, $\alpha_G = 4^\circ$	104
E-9	Yaw Angle Surveys, $X = 5.1$ inches, $\alpha_G = 4^\circ$	105
E-10	Yaw Angle Surveys, $X = 7.6$ inches, $\alpha_G = 10^\circ$	106
E-11	Yaw Angle Surveys, $X = 7.6$ inches, $\alpha_G = 10^\circ$	107
E-12	Yaw Angle Surveys, $X = 7.6$ inches, $\alpha_G = 10^\circ$	108
E-13	Yaw Angle Surveys, $X = 7.6$ inches, $\alpha_G = 10^\circ$	109
E-14	Yaw Angle Surveys, $X = 7.1$ inches, $\alpha_G = 10^\circ$	110
E-15	Yaw Angle Surveys, $X = 5.1$ inches, $\alpha_G = 10^\circ$	111

LIST OF ILLUSTRATIONS
(cont.)
APPENDICES A-J

Figure No.	Title	Page
APPENDIX F		
F-1	Pitot Pressure Surveys, $X = 3.56$ inches, $\alpha_G = 0^\circ$. . .	112
F-2	Pitot Pressure Surveys, $X = 7.6$ inches, $\alpha_G = 4^\circ$. . .	113
F-3	Pitot Pressure Surveys, $X = 7.6$ inches, $\alpha_G = 4^\circ$. . .	114
F-4	Pitot Pressure Surveys, $X = 7.6$ inches, $\alpha_G = 4^\circ$. . .	115
F-5	Pitot Pressure Surveys, $X = 7.6$ inches, $\alpha_G = 4^\circ$. . .	116
F-6	Pitot Pressure Surveys, $X = 7.6$ inches, $\alpha_G = 4^\circ$. . .	117
F-7	Pitot Pressure Surveys, $X = 7.1$ inches, $\alpha_G = 4^\circ$. . .	118
F-8	Pitot Pressure Surveys, $X = 7.1$ inches, $\alpha_G = 4^\circ$. . .	119
F-9	Pitot Pressure Surveys, $X = 5.1$ inches, $\alpha_G = 4^\circ$. . .	120
F-10	Pitot Pressure Surveys, $X = 7.6$ inches, $\alpha_G = 10^\circ$. . .	121
F-11	Pitot Pressure Surveys, $X = 7.6$ inches, $\alpha_G = 10^\circ$. . .	122
F-12	Pitot Pressure Surveys, $X = 7.6$ inches, $\alpha_G = 10^\circ$. . .	123
F-13	Pitot Pressure Surveys, $X = 7.6$ inches, $\alpha_G = 10^\circ$. . .	124
F-14	Pitot Pressure Surveys, $X = 7.1$ inches, $\alpha_G = 10^\circ$. . .	125
F-15	Pitot Pressure Surveys, $X = 5.1$ inches, $\alpha_G = 10^\circ$. . .	126
APPENDIX G		
G-1	Static Pressure Surveys, $X = 7.6$ inches, $\alpha_G = 4^\circ$. . .	127
G-2	Static Pressure Surveys, $X = 7.6$ inches, $\alpha_G = 4^\circ$. . .	128
G-3	Static Pressure Surveys, $X = 7.6$ inches, $\alpha_G = 4^\circ$. . .	129
G-4	Static Pressure Surveys, $X = 7.6$ inches, $\alpha_G = 4^\circ$. . .	130
G-5	Static Pressure Surveys, $X = 5.1$ inches, $\alpha_G = 4^\circ$. . .	131
G-6	Static Pressure Surveys, $X = 7.6$ inches, $\alpha_G = 10^\circ$. . .	132

LIST OF ILLUSTRATIONS
(cont.)
APPENDICES A-J

Figure No.	Title	Page
G-7	Static Pressure Surveys, $X = 7.6$ inches, $\alpha_G = 10^\circ$. . .	133
G-8	Static Pressure Surveys, $X = 7.6$ inches, $\alpha_G = 10^\circ$. . .	134
G-9	Static Pressure Surveys, $X = 7.6$ inches, $\alpha_G = 10^\circ$. . .	135
G-10	Static Pressure Surveys, $X = 5.1$ inches, $\alpha_G = 10^\circ$. . .	136
APPENDIX H		
H-1	Total Temperature Surveys, $\alpha_G = 0^\circ$ and 4°	137
H-2	Total Temperature Surveys, $X = 7.6$ inches, $\alpha_G = 4^\circ$	138
H-3	Total Temperature Surveys, $X = 7.6$ inches, $\alpha_G = 4^\circ$	139
H-4	Total Temperature Surveys, $X = 7.6$ inches, $\alpha_G = 4^\circ$	140
H-5	Total Temperature Surveys, $X = 5.1$ inches, $\alpha_G = 4^\circ$	141
H-6	Total Temperature Surveys, $X = 7.6$ inches, $\alpha_G = 10^\circ$	142
H-7	Total Temperature Surveys, $X = 7.6$ inches, $\alpha_G = 10^\circ$	143
H-8	Total Temperature Surveys, $X = 7.6$ inches, $\alpha_G = 10^\circ$	144
H-9	Total Temperature Surveys, $X = 5.1$ inches, $\alpha_G = 10^\circ$	145
APPENDIX I		
I-1	Pitot Pressure Surveys, $X = 7.6$ inches, $\alpha_G = 4^\circ$. . .	146
I-2	Pitot Pressure Surveys, $X = 7.6$ inches, $\alpha_G = 4^\circ$. . .	147
I-3	Pitot Pressure Surveys, $X = 7.6$ inches, $\alpha_G = 10^\circ$. . .	148
I-4	Pitot Pressure Surveys, $X = 7.6$ inches, $\alpha_G = 10^\circ$. . .	149

LIST OF ILLUSTRATIONS
(cont.)
APPENDICES A-J

<u>Figure No.</u>	<u>Title</u>	<u>Page</u>
	APPENDIX J	
J-1	Total Temperature Profiles, $X = 7.6$ inches, $\alpha_G = 4^\circ$	150
J-2	Total Temperature Profiles, $X = 7.6$ inches, $\alpha_G = 4^\circ$	151
J-3	Total Temperature Profiles, $X = 7.6$ inches, $\alpha_G = 10^\circ$	152
J-4	Total Temperature Profiles, $X = 7.6$ inches, $\alpha_G = 10^\circ$	153
J-5	Total Temperature Profiles, $X = 7.6$ inches, $\alpha_G = 10^\circ$	154

LIST OF TABLES

Table No.	Title	Page
I	Shock Generator Instrumentation Location	9
II	Temperature Test Conditions for Surface Static Pressure and Flow Field Measurements	11
III	Temperature Test Conditions for Heat Transfer Tests	12
IV	Transducer Accuracies	24
V	Shock Generator Angles (Degrees)	25
VI	Summary of Data Uncertainties	44
VII	Yaw-Pitot Survey Groupings	45
VIII	Static Pressure Surveys Groupings	46
IX	Total Temperature Survey Groupings	47

LIST OF SYMBOLS

a	local speed of sound
A_s	surface area of slug
$C_f = \frac{\tau_w}{\frac{1}{2} \rho_1 u_1^2}$	skin friction coefficient
$C_h = \frac{q_c}{\rho_1 u_1 c_p (\tau_w - \tau_{aw})}$	heat transfer coefficient
c_p	specific heat at constant pressure
c_s	specific heat of slug material
c_v	specific heat at constant volume
e	displacement of effective center of static-hole
H	probe tip height
m_s	mass of slug
$M = \frac{\sqrt{u^2 + v^2}}{a}$	Mach number
NSGA	nominal shock generator angle
p or P	static pressure
p_p	pressure indicated by probe
p_t or PT	pitot pressure
p_0	tunnel stagnation pressure
p_1	static pressure ahead of interaction
PT_1	pitot pressure in free stream ahead of interaction
q_c	convective heat transfer rate
r	recovery factor
R	gas constant
$Re_{inch} = \frac{u_1 \rho_1}{\mu_1}$	Reynolds number per inch

$Re = \frac{u_1 \rho_1 \theta}{\mu_1}$	Reynolds number based on momentum defect thickness
$s = 2 C_h / C_f$	Reynolds analogy factor
t	time
t_0	time at which $T_s = T_w$
T	static temperature
T_t	local total temperature
$TT = T_{wi} / 0.948$	redefined wire recovery temperature
T_{wi}	wire recovery temperature
T_0 or TSTAG	tunnel stagnation temperature
u, v and w	velocity components in X, Y and Z-direction
W	probe tip width
X	coordinate parallel to tunnel axis measured from leading edge of shock generator
Y	coordinate normal to X-axis in plane of test surface measured from leading edge of shock generator
$YG = Y - X \tan(FIE G)$	Y-coordinate measured from surface of shock generator
Z	coordinate normal to X- and Y-axis measured from test surface
α or ALFA = $\tan^{-1}(\frac{v}{u})$	yaw angle
α_G or ALFA G	effective shock generator angle
α_p	probe deflection angle
$\beta = \tan^{-1}(\frac{w}{u})$	pitch angle
γ or GAMMA = $\tan^{-1}(\frac{w}{\sqrt{u^2+v^2}})$	pitch angle
$\gamma = \frac{c_p}{c_v}$	ratio of specific heats
δ	boundary layer thickness
$\delta^* = \int_0^\delta [1 - \frac{\rho u}{(\rho u)_\infty}] dz$	boundary layer displacement thickness

Δ	effective displacement of pitot probe tip
Δp	pressure difference between outer tubes of cobra probe
$\theta = \int_0^\delta [1 - \frac{u}{u_\infty}] \frac{\rho u}{(\rho u)_\infty} dz$	boundary layer momentum defect thickness
μ	viscosity
ρ	density
ϕ_G or FIE G	geometrical shock generator angle
τ_w	skin friction

Subscripts

1	as in free stream ahead of interaction
2	uniform conditions behind shock wave as calculated from oblique shock theory
ave	averaged value
aw	adiabatic wall condition
i	successive time index
s	slug calorimeter
vD	predicted by van Driest method
w	wall condition

1. INTRODUCTION

Accurate knowledge of heat transfer is required as it determines the structural requirements of high speed vehicles. Thermal design of the structures and material selection depend heavily on engineering estimates of the local heat transfer rates. In the case of turbulent boundary layers, one has to rely heavily on experimental data, since no theories are able to predict the turbulent heat transfer rate without incorporating a large amount of experimental data. A recent evaluation of such empirical theories for predicting heat transfer in constant pressure turbulent boundary layers at supersonic and hypersonic Mach numbers is given by Hopkins and Inouye in Ref. 1.

These empirical theories are not completely adequate, however, to predict the heating rates on actual geometries, since extensive viscous-inviscid interactions will be present and cause heating rates many factors higher than the associated flat plate values. These high local heating rates can pose a major design difficulty as discussed by Korkegi in Ref. 2.

Many of these viscous-inviscid interactions are caused by shock waves interacting with the turbulent boundary layer on the body and result in significantly higher heating rates. Many experimental studies have been conducted to determine the magnitude of these heating peaks, compared to the flat plate values, plus their location with respect to the provoking agency. Although many of these studies have been carried out with nominal two-dimensional flow configurations, there have also been a number of studies, e.g. Neumann and Token, Ref. 3, that do consider a particular kind of shock wave/boundary layer interaction which has essentially three spatial dimensions. Several empirical

correlations of heat transfer amplification factors, with respect to flat plate values, have been reported for various viscous-inviscid interactions. These, however, are generally limited to particular geometries and test conditions because they have not incorporated a sufficiently deep physical understanding of the phenomena involved. Such hit and miss empiricisms almost require every new geometry or flow configuration to be experimentally tested before the interaction effects can be appraised properly. This, however, can be a very costly and time consuming proposition.

Recently there has been a series of developments in the general area of numerical, computational techniques and high speed computers pointing the way to solving the full time-averaged Navier-Stokes equations on a routine basis. Fundamental problems remain since these computer codes incorporate empirical information in the form of the turbulent Reynolds stresses, the so-called turbulence models. Thus it would appear that these elaborate computational techniques suffer the same kind of deficiencies as the more simplistic empiricisms, e.g., for predicting peak heating rates. These drawbacks can hopefully be overcome based upon the argument that the high level of sophistication will give the turbulence models a universal applicability depending only upon a basic set of non-dimensional parameters. It is in this area of computational fluid dynamics that large bodies of sufficiently accurate experimental data for well defined problems are needed to guide the development of these turbulence models.

The objective of the present study is two-fold. The first one is to provide a detailed set of surface data, complemented by a complete survey of the associated flow field, from which detailed flow models can be constructed which may lead to a better understanding of the physical phenomena. This

would be particularly useful for obtaining direct design estimates of the particular problem under consideration. A second and more far-sighted objective is to describe and document a well defined, physically significant problem, that has been investigated experimentally, which can guide the development and validate future computer codes and turbulence models.

With these objectives in mind, the present study considers the interaction flow field and surface phenomena created by the three-dimensional, experimental configuration depicted in Fig. 1. The coordinate system used for the present problem is shown as Fig. 2. This study is actually a continuation of the earlier work by Oskam, Bogdonoff and Vas, Ref. 4, the main difference being that the region under study is extended into the streamwise corner formed by the shock generator and the tunnel test wall. The instrumentation rows have therefore been taken parallel to the Y direction instead of being parallel to the X direction.

This document is basically divided into three parts. The first one describes the environment under which the tests have been conducted. Special attention is paid to the definitions of the physical boundary conditions under which the experimental data are obtained. This is of particular importance for the heat transfer studies where results have been obtained for a uniform temperature test wall on which the variable heat transfer rates have been measured. A second part deals with description of the apparatus used in obtaining the various data. The process of data reduction and the estimates of data accuracy are presented in the third part. Much attention has been given in this respect to possible limitations of the techniques employed and the resulting accuracies are tabulated.

The final data has been plotted in 10 detailed appendices, but can also be obtained from detailed tabulations as given by Oskam, Vas and Bogdonoff in Ref. 5.

2. EXPERIMENTAL PROGRAM

2.1 General Objectives

In an attempt to conduct an experimental program which gave the optimum amount of relevant data, special attention has been paid to an exhaustive series of details which, hopefully, give the final results a more easily understood meaning and eventually will lead to a more basic understanding of the physical phenomena involved.

A special wind tunnel test section, designed and constructed during the earlier work by Oskam, Bogdonoff and Vas (Ref. 4), was shown to be an efficient experimental configuration which has a relatively thick, high Reynolds number, turbulent boundary layer, of superior transverse uniformity compared to previous studies performed with tunnel wall boundary layers as discussed in Section 2.5. The maximum shock generator angles were limited, however, by the interaction resulting from reflection of the oblique shock wave at the tunnel sidewall causing the tunnel to stall at shock generator angles larger than 14°. This test section features two large observation/instrumentation ports (12 inch diameter) which rendered flexibility for mounting optical windows, surface instrumentation and probe drives covering the complete area of interest without affecting the shock generator model configuration.

The region studied in the course of this investigation extends from the area under the shock wave towards the axial corner formed by the test surface and the shock generator, including the turbulent boundary layer on the shock generator itself. The practical importance of this axial corner interaction in high speed flow stems from the observation of high local heating rates in

the immediate vicinity of the shock generator. A new probe drive mechanism has therefore been constructed, accompanied with angle sensitive probes, total temperature probes and a static pressure probe, and has been employed to resolve the flow field, including all three velocity components, up to the surface of the shock generator.

Special attention is given in this study to check the validity of the experimental techniques employed. The heat transfer technique is described in detail together with the precise definition of the coefficients employed to present the data.

The question of data accuracy has extensively been discussed in this document since the final analysis of the data will heavily depend on the accuracy that has been achieved. The accuracies of the various types of data are given in terms of estimated uncertainties which should be considered to be upper bounds since they were obtained by considering the largest possible errors which could only occur at certain locations of the region studied.

2.2 Test Environment

2.2.1. Windtunnel facility

The Aeronautical Engineering Department at Princeton University started its study of viscous phenomena in supersonic flows in 1946. This interest led to the design, construction and operation of the 4 x 8 inch variable density supersonic tunnel. That tunnel had specifically been designed to cover the range of Reynolds numbers up to full scale and provided experimental information in a test range not covered by any other supersonic testing facility at that time (Ref. 6). After many projects had successfully been completed the facility was moth-balled due to the laboratory's emphasis on higher Mach number studies.

More recently, however, there has been renewed interest in high Reynolds number studies because of difficulties encountered with extrapolating wind tunnel data to actual flight conditions. As a result the original high Reynolds number facility was put back into operation in 1970 but with a new Mach 3 nozzle and longer test section (Ref. 7). In this new 108 inch long boundary layer channel, with a cross sectional area of 8 x 8 inches, one can obtain Reynolds numbers, based on the turbulent boundary layer running length, of the order of 10^9 at a tunnel stagnation pressure of 500 psia. These newly constructed test sections are flexible, easily modified and readily adapted to testing of various configurations.

The high pressure air for the facility is provided by four Worthington four stage compressors, driven by 100 horsepower induction motors, which can pump from atmospheric up to 3200 psia. A drying system, operating at 3200 psia, removes all the moisture from the high pressure air to eliminate the possibility of the adverse effects of condensation shocks in the supersonic tunnel. Four tanks, situated above the ground, provide a storage capacity of 2000 cubic feet at a maximum pressure level of 3200 psia.

The stagnation pressure is regulated by an 8 inch hydraulically actuated valve during tunnel operation. A control system, which can be operated either manually or automatically, is used to maintain the desired stagnation pressure. A tunnel run has to be terminated if the tank pressure drops so low that the main regulator valve reaches maximum opening so that the desired stagnation pressure can no longer be maintained.

Since the tunnel is not provided with a heat exchanger, it is to be expected that the stagnation temperature will change from day-to-day as well as during tunnel operation. The day-to-day change is determined by the

variation in the ambient temperature since this controls the initial temperature of the storage tanks. The actual stagnation temperature level in the test section is also determined by the Joule-Thompson drop across the main regulator valve, and a significant amount of heat transfer to the air from the inlet piping, in addition to the initial tank temperature. This leads to a drop in tunnel stagnation temperature with time during operation. The observations that the tunnel walls are initially at room temperature, and that the stagnation temperature is always below room temperature, explain the experienced heat transfer from the walls to the gas and result in a drop of the tunnel wall temperature with time. The magnitude of the stagnation temperature decrease being slightly larger than the wall temperature decrease with time, imposes a permanent driving potential for the wall heat transfer during operation. This enables one to study heat transfer rates on tunnel-wall mounted models without being in direct control of either the stagnation or the tunnel wall temperature.

The above mentioned variations in temperature conditions from run to run and also during a single run do require, however, special data reduction procedures which will be discussed later. It should also be noted that the free stream Reynolds number is a direct function of the stagnation temperature and is thus subject to similar variations.

2.2.2. Test Section and Shock Generator Apparatus

The model configuration, which was used previously (Ref. 4), consists of a sharp flat plate, 8 inches by 10 inches long, called the shock generator, mounted vertically between tunnel top and bottom wall and pivoted about a center close to its leading edge. This shock generator and its bearings, which are held in the top and bottom walls, were constructed out of one piece to avoid leakage beneath the leading edge along the tunnel wall. The remaining edges

of the shock generator were lined with nylon to provide the seal.

The main support of this generator is provided by an arm which extends through the tunnel side-wall and is linked to a screw mechanism. The housing for this mechanism is sealed to the side-wall of the tunnel and has an external drive wheel, so one can manually rotate the shock generator from outside the tunnel. A range of shock generator deflection angles from 0° up to 14° has been used during the investigation. Since sizeable two-dimensional models at large deflection angle are particularly susceptible to tunnel starting problems, the starting procedure adopted was to initially set the shock generator at an angle not exceeding 8° and to increase its deflection angle after the supersonic flow was established if desired. Permanent tunnel stall was experienced, however, above 14° .

Four static pressure taps, located in the surface of the shock generator, are connected with flexible tubing to a plug in the mechanism housing. Moreover, two thermocouples are spot welded to the generator to measure its temperature. The coordinates (with $\alpha_G = 0$) of the static pressure taps and the thermocouples are given in Table I.

TABLE I: SHOCK GENERATOR INSTRUMENTATION LOCATION

Static Pressure Tap No.	Thermocouple Number	X Inches	Z Inches
1	1	2.0	2.0
2		5.0	2.0
3	2	7.0	2.0
4		2.0	6.0

Upstream of the shock generator leading edge, one thermocouple is located in the tunnel top wall to indicate the wall temperature.

A photograph of the test section, installed between the nozzle and a second test section, as well as a line drawing of the shock generator actuating mechanism are presented in Figs. 3 and 4, respectively.

2.2.3. Test Conditions

The test section was mounted in a position immediately downstream of the nozzle, where the flow uniformity is optimal, and the starting problems are minimal. The nominal free stream Mach number at a location upstream of the interaction is 2.94. The turbulent boundary layer on the tunnel wall entering the interaction is approximately 0.55 inches thick, depending on the exact location under consideration. Only part of the heat transfer studies were performed over a range of stagnation pressures from 75 to 200 psia (see Section 2.4.4.4). All of the remaining tests were carried out with a constant stagnation pressure of 100 psia held to within 0.5% during tunnel operation. At this 100 psia level, a maximum running time of 7 minutes can be sustained, if the storage tanks are at a pressure of 3000 psia initially.

Before we state the various temperature test conditions, it is most helpful to appraise some of the temperature-time variations mentioned earlier in Section 2.2.1. Figure 5 shows these variations versus time for a run consisting of two separate tests, 15 minutes apart, and each approximately 180 seconds long, at a stagnation pressure of 100 psia. One may observe from the data that after an initial temperature start-up process of about 30 seconds, the wall temperature and stagnation temperature decrease almost linearly with time. Approximate values are:

$$\frac{dT_w}{dt} \approx -0.13 \left[\frac{^{\circ}R}{sec} \right] \text{ and } -0.22 \leq \frac{dT_o}{dt} \leq -0.15 \left[\frac{^{\circ}R}{sec} \right].$$

The shock generator, however, due to its large surface area and smaller heat capacity compared to the 3 inch thick aluminum tunnel wall, decreases much faster in temperature than the tunnel wall. After a time of about two minutes it asymptotes to a level close to an adiabatic wall temperature which is proportional to the tunnel stagnation temperature. The actual proportionality factor depends somewhat on the shock generator angle under consideration, and is measured to be 0.956 and 0.944 for shock generator angles of 10° and 4° respectively.

Since the test times typically varied between 1 and 3 minutes, it is necessary to quote values of stagnation and wall conditions time-averaged over the actual length of a test. These averages, and the resulting Reynolds number per inch, are tabulated in Table II for the measurements of surface static pressure and flow field quantities. The variations of these averages resulted from the day-to-day change in ambient conditions:

TABLE II: TEMPERATURE TEST CONDITIONS FOR SURFACE STATIC PRESSURE AND FLOW FIELD MEASUREMENTS

$T_{o\text{ave}} = 445 \pm 18^{\circ}R$
$T_{w\text{ave}} = 503 \pm 17^{\circ}R$
$Re_{\text{inch ave}} = 1.76 \times 10^6 \pm 6\%$

The test times for heat transfer studies were significantly shorter, with a maximum of 30 seconds. Actual data was only taken for about 7 seconds, resulting in an insignificant change in temperature conditions during the data taking process, thus eliminating the need for averaging. The variations from run-to-run, however, are still experienced as indicated in Table III.

TABLE III: TEMPERATURE TEST CONDITIONS FOR HEAT TRANSFER TESTS

$T_o = 480 \pm 15^{\circ}R$
$T_w = 510 \pm 15^{\circ}R$
$Re_{inch} = 1.57 \times 10^6 \pm 5\% \quad (P_o = 100 \text{ psia})$
$\frac{T_w}{T_{aw}} = 1.15 \pm 0.04$
$50^{\circ}R < (T_w - T_{aw}) < 85^{\circ}R$

2.3 Instrumentation and Techniques

2.3.1. Eccentric, Rotatable System

The test section features two 12 inch diameter observation/instrumentation ports (see Fig. 4) which render a unique flexibility for mounting optical windows, surface instrumentation, and probe drives for covering the complete area of interest without affecting the shock generator positioning and actuating mechanism. A line drawing of the eccentric, rotatable system which can accomodate surface instrumentation as well as probe drives is shown in Fig. 6. It consists of a large 12 inch diameter plug carrying a smaller 7 inch diameter plug 2 inches off center. This smaller plug has a 2 inch diameter hole located again 2 inches

off center. The actual instrumented plugs are located in this 2 inch hole. The various plugs were fabricated to close tolerances to get a flush surface inside the tunnel and sealed with O-rings. The rotatable system has been provided with scales on the outside so one can reach a given location by rotation to the desired angles.

2.3.2. Static Pressure Plug and Scanivalve

The 2 inch diameter surface static pressure plug contains 45 static pressure holes distributed in 3 rows of 15 each (see Fig. 7). The typical spacing of taps in a row is 0.100 inches. The tap diameter is 0.032 inches for the 2 outer rows and 0.024 inches for the middle row. Although there is, in practice, no upper limit to the instrumentation density that can be obtained with the eccentric, rotatable system, the static pressure plug has been designed in such a way that a simple 180° turn of the instrumented plug relocates the taps at positions midway between their location before the 180° rotation. This effectively produced an instrumentation density of one tap per 0.050 inches, or 10 taps per initial boundary layer thickness.

The 45 surface pressures were sampled by a 48-port Model 48J4 Scanivalve which was connected to the taps by plastic tubing. The pressures were converted to electrical signals by a Pace transducer. Although the volume between the Scanivalve and the Pace transducer was minimal and the Scanivalve case was vented to a reservoir held at the undisturbed tunnel static pressure, the scanner still required a minimum of 0.4 seconds per reading to avoid problems with pressure-time lag at the transducer when the Scanivalve was stepped through a pressure gradient.

An absolute upper bound to the errors caused by pressure-time lag in the scanner has been obtained without effort. The 180° turn of the plug to

obtain the higher instrumentation density, while keeping the same plastic tubing connections and the same Scanivalve rotation direction, reverses the apparent sign of the pressure gradient as observed by the Scanivalve. The true static pressure distribution is thus bound by the two sets of data obtained for different plug orientations.

Two of the four static pressure taps on the shock generator were also sampled by the Scanivalve; the remaining two were measured by two separate Pace transducers connected to spare channels of the electronic data system.

2.3.3. Heat Transfer Measurement

2.3.3.1. Introduction

The experimental method used to determine the local convective heat transfer rates was quasi-transient and calorimetric in nature. The temperature decrease with time of a piece of copper of known mass and exposed surface area gave the heat transfer rate directly. The driving potential for this heat transfer is determined by the tunnel operating characteristics as discussed in Section 2.2.1. To prevent the small pieces of copper, called slug calorimeters, from reaching the adiabatic wall temperature shortly after tunnel start, a tiny jet of hot air was impinged on the rear side of the slug calorimeter to control its temperature while the tunnel was running.

The heat transfer data was derived under the condition of uniform wall temperature along the test surface. To satisfy this condition, the slug calorimeter temperature was raised by the jet to about 40°R above the surrounding wall temperature while the tunnel was running. At that time, the heating jet was cut off and the high speed data acquisition system started. After about 3 to 7 seconds, the slug calorimeter had reached a temperature well below the wall temperature of the tunnel, and the data system was stopped. The

temperature-time gradient, from which the heat transfer rate was calculated, was then evaluated at the time that the slug calorimeter temperature equaled the surrounding tunnel wall temperature, so that non-uniformities in test surface temperature were avoided.

The cycle of heat transfer measurement can be repeated during a tunnel run. The restriction in the number of cycles taken was determined by the data processing rate of the acquisition system.

2.3.3.2. Hardware

A photograph of the 2 inch diameter heat transfer plug, which could be located in the eccentric, rotatable system, is shown in Fig. 8. This instrumentation is a later development of two similar heat transfer plugs used in the earlier work (Ref. 4). The detailed geometry of the slug calorimeter arrangement and the hot air supply tube is shown in a line drawing presented in Fig. 9. The eight slug calorimeters are each 0.088 inch in diameter and 0.040 inch thick and are separated from the 2 inch brass plug by insulators made of linen based phenolic. Alumel-chromel thermocouple wires, 0.005 inch in diameter, were used to measure the temperature of the slugs. Two tiny holes of 0.006 inch diameter were drilled through each slug near its center to accommodate the wires. They were soldered to form a thermocouple junction within the copper slug.

Small tubes, with an inside diameter of 0.040 inches, are located within 0.12 inches of the back of the slugs. These eight tubes were scaled up-and connected to a single half inch diameter supply tube within the 2 inch plug itself. Compressed air was tapped from the shop air system at a maximum pressure of 120 psia, passed through a boiling water heat exchanger and supplied to the half-inch tube. A three-way valve located in the line immediately before

the 2 inch plug, could exhaust the hot air to the tunnel room or to the instrumentation.

Two wall temperature sensors are located in the 2 inch brass plug between the 8 slug calorimeters. All thermocouple wires were led to a single reference temperature bath. Both legs of each thermocouple junction, the alumel and chromel wires were connected to copper lead wire, and these two new junctions (chromel-copper, alumel-copper) were held at the water-ice point. These copper wires were connected to the inputs of very high impedance linear amplifiers. This procedure of referencing both legs avoids the generation of thermal emfs at the input terminals of the amplifier.

2.3.3.3. Test Procedures

Periodic checks of the thermocouples were made at room temperature. This was done by removing the instrumentation from the tunnel and placing it in an isothermal enclosure together with a mercury thermometer. At this known temperature, the output of the data system, after calibration with an accurate millivolt source, was compared with the standard for alumel-chromel thermocouples as determined by the U. S. National Bureau of Standards.

The actual procedure for taking heat transfer measurements consisted of starting the tunnel and keeping the slug calorimeters at a temperature close to the tunnel wall temperature. After the shock generator was rotated to the desired angle, and the slugs were heated to about 40°R above the wall temperature, the data acquisition system was started and the three way valve in the hot air supply line was turned to exhaust to the tunnel room. This suddenly stopped the heating process and consequently the slugs decreased in temperature. After about 7 seconds the data system was stopped. A typical slug temperature-time trace during this process is shown in Fig. 10.

The actual speed of the multiplexer was 200 readings per second. With 10 channels this results in 20 readings per thermocouple per second. Although the in-house IBM System 7 computer can record as many as 1000 readings per second, and store up to 1600 readings, the overall data through-put rate was limited by the connection between the System 7 and the main computer, which operates on a time sharing basis. This resulted in a time-averaged data flow rate to the main computer of about 10 readings per second. Thus, short heat transfer runs could be made successively with time intervals of about 5 minutes.

The spacing between the slug calorimeters was 0.45 inches. Their location was such that a simple 180° turn of the 2 inch plug resulted in a doubling of the instrumentation density.

2.3.4. Probe Drive Mechanism

To carry out detailed flow field measurements in the region of interest, a probe drive system was built and is attached to its own 7 inch plug that fitted into the eccentric, rotatable system. A photograph and a line drawing of the assembly are presented as Figs. 11 and 12, respectively. This probing system is different from the one used in the earlier work (Ref. 4), although some parts are the same. The earlier work was performed with a probe system that extended all the way across the tunnel to measure the boundary layer interaction on the wall opposite to the one on which the probe drive was mounted. Since the region of interest extended into the streamwise corner formed by the test wall and the shock generator, the earlier system would be expected to cause local flow blockage if the main streamlined probe support were mounted close to the shock generator. Therefore, a new mechanism was designed with the probe extending from the wall on which the interaction is to be measured.

The assembly can move a probe normal to the wall and also yaw it around its tip simultaneously. This was made possible by locating the probe stem 0.75 inches off center in a 2 inch plug that is free to rotate. To obtain a good bearing, the 2 inch plug was fabricated from stainless steel and matched to an aluminum-bronze bushing in the larger plug. The rotation of the probe and the 2 inch plug was provided by a reversible d.c. motor with an integral reduction gear box. A worm, mounted on a short shaft connected to the motor by a set of bevel gears, turned the worm wheel that is doweled into the main probe holder shaft, which rotates the 2 inch plug. This probe holder shaft has a cam that can slide up and down in a slot to allow the movement of the probe normal to the wall.

The translation of the probe was achieved by moving the complete yaw actuator with a precision screw drive. This screw was connected by a coupling to a second reversible d.c. motor.

The vertical movement was measured by a precision linear transducer, which was calibrated against a dial gage. A ten turn potentiometer connected by a reduction gear to the small shaft of the worm, indicated the angular displacement. It was found essential to be able to repeat very accurately the angular settings of the probe with respect to a fixed reference, even after the assembly had been relocated by turning it. This objective was achieved by mounting a small mirror on top of the probe holder shaft and using the reflected image of a small helium-neon laser beam at a distance of 4 feet as an angle indicator.

Five different probes that can be mounted in the probe holder shaft, were constructed, see Fig. 13. These probes were sealed with an O-ring against the 2 inch plug. The probes will be discussed in the next three sections.

2.3.5. Cobra Probes

2.3.5.1. Yaw Angle - Pitot Pressure Probe

All probes were fabricated from stainless tubing of various sizes.

The probe stem, made of two concentric tubes silver soldered together, has a final outside and inside diameter of 0.125 and 0.074 inches respectively, to provide the structural stiffness required for its maximum extension of 2.1 inches from the wall. These stems were not streamlined, like the cobra probe used in a similar study by Peake (Ref. 8), since large flow angle variations with distance from the wall are present and can be expected to result in a greatly enlarged apparent size of a streamlined probe stem to the cross flow, resulting in extraneous flow interference.

The yaw-pitot probe tip, extending 0.75 inches upstream of the stem, was manufactured from a set of three hypodermic tubes soldered together for rigidity. These three tubes had an original outside diameter of 0.024 inch, but were rolled flat, resulting in a tip height of 0.016 and a width of 0.080 inch. The outer tubes were cut back at 45 degrees to form a cobra probe, of which the center tube functions as a rectangular pitot. A frontal view of the actual probe, photographed through a microscope after all the tests had been completed, is shown at 37 times true size in Fig. 14. The three small tubes were stepped up to an outside diameter of 0.033 inches and led through the probe stem.

Although the angle sensitivity of this yaw probe has been calibrated, as will be discussed in Section 2.4.5., it was mainly operated as a null device. The probe was moved continuously through the flow at a varying extension rate, while being kept aligned by observing the differential pressure of the outer tubes. This resulted in a total time for a 2 inch survey of 2 to 4 minutes,

depending upon the skewness of the profile obtained. This extension rate was sufficiently slow so that no pressure-time lag occurred.

Periodic checks of the null position of the probe were made by locating it in the free stream upstream of the interaction region with an undeflected shock generator. A hysteresis of 0.16 degrees was observed in the null position of the probe if this angular setting was approached from different directions. To avoid any errors, it was necessary to approach the null from the same direction in any particular survey, if possible. Yaw angle surveys that have a change of sign in the angle variation with distance from the wall have been corrected for the hysteresis error of 0.16 degrees *a posteriori*.

2.3.5.2. Pitch Angle-Pitot Pressure Probe

To investigate the boundary layer on the surface of the shock generator, it was found important to fabricate a cobra probe that is angle sensitive in a plane rotated 90° from the one of the yaw-pitot probe. The drive mechanism used for this probe is the same as for the yaw-pitot probe. The operating procedure, however, had to be different, since the drive cannot vary the pitch angle of a probe, thus eliminating the possibility of using this probe as a nulling device.

The movement of the probe tip normal to the surface of the shock generator was made possible by mounting the probe in the probe holder shaft with a 180° difference in orientation, with a probe tip location 1.5 inches away from the center of rotation, and subsequently yawing the mechanism. The pitch angle of the flow was derived by using the angle calibration obtained for the yaw-pitot probe.

The minimum outside dimension of the tip is 0.011 inches as shown in Fig. 15. This small size of the tip resulted in a slower time response to a

pressure change, which made it more practical to measure the profiles point by point, rather than through continuous movement. An enlarged photograph of the tip is shown in Fig. 14.

2.3.6. Static Pressure Probe

To obtain local values of the static pressure in the flow field, a small cone-cylinder probe was designed, to be used in conjunction with the drive mechanism. The design consists of a 20° half-angle cone tip on a cylindrical body constructed from 0.025 inch hypodermic tubing. Two static pressure orifices of 0.008 inch diameter, 180° apart, 11 diameters downstream of the tip, and followed by a 10 diameter length of straight tubing, are shown in Fig. 15. These orifices are located at the center of rotation of the probe. Photographs, taken through a microscope, of both the tip and the static pressure orifices are shown in Fig. 16.

The probe was traversed continuously, while being kept aligned. This procedure involves an X-Y plotter, which displays the position and the angular orientation of the probe. The probe was traversed in such a way that the plotter pen followed an already drawn line that represented the angle information obtained from the yaw-pitot probe. This procedure is straightforward but tedious.

Some probe-wall interference, angle sensitivity and probe to oblique shock wave interaction has been observed and will be discussed in Section 2.4.6 under data uncertainties.

2.3.7. Total Temperature Probes

Two fine wire probes were constructed, according to a design based on hot-wire concepts, to measure the local total temperature through the interaction flow field. The probes basically consist of a fine thermocouple wire

spanning two supports. These probes can be used close to the test surface by making the supports at a slight angle with respect to that surface and the wire parallel to it. Two probes of this type were made, one with the wire parallel to the tunnel wall, indicated as total temperature probe I in Fig. 13, and one with the wire parallel to the shock generator surface, total temperature probe II.

The actual sensing element is a chromel-alumel thermocouple junction midway between the two supports, which were also made of chromel and alumel. All joints were welded for strength purposes. The two supports pass through a ceramic insulator held in the probe stem with epoxy. The diameter of the fine wire is 0.002 inch and the overall aspect ratio was 50, as shown in Fig. 15. Two photographs of the tips of one of the probes are presented as Fig. 17 at approximately 60 times true size. One can observe the thermocouple junction in the fine wire and can also notice that the support tips have been cut back to form a wedge.

The total temperature surveys were performed using the same procedure as was used for the static pressure probe in keeping the probe aligned with the known flow direction while making a traverse.

2.3.8. Data Acquisition Systems

During the course of the study many different configurations of the electronic data gathering system were employed, as was also reported in the earlier study (Ref. 4). The basic variation is the rate at which the data was taken, the system involving the Scanivalve being the slowest, and the heat transfer studies having the highest data rate. The major improvement compared to the earlier work, concerned the speed of the ITI multiplexer, which has been increased from 100 to 200 readings per second in order to be able to evaluate

the temperature-time gradients in the heat transfer technique more accurately. Periodic checks were made by comparing standard inputs with the final output at the computer end to insure that the complete system operated up to its specifications. A typical flow diagram showing a system configuration for flow field surveys, is shown as Fig. 18 for completeness.

2.4 Estimated Uncertainties and Reduction of Data

2.4.1. Transducer Calibrations

All the pressures in the study were measured by Pace variable reluctance transducers referenced to vacuum. These transducers have interchangeable diaphragms and their pressure operating range can thus be changed. They were calibrated against accurate Heise and Wallace & Tiernan gauges.

The thermocouple signals were fed into high impedance Datel linear amplifiers. The calibration was made by switching a standard millivolt source to the input of the amplifiers and using the temperature-millivolt tables issued by the U. S. National Bureau of Standards.

The traverse distance and the angular displacement of the probe were indicated by a linear transducer and ten turn potentiometer respectively, which were calibrated against dial indicators.

All the transducers were calibrated before each run. Great care was taken in obtaining precise calibrations; they were observed to be linear and repeatable within the accuracies quoted in Table IV.

TABLE IV: TRANSDUCER ACCURACIES

Transducer	Full Scale	Accuracy	% of F.S.
stagnation pressure	200 psia	± 0.4 psia	± 0.2
pitot pressure	50 psia	± 0.1 psia	± 0.2
surface static pressure	15 psia	± 0.02 psia	± 0.14
flow static pressure	10 psia	± 0.04 psia	± 0.4
Δp pressure	5 psia	± 0.005 psia	± 0.1
temperatures	530 °R	± 1.0 °R	± 0.2
angular displacement: α	60°	± 0.05 °	± 0.08
probe traverse distance: Z	2.1 inch	± 0.001 inch	$\pm 0.05\%$

2.4.2. Shock Generator Deflection Angles

The shock generator was moved manually by means of a screw drive manufactured to close tolerances (see Fig. 4). Its deflection angle is directly related to a mechanical counter geared to the drive shaft and the various deflection angle settings could be repeated to within 0.05 degrees.

Two shock generator deflection angles are defined in this study. One is the geometrical generator angle, ϕ_G , which represents the physical position of the shock generator surface with respect to the tunnel axis. A second is the effective shock generator angle, α_G , which is a number computed from the average value measured by the static pressure taps on the generator and the upstream free stream Mach number using oblique shock theory. It should be noticed here that these effective shock generator angles will slightly depend upon the particular location of the generator taps since it can be expected that the generator surface static pressure distribution is not uniform. The

"nominal shock generator angle" has been adopted as the nomenclature, indicating the effective or geometrical one rounded off to an integer value.

The displacement effect of the boundary layer growing on the surface of the generator is considered to be a first order approximation of the difference between the effective and geometrical shock generator angles. This displacement thickness, as will be discussed later, was measured at $X = 7.6$ inches for nominal generator angles of 4 and 10 degrees and was found to be 0.0287 and 0.0269 inches respectively. This allows one, by assuming linear growth of the displacement thickness, to compute $(\alpha_G - \phi_G)$ for 4° and 10° and to compare it with the actual difference found. The results, for all the shock generator angles considered in this study, are presented in Table V.

TABLE V: SHOCK GENERATOR ANGLES (DEGREES)

Nominal S.G. Angle	ϕ_G Geometrical	α_G Effective	$(\alpha_G - \phi_G)$ Measured	$(\alpha_G - \phi_G)$ Computed from δ^*
2	1.65	2.00	0.35	
4	3.75	4.00	0.25	0.22
6	5.65	6.10	0.45	
8	7.65	8.00	0.35	
10	9.75	10.00	0.25	0.20
12	11.80	12.05	0.25	
13	12.80	13.10	0.30	
14	13.80	14.10	0.30	

2.4.3. Surface Static Pressure

The most usual method of measuring surface static pressure (also employed in this study) by using a hole drilled in and normal to the test surface, is subject to errors. Great care has been taken to avoid burrs, rounded edges or other imperfections, but even when the hole has a near perfect geometry a residual error remains. Franklin and Wallace (Ref. 9) have measured this residual "static-hole" error in a most definitive study by using transducers mounted flush with the surface.

We may compute this "static-hole" error, using the universal relation presented in Ref. 9 and extending it to compressible flow by evaluating the density and kinematic viscosity at the wall temperature. The resulting "static-hole" error for the initial boundary layer flow with a hole diameter of 0.032 inch is found to be 10% of the local shear stress. But since the shear stress is only 0.7% of the local static pressure level, this does not produce any significant error even if the shear stress is allowed to increase by a factor of five in the interaction area. It is interesting to note that this result does not directly depend upon the relative size of the hole compared to the spatial scale of the boundary layer.

There will be a second error in the static-hole reading if pressure gradients are present, which the Franklin and Wallace correlation did not take into account. This error can also be expressed in terms of displacement, e , of the effective center from the geometrical center and can accordingly be estimated by making the physical assumption that the effective center remains within the hole diameter, d (e.g., $-\frac{1}{2} < \frac{e}{d} < \frac{1}{2}$). The maximum pressure gradient in the present work has been observed to be 70% per inch and this results,

with a maximum hole diameter of 0.032 inch, in an upper bound of the pressure gradient related static-hole error of $\pm 1\%$.

Additional uncertainties in the data obtained, arise from the geometry of the test surface. Examples of these would be leaks along the edges of the 2 inch static pressure plug, however small, which could not be eliminated, and the pressure-time lag in the Scanivalve (see Section 2.3.2). These two items can be appraised if one realizes that any one static pressure trace consists of at least four different plug locations, each sampled with opposite directions in Scanivalve rotation.

The overall uncertainty of the static pressure data is estimated to be less than $\pm 2\%$ of the upstream static pressure level.

2.4.4. Heat Transfer Studies

2.4.4.1. Heat Transfer Data Reduction

The procedure for taking the actual measurements has been described in Section 2.3.3 and typical temperature-time traces have been presented as Fig. 10.

Let t_0 indicate the time at which the slug and tunnel wall have the same temperature and evaluate the heat transfer rate at time t_0 . From an exponential curve, fitted to a total of N points symmetrically distributed around time t_0 , one can evaluate the temperature-time gradient of the slug as given by Equation 1.

$$\left[\frac{dT_s}{dt} \right]_{t_0} = (T_w - T_{aw}) \frac{\sum_{i=1}^N (t_i - t_0) \ln \left\{ \frac{T_{si} - T_{aw}}{T_w - T_{aw}} \right\}}{\sum_{i=1}^N (t_i - t_0)^2} \dots \quad (1)$$

where i is a successive time-index of data points in a trace.

The conservation of energy requires that the rate decrease of the internal energy of the slug is equal to the sum of the convection, radiation and conduction. By neglecting radiation and conduction one can compute the convective heat transfer rate directly from Equation 2:

$$q_c = - \frac{m_s c_s}{A_s} \left(\frac{dT_s}{dt} \right)_{t_0} \quad (2)$$

Finally, the heat transfer coefficient follows from:

$$C_h = \frac{q_c}{\rho_1 u_1 c_p (T_w - T_{aw})} \quad (3)$$

It should be noted here that this heat transfer coefficient, as it is evaluated within the interaction region, has been non-dimensionalized by the mass flow rate, $\rho_1 u_1$, in the free stream ahead of the interaction. This definition also incorporates the assumption that q_c is proportional to $\rho_1 u_1 (T_w - T_{aw})$ for small test to test variations in tunnel total temperature and wall temperature. This means that if ρ_1 , u_1 , T_w and T_{aw} are evaluated at the specific conditions of each individual measurement point, C_h will be invariant for small changes in test conditions. This procedure has also been followed in the earlier work (Ref. 4).

Equation (1) has been evaluated with $N = 18$ in this study and since the time between data points in a trace is 50 milliseconds, the exponential curve spans a time period of 0.85 seconds. To check whether the results are consistent with the data points from which they are derived, a second data reduction scheme, replacing Equation (1), has also been employed. This second method divided the set of $N = 18$ points into 12 subsets of 7 consecutive points each.

For each subset the temperature-time derivative was evaluated by fitting a straight line through the 7 points. The heat transfer coefficient was obtained from Equations (2) and (3), in which the slug temperature at the central point of each subset of 7 was substituted for the wall temperature. The final heat transfer coefficient was obtained by summing the 12 coefficients obtained for the subsets and dividing by 12.

This second procedure was used to screen the coefficients derived with the use of Equation (1) for consistency with the original data, i.e. if the two methods produced coefficients that were not within 5% of each other, the trace was discarded. This requirement, however, turned out to be satisfied for 99% of the data, proving the consistency of the results obtained.

2.4.4.2. Adiabatic Wall Temperature

To measure the local adiabatic wall temperature in the interactions one needs to satisfy some very stringent requirements. The principal one is that the device used to measure it should not change the conditions of heat transfer that would exist if it were absent. This eliminates all conventional instrumentation that indicates the adiabatic wall temperature directly. An often employed alternative is to measure heat transfer rates at many different driving potentials ($T_w - T_{aw}$) and parameterizing the resulting heat transfer coefficients with respect to the unknown T_{aw} . The local adiabatic wall temperature can then be determined from the requirement that the heat transfer coefficient shall be invariant for various ($T_w - T_{aw}$). This method, however, could not be used because the driving potential is a characteristic of the present facility and cannot be changed at will for a tunnel wall mounted model.

A completely different and simple way of solving this potential problem is to discard the idea of a local adiabatic wall temperature in the interaction entirely as done in this study.

Measurements of recovery factors, r , have been obtained for supersonic flows on insulated surfaces with constant pressure and have been reported to be approximately 0.89 where r is defined in Equation (4):

$$r = \frac{T_{aw} - T_{\infty}}{T_0 - T_{\infty}} \quad (4)$$

This can be used to write the adiabatic wall temperature directly in terms of stagnation pressure for a fixed Mach number:

$$\frac{T_{aw}}{T_0} = r + (1-r) \frac{T_{\infty}}{T_0} \quad (5)$$

Hence, with $r = 0.89$, $M = 2.94$ and $\frac{T_{\infty}}{T_0} = 0.3665$ this results in

$$T_{aw} = 0.930 T_0 \quad (6)$$

Equation (6) is valid for the initial constant pressure turbulent boundary layer in this study. This relation for T_{aw} , evaluated with T_0 for every specific test, has been used throughout this study. If used in Equation (3) it results in a concise definition of the heat transfer coefficient, since the coefficient becomes directly proportional to the dimensional heat transfer rate in nonadiabatic, physical situation and no computations involving local adiabatic wall temperatures have to be executed.

2.4.4.3. Van Driest II Skin Friction Formula

It is recommended by Hopkins and Keener (Ref. 1) that the van Driest II correlation with a Reynolds analogy factor of 1.2 be used to calculate the heat transfer coefficient for near adiabatic tunnel walls exposed to supersonic Mach numbers. This scheme is claimed to predict the heat transfer coefficient within $\pm 10\%$ for near adiabatic temperature conditions. A summary of the scheme, presented as a transformation to an incompressible situation (Ref. 1), is given in the following equations.

$$\overline{Re}_\theta = \frac{\mu_\infty}{\mu_w} Re_\theta \quad (7)$$

$$1/\overline{C}_f = 17.08 (\log_{10} \overline{Re}_\theta) + 25.11 \log_{10} \overline{Re}_\theta + 6.012 \quad (8)$$

Karman-Schoenherr Eq.

$$C_f = \overline{C}_f / F_c \quad (9)$$

where

$$F_c = \frac{(\gamma-1)}{2} r M_\infty^2 / (\sin^{-1} \alpha' + \sin^{-1} \beta')^2$$

and

$$\alpha' = (2A^2 - B) / (4A^2 + B^2)^{1/2}$$

$$\beta' = B / (4A^2 + B^2)^{1/2}$$

$$A^2 = \frac{(\gamma-1)}{2} r M_\infty^2 \frac{T_\infty}{T_w}$$

$$B = (1 + r \frac{\gamma-1}{2} M_\infty^2 - \frac{T_w}{T_\infty}) \frac{T_\infty}{T_w}$$

$$C_{h_{VD}} = \frac{s}{2} C_f = 0.6 C_f \quad (10)$$

The heat transfer coefficients in the boundary layer upstream of the interaction are computed for the range of test conditions specified in Table III of Section 2.2.3 and using the following data:

$$p_0 = 100 \text{ (psia)}$$

$$\theta = 0.025 \text{ inch}$$

$$r = 0.89$$

$$s = 1.2$$

$$M_\infty = M_1 = 2.94$$

$$T_\infty = T_1 = 0.3665 T_0$$

$$\mu_\infty = \mu_1$$

resulting in: $C_{h_{VD}} = 0.000711 \pm 0.000012$.

These results show that, theoretically, the variations of temperature conditions amount only to a $\pm 1.7\%$ variation of the heat transfer coefficient in the upstream boundary layer flow.

2.4.4.4. Heat Transfer Variation with Reynolds Number

Prior to making the heat transfer measurements in the interaction region at 100 psia stagnation pressure, some preliminary measurements were carried out in the boundary layer upstream of the interaction region with an undeflected shock generator and a variable stagnation pressure ranging from 75 to 200 psia. The resulting heat transfer coefficients of these measurements divided by the van Driest value, computed as set out in Section 2.4.4, are presented in Fig. 19 as a function of both Reynolds number based on momentum defect thickness as well as stagnation pressure in psia. One observes that the measurement points are,

on the average, 10% higher than the predicted value, and fall within a band between -15% and +10%. If one realizes that the dimensional heat transfer rate varied from 0.6 to 2.4 (Btu/ft²sec.), although the heat transfer coefficient does not change significantly over the Reynolds number range, and that the same range in dimensional heating rates has been observed in the interaction, one can conclude that the technique employed certainly should indicate the correct trends and levels of C_h in the interaction region. In other words, one can consider the correct verification of the change in C_h with Re_θ to be a calibration of the technique, although it is not used as such.

2.4.4.5. Heat Transfer Data Uncertainty

Assumptions of the technique, e.g. neglection of radiation and conduction losses, have been verified and found to be correct. A good estimate of these errors has been given by Reinecke (Ref. 10) and will not be repeated here. The largest source of error in the present results, although improved compared to the earlier work (Ref. 4), is found to be in the basic inaccuracies of the temperature measurements, ($\pm 1.0^\circ R$) followed by a differentiation of the data. The final heat transfer data in the interaction is considered to have an accuracy of $\pm 15\%$ of the van Driest value. Averaged values of the results obtained, however, are believed to be much better than the number quoted above.

2.4.5. Cobra Probe Surveys

2.4.5.1. Cobra Probe Displacement Effect

A pitot probe or a cobra probe placed in a shear flow does not measure the true pressure that exists at the geometric center of the probe in a flow with no shear. The effective center is said to be "displaced" from the geometric center. If the magnitude and the direction of this displacement, Δ , are known, corrections to the pitot-probe measurements can be made for this effect.

Experiments to appraise this effect have been made by Young and Maas (Ref. 11) at low subsonic speeds. They found that the displacement towards the region of higher velocity, Δ , divided by the probe height, H , had a constant value of 0.18. This value of $\Delta/H = 0.18$ was revealed to be independent of H , the mean pitot pressure, and the magnitude of the transverse total head gradient across the probe face. More recently Allen (Ref. 12) studied this displacement effect in a turbulent boundary layer at a Mach number of 2 and his experiment yielded an average value of 0.38 for Δ/H ; it is interesting to note that Allen also observed Δ/H to be independent of H , pitot pressure, and its gradient across the probe face. An experimental study by Johannesen and Maier (Ref. 13) at a Mach number of 1.98, however, showed that there was no displacement effect in supersonic shear flow.

In view of the contradictory findings at Mach 2 and the fact that the height of the present yaw-angle/pitot-pressure probe is only 3.2% of the initial boundary layer thickness, no correction to yaw-pitot measurements have been made. This will not affect the uncertainty of the measurements in general, but may be important for the measurement points within one probe height from the test wall.

2.4.5.2. Cobra Probe Angle Sensitivity

Although the yaw angle-pitot pressure probe has mainly been used as a nulling device, it was nevertheless calibrated as a direct reading device. This calibration was achieved by moving the probe off the null position and observing the difference in pressure in the outer tubes, Δp . The procedure, performed at various static pressure levels and pitot pressures, showed that Δp varied linearly with the probe deflection angle, α_p , for small deflections ($-10^\circ < \alpha_p < 10^\circ$). The data obtained can be correlated according to

Equation (11) as shown in Fig. 20.

$$\frac{d}{d\alpha_p} \left(\frac{\Delta p}{p} \right) = C_1 \left(\frac{p_t}{p} - 1 \right) \quad (11)$$

where $C_1 = 0.036 \pm 0.004 \text{ (deg}^{-1}\text{)}$ for $-10^\circ < \alpha_p < 10^\circ$ and $1.1 < M < 3.0$.

This equation simply says that the pressure difference, Δp , is proportional to α_p and is also proportional to the difference between pitot pressure and static pressure. For supersonic flow the angle sensitivity can also be expressed with Mach number dependence only by using the Rayleigh pitot formula and $\gamma = 1.4$.

$$\frac{d}{d\alpha_p} \left(\frac{\Delta p}{p} \right) = C_1 \left\{ \left(\frac{6M^2}{5} \right)^{3.5} \left(\frac{6}{7M^2 - 1} \right)^{2.5} - 1 \right\} \quad (12)$$

$1.1 < M < 3.0$

The constant C_1 is primarily a function of the angle at which the outer tubes are cut back (45° in this study) and the ratio of the probe tip width, W , over the height, H . ($W/H = 6$ for the yaw-pitot probe.)

2.4.5.3. Cobra Probe Data Uncertainties

As discussed in Section 2.3.5.1. the yaw-pitot probe has mainly been operated as a null device. Small misalignment, however, could still occur and this has been corrected for by using Equation (11). The minimum accuracy of the flow angles obtained can be assessed by combining the accuracy of the Δp transducer with the angle sensitivity of the probe. From Equation (12) one obtains for

$$M = 1.1: \quad \Delta p / \Delta \alpha_p = 0.041 p_1 \text{ (deg}^{-1}\text{)}$$

$$\text{and} \quad M = 3.0: \quad \Delta p / \Delta \alpha_p = 0.40 p_1 \text{ (deg}^{-1}\text{)} .$$

The minimum static pressure is 3 psia; this combined with the lowest angle sensitivity at $M = 1.1$ gives:

$$(\Delta p / \Delta \alpha_p)_{\min} = 0.041 * 3 = 0.123 \text{ (psia/deg)}$$

With an accuracy of ± 0.005 (psia) for the Δp transducer, there results a maximum error for the flow angle due to probe misalignment of $\pm 0.04^\circ$.

These estimates combined with the α transducer accuracy of $\pm 0.05^\circ$ and the repeatability of angular settings of the probe drive mechanism results in the overall estimate that the flow angles measured by the yaw-pitot probe are accurate within ± 0.1 (degrees).

There is usually no problem, as there is with a static pressure probe, in obtaining accurate pitot tube measurements across an oblique shock wave, since the pitot pressure is influenced by the bow shock/oblique shock interaction at distances less than one tip height as shown by Bannink and Nebbeling (Ref. 14). The overall accuracy of the pitot measurements is therefore estimated to be well within $\pm 1\%$ of the maximum pitot pressure.

2.4.6 Static Pressure Surveys

The particular types of static pressure probe employed in this study, the cone-cylinder type, is known to create extraneous interference if the probe extends across an oblique shock wave. Back and Cuffel (Ref. 15) have appraised this interference effect between the probe bow shock and the oblique shock wave at a Mach number of 3.5 and with an oblique shock wave created by an 8.3° flow deflection. Errors up to 50% of the static pressure difference across the shock were measured. It should be remembered, however, that these errors only occur if the probe, which is approximately 20 diameters long,

extends across the oblique shock wave and thus only affects the measurements in the vicinity of the shock.

A superior method of making static pressure measurements in the vicinity of oblique shock waves is the conical static pressure probe technique, which employs a static hole on the conical surface of a probe tip. This method has the advantage that the static pressure can be measured up to one cone-tip length from the shock, similar to the behavior of a pitot probe in the vicinity of a shock. This conical static pressure probe technique has some drawbacks, namely an extensive Mach number calibration is needed, and the probe does not read the static pressure directly. An iterative procedure is then required because the Mach number is not known independently from the static pressure to be measured. The angle sensitivity of this probe, as reported by Norris (Refs. 16 & 17), can be viewed as an advantage since it could be used as a yaw meter, although this sensitivity is not as large as the one for the cobra probe employed in this study. This conical probe has not been employed in the present study because of its limited usefulness compared to the effort required.

The angle sensitivity of the cone-cylinder probe has been determined in the constant pressure boundary layer upstream of the interaction, as this might give an insight to the errors caused by an misalignment that might occur in the operational procedure described in Section 2.4.6. The results are shown in Fig. 21. One can observe that, with the probe aligned, the direct reading is within $\pm 0.4\%$ of the correct value, which compares favorably with the results obtained by Cronvich (Ref. 18). With a misalignment angle within $\pm 4^\circ$ the probe still records the correct value within $\pm 1.6\%$. Above 12° , however, the reading rapidly deteriorates.

The cone-cylinder probe also causes a wall interference at some distance from the test wall as the tip bow shock reflects from the wall and impinges on the cylinder in the neighborhood of the static-holes. This problem does not arise when the probe body is sufficiently close to the wall as shown in Fig. 21, where the data for a static-hole to wall distance of 0.050 inch is shown; in that case the probe reads the correct pressure as indicated by a wall surface static-hole.

Other uncertainties in the static probe readings remain because of its long body (20 diameters), and thus its unknown capability to resolve continuous static pressure gradients, and its unknown response to strong streamline curvature. With the exclusion of the data obtained within the vicinity of the oblique shock wave and the data that shows obvious wall interference, the readings of the cone-cylinder static pressure probe are nevertheless estimated to have an accuracy within $\pm 5\%$ of the upstream static pressure, p_1 .

2.4.7. Total Temperature Surveys

The fine wire probes used in this study are designed according to hot-wire concepts and do not record the total temperature directly, but rather indicate a wire recovery temperature, which is equal to the adiabatic wire recovery temperature if conduction and radiation losses can be neglected. Even if these radiation and conduction losses cannot be neglected, as is the case in high temperature, low density flows, it has been shown by Vas (Ref. 19) that the local total temperature can still be determined with sufficient accuracy by such a fine wire probe.

The adiabatic wire recovery temperature, as reported by Dewey (Ref. 20) is equal to 0.950 times the stagnation temperature at Mach 3. The present experiments have shown a wire recovery temperature of $0.948 T_0$ in the free

stream and thus indicates a loss by conduction of 0.2%. The present wire temperatures have been reduced to local total temperatures by assuming a constant recovery factor for the fine wire. The recovery factor is defined as a nondimensional enthalpy increase:

$$r = \frac{T_{wi} - T}{T_t - T} \quad (13)$$

with $M = 2.94$, $\frac{T}{T_0} = 0.3665$, $T_{wi} = 0.948 T_0$ and $T_0 = T_t$ in free stream, hence

$$r = \left(\frac{T_{wi} - T}{T_0} \right) / \left(1 - \frac{T}{T_0} \right) = 0.918$$

From this result we can immediately compute the total temperature as a function of Mach number from:

$$\frac{T}{T_t} = (1 + 0.2 M^2)^{-1} \quad \text{with } \gamma = 1.4 \quad (14)$$

and from Equation (13)

$$\frac{T_{wi}}{T_t} = r + \frac{T}{T_t} (1-r) \quad (15)$$

Substitute (14) in (15)

$$\left. \begin{aligned} \frac{T_t}{T_0} &= \frac{T_{wi}/T_0}{r + (1-r)(1+0.2M^2)^{-1}} \\ r &= 0.918 \end{aligned} \right\} \quad (16)$$

with

T_0 : tunnel stagnation temperature

T_t : local total temperature

T_{wi} : wire recovery temperature

M : local Mach number

This Mach number dependence does not result in any difficulties, since it is already known from the pressure measurements.

It has been assumed that the variations in the ratio of tunnel wall temperature to tunnel stagnation temperature do not influence the values obtained for T_t/T_0 in the interaction flow field. This is based on the observations that the ratio $\frac{T_w}{T_{aw}}$ is nearly a constant of 1.21 ± 0.04 . The small variations in this parameter are mainly limited to the laminar sublayer, which is of such a small physical extent from the wall that no data points have been obtained in it.

The total uncertainty of the total temperature results is estimated to be within $\pm 1\%$ of the tunnel stagnation temperature.

2.4.8. Derived Flow Field Variables

With the measured values of pitot pressure, static pressure, yaw angle and total temperature one can compute the Mach numbers, u and v velocity components and the densities throughout the flow field. But since the various measured surveys do not have an identical number of points in the Z-direction, one has to set up a standard array of Z values at which the measured quantities are to be known. This process does not involve any data interpolation since continuous surveys have been taken with many more data points than needed for the actual standard Z array.

The values of Mach number, u and v velocity components and density follow from the following equations:

$$\frac{P_t}{p} = \left(1 + \frac{\gamma-1}{2} M^2\right)^{\frac{\gamma}{\gamma-1}} \quad \text{if} \quad \frac{P_t}{p} < 1.893 \quad (17)$$

$$\frac{P_t}{p} = \left[\frac{(\gamma+1)M^2}{2}\right]^{\frac{\gamma}{\gamma-1}} \left[\frac{\gamma+1}{2\gamma M^2 - (\gamma-1)}\right]^{\frac{1}{\gamma-1}} \quad \text{if} \quad \frac{P_t}{p} > 1.893 \quad (18)$$

$$T = T_t / \left(1 + \frac{\gamma-1}{2} M^2\right) \quad (19)$$

$$\rho = P/RT \quad (20)$$

$$u = M\sqrt{\gamma RT} \cos \alpha \quad (21)$$

$$v = M\sqrt{\gamma RT} \sin \alpha \quad (22)$$

In addition, the velocity component in the Z-direction can be deduced from the u , v components and the density ρ by integration of the continuity equation:

$$w = -\frac{1}{\rho} \int_0^Z \left\{ \frac{\partial}{\partial x} (\rho u) + \frac{\partial}{\partial y} (\rho v) \right\} dz \quad (23)$$

It should be noted that the actual values of w obtained should be small compared to $\sqrt{u^2+v^2}$ since the total Mach number is based upon the u and v velocities only and could be considerably in error if large relative values of w are found. This requirement can be checked a posteriori however. Two pitch angles can now be defined, β and γ :

$$\beta = \tan^{-1} \left(\frac{w}{u} \right) \quad (24)$$

$$\gamma = \tan^{-1} \left(\frac{w}{\sqrt{u^2+v^2}} \right) \quad (25)$$

2.5 Uniformity of Initial Boundary Layer Flow

Most of the previous experiments, Stanbrook (Ref. 21), McCabe (Ref. 22), Lowrie (Ref. 23), Token (Ref. 24) and Peake (Ref. 25), have been conducted with the turbulent boundary layer developing on the sidewall of a two-dimensional nozzle. This sidewall boundary layer will be transversely non-uniform due to the presence of transverse pressure gradients in the expanding part of the nozzle which causes the boundary layer flow in the nozzle to accumulate near the center of the sidewall. The magnitude of this undesired effect increases as the nozzle Mach number increases.

In some of these studies the non-uniformity has been reduced by taking appropriate counter measures. Lowrie re-designed the nozzle layout. Peake installed a V-type vortex generator at Mach 4 to "smear out" the non-uniformity, but was only moderately successful because large transverse non-uniformities still remained which at Mach 4 reportedly are of the order of $\pm 8\%$ in static pressure and $\pm 50\%$ in displacement and momentum defect thickness. The best counter measure has probably been taken by Token who only used the central 33% of the sidewall as a test region but still was left with a 13 inch wide area. In that study, however, transverse pressure differences of $\pm 3.5\%$ remained in the test region. These non-uniformities basically limit the experimental accuracies that can be obtained within the shock wave/boundary layer interaction.

Recognizing this potential problem, the test section and shock generator have been designed such that the boundary layer entering the interaction

originates from the contoured wall in the two-dimensional nozzle, as is shown in Fig. 22. This boundary layer has been surveyed extensively and shown to be extremely uniform transversely across the central 6 inches of the 8 inch wide test section. The magnitude of the uniformity is measured to be $\pm 0.7\%$ in static pressure and $\pm 5\%$ in boundary layer displacement and momentum defect thicknesses (Fig. 23). This level of uniformity is considered to be an important improvement over previous studies in which flow field yaw angles have been measured.

2.6 Summary of Estimated Uncertainties of Data

The final experimental uncertainties, as discussed in Section 2.4, are larger than the accuracies of the transducers used to obtain the various data. This, however, does not imply that the uncertainties are inherent to the basic instrumentation techniques employed. The specific application of the techniques in each part of the interaction is the factor which determines the final uncertainty of the data. The percentages given are therefore an upper bound for the accuracy and many results are believed to be more accurate than the numbers quoted in Table VI.

TABLE VI: SUMMARY OF DATA UNCERTAINTIES

Quantity Measured	Symbol	Uncertainty
stagnation pressure	p_0	$\pm 0.5\%$ at 100 psia
stagnation temperature	T_0	$\pm 0.5\%$ of 450°R
surface static pressure	p	$\pm 2\%$ of p_1
surface heat transfer	C_h	$\pm 15\%$ of C_{h1}
flow static pressure	p	$\pm 5\%$ of p_1
pitot pressure	p_t	$\pm 1\%$ of p_{t1}
local total temperature	T_t	$\pm 1\%$ of T_0
flow yaw angle	α	± 0.1 degree
probe location	Z	± 0.002 inch
effective shock generator angle	α_G	± 0.1 degree

2.7 Summary of Data

The data obtained is graphically presented in 10 detailed appendices, A through J.

Appendix A contains the surface static pressure distributions obtained along instrumentation lines parallel to the Y axis for various shock generator angles and X locations. Both the computed shock location as well as the static pressure level measured at the surface of the shock generator are indicated for each trace.

Appendix B shows the isobar patterns obtained directly from the data in Appendix A. The pressure p_1 and p_2 are the static pressures in front of the interaction and on the surface of the generator. The increase in surface

static pressure, going from p_1 to p_2 , is divided into 10 equal steps and the corresponding 10 isobars at constant values of $(\frac{p-p_1}{p_2-p_1})$ are shown in the figures of the appendix.

Appendix C summarizes the heat transfer results, non-dimensionalized by the computed van Driest II values, obtained for the initial boundary layer (see Section 2.4.4.3). The data shown is taken at instrumentation stations parallel to the Y axis at various X locations and for 7 shock generator angles ranging from 2° to 14° in 2° increments. The corresponding surface heat transfer patterns are presented in Appendix D.

Appendices E and F contain the results obtained with the yaw-angle/pitot-pressure probe. The tick marks on the $Z = 2.0$ inches axis indicate the level which the traces theoretically should approach at large distances from the wall. The Appendices total 49 surveys each, which can be divided into 7 groups as shown in Table VII.

TABLE VII: YAW-PITOT SURVEY GROUPINGS

NSGA degrees	X inches	Number of surveys
0	3.561	5
4	7.579	16
4	7.079	5
4	5.079	3
10	7.599	14
10	7.099	3
10	5.099	3

Appendix G presents, in graphical form, the results of the flow field measurements. The data affected by probe-wall interference (Section 2.4.6) has been eliminated and replaced by a linear interpolation of the values measured at $Z = 0.25$ inch and by the surface instrumentation. Figure G-8 shows two profiles where the cone-cylinder static pressure probe interfered with the shock-wave at larger values of Z resulting in off scale values which have been replaced by a constant estimated level. A total of 29 surveys are plotted which can be divided into groups as shown in Table VIII:

TABLE VIII: STATIC PRESSURE SURVEY GROUPINGS

NSGA degrees	X inches	Number of surveys
4	7.579	12
4	5.079	3
10	7.599	11
10	5.099	3

The data obtained with the fine-wire thermocouple probe I is plotted in Appendix H. This data can be divided into similar groups as the data of Appendix G, as shown in Table IX.

The final two Appendices, I and J, contain the results obtained with the pitch-pitot probe and thermocouple probe II respectively. The final three traces of Appendix J, taken at the same location, with the same shock generator angle, but with different shock generator temperatures (see Ref. 5), show the

limited extent to which the shock generator temperature influences the total temperature distribution in the interaction flow field.

TABLE IX: TOTAL TEMPERATURE SURVEY GROUPINGS

NSGA degrees	X inches	Number of surveys
0	3.561	1
4	7.579	10
4	5.079	3
10	7.599	9
10	5.099	3

3. CONCLUDING REMARKS

A detailed study of three-dimensional flow fields and surface phenomena caused by the interaction of an oblique shock wave, a shock generator and a high Reynolds number turbulent boundary layer, was carried out. This initial turbulent layer has been shown to be uniform in the transverse direction across the central part of the test wall. The main results obtained during the present contract effort include detailed surface static pressure distributions and surface heat transfer patterns from which a physical insight into the spatial scale of the phenomena may be derived. In addition, detailed flow field measurements were conducted to fully resolve the flow field, including all three velocity components. This combination of detailed surface data and associated flow field surveys provides the opportunity to check how the two sets are related and may lead to a deeper understanding of the problem under consideration.

Special attention was given to the mathematical formulation of the physical boundary conditions which existed in the experimental configuration. In addition, the validity of the experimental methods employed to obtain the various data was discussed extensively and was complemented by a detailed tabulation of the estimated upper bounds for the accuracies of the various data. These considerations are considered to be important since the final analysis of the experimental data obtained, will heavily rely on the accuracy achieved. No discussion in terms of the physical interpretation of the presented data in relation to the problems of viscous-inviscid interactions is given.

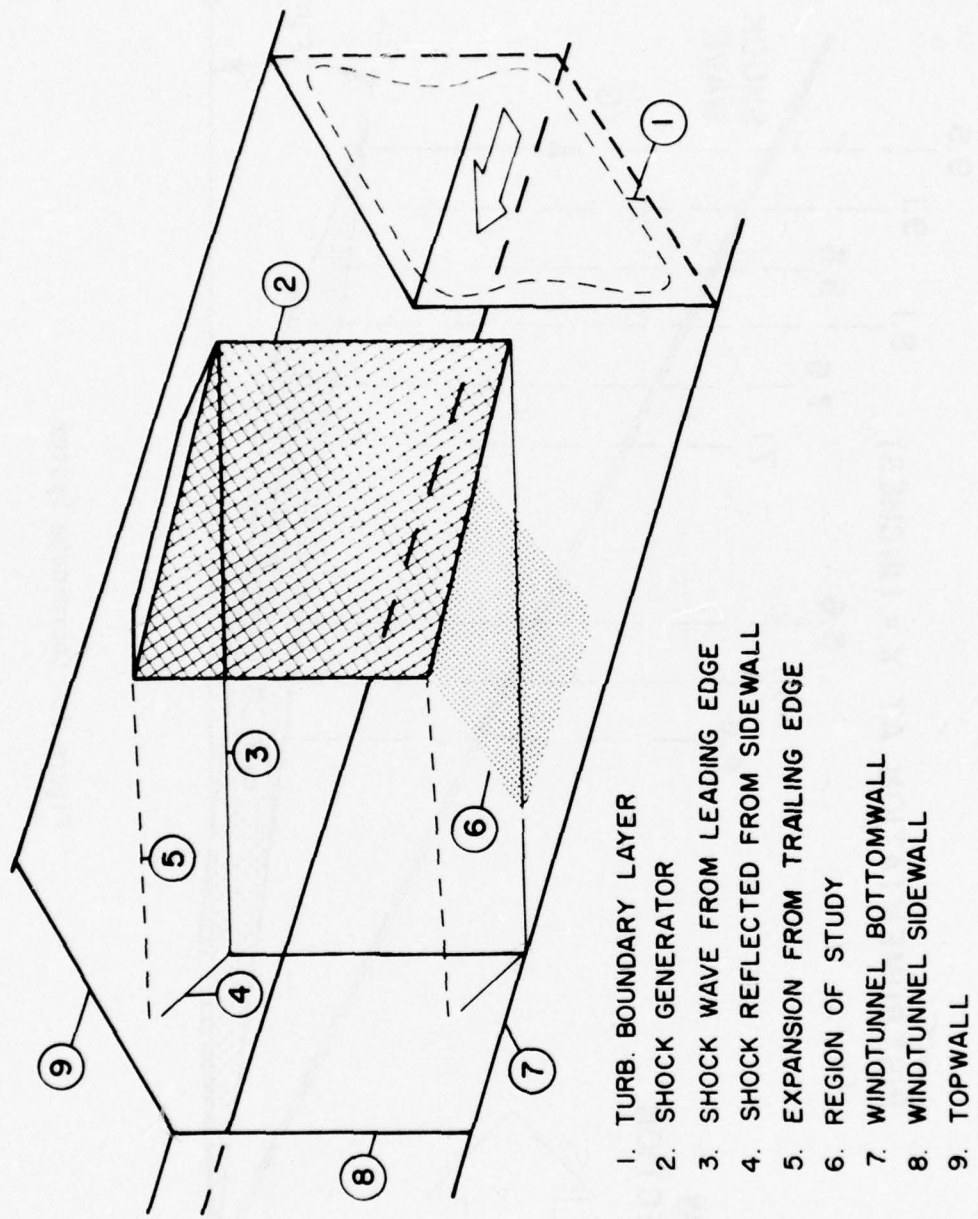


Figure 1. Schematic of Experimental Configuration.

$$Y_G = Y - X \cdot \tan(FIE_G)$$

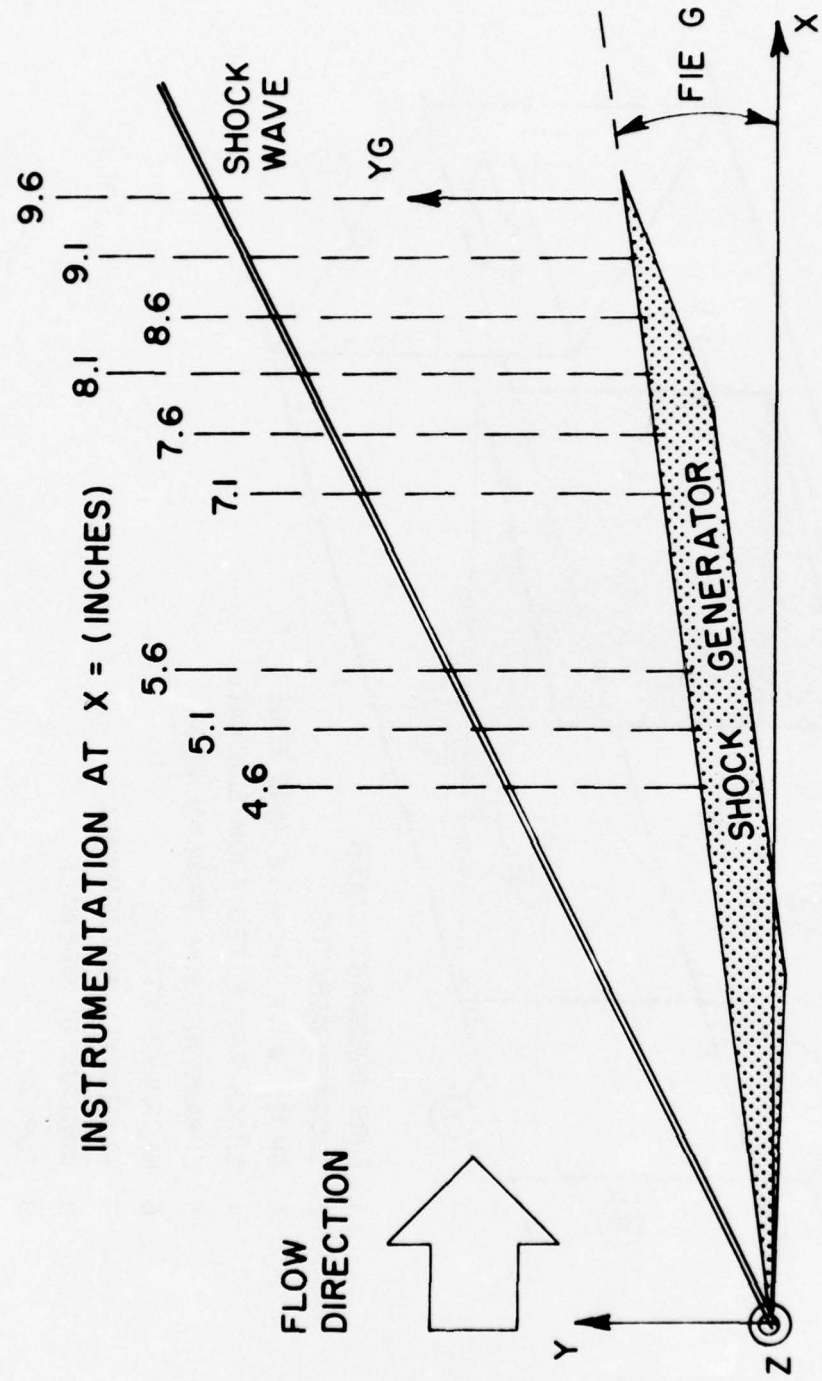


Figure 2. Coordinate System.

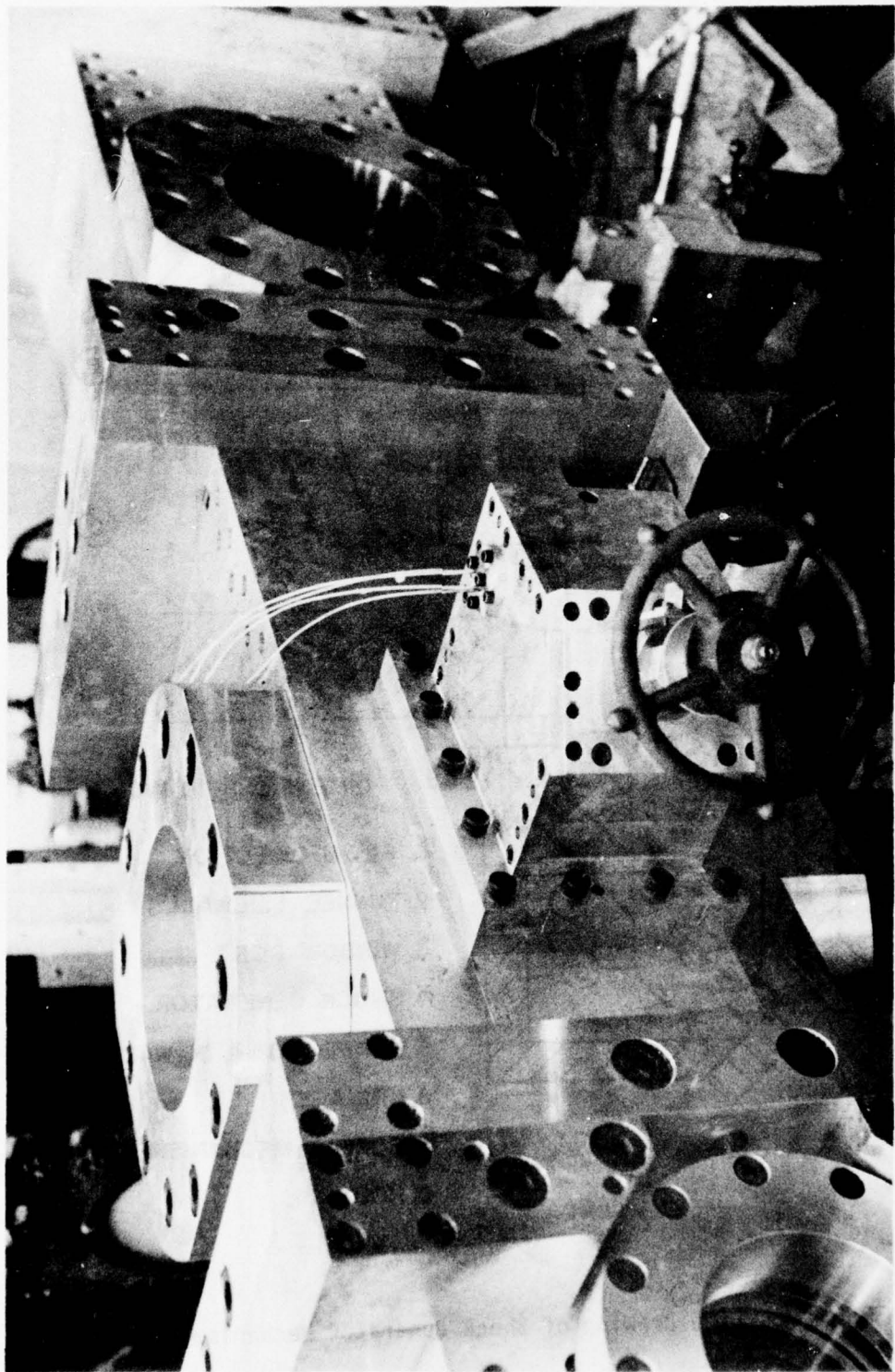


Figure 3. Photograph of Wind Tunnel Test Section.

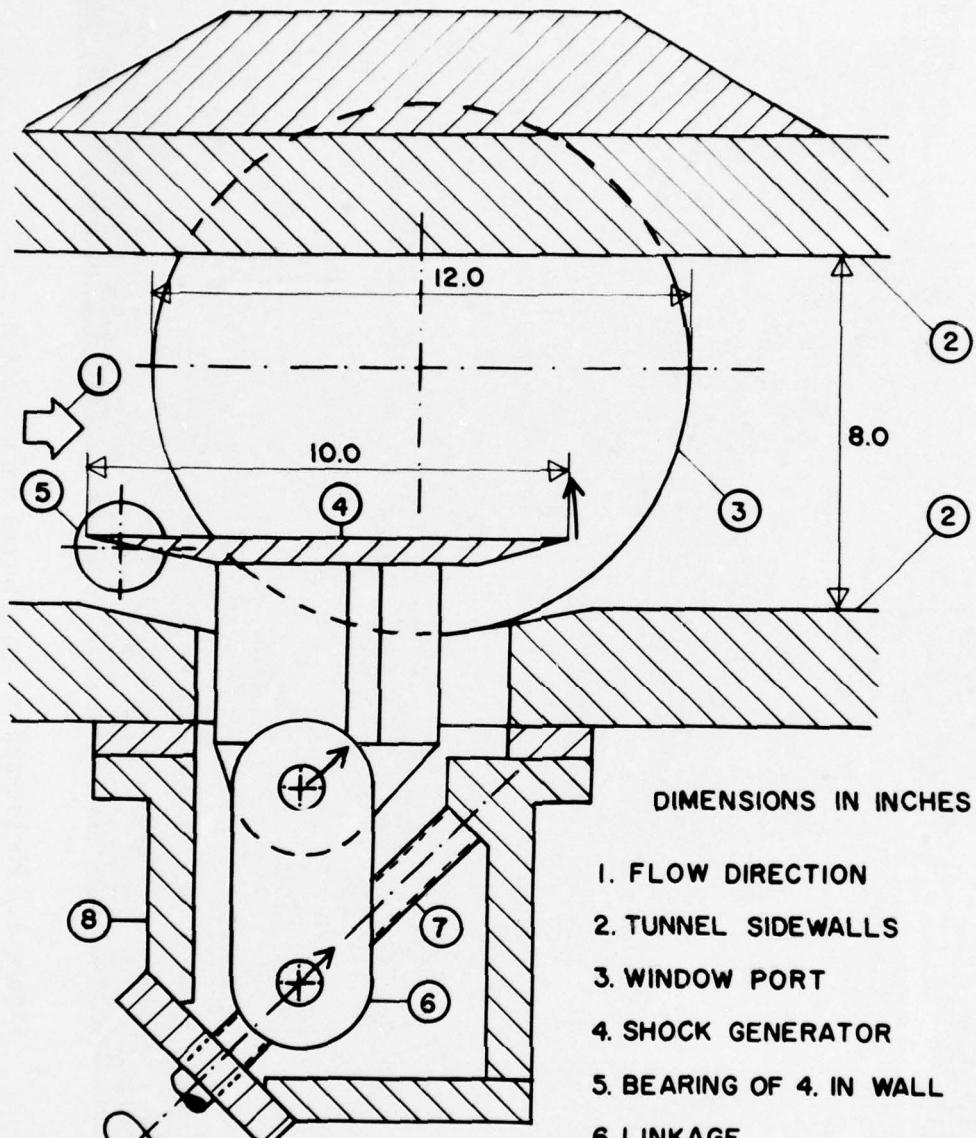


Figure 4. Line Drawing of Shock Generator Mechanism.

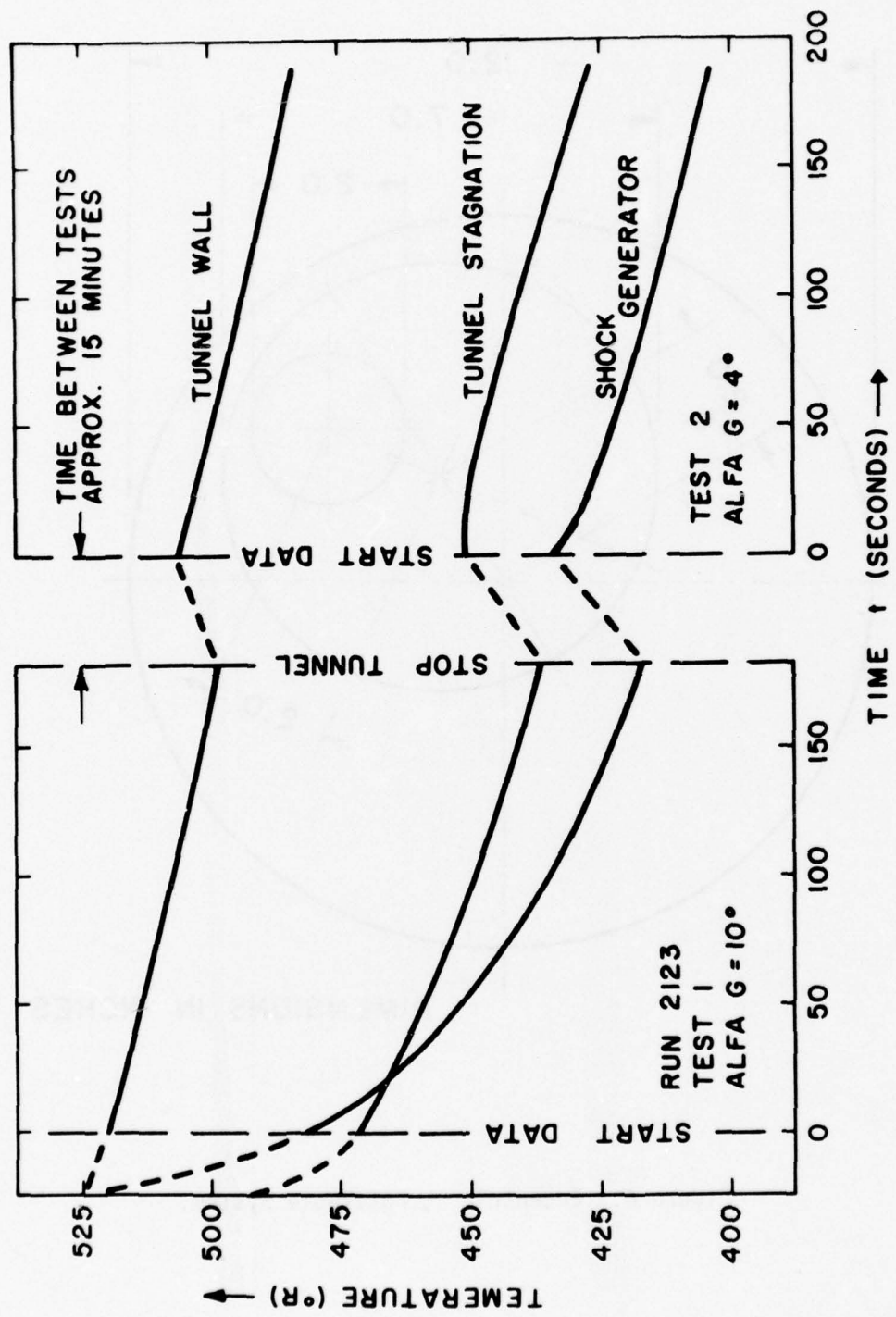


Figure 5. Tunnel Temperature Variations with Time.

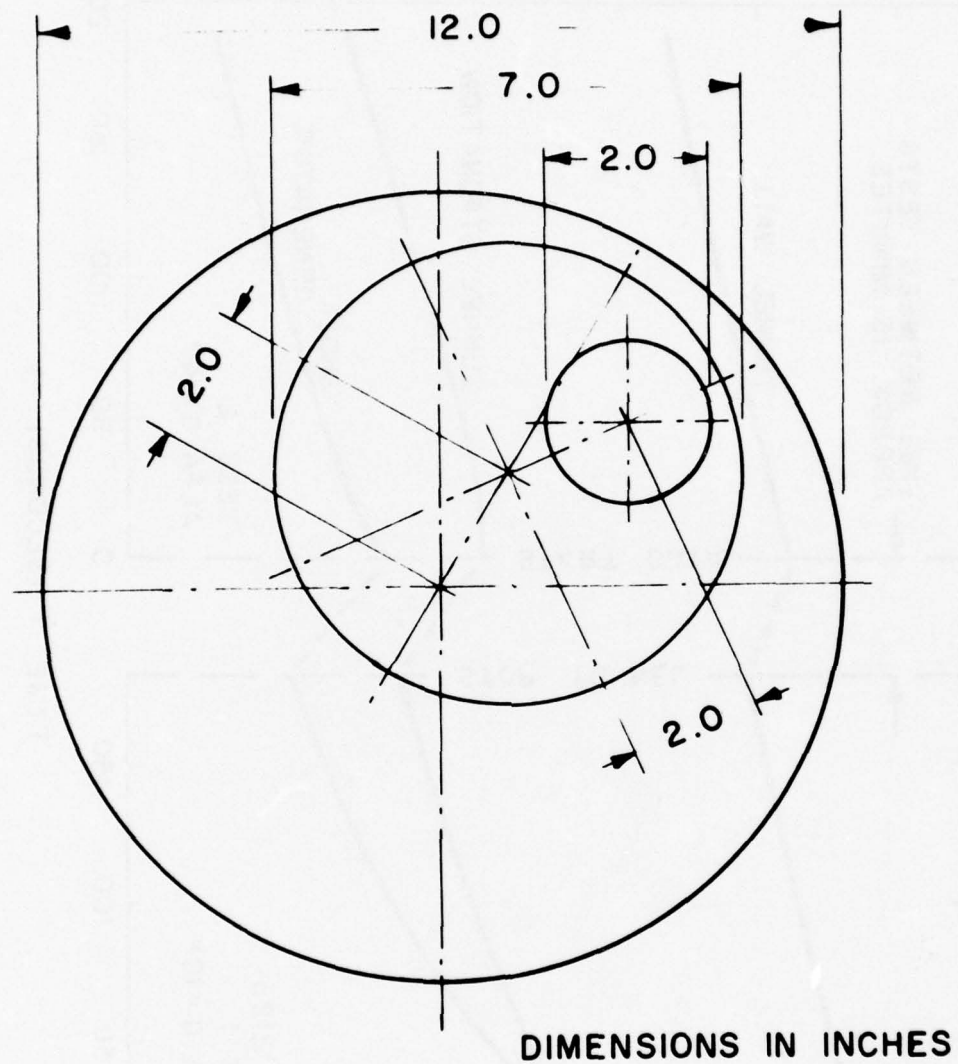


Figure 6. Eccentric , Rotatable System.

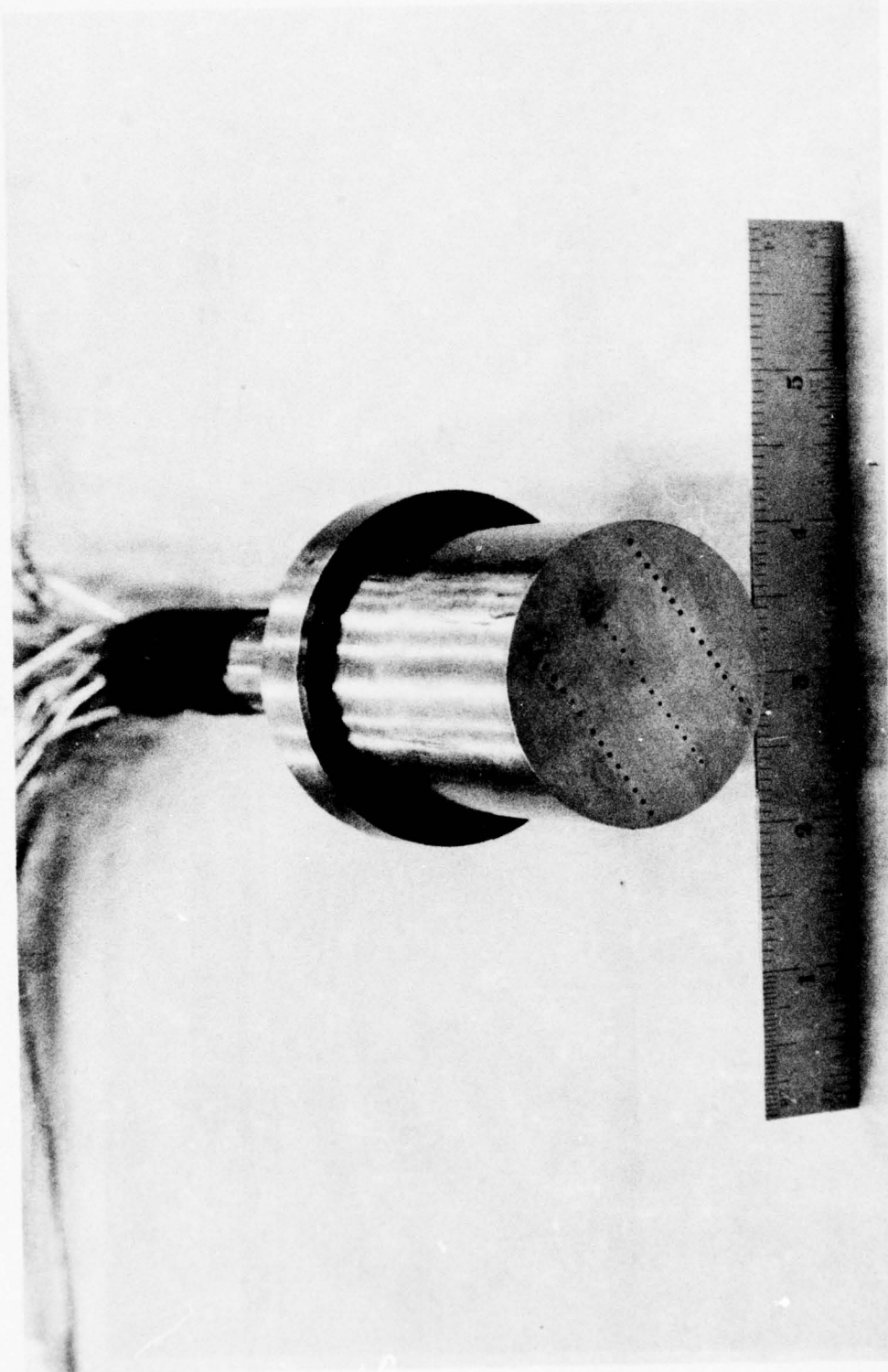


Figure 7. Photograph of Static Pressure Plug.



Figure 8. Photograph of Heat Transfer Plug.

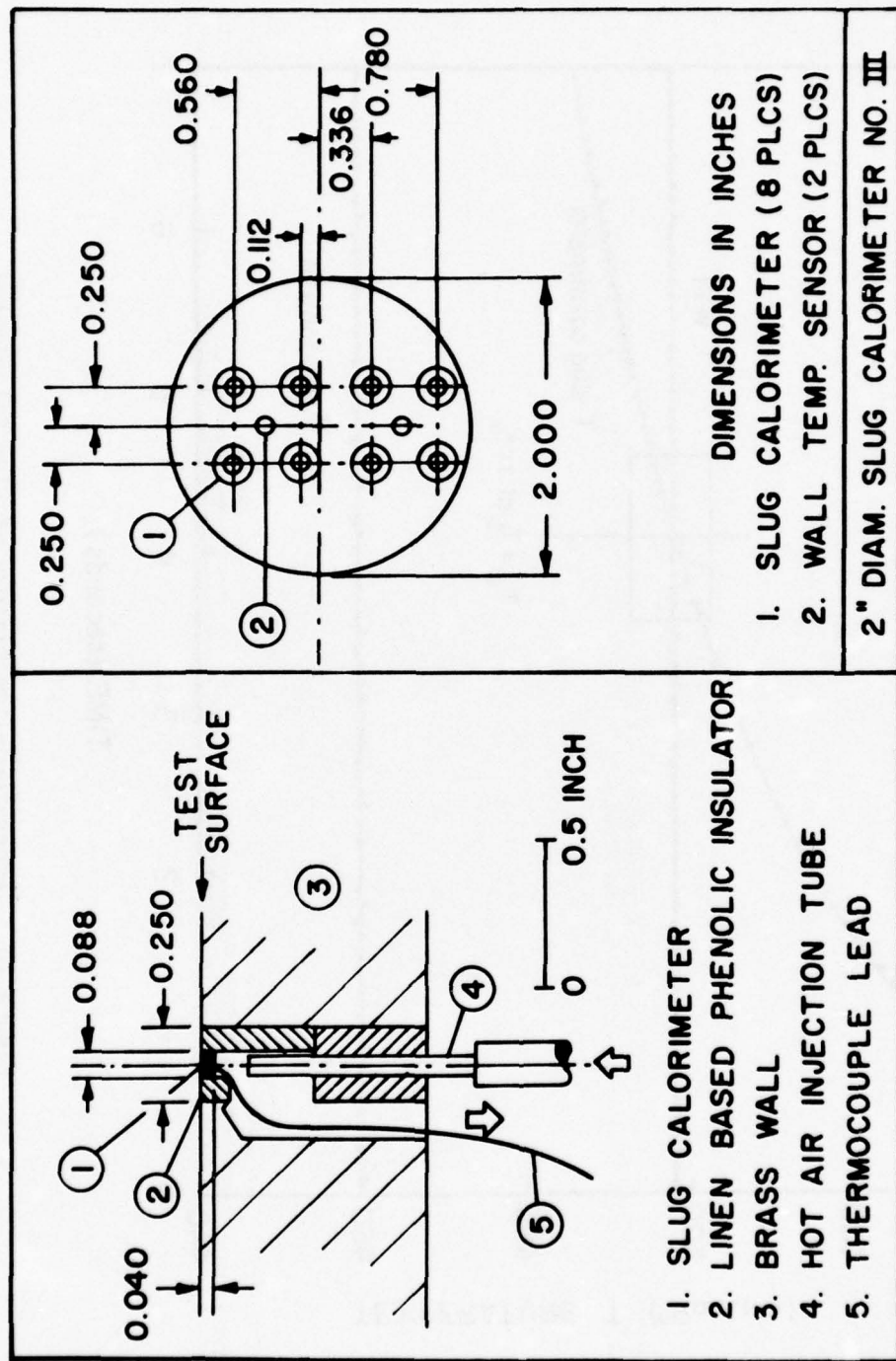


Figure 9. Drawing of Slug Calorimeter Arrangement.

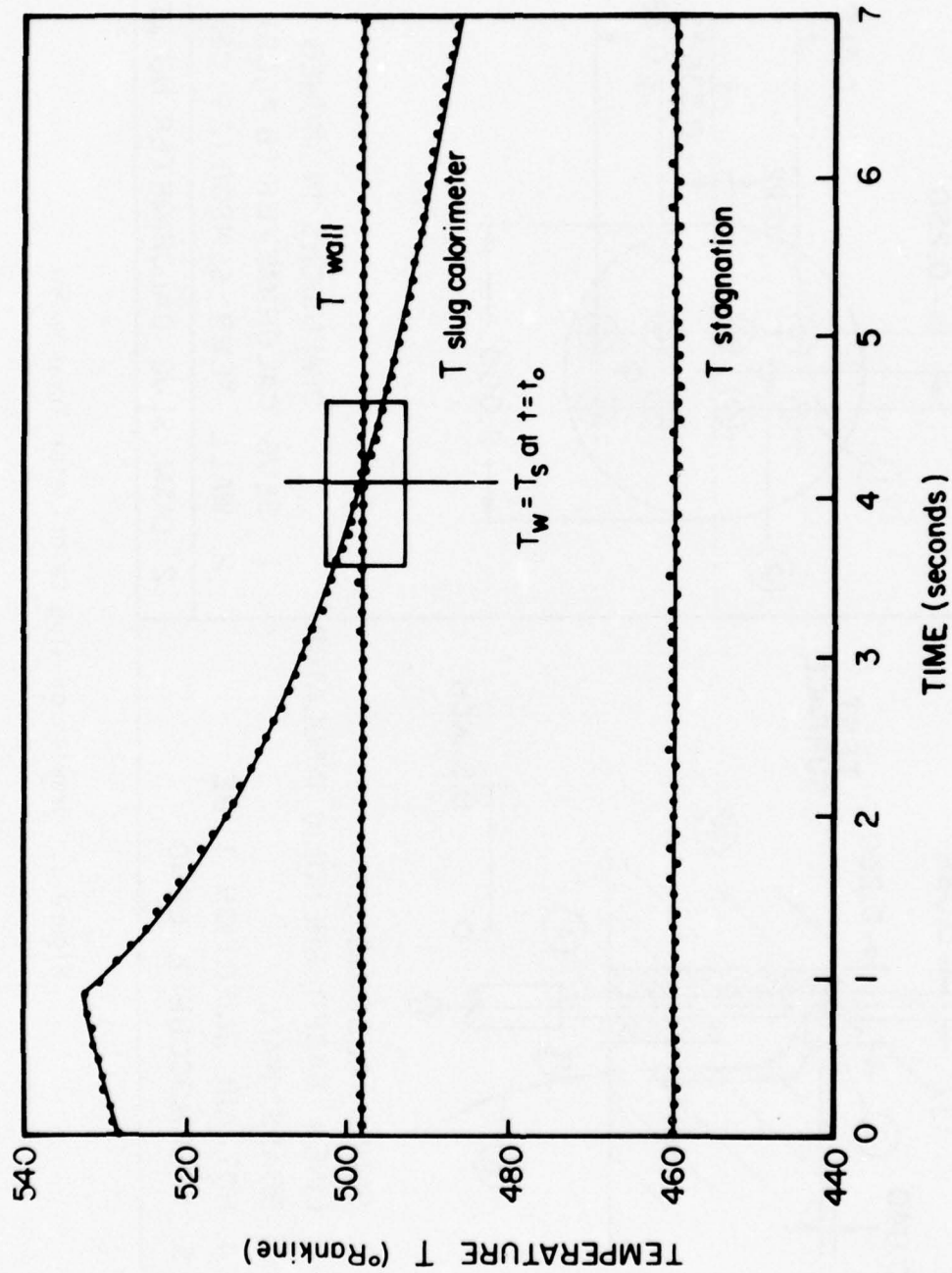


Figure 10. Temperature-Time history of Slug Calorimeter.

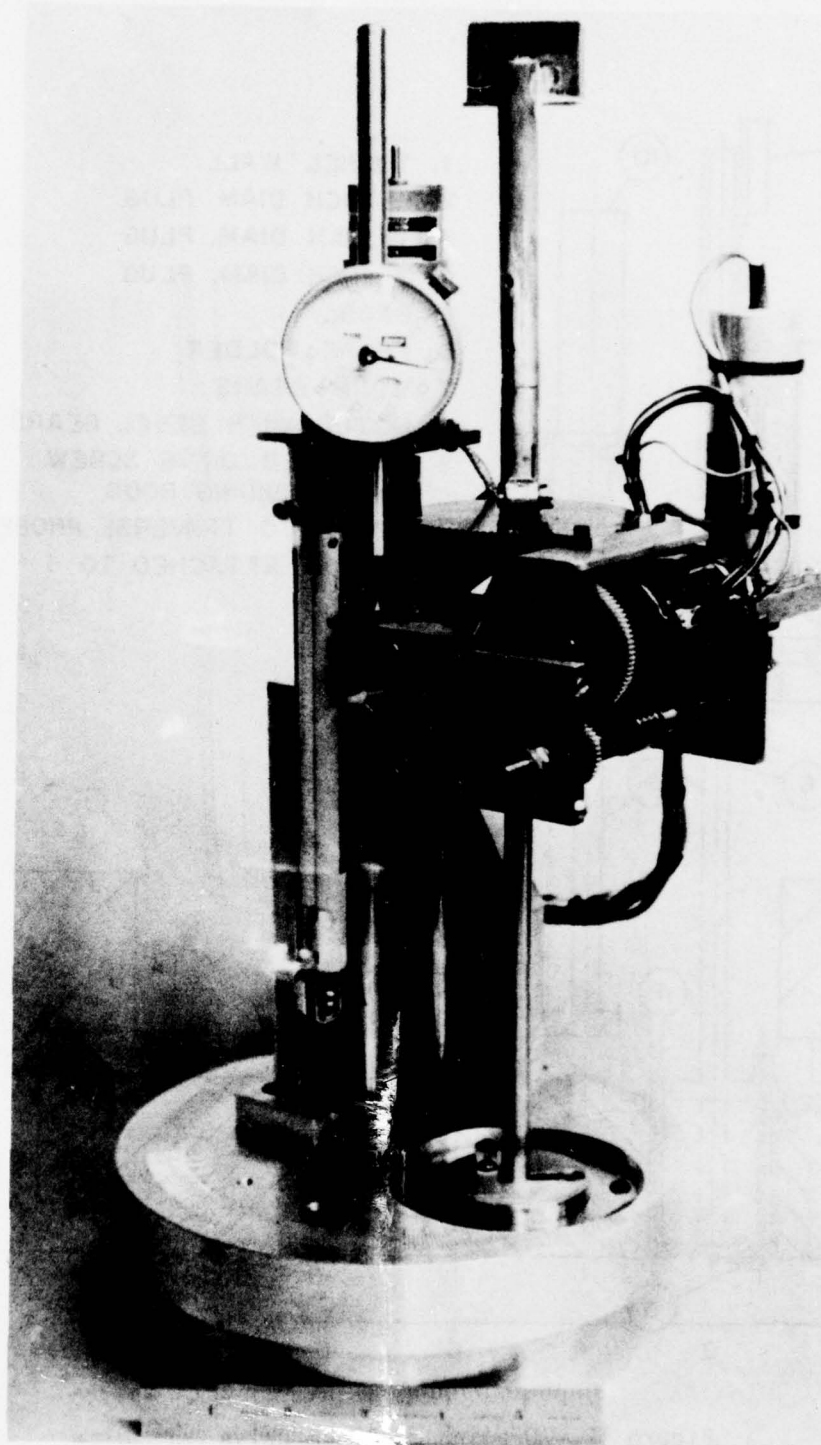


Figure 11. Photograph of Probe Drive Mechanism.

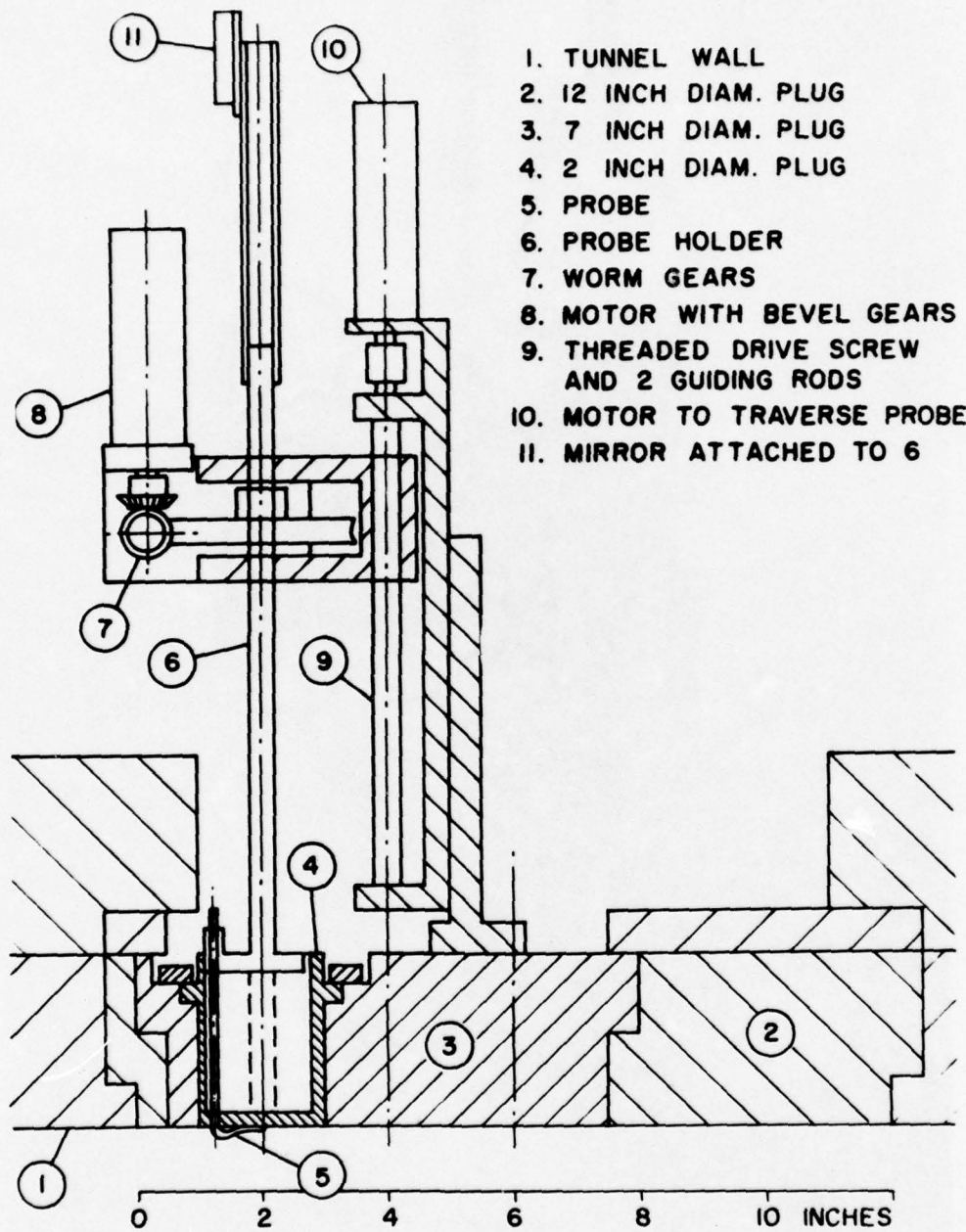


Figure 12. Drawing of Probe Drive Mechanism.

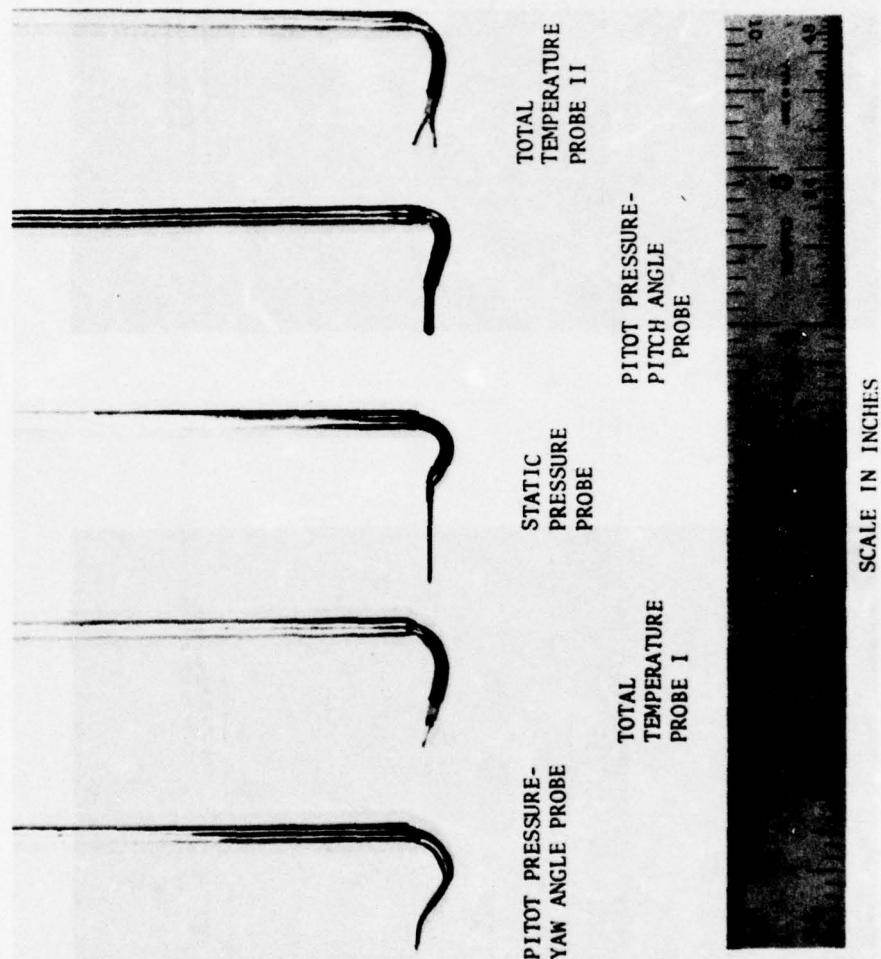


Figure 13. Photograph of Five Flow Field Probes.



Figure 14. Frontal View of Yaw-Pitot Probe (above) and Pitch-Pitot Probe (below).

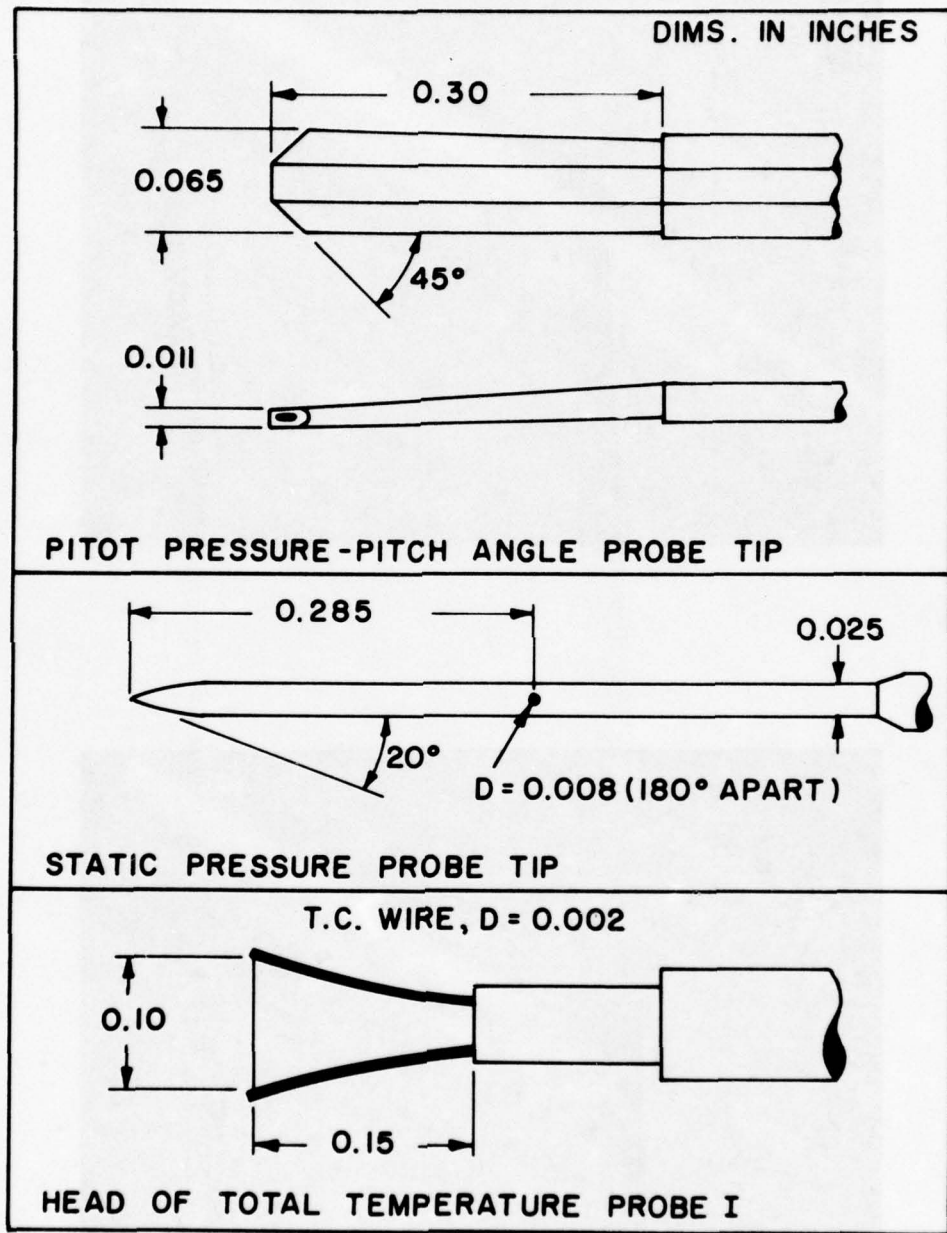


Figure 15. Line Drawing of Probe Tips.

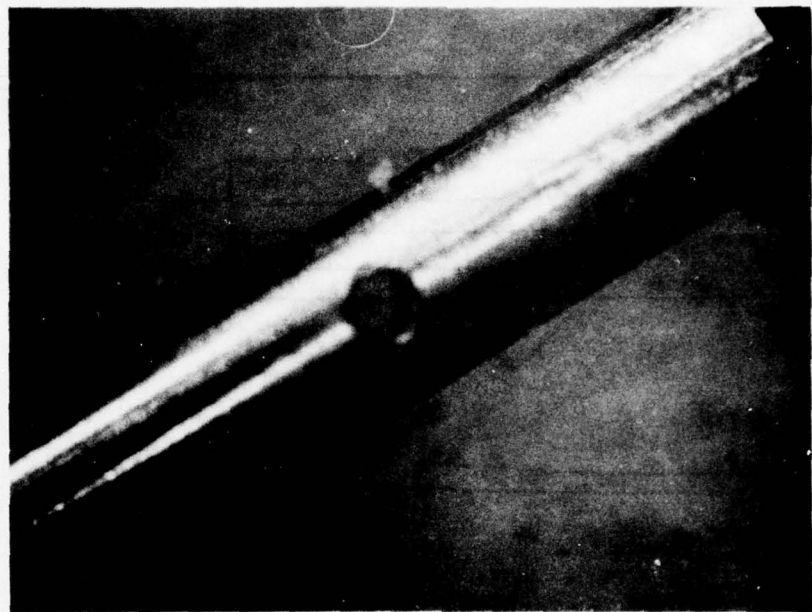


Figure 16. Photograph of Static Pressure Probe Tip.

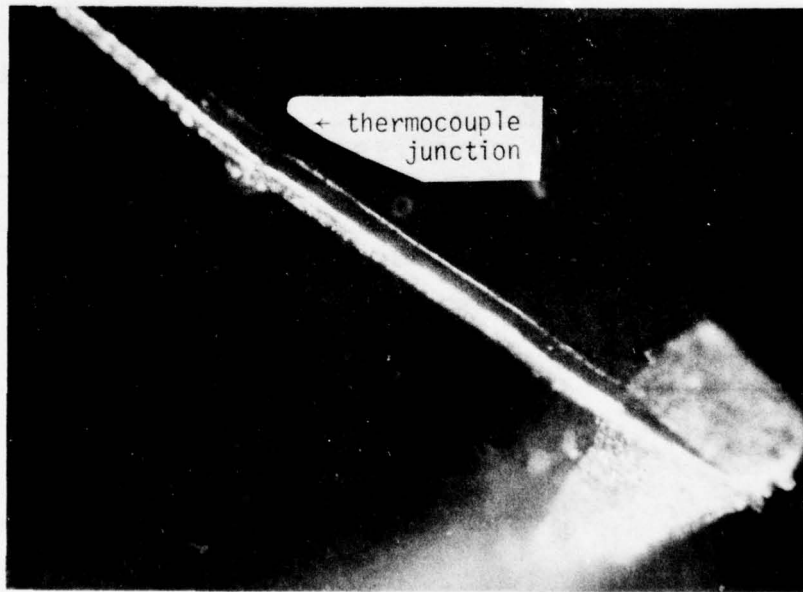
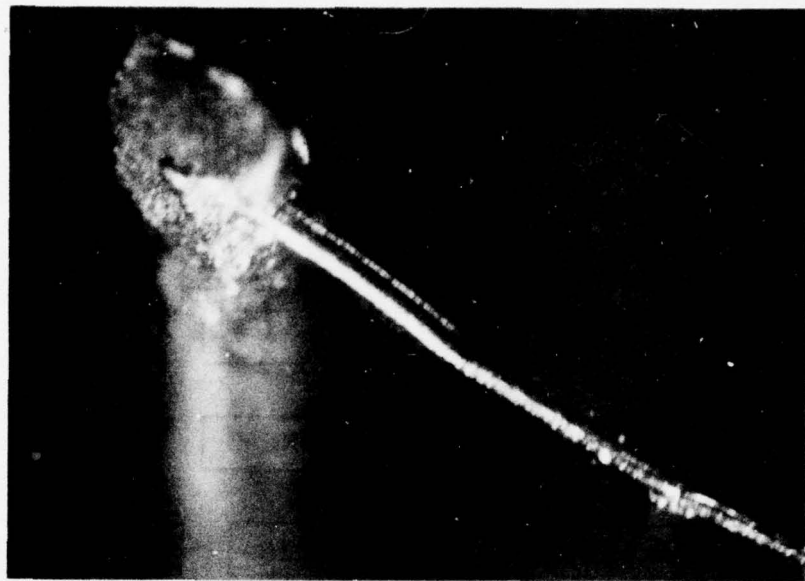


Figure 17. Photograph of Total Temperature Probe Supports and Thermocouple Junction.

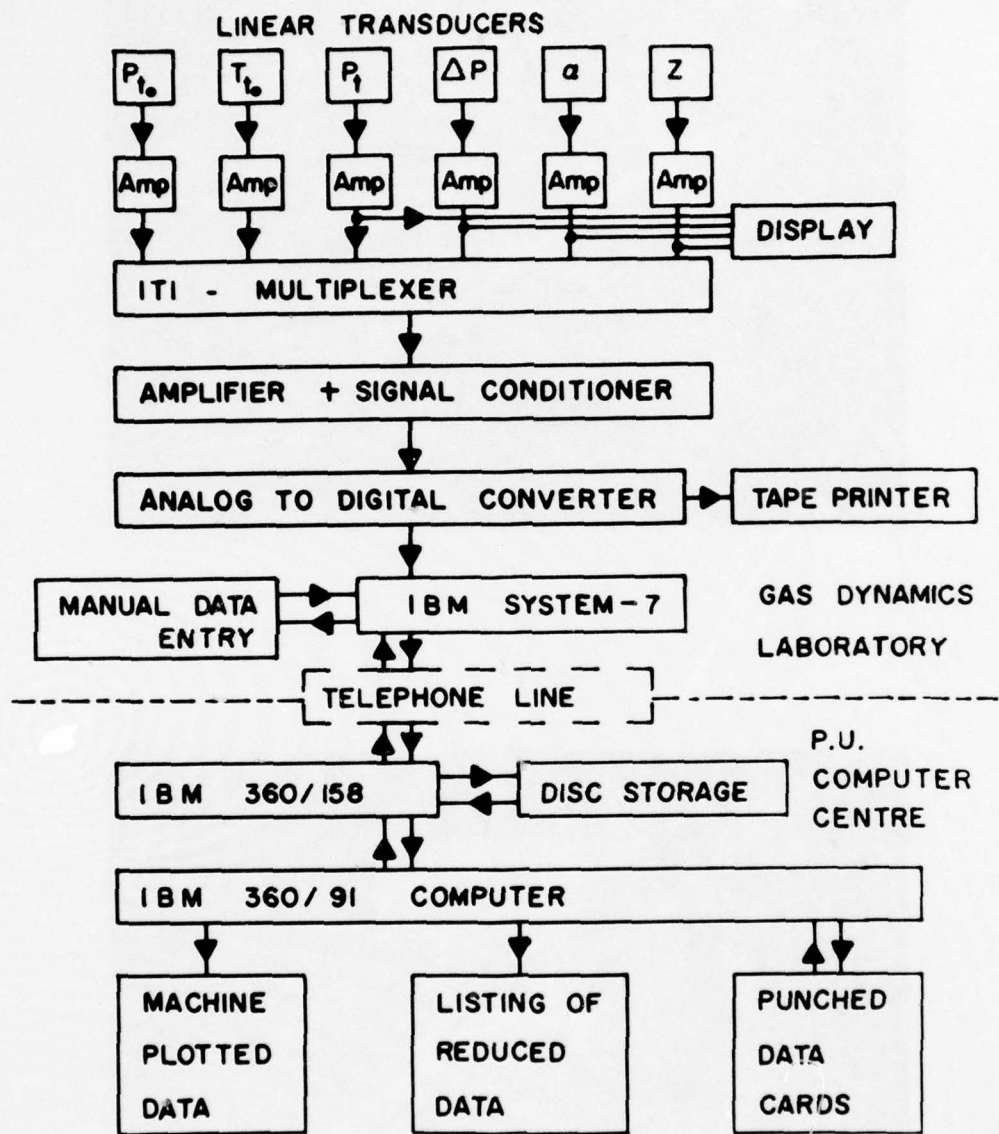


Figure 18. Typical Flow Chart of Data Acquisition System.

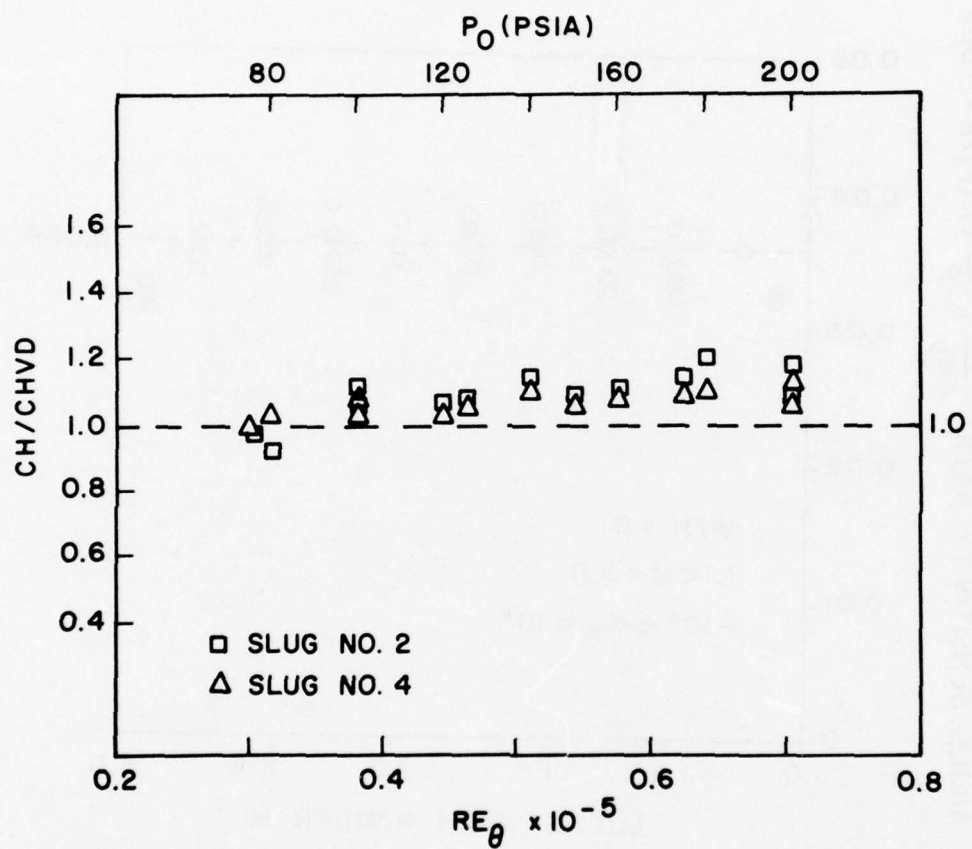


Figure 19. Heat Transfer Versus Reynolds Number.

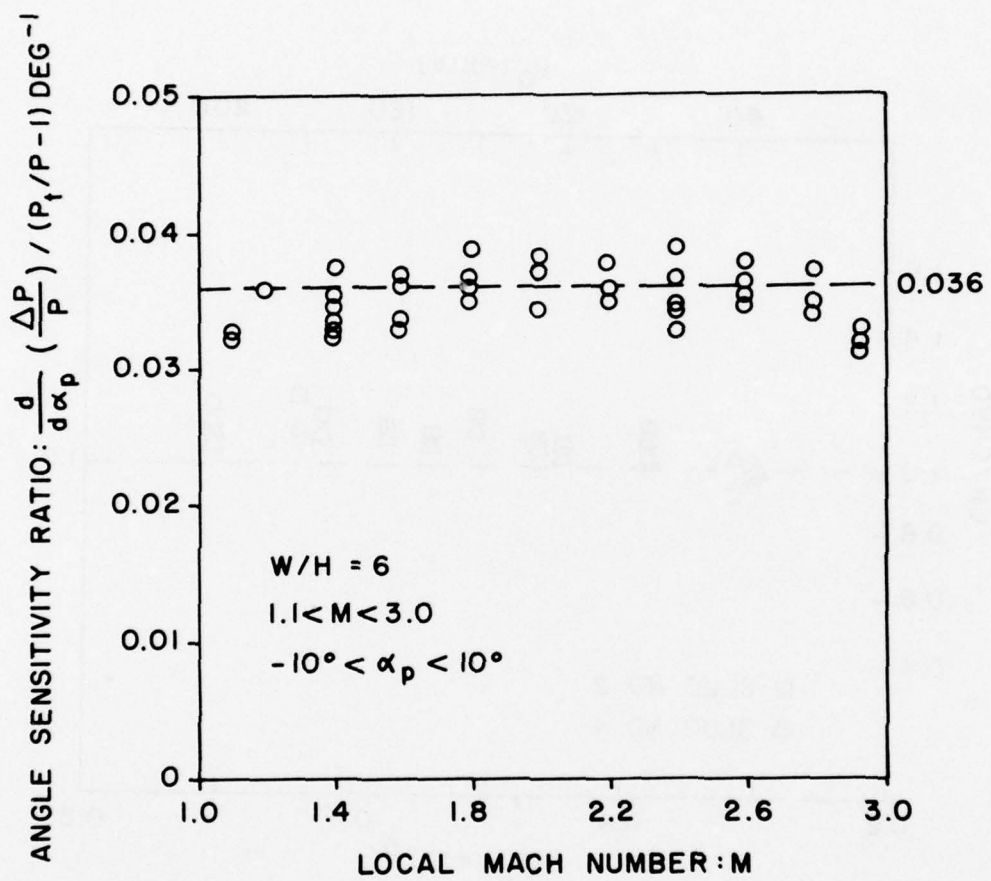


Figure 20. Angle Sensitivity of Yaw Pitot Probe.

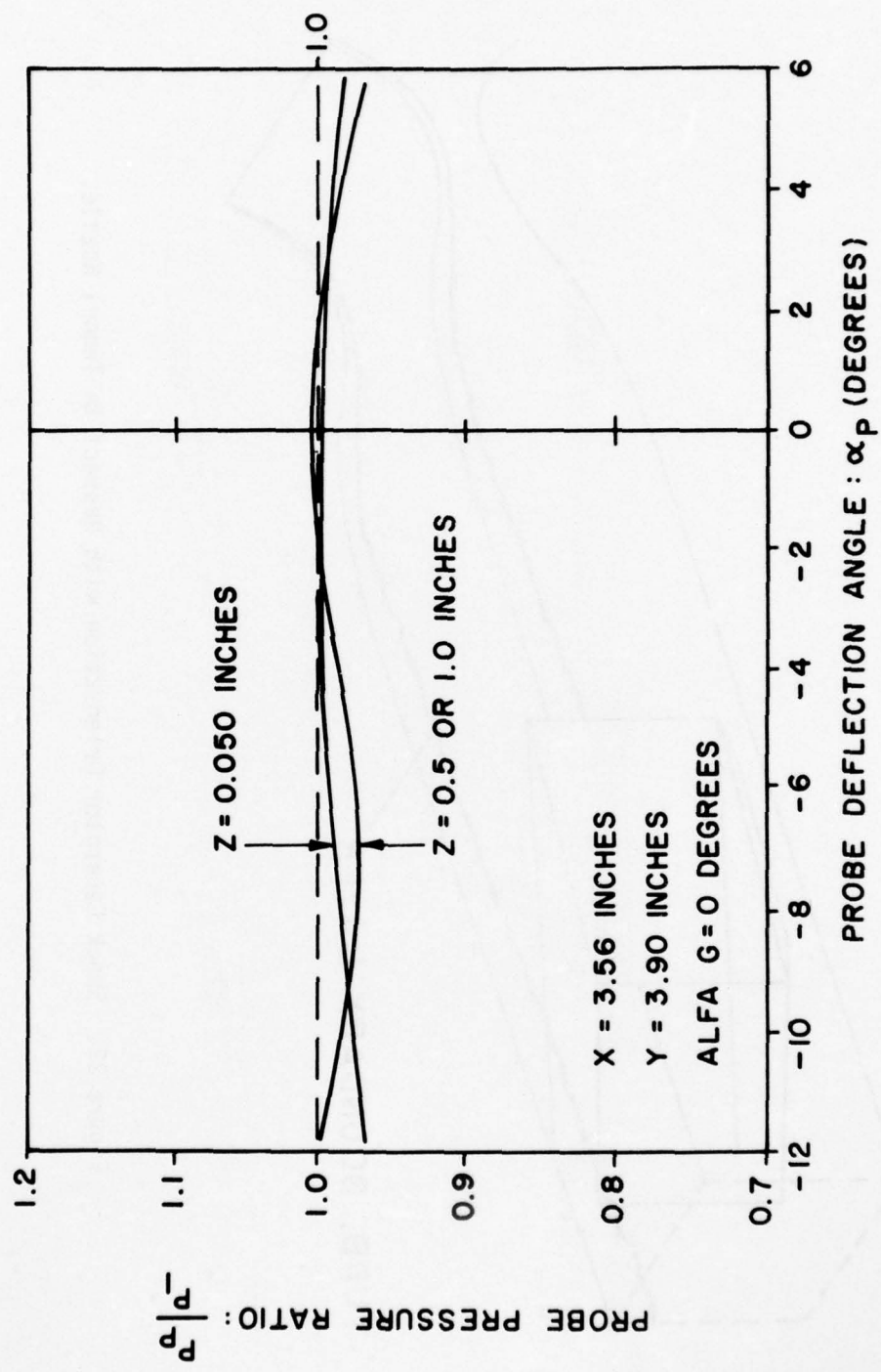


Figure 21. Angle Sensitivity of Static Pressure Probe.

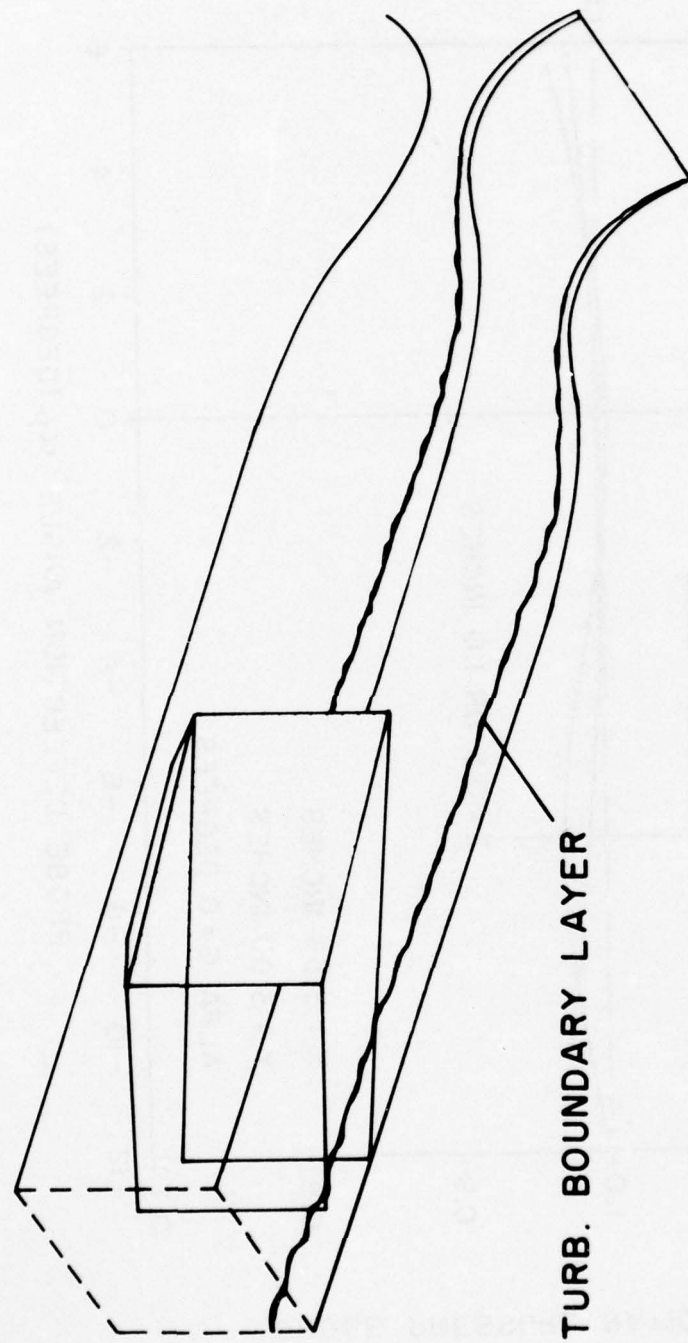


Figure 22. Shock Generator Orientation with Respect to Tunnel Nozzle.

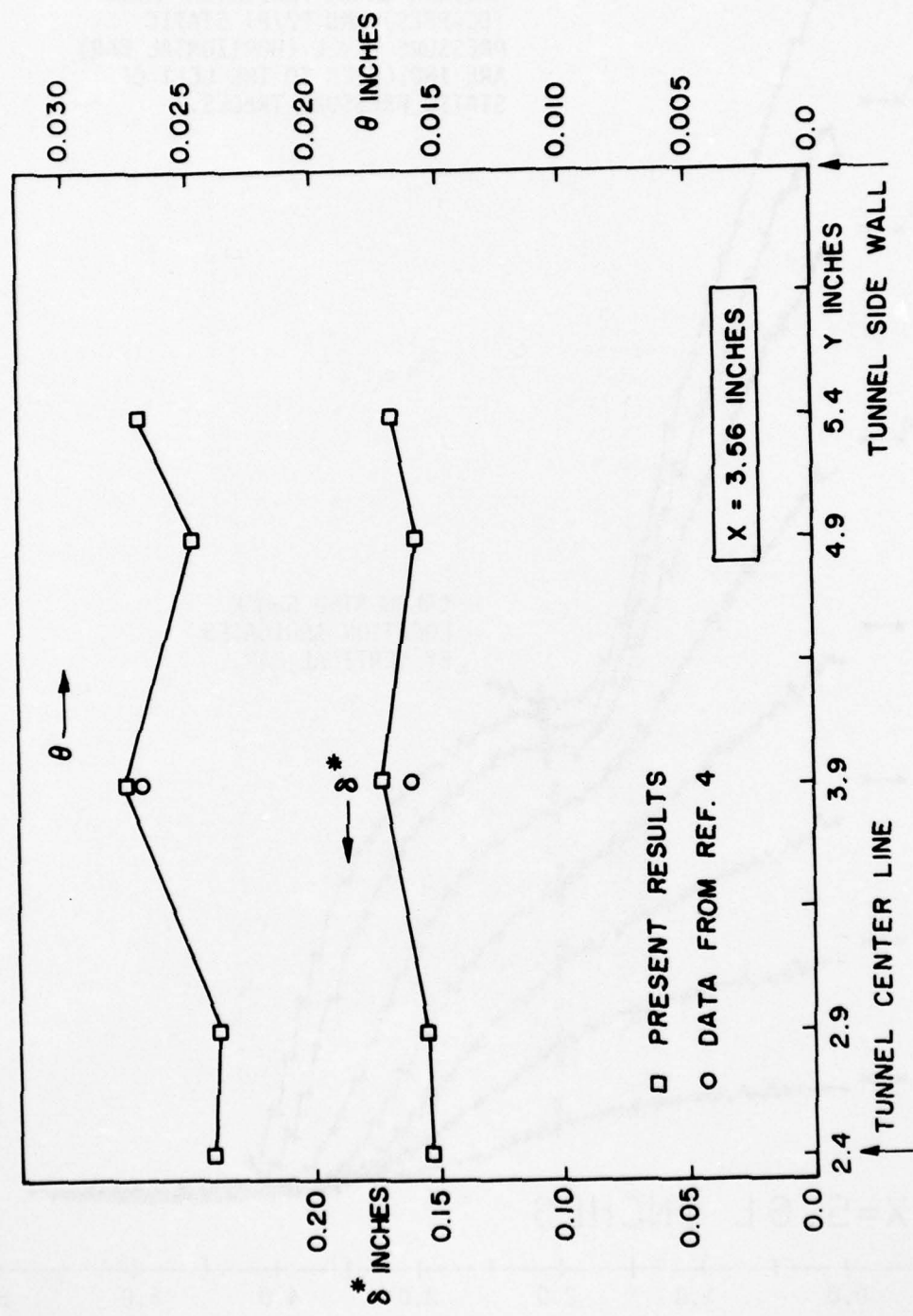


Figure 23. Two-Dimensionality of Initial Boundary Layer Flow.

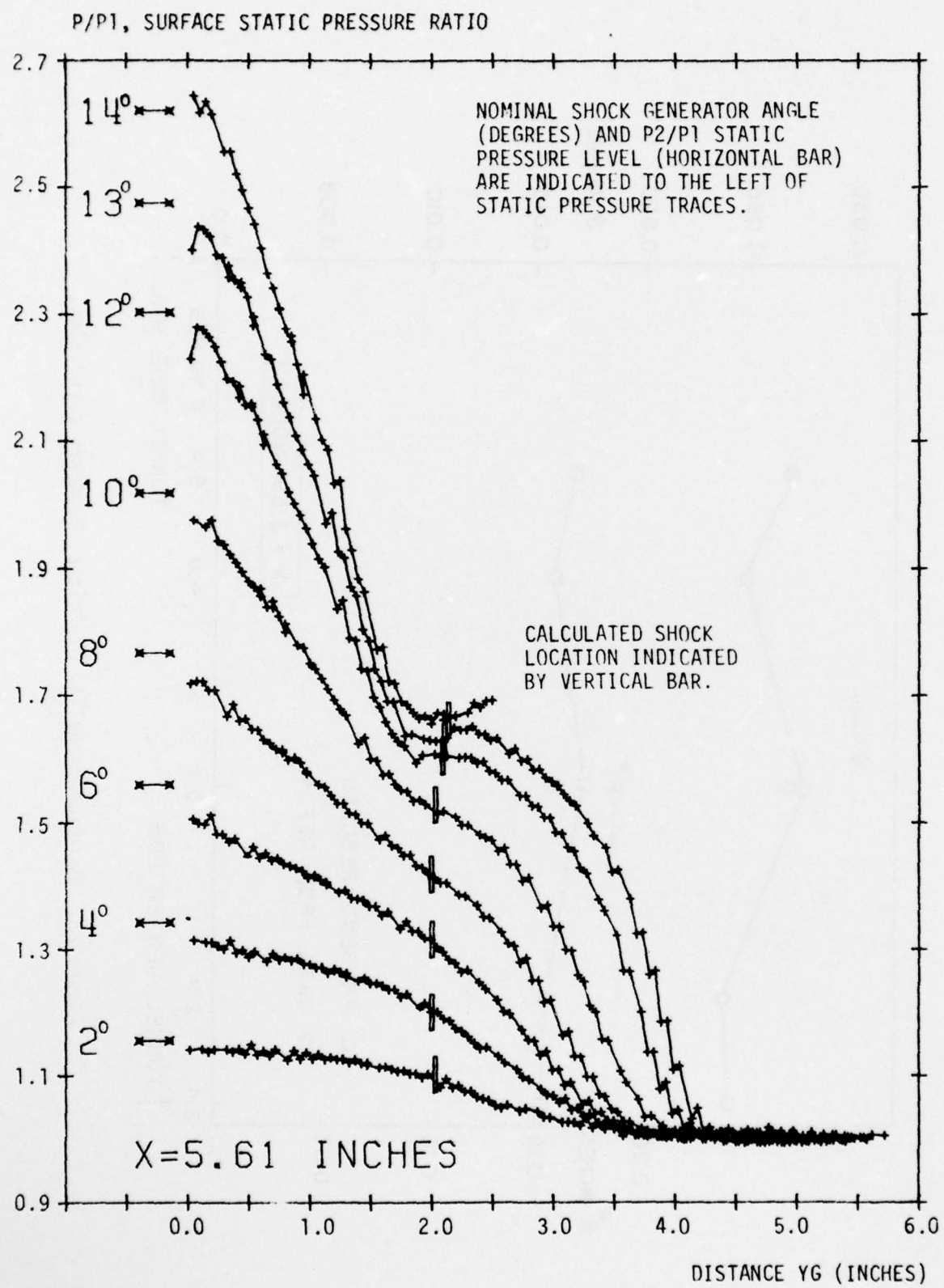


Figure A-1: Surface Static Pressure, X = 4.6 inches.

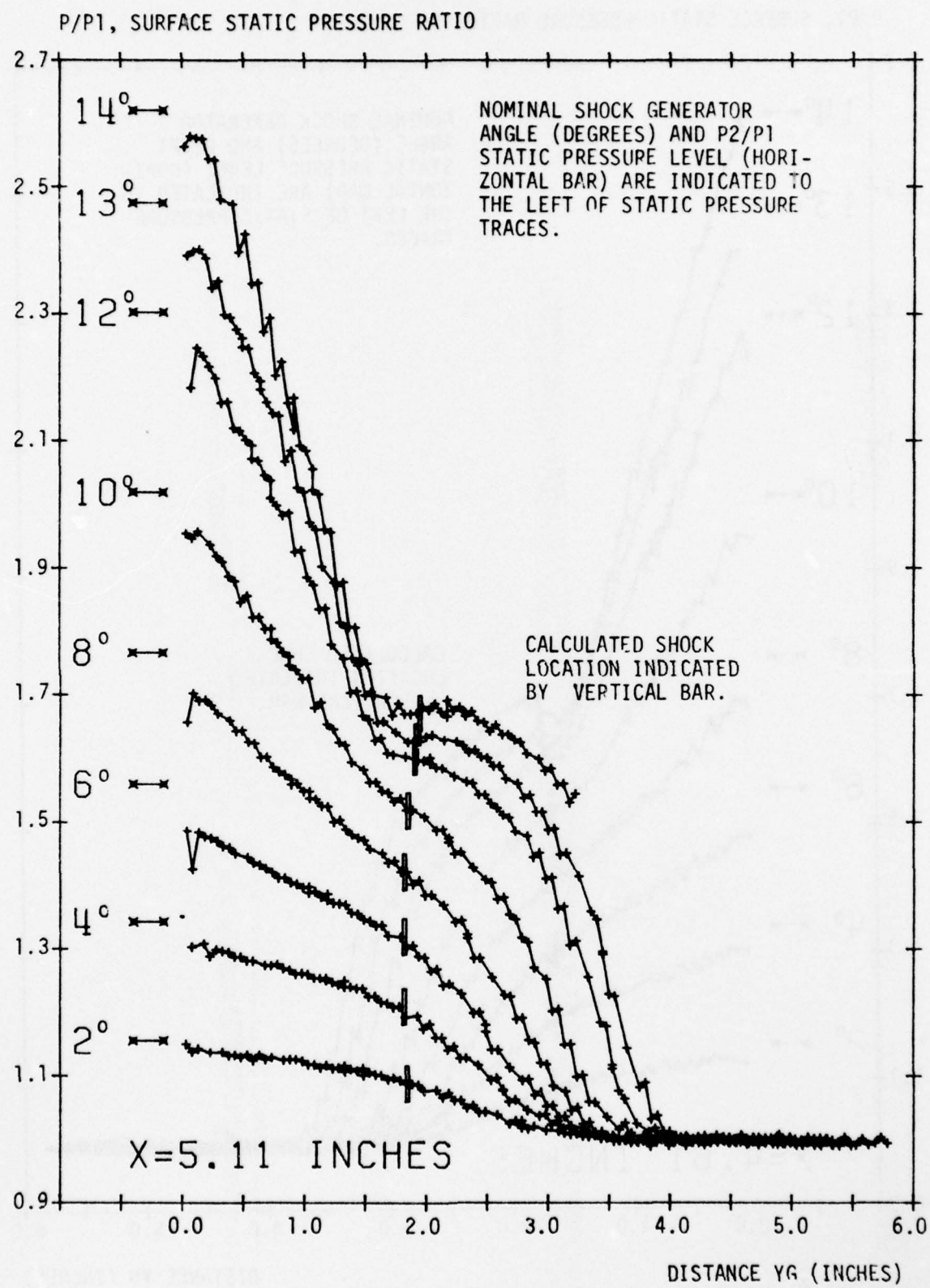


Figure A-2: Surface Static Pressure, X = 5.1 inches.

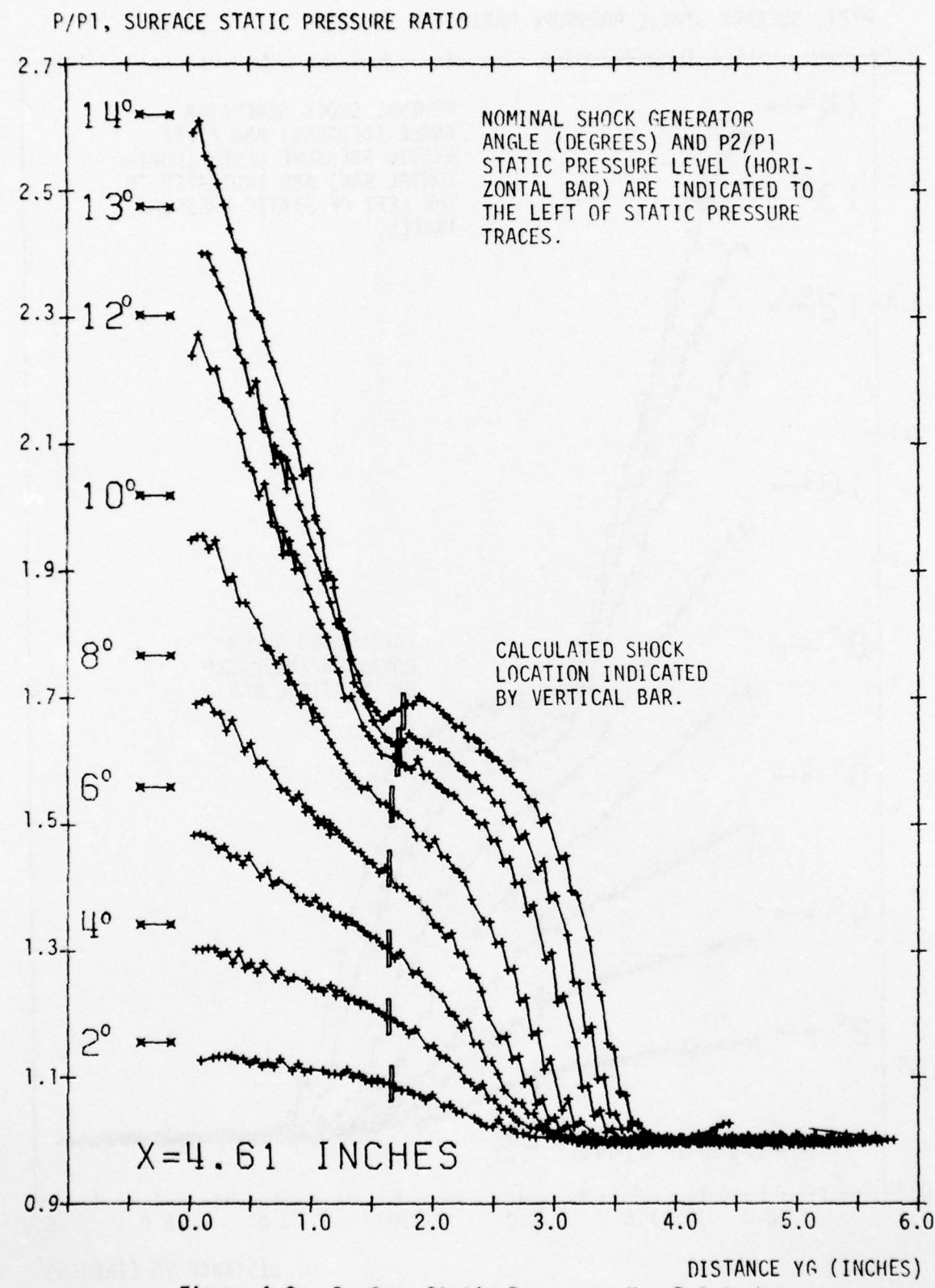


Figure A-3: Surface Static Pressure, X = 5.6 inches.

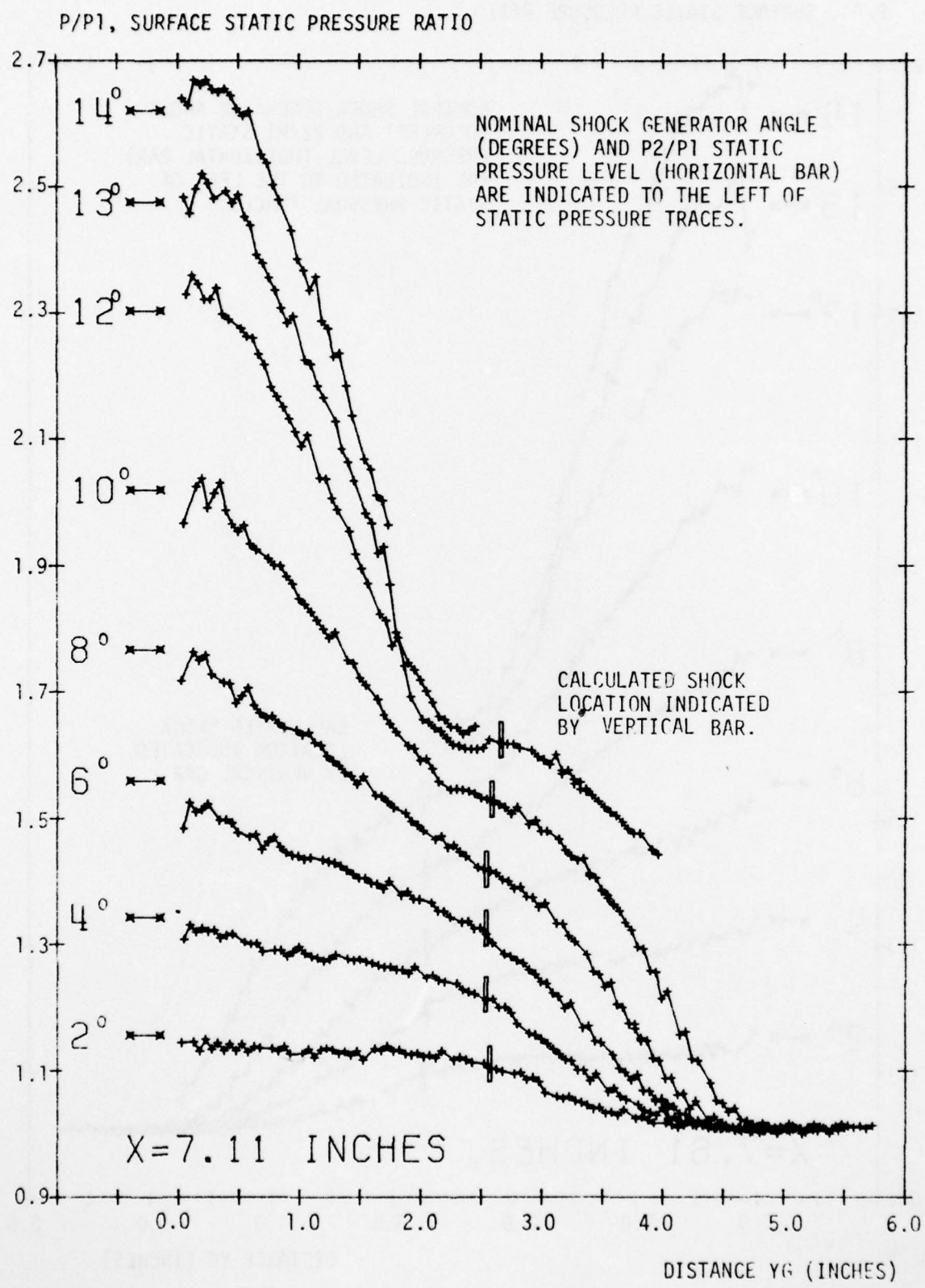


Figure A-4: Surface Static Pressure, X = 7.1 inches.

P/P₁, SURFACE STATIC PRESSURE RATIO

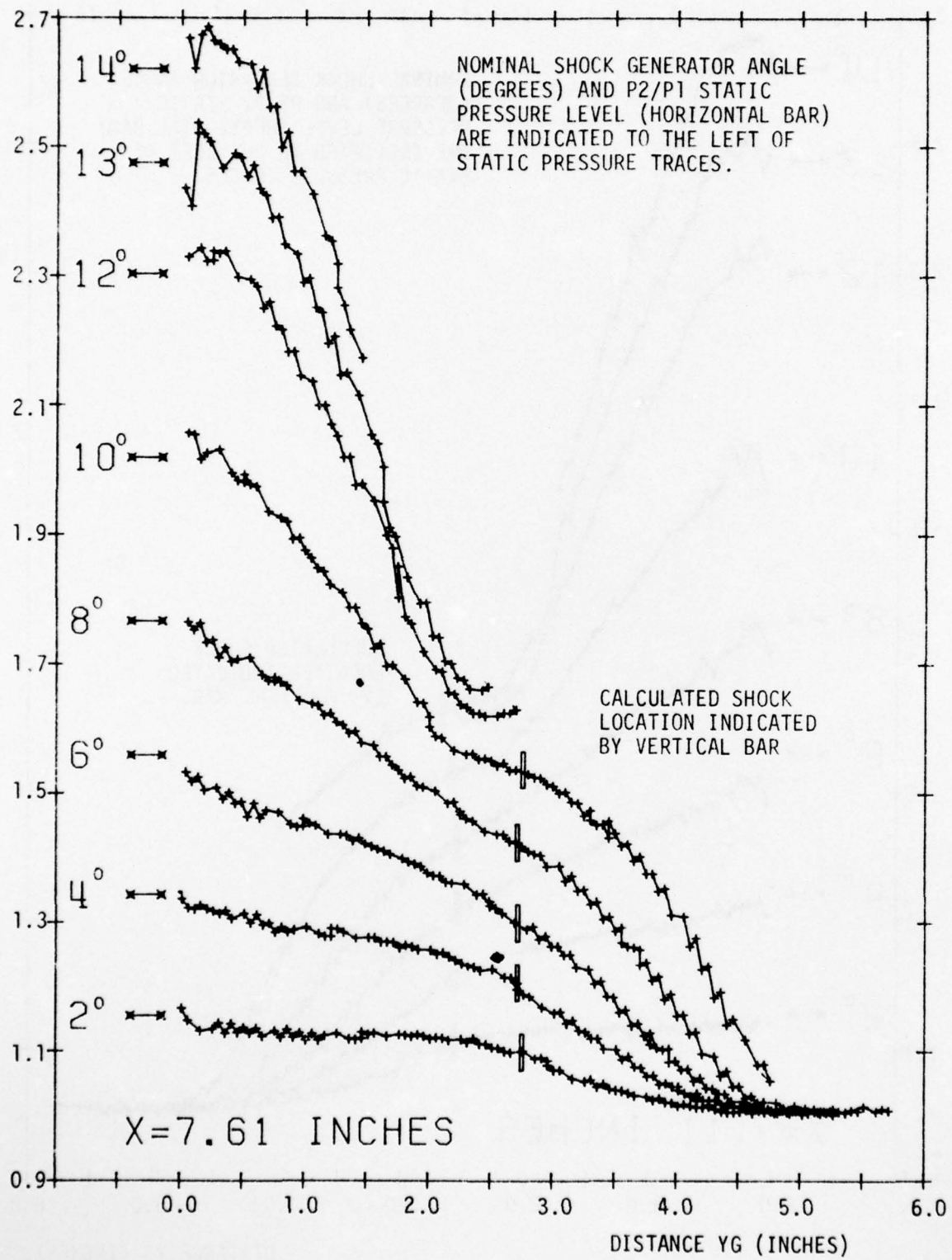


Figure A-5: Surface Static Pressure, X = 7.6 inches.

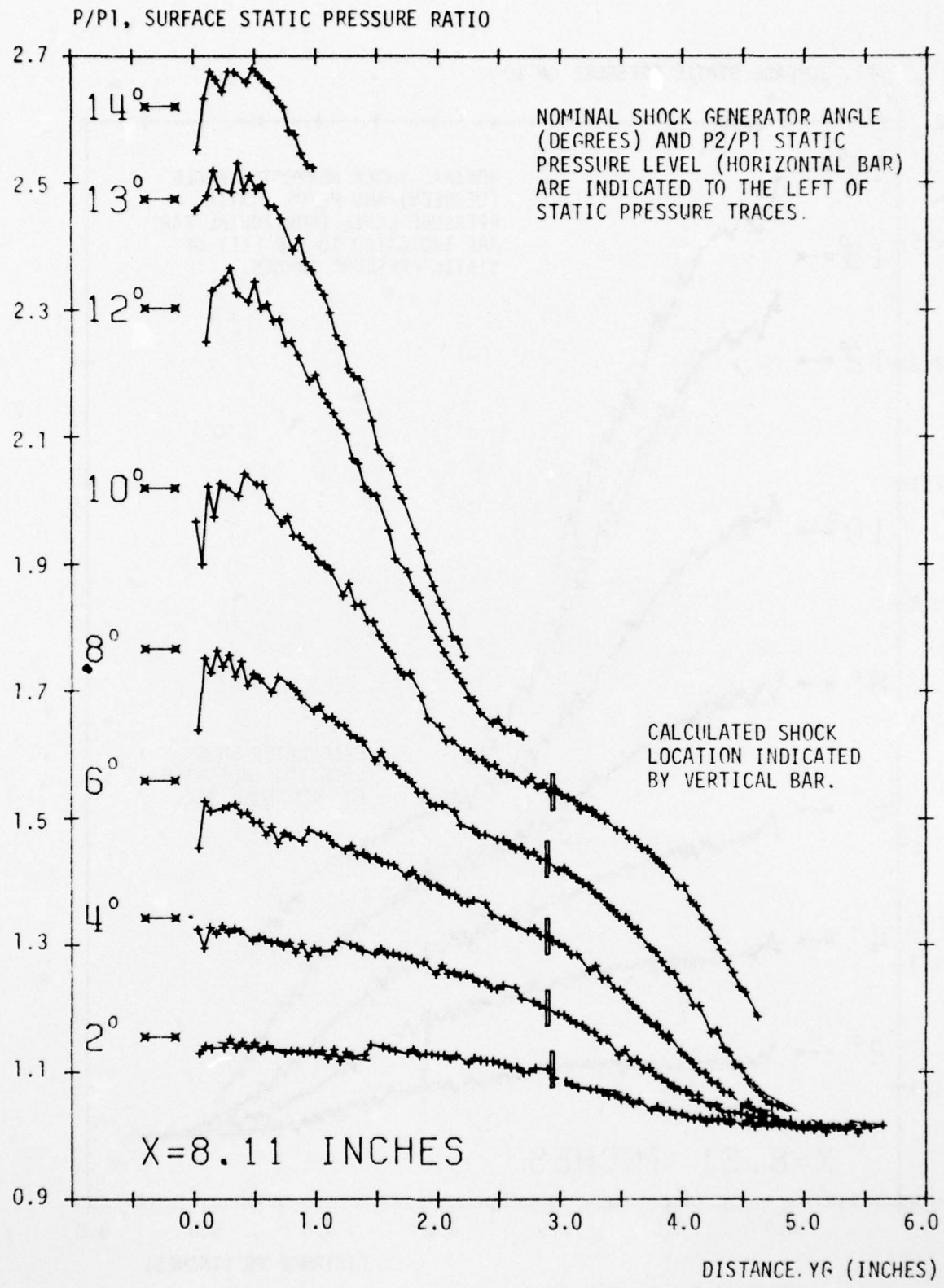


Figure A-6: Surface Static Pressure, X = 8.1 inches.

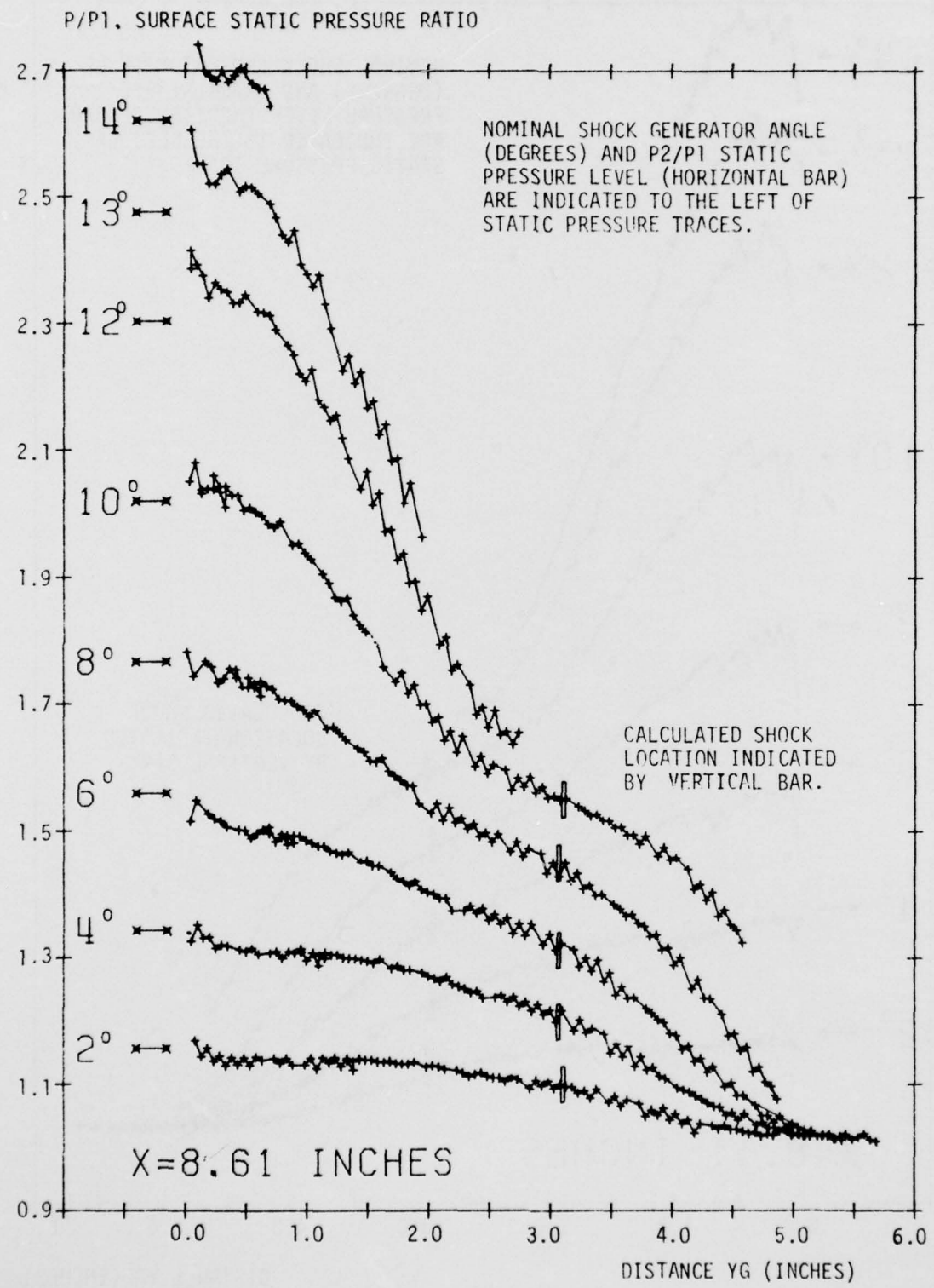


Figure A-7: Surface Static Pressure, X = 8.6 inches.

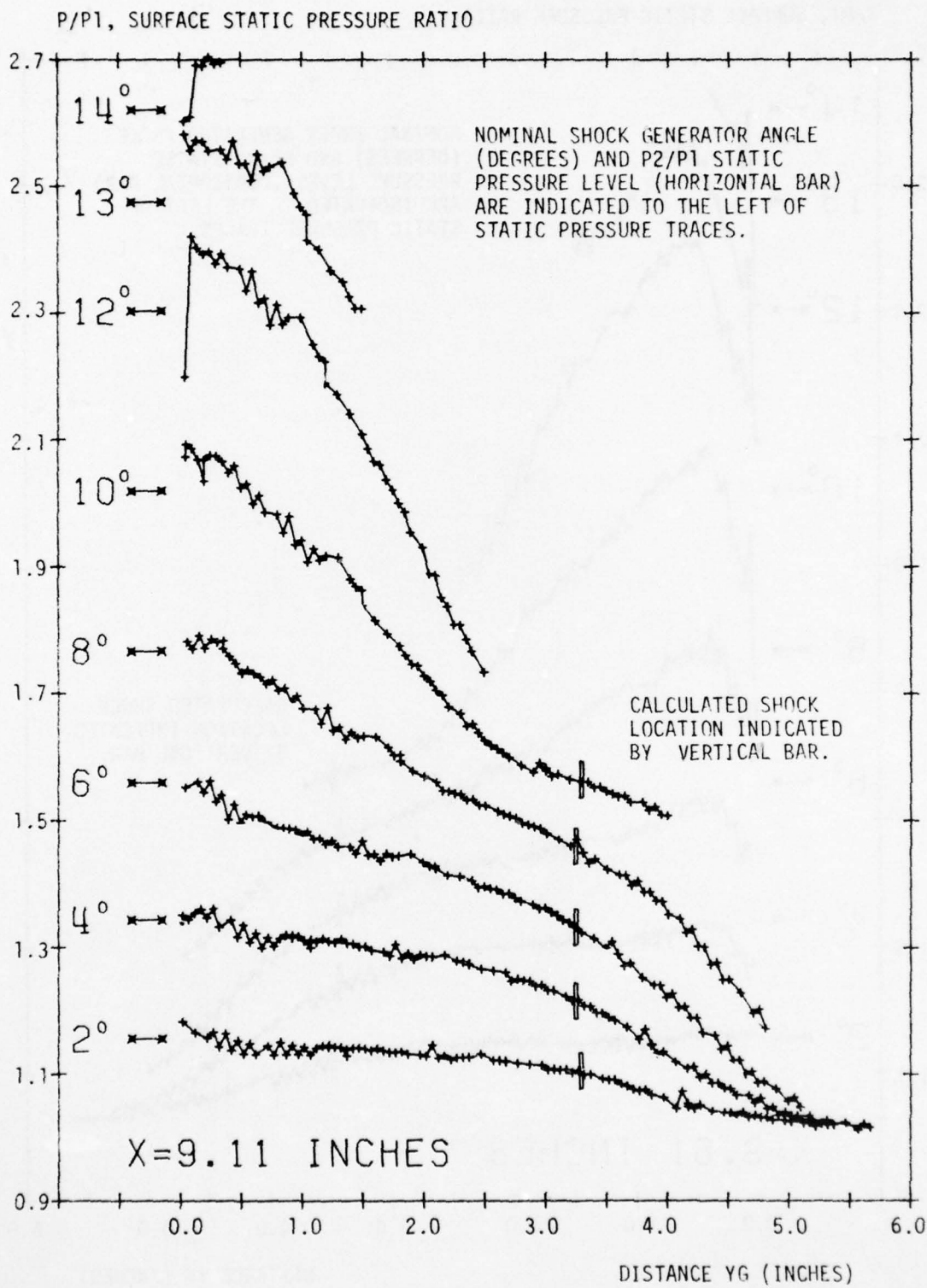


Figure A-8: Surface Static Pressure, $X = 9.1$ inches.

AD-A033 386

PRINCETON UNIV N J GAS DYNAMICS LAB

F/G 20/4

OBLIQUE SHOCK WAVE/TURBULENT BOUNDARY LAYER INTERACTIONS IN THR--ETC(U)

JUN 76 B OSKAM, I E VAS, S M BOGDONOFF

F33615-75-C-3126

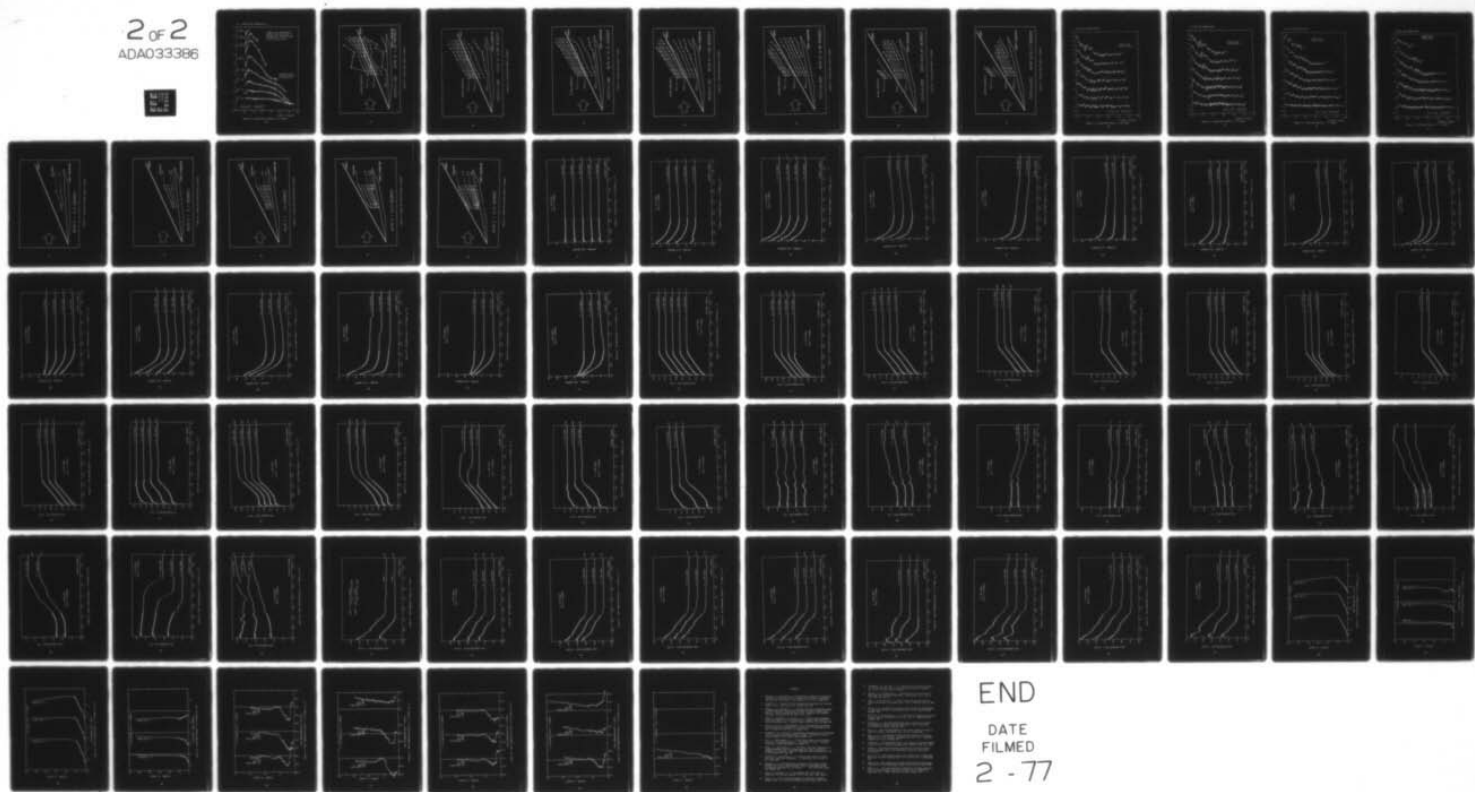
UNCLASSIFIED

1292

AFFDL-TR-76-48-PT-1

NL

2 OF 2
ADA033386

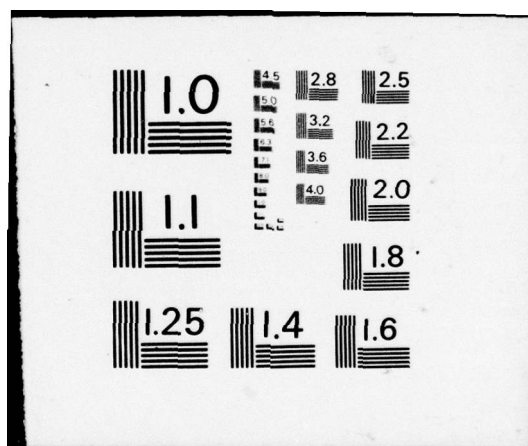


END

DATE

FILMED

2 - 77



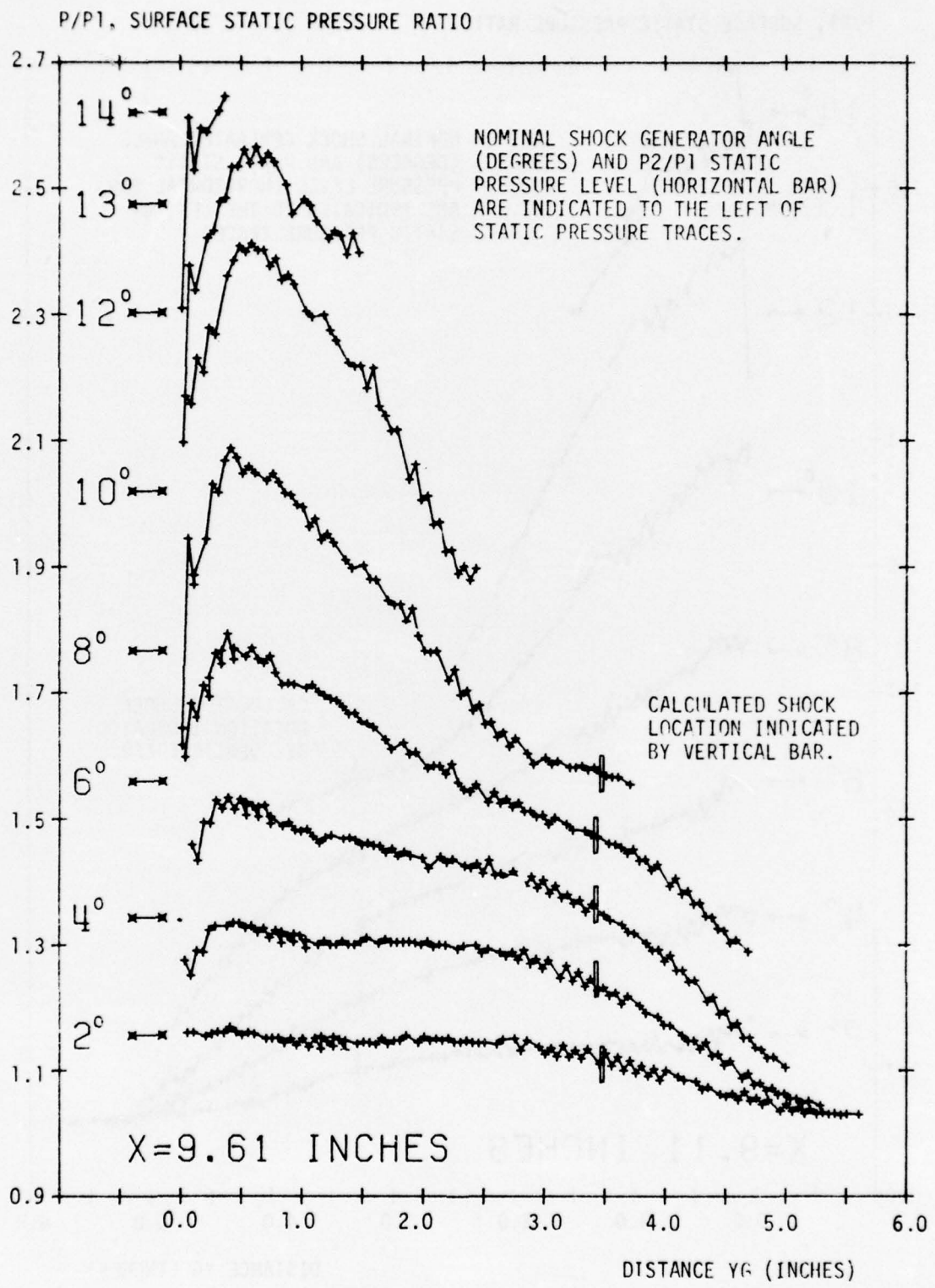


Figure A-9: Surface Static Pressure, X = 9.6 inches.

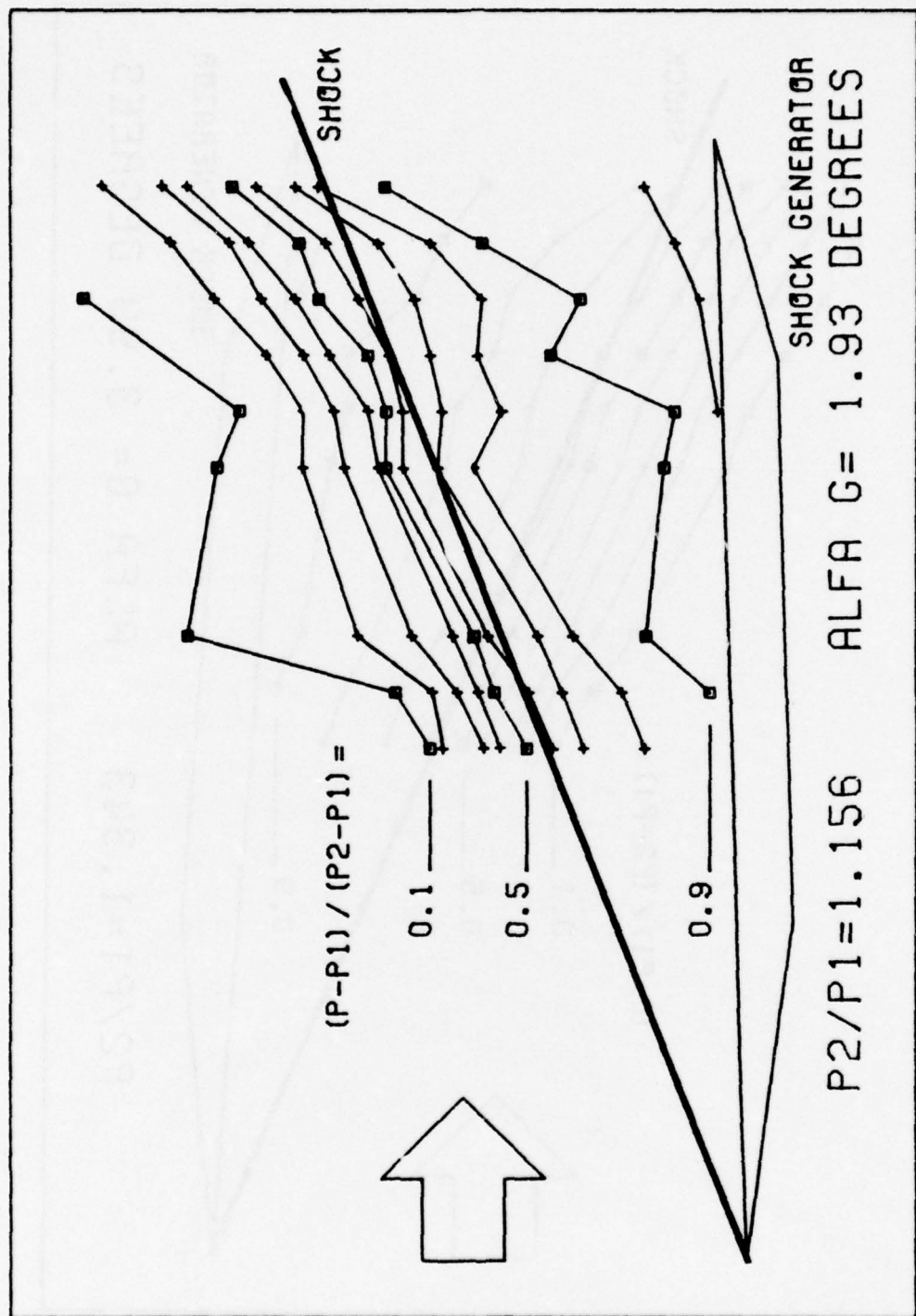


Figure B-1: Surface Isobar Pattern, 2 degrees.

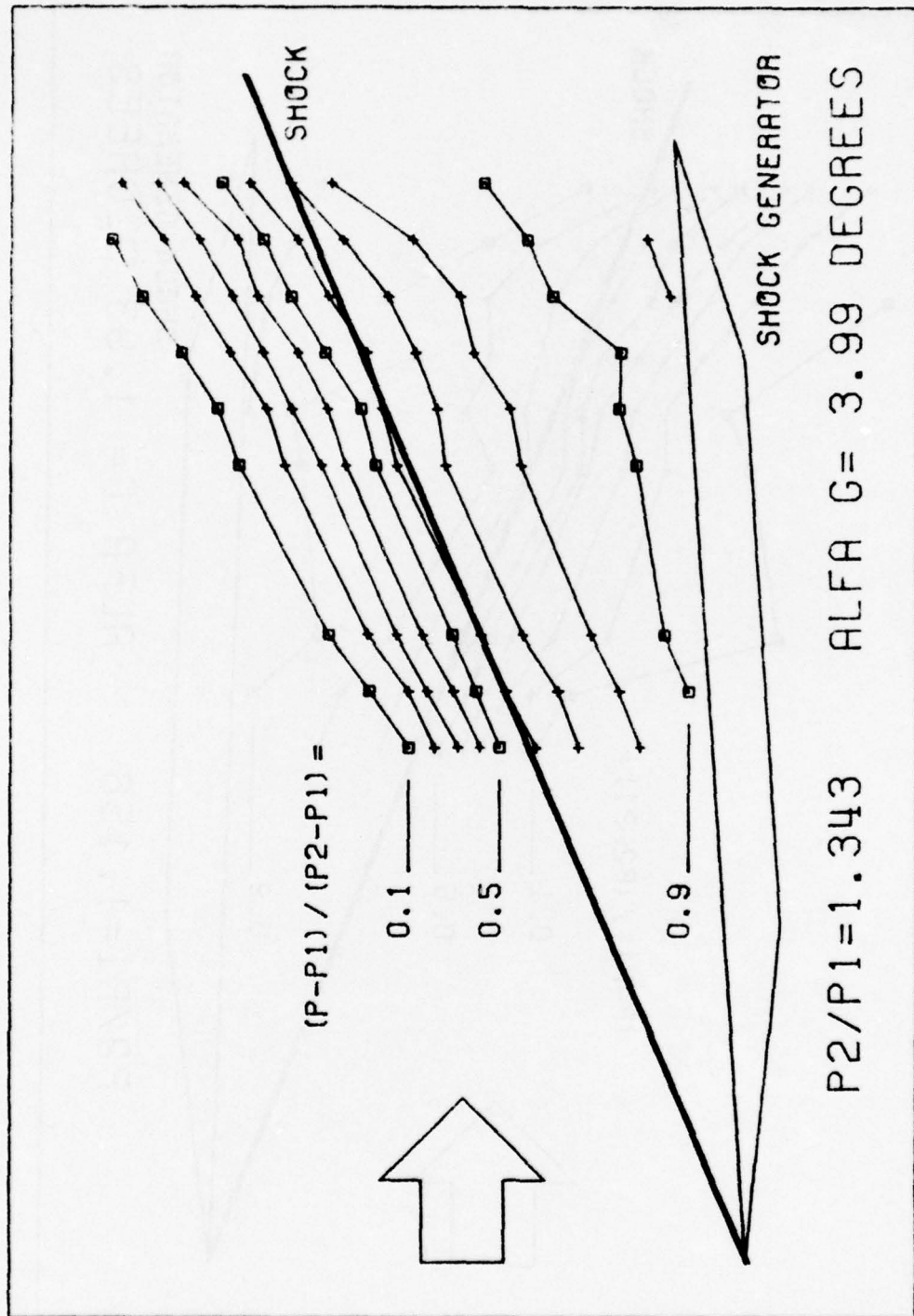


Figure B-2: Surface Isobar Pattern, 4 degrees.

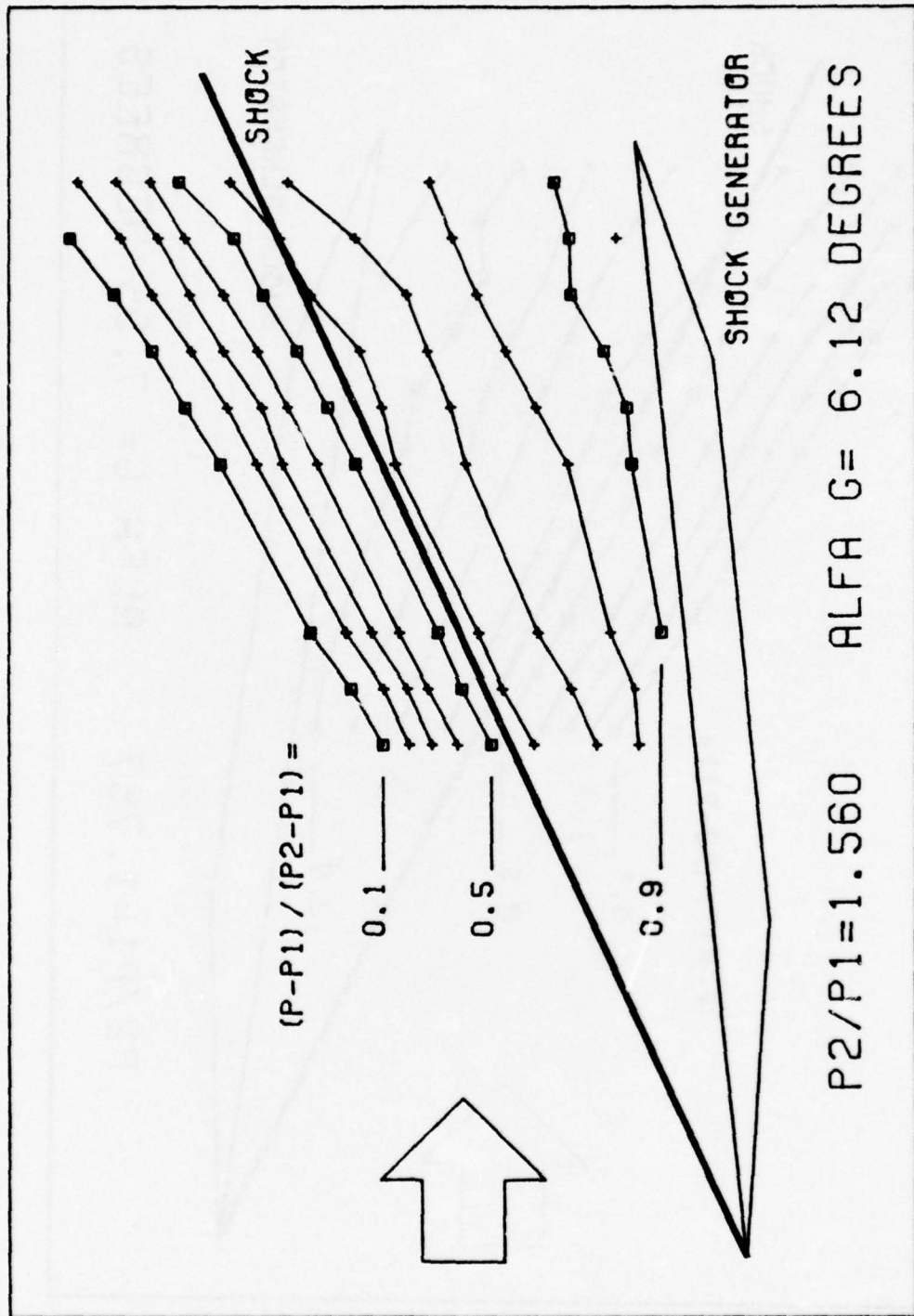


Figure B-3: Surface Isobar Pattern, 6 degrees.

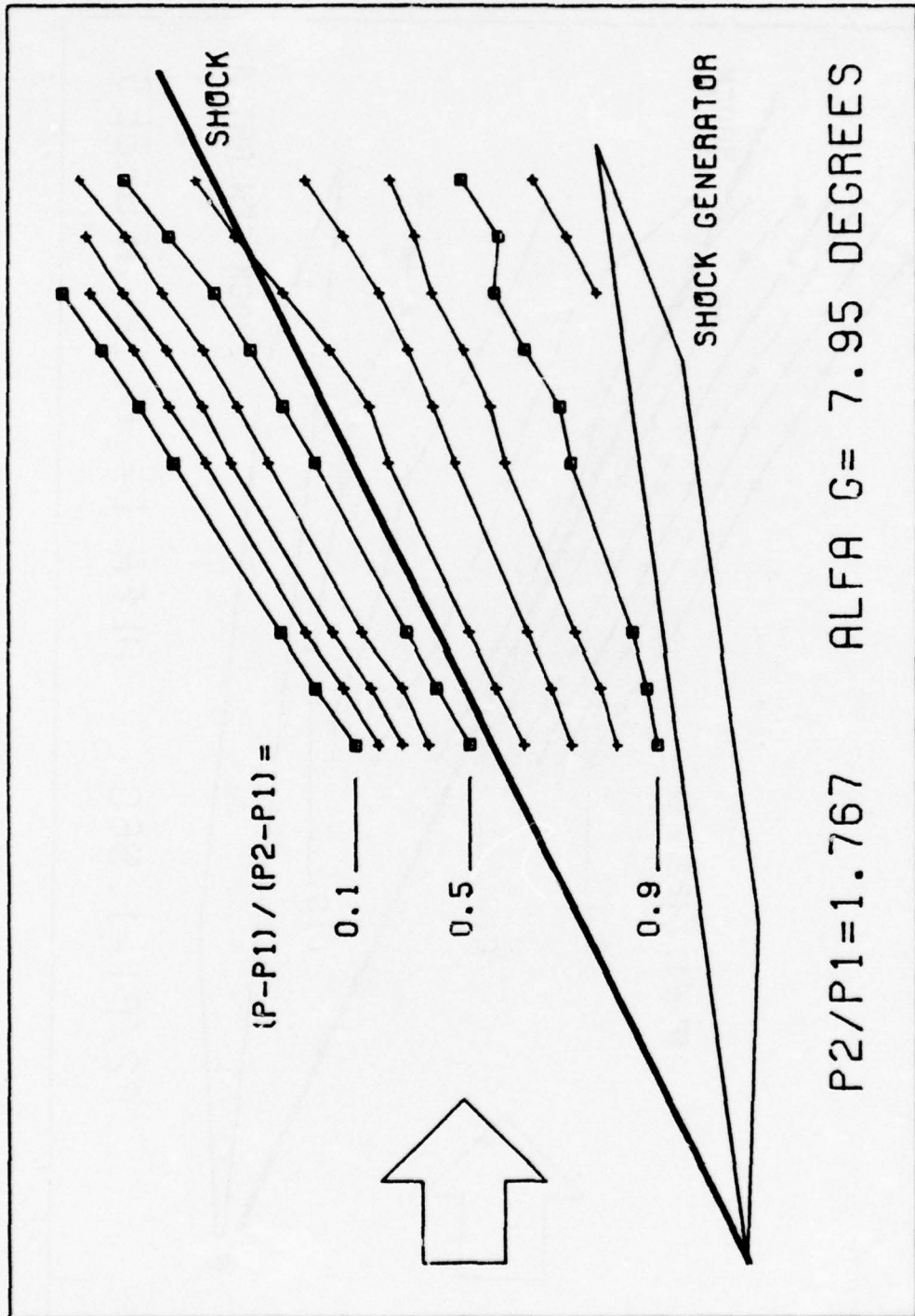


Figure B-4: Surface Isobar Pattern, 8 degrees.

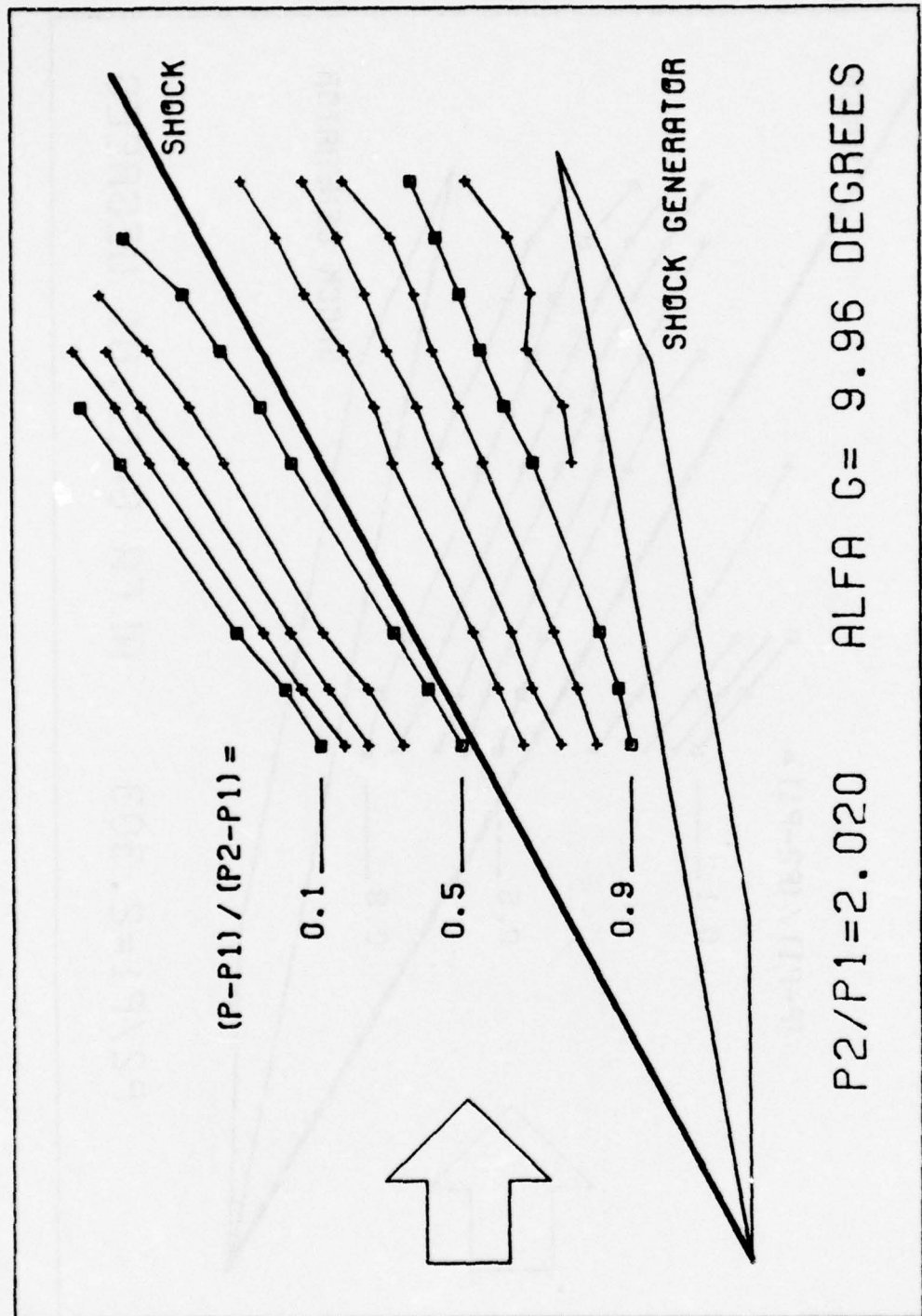


Figure B-5: Surface Isobar Pattern, 10 degrees.

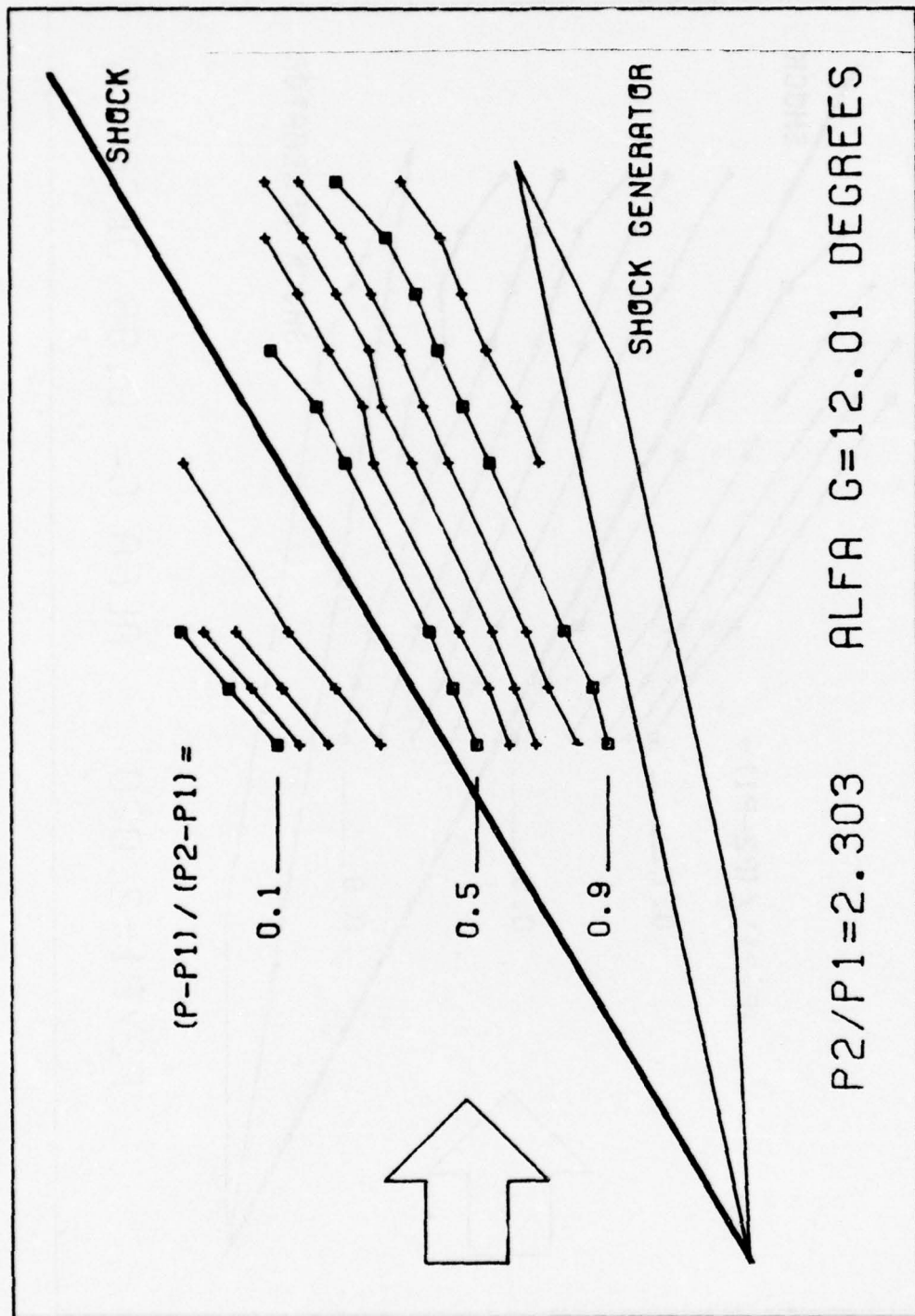


Figure B-6: Surface Isobar Pattern, 12 degrees.

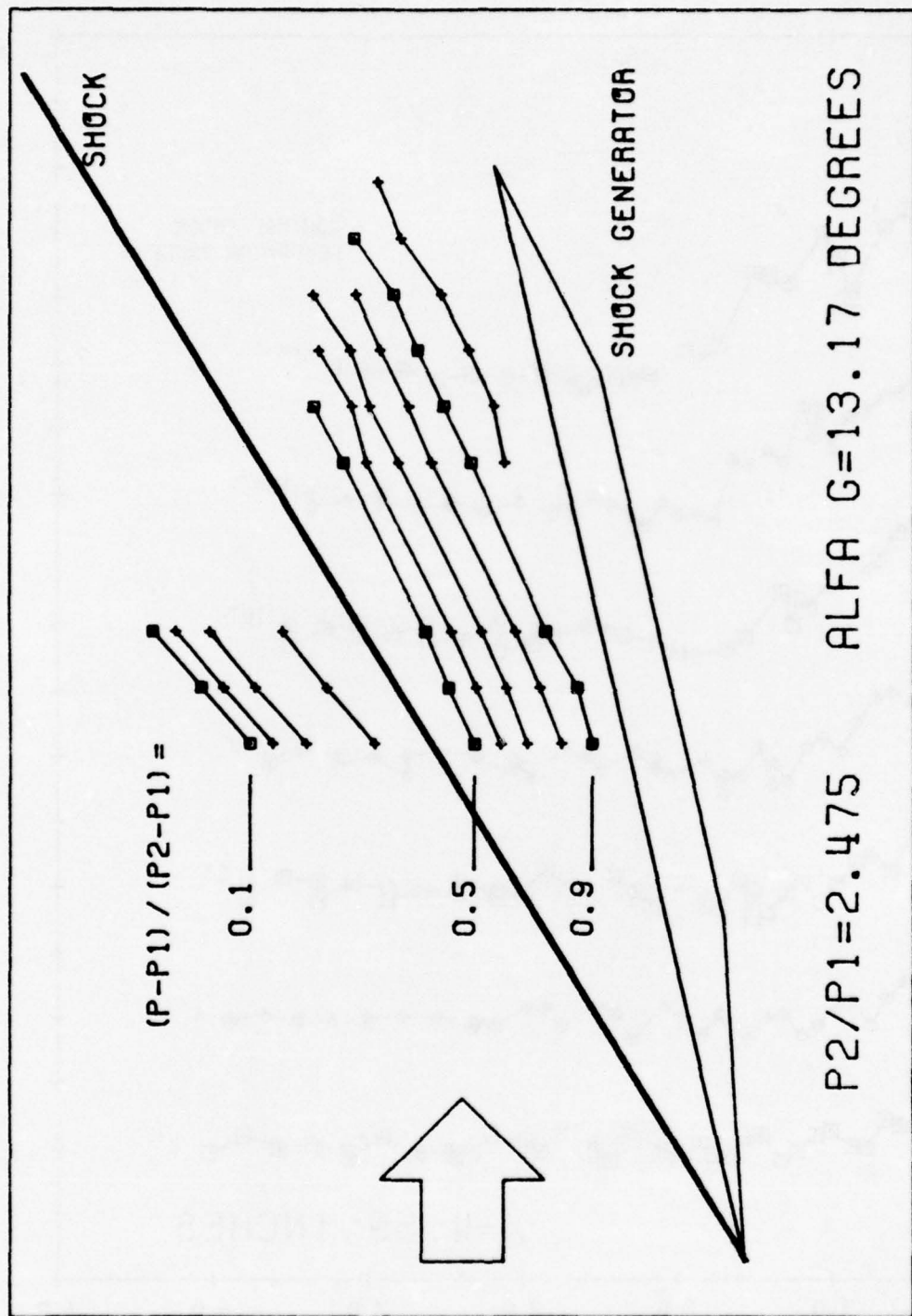


Figure B-7: Surface Isobar Pattern, 13 degrees.

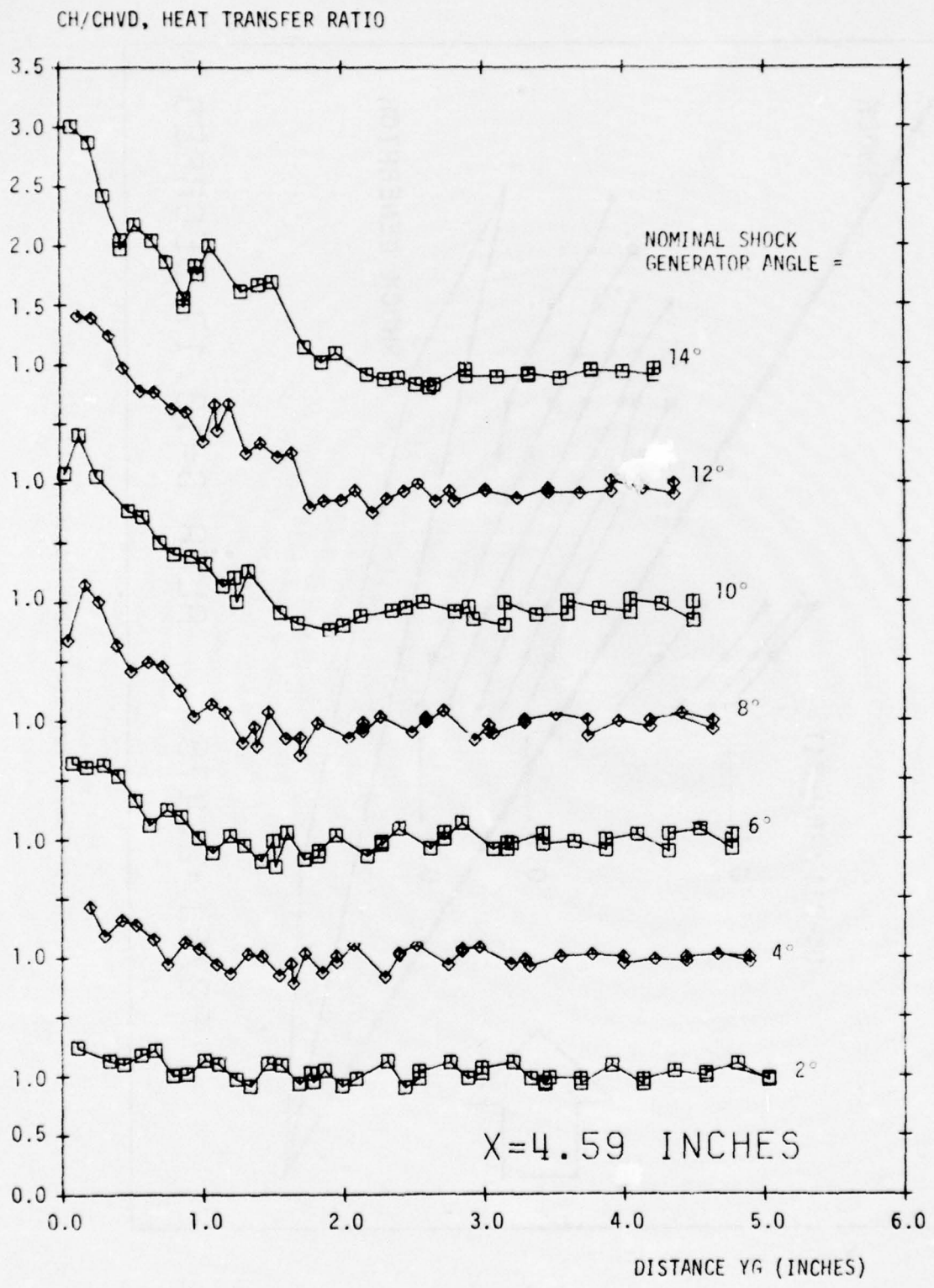


Figure C-1: Surface Heat Transfer, X = 4.6 inches.

CH/CHVD. HEAT TRANSFER RATIO

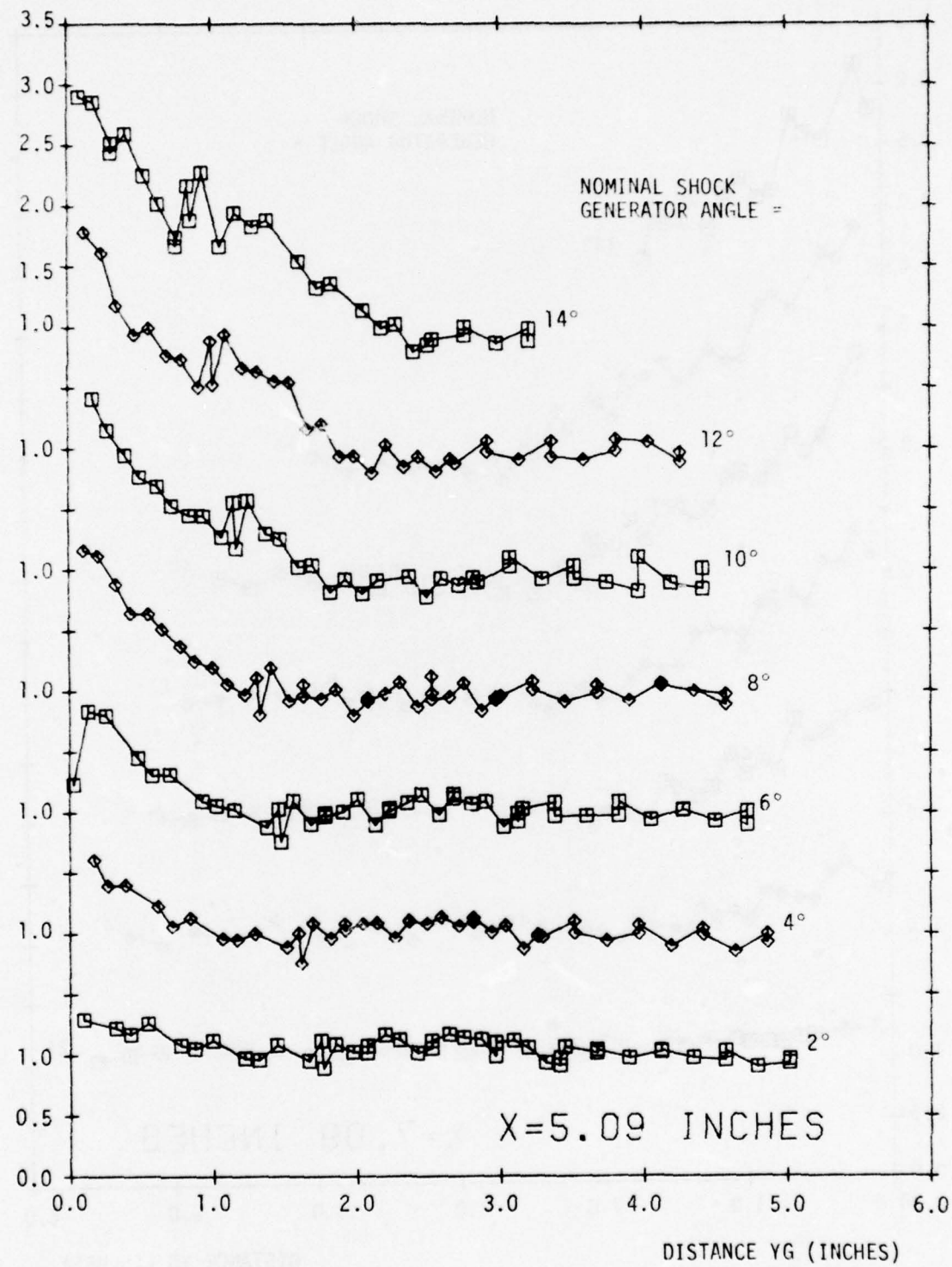


Figure C-2: Surface Heat Transfer, X = 5.1 inches.

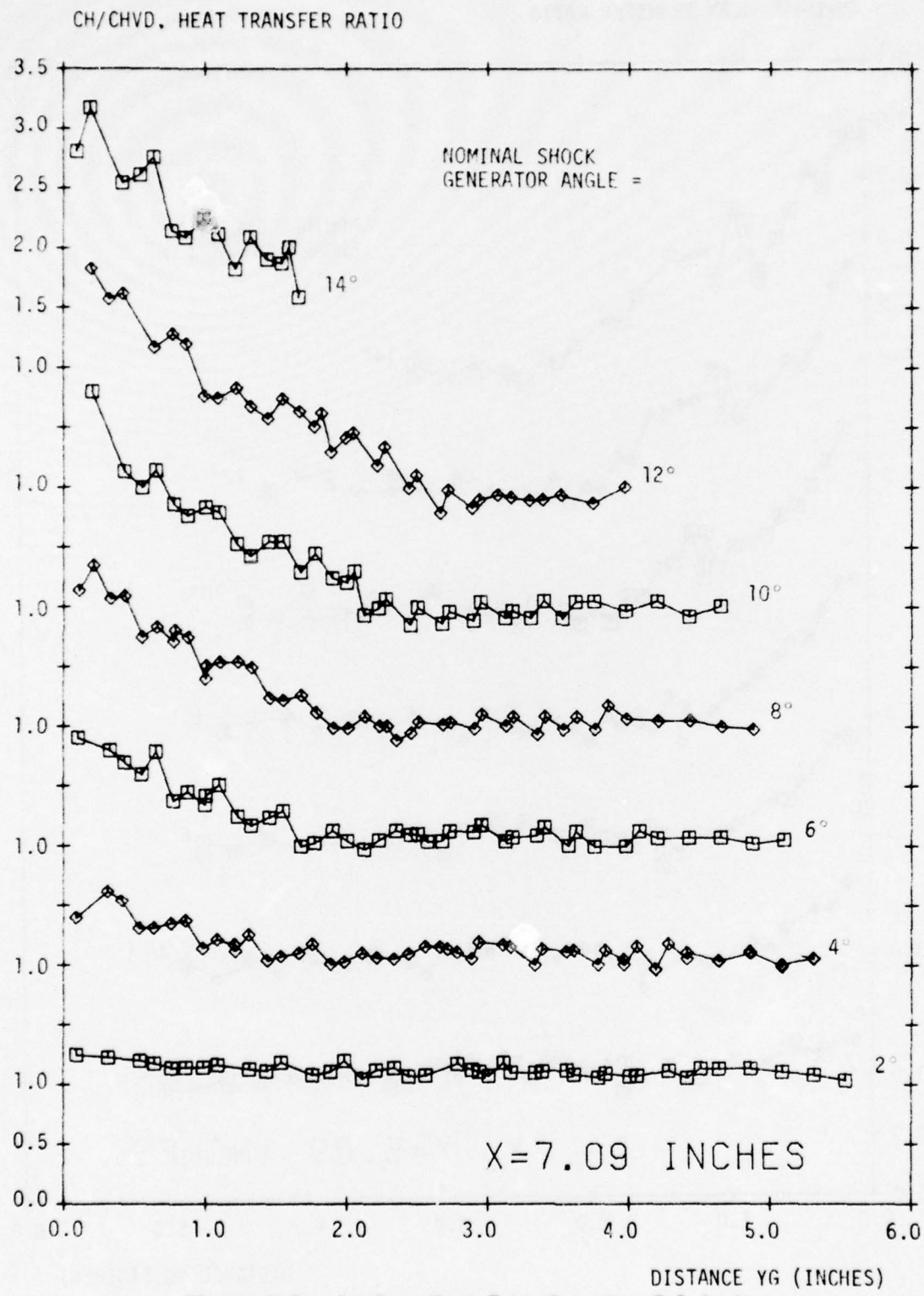


Figure C-3: Surface Heat Transfer, X = 7.1 inches.

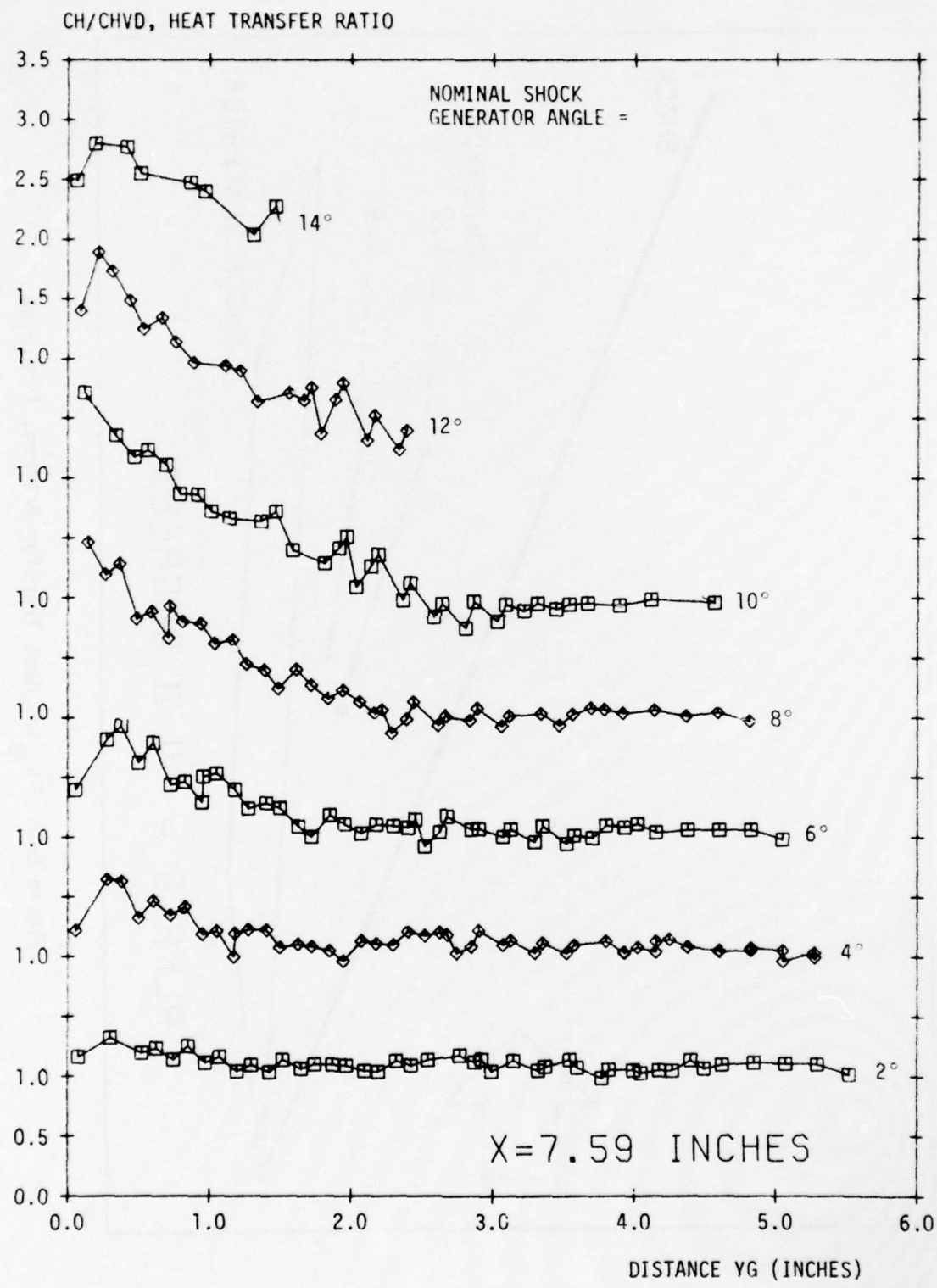


Figure C-4: Surface Heat Transfer, X = 7.6 inches.

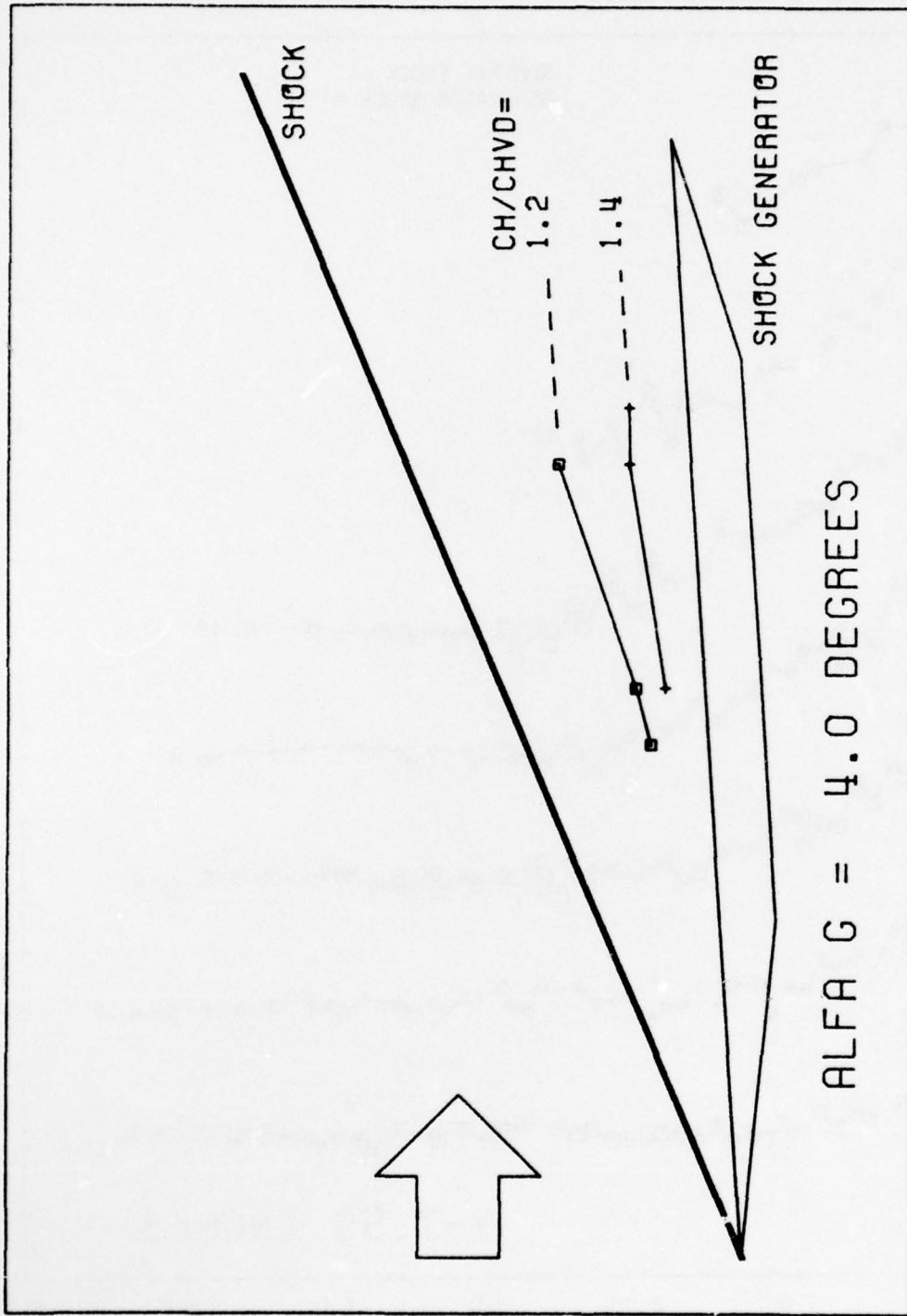


Figure D-1: Surface Heat Transfer Pattern, 4 degrees.

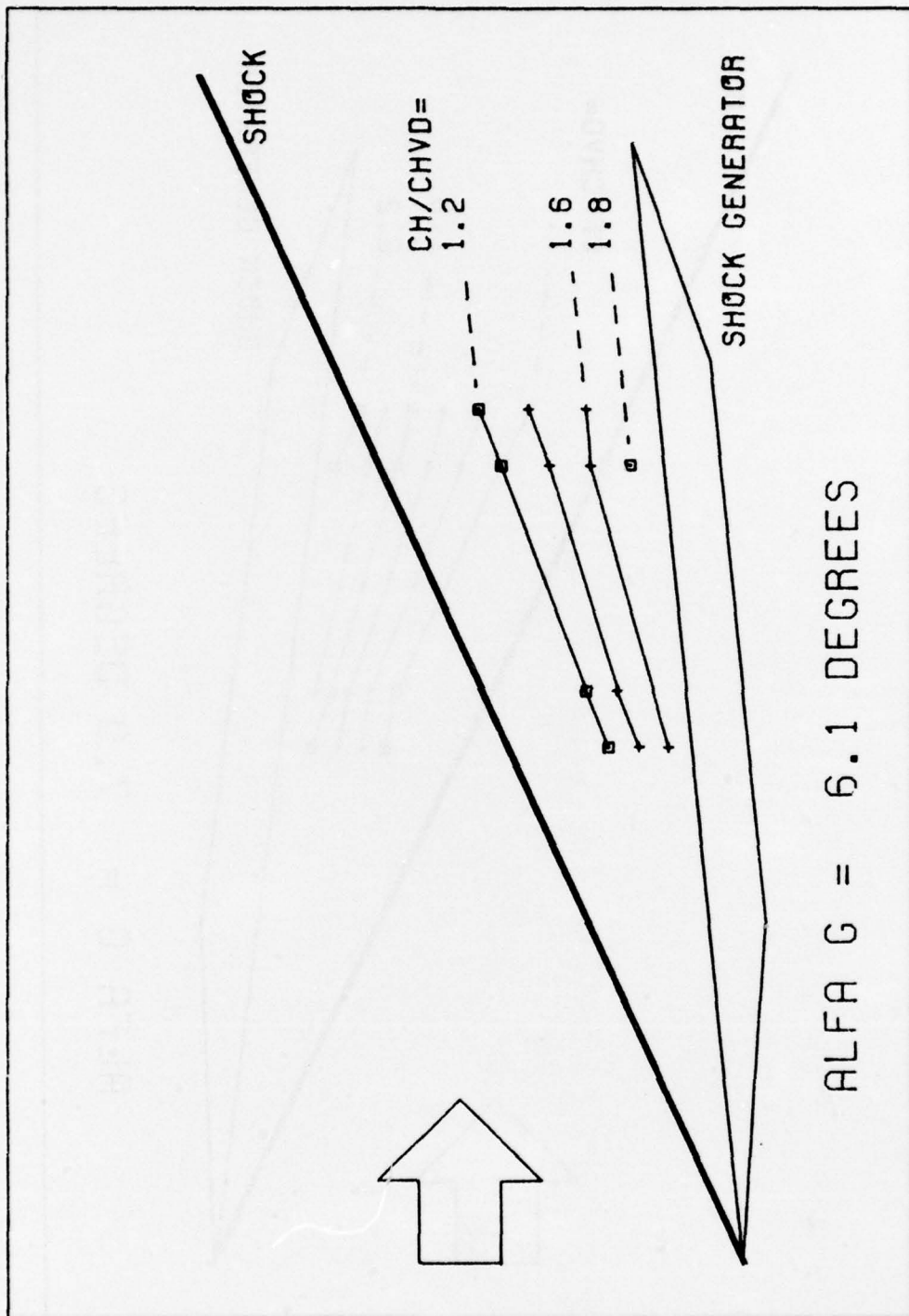


Figure D-2: Surface Heat Transfer Pattern, 6 degrees.

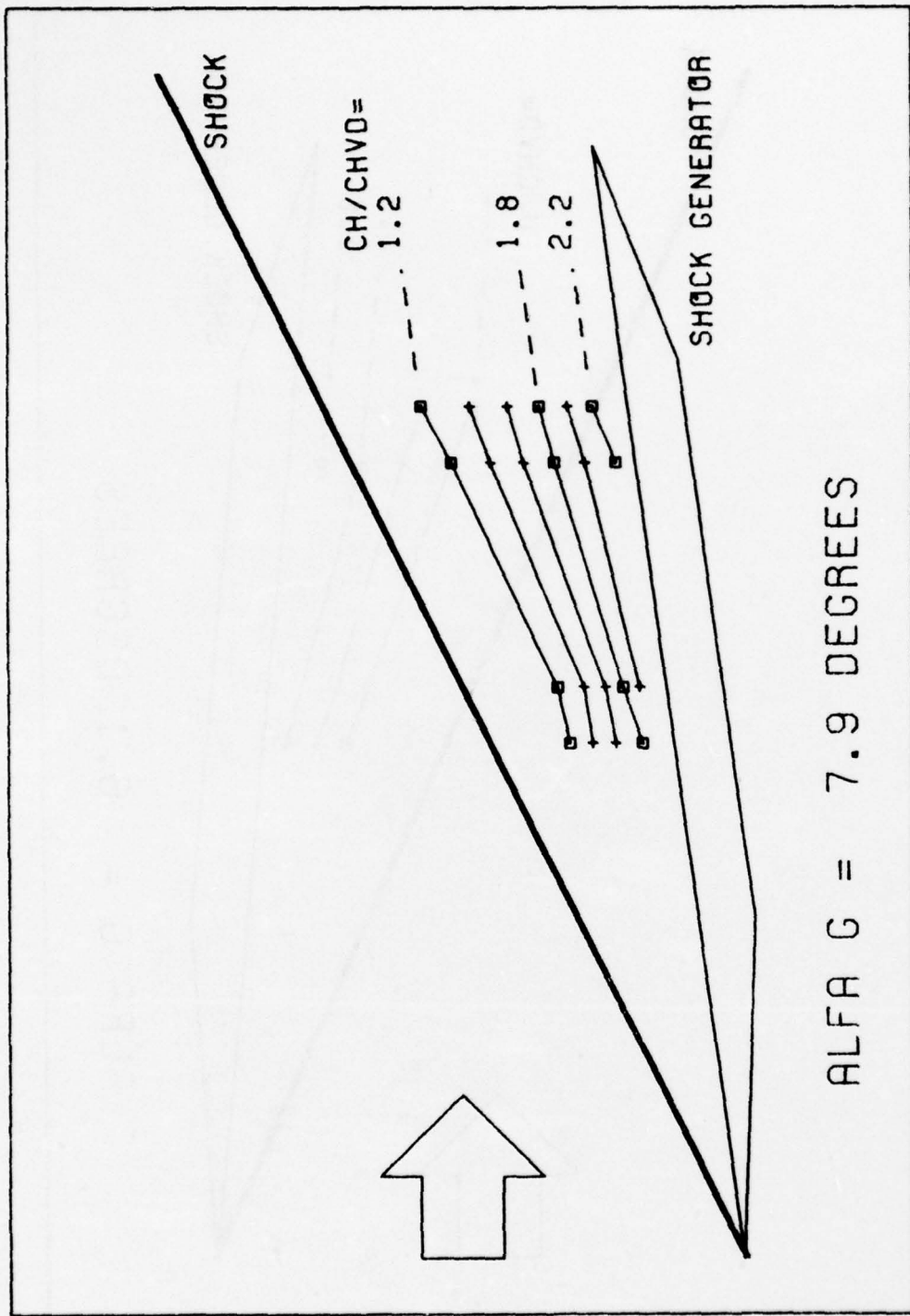


Figure D-3: Surface Heat Transfer Pattern, 8 degrees.

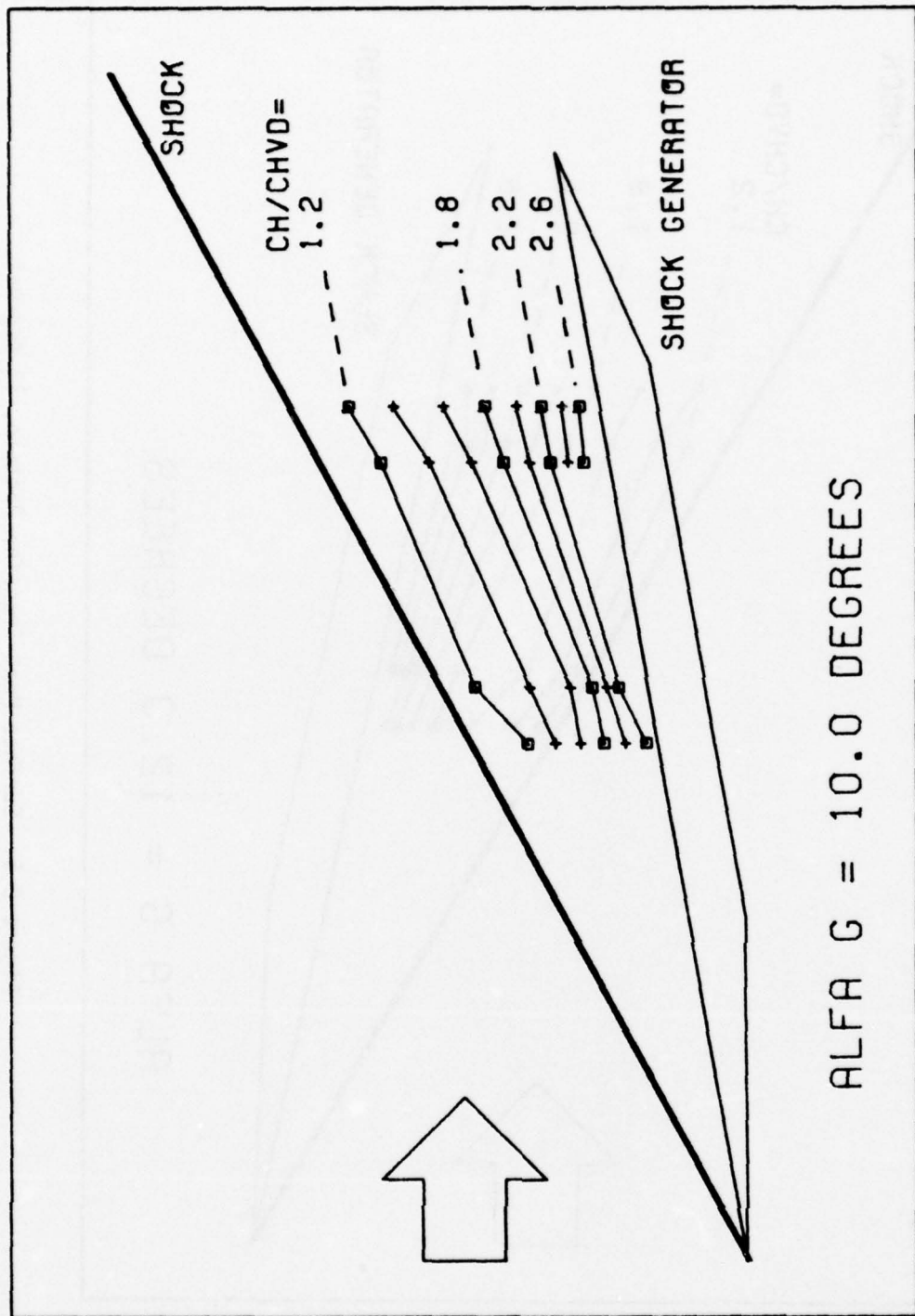


Figure D-4: Surface Heat Transfer Pattern, 10 degrees.

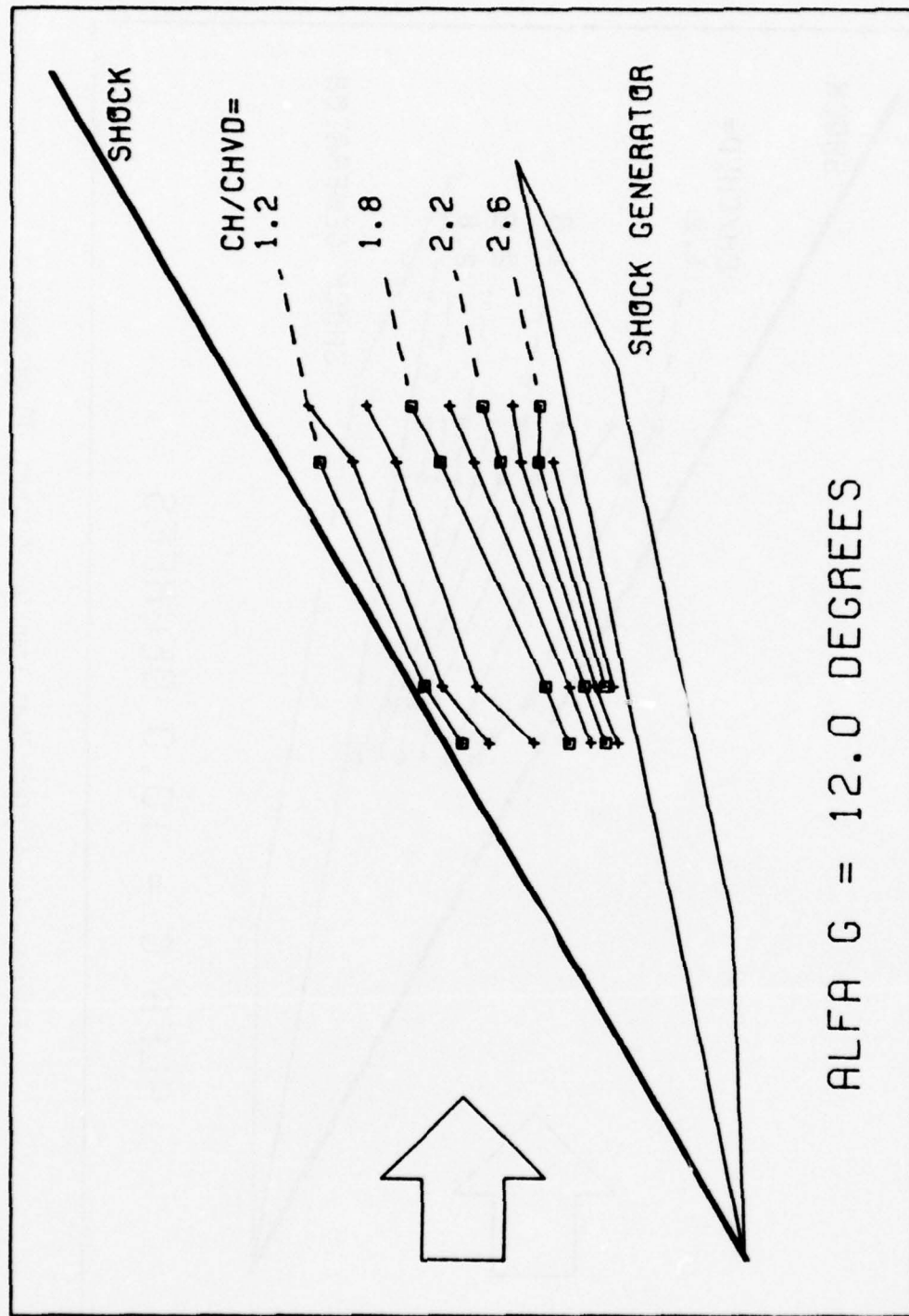


Figure D-5: Surface Heat Transfer Pattern, 12 degrees.

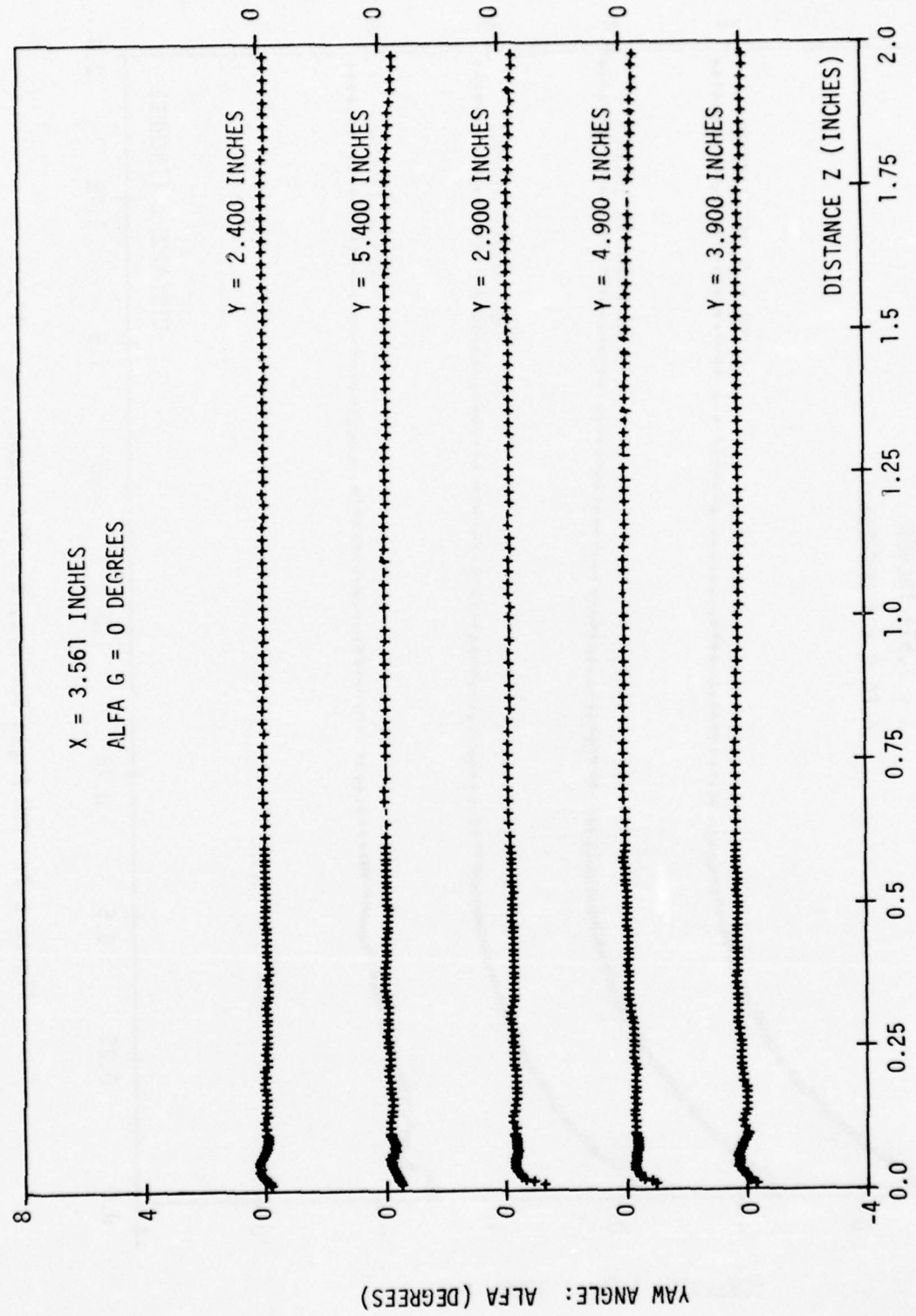


Figure E-1: Yaw Angle Surveys, $X = 3.56$ inches, $\alpha_G = 0^\circ$.

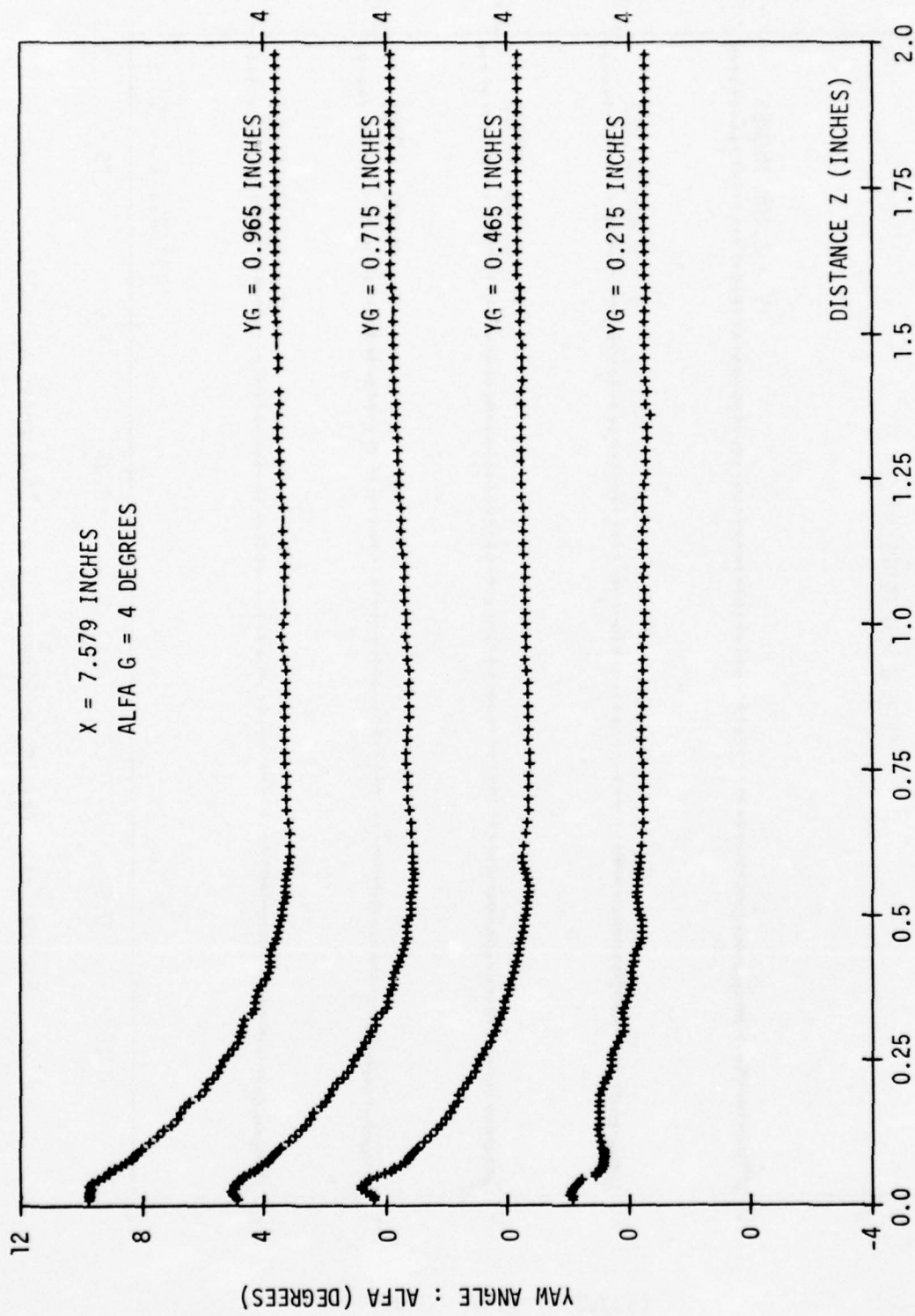


Figure E-2: Yaw Angle Surveys, $X = 7.6$ inches, $\alpha_G = 4^\circ$.

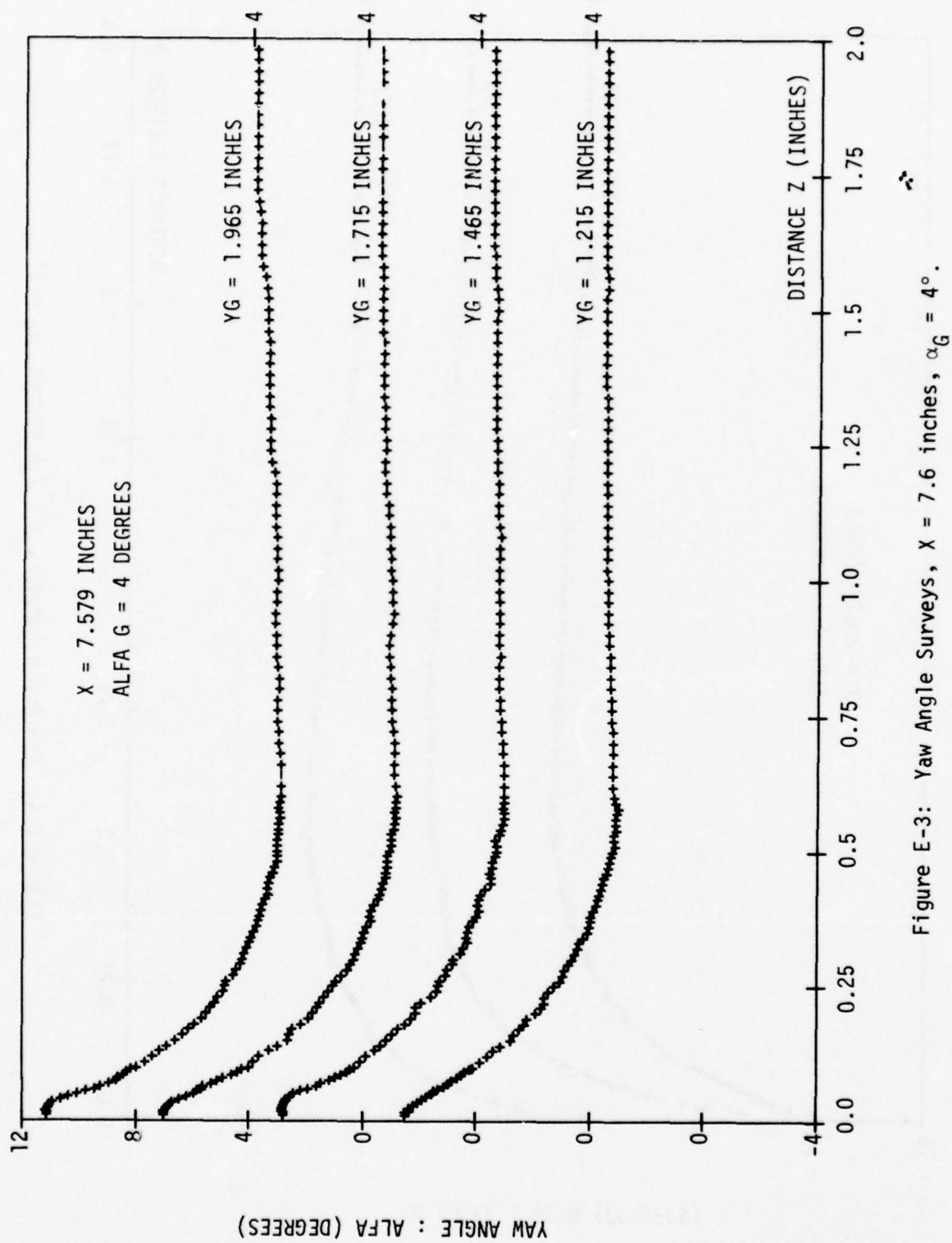


Figure E-3: Yaw Angle Surveys, $X = 7.6$ inches, $\alpha_G = 4^\circ$.

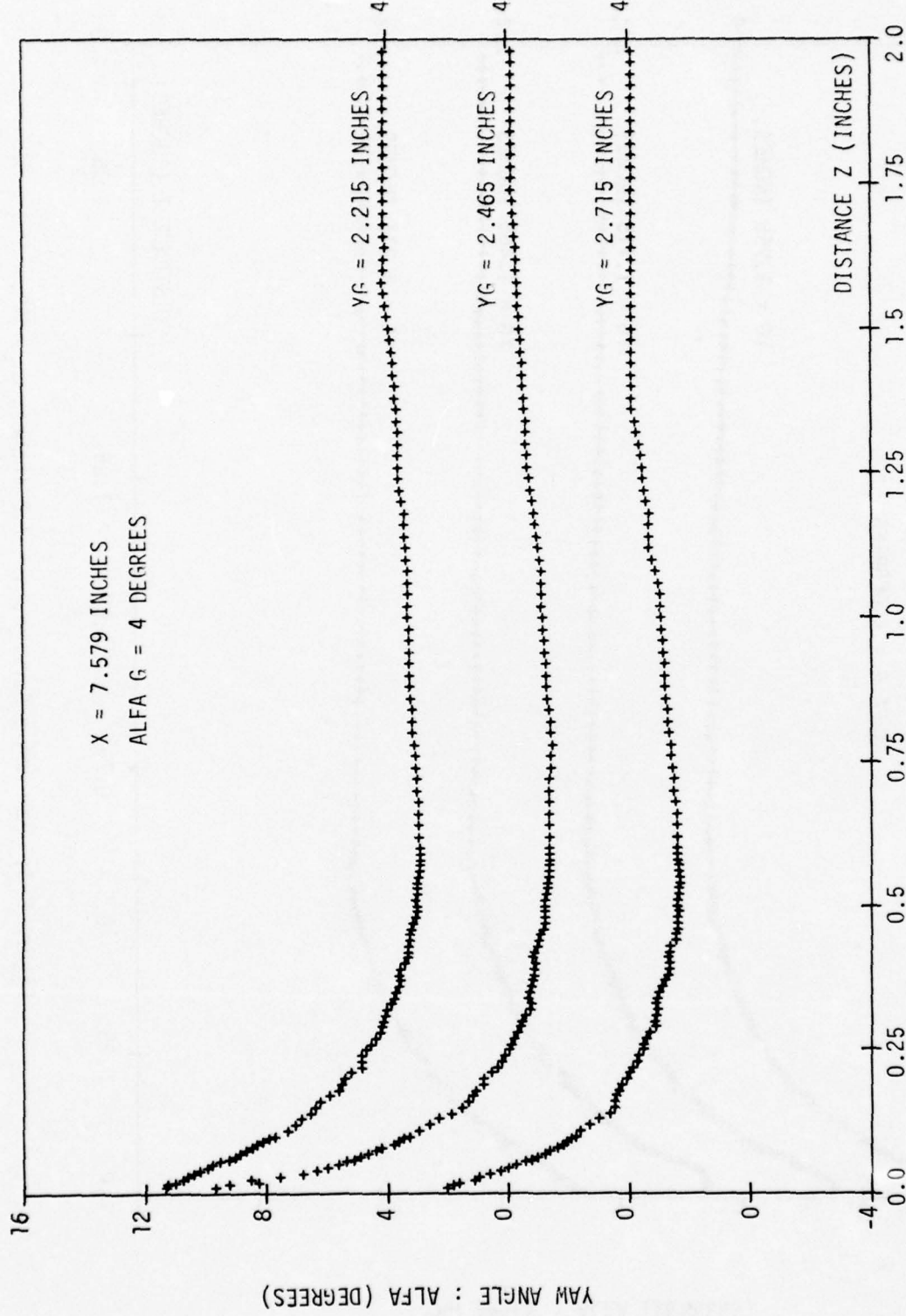


Figure E-4: Yaw Angle Surveys, $X = 7.6$ inches, $\alpha_G = 4^\circ$.

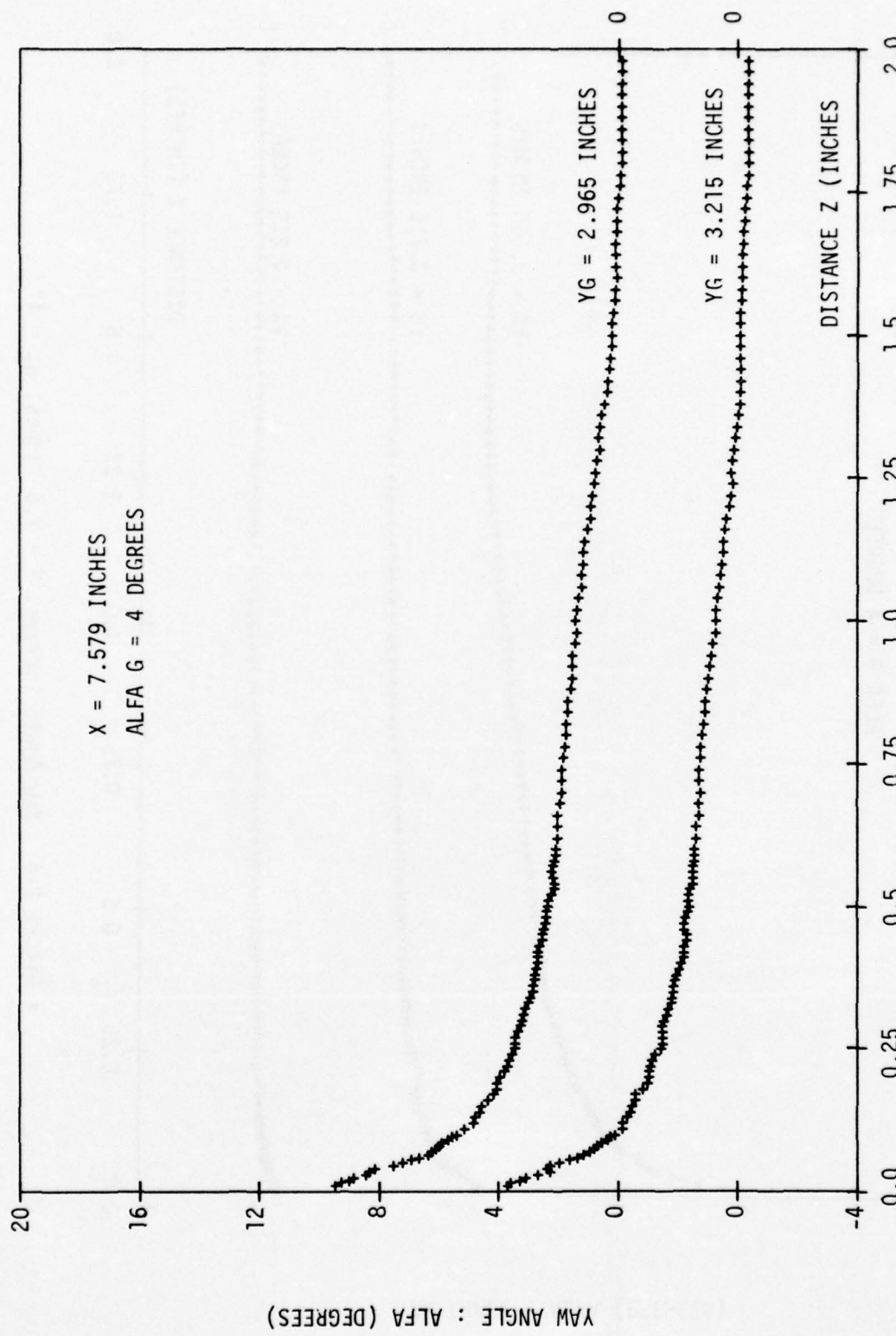


Figure E-5: Yaw Angle Surveys, $X = 7.6$ inches, $\alpha_G = 4^\circ$.

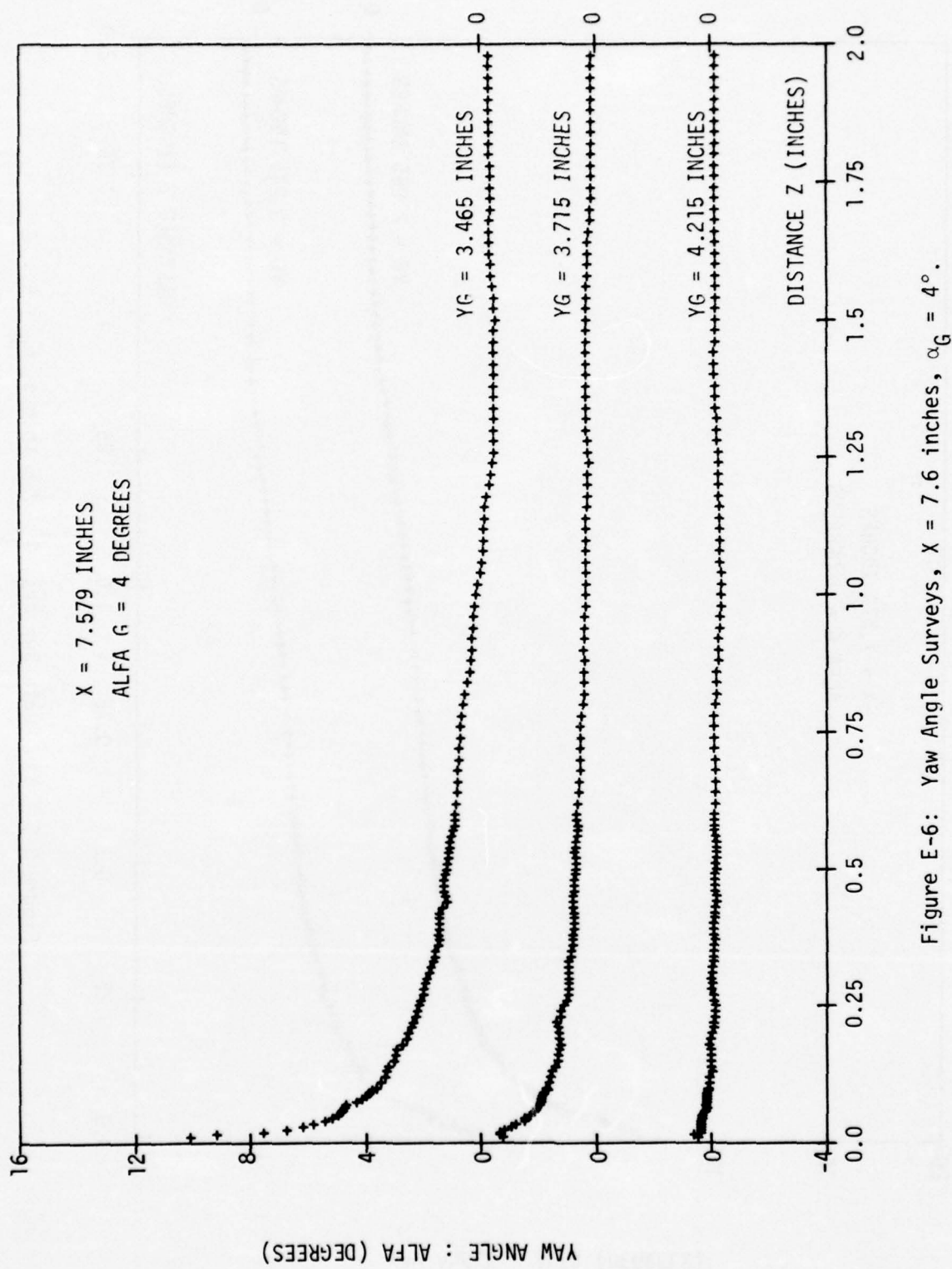


Figure E-6: Yaw Angle Surveys, $X = 7.6$ inches, $\alpha_G = 4^\circ$.

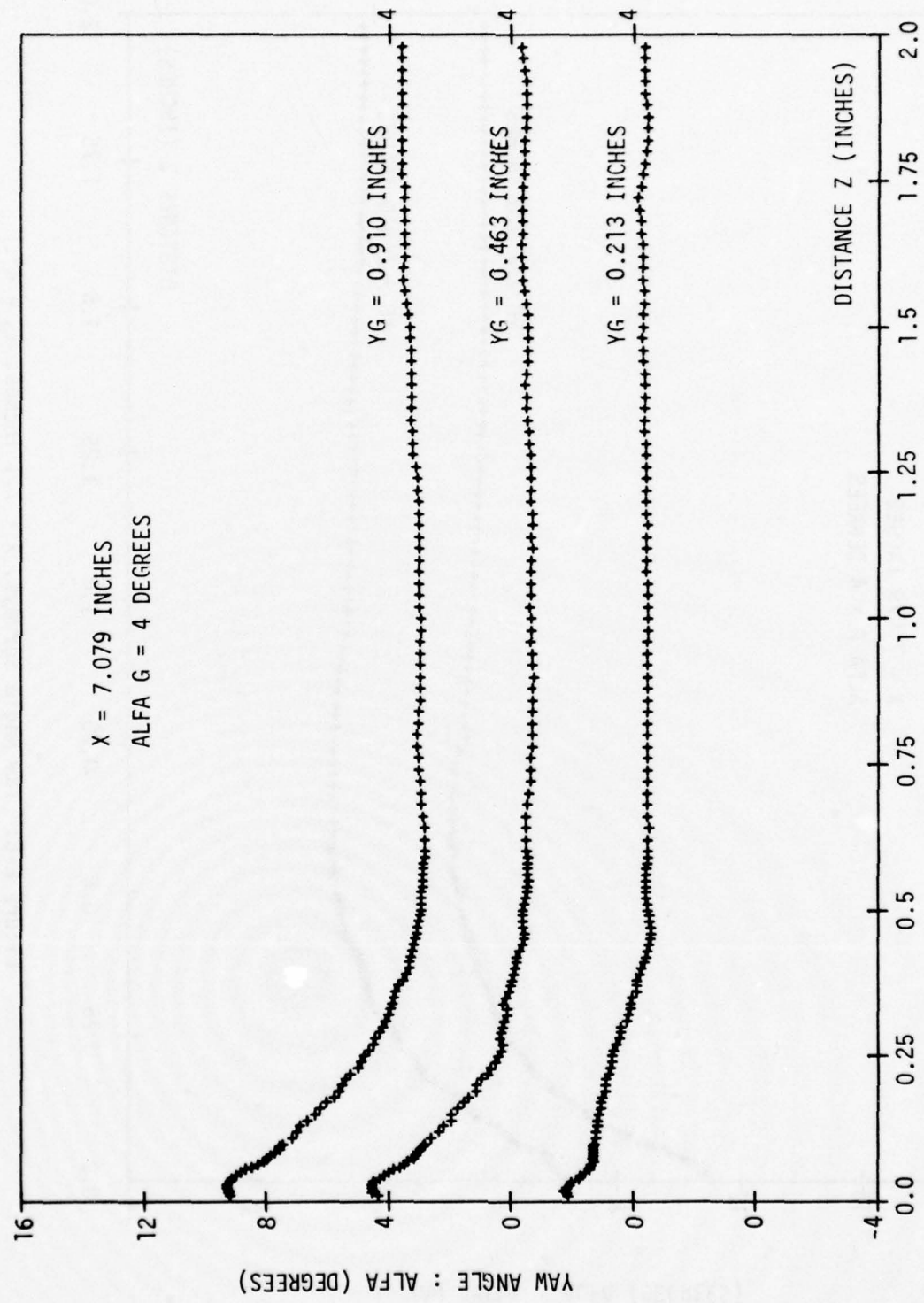


Figure E-7: Yaw Angle Surveys, $X = 7.1$ inches, $\alpha_G = 4^\circ$.

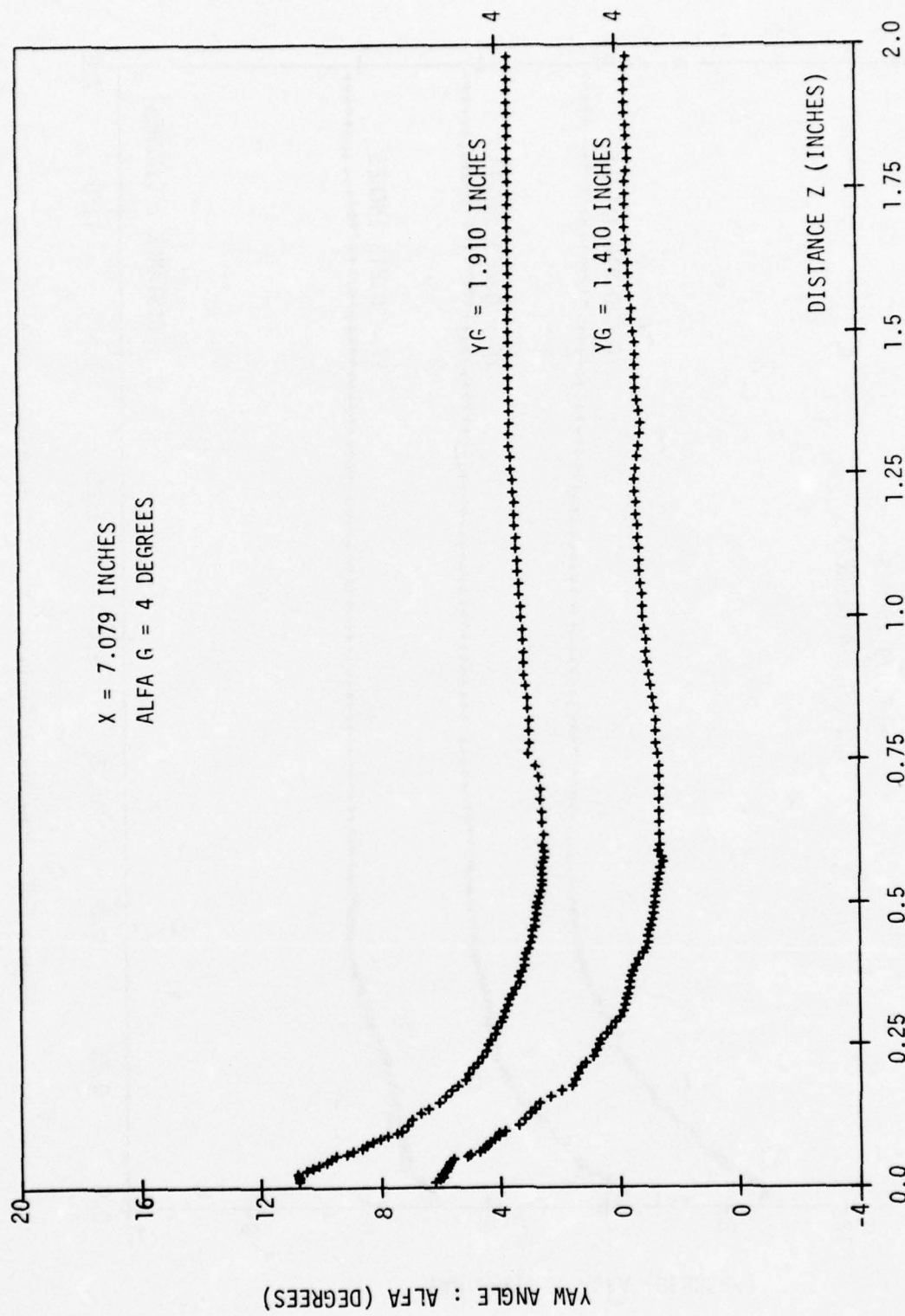


Figure E-8: Yaw Angle Surveys, $X = 7.1$ inches, $\alpha_G = 4^\circ$.

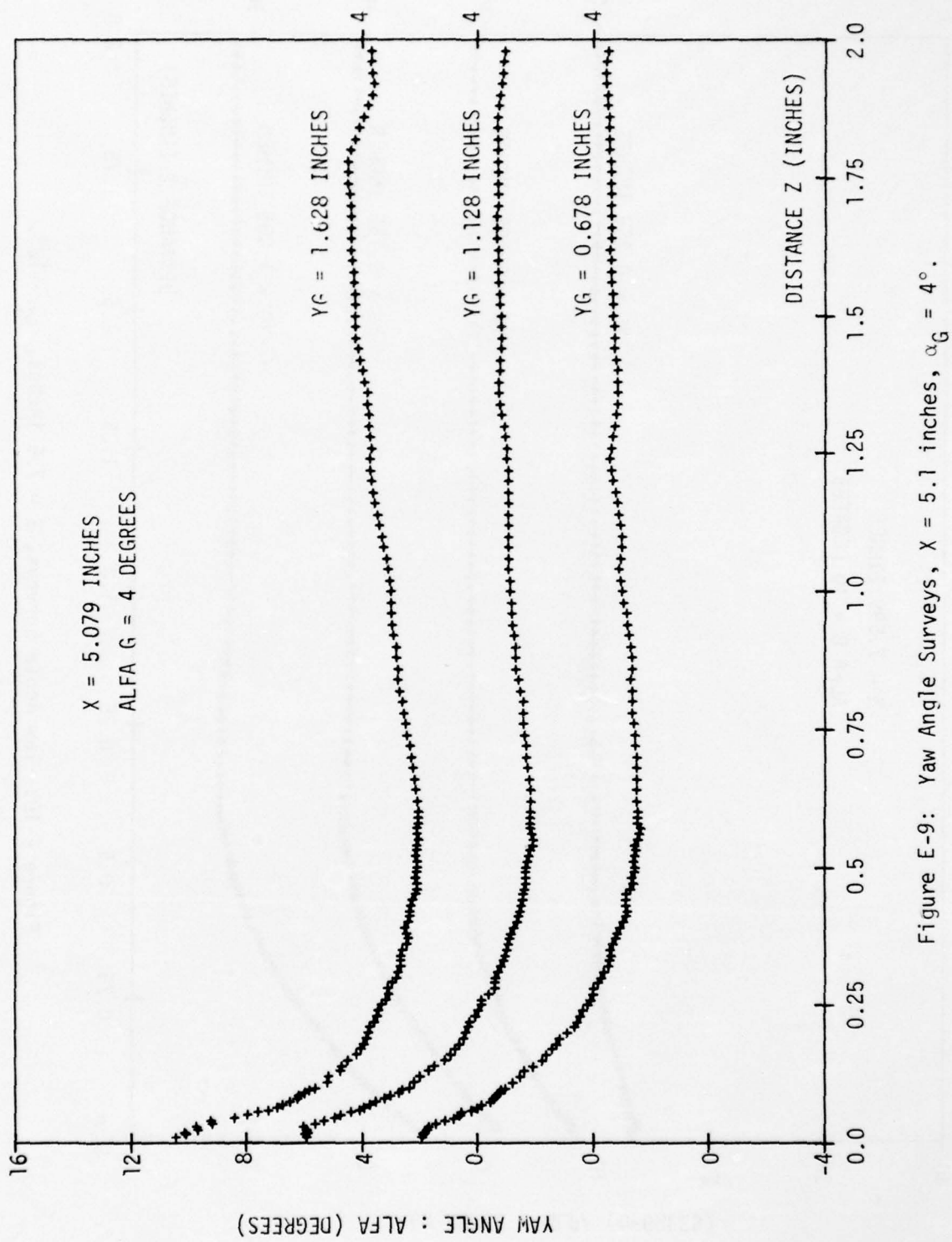


Figure E-9: Yaw Angle Surveys, $X = 5.1$ inches, $\alpha_G = 4^\circ$.

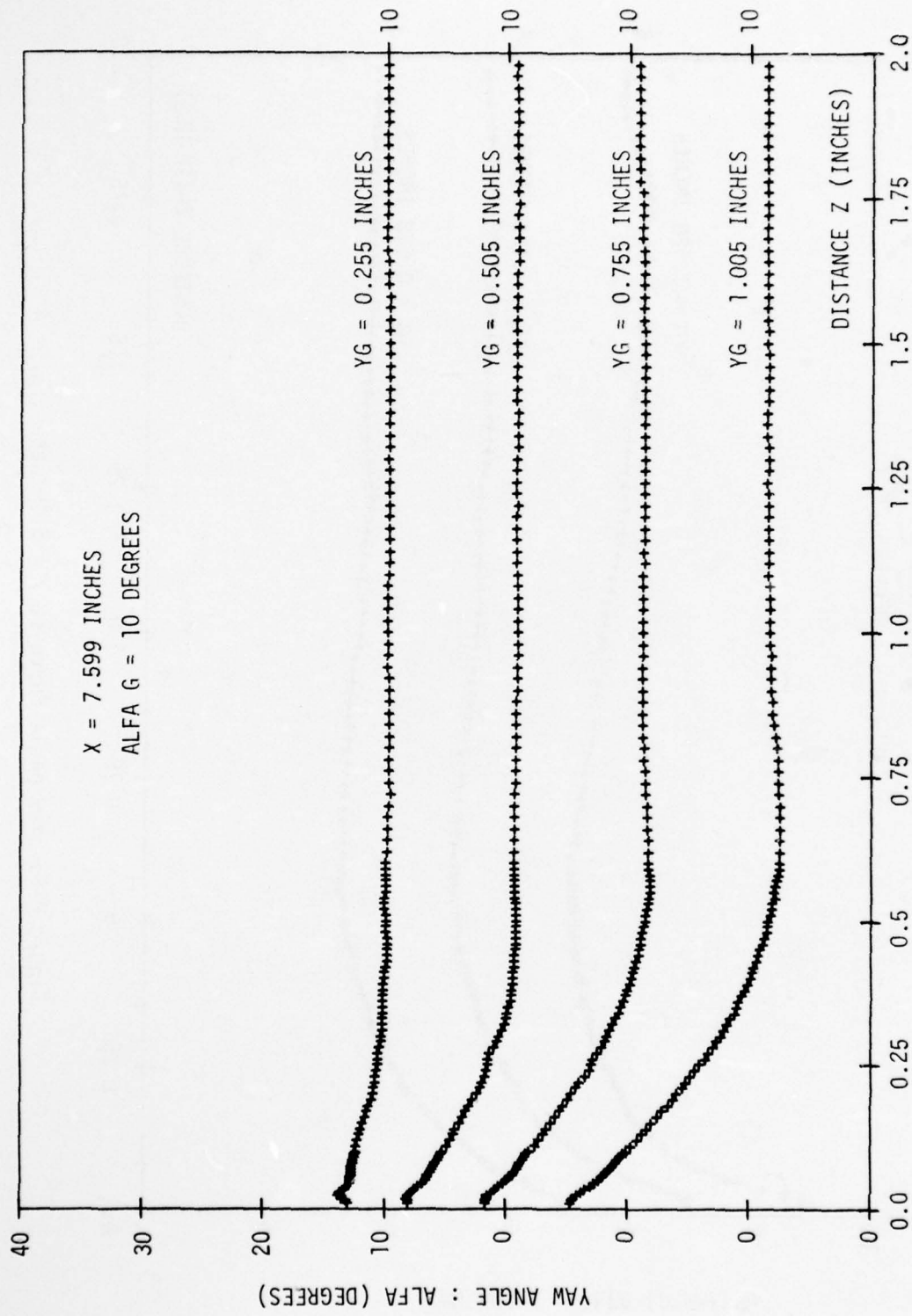


Figure E-10: Yaw Angle Surveys, $X = 7.6$ inches, $\alpha_G = 10^\circ$.

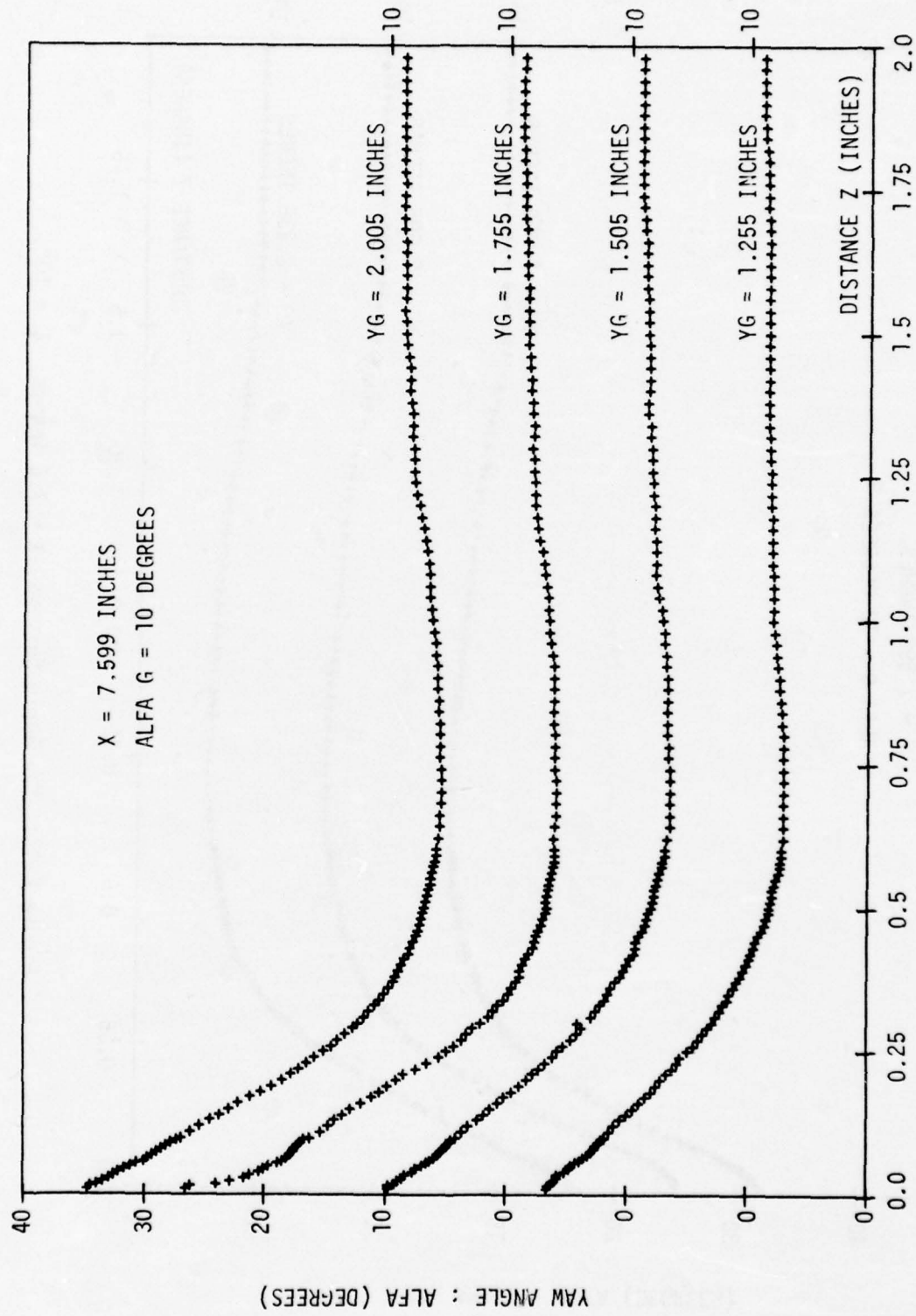


Figure E-11: Yaw Angle Surveys, $X = 7.6$ inches, $\alpha_G = 10^\circ$.

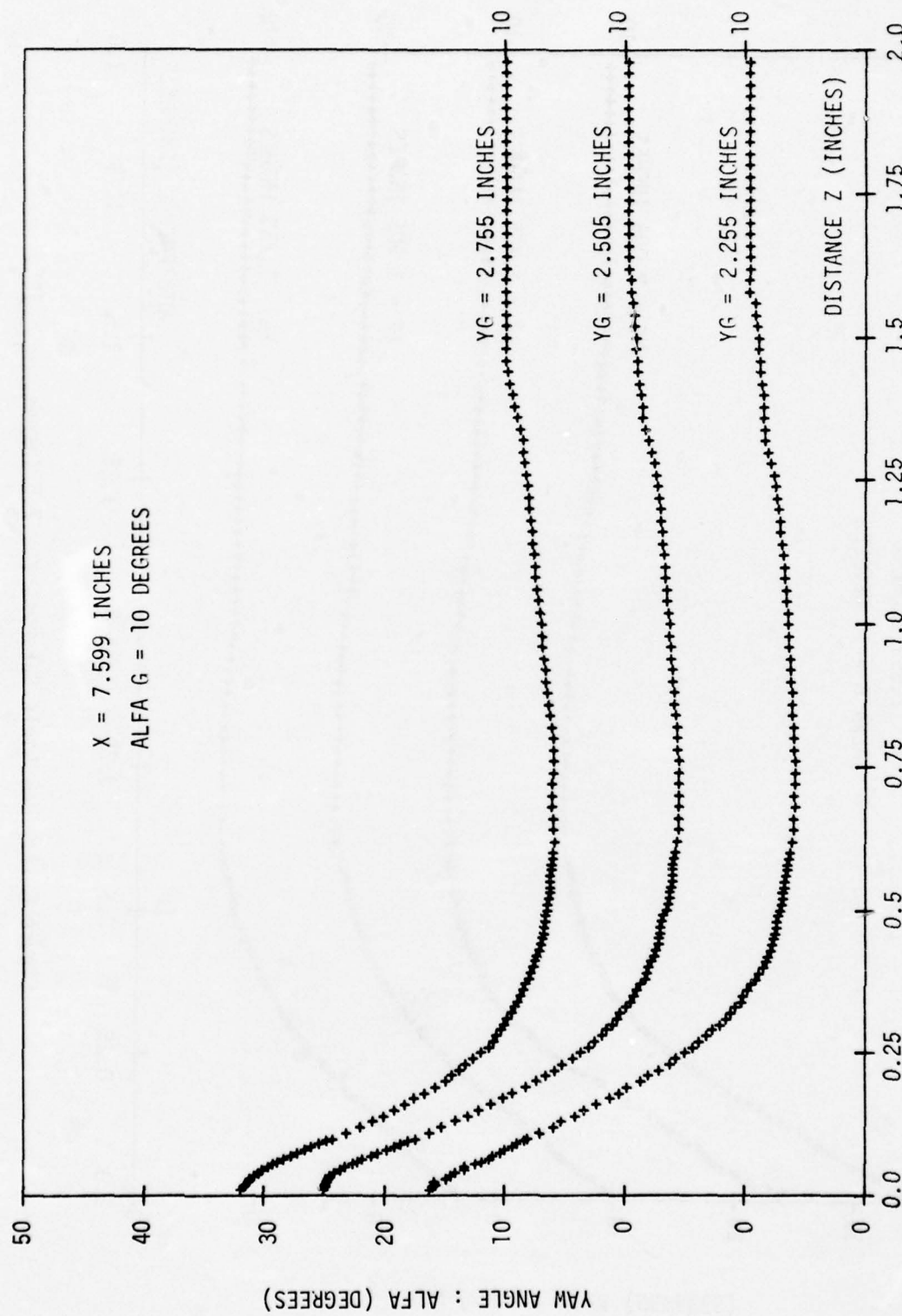


Figure E-12: Yaw Angle Surveys, $X = 7.6$ inches, $\alpha_G = 10^\circ$.

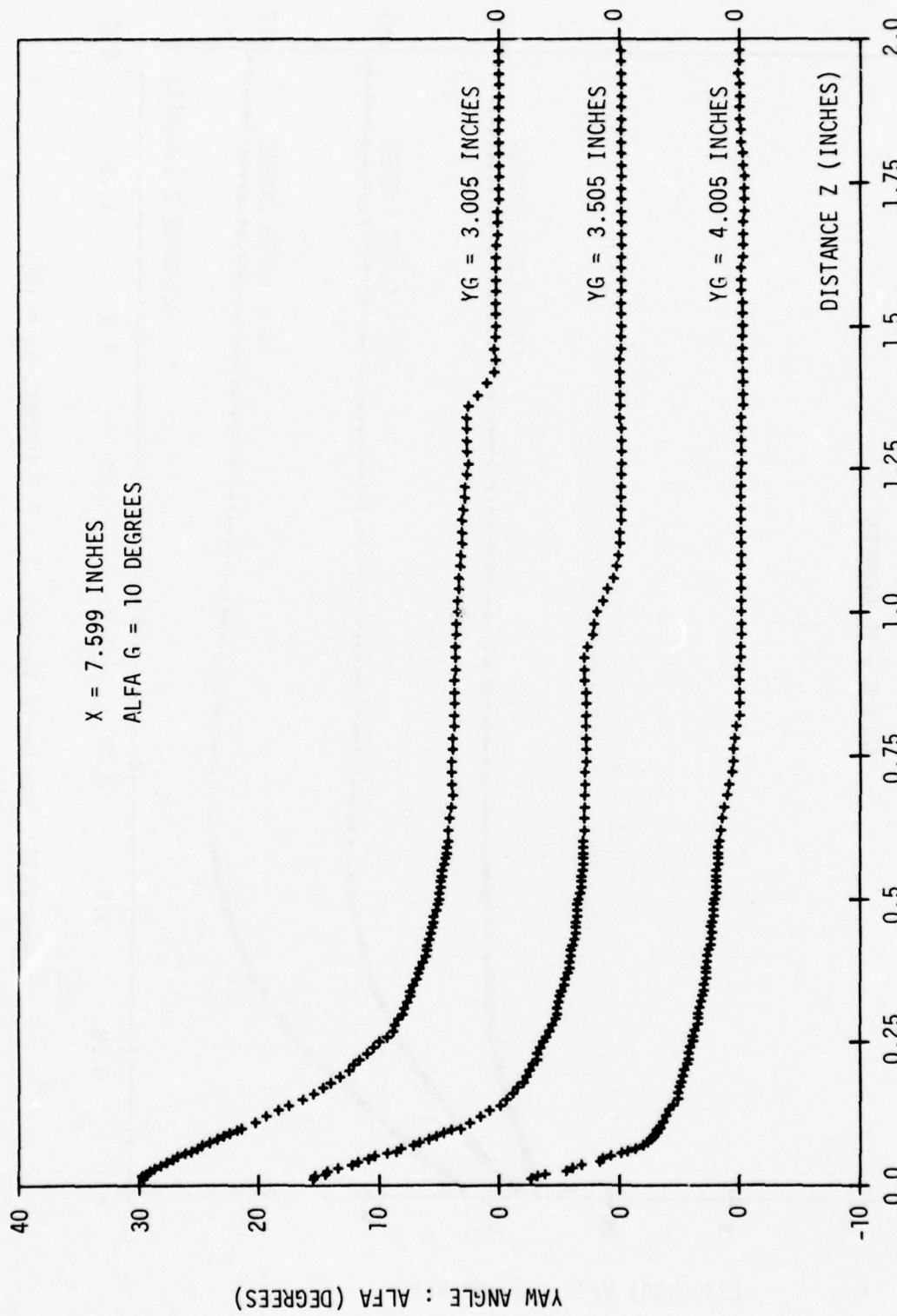


Figure E-13: Yaw Angle Surveys, $X = 7.6$ inches, $\alpha_G = 10^\circ$.

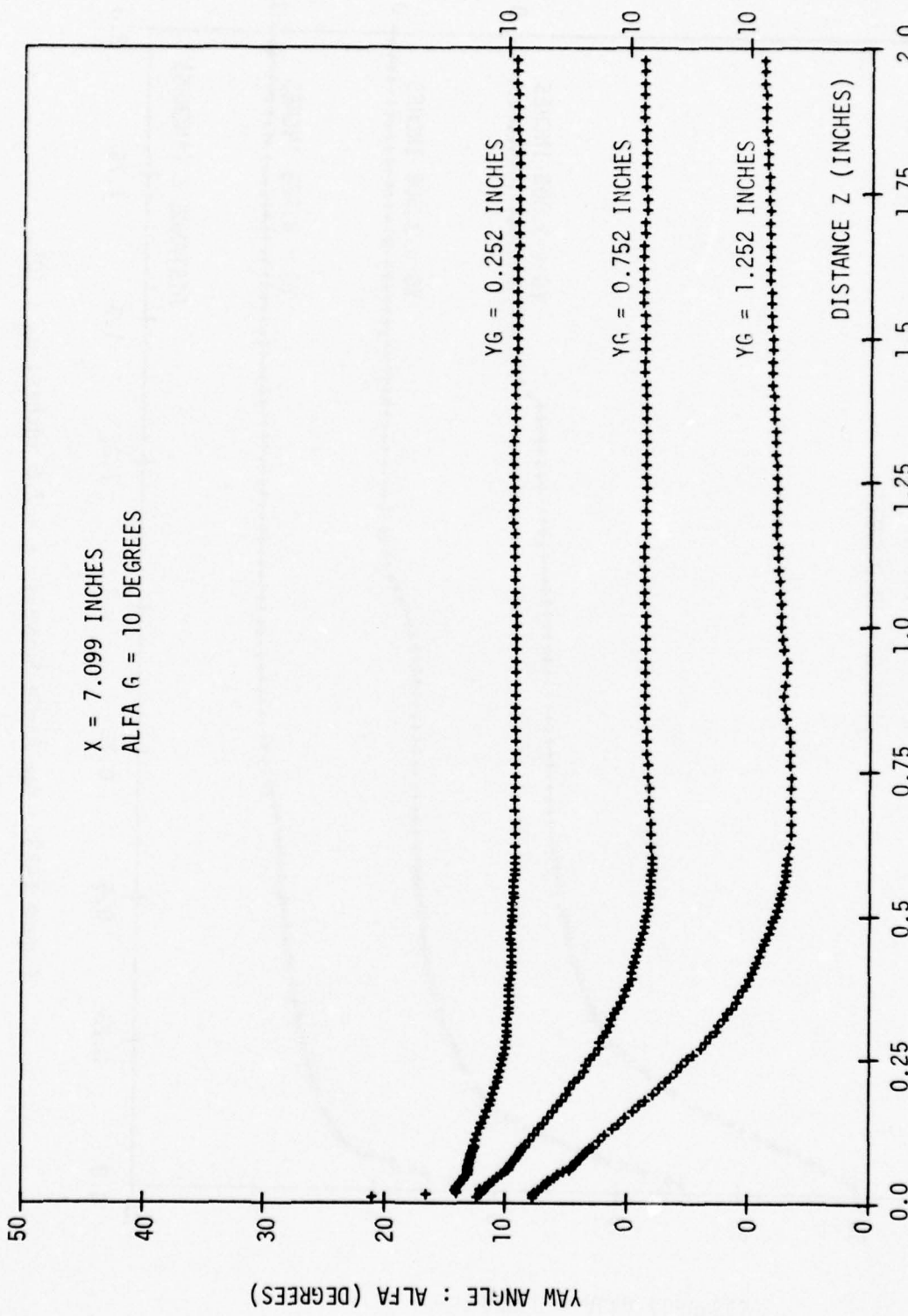


Figure E-14: Yaw Angle Surveys, $X = 7.1$ inches, $\alpha_G = 10^\circ$.

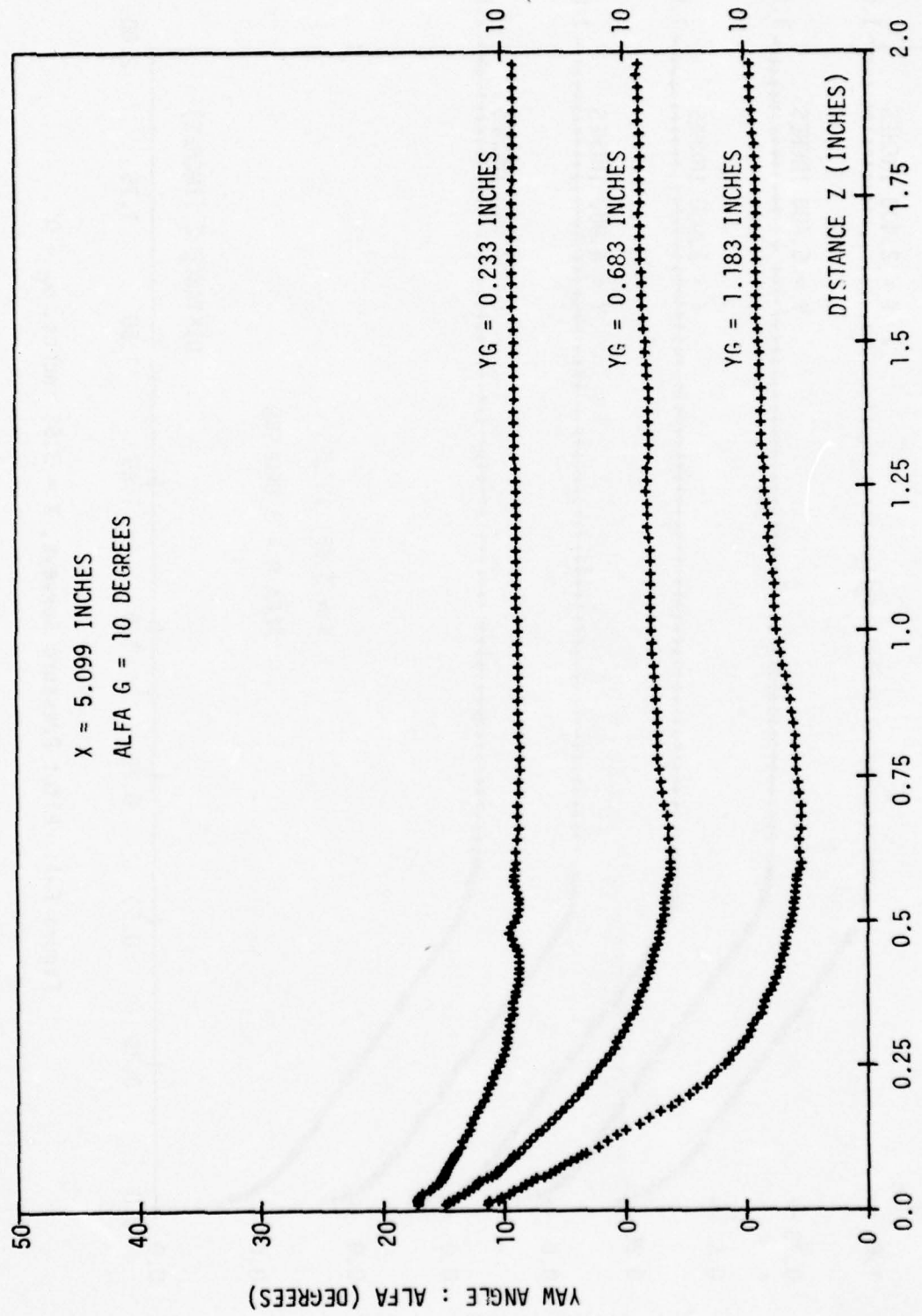


Figure E-15: Yaw Angle Surveys, $X = 5.1$ inches, $\alpha_G = 10^\circ$.

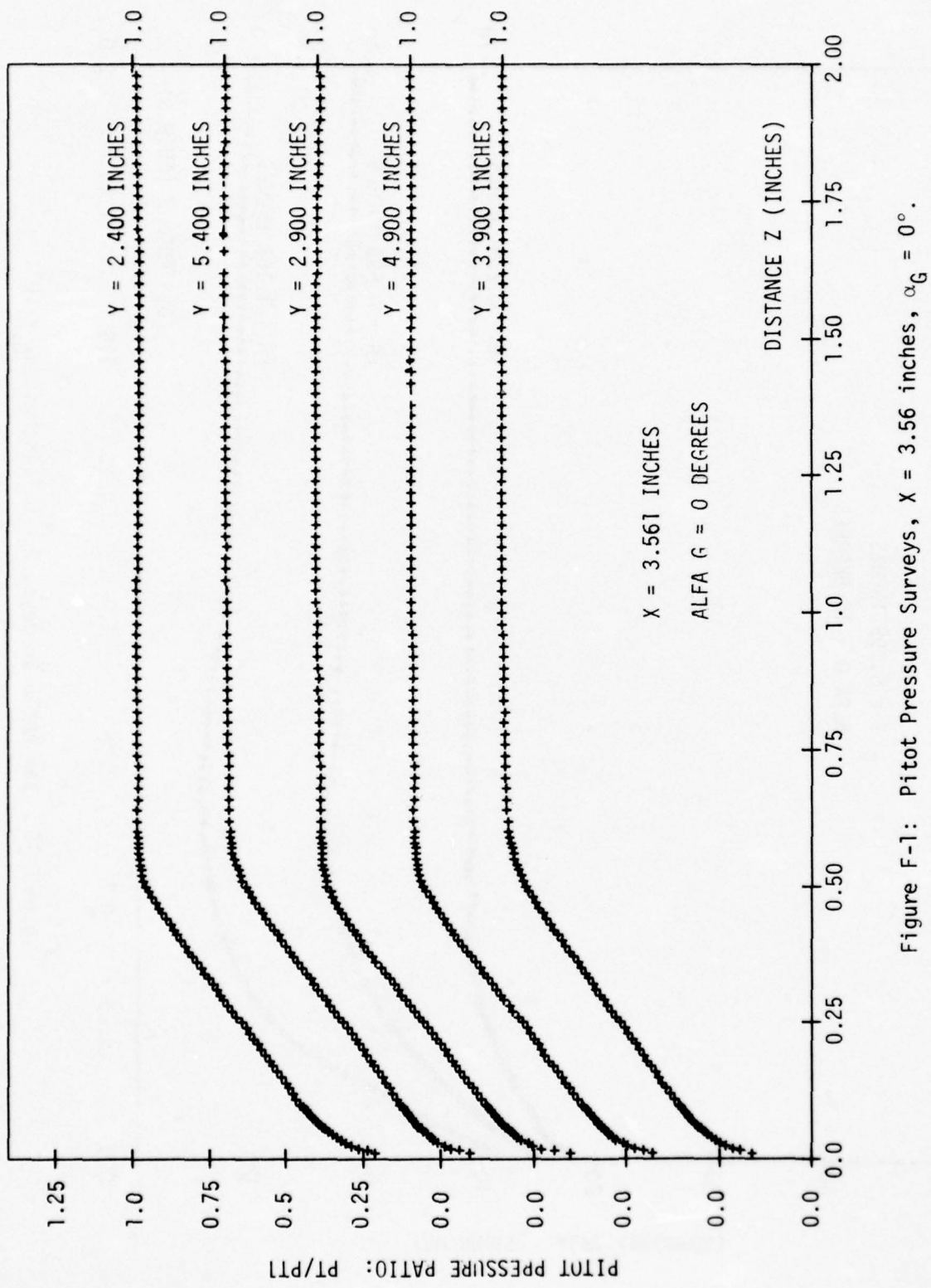


Figure F-1: Pitot Pressure Surveys, $X = 3.56$ inches, $\alpha_G = 0^\circ$.

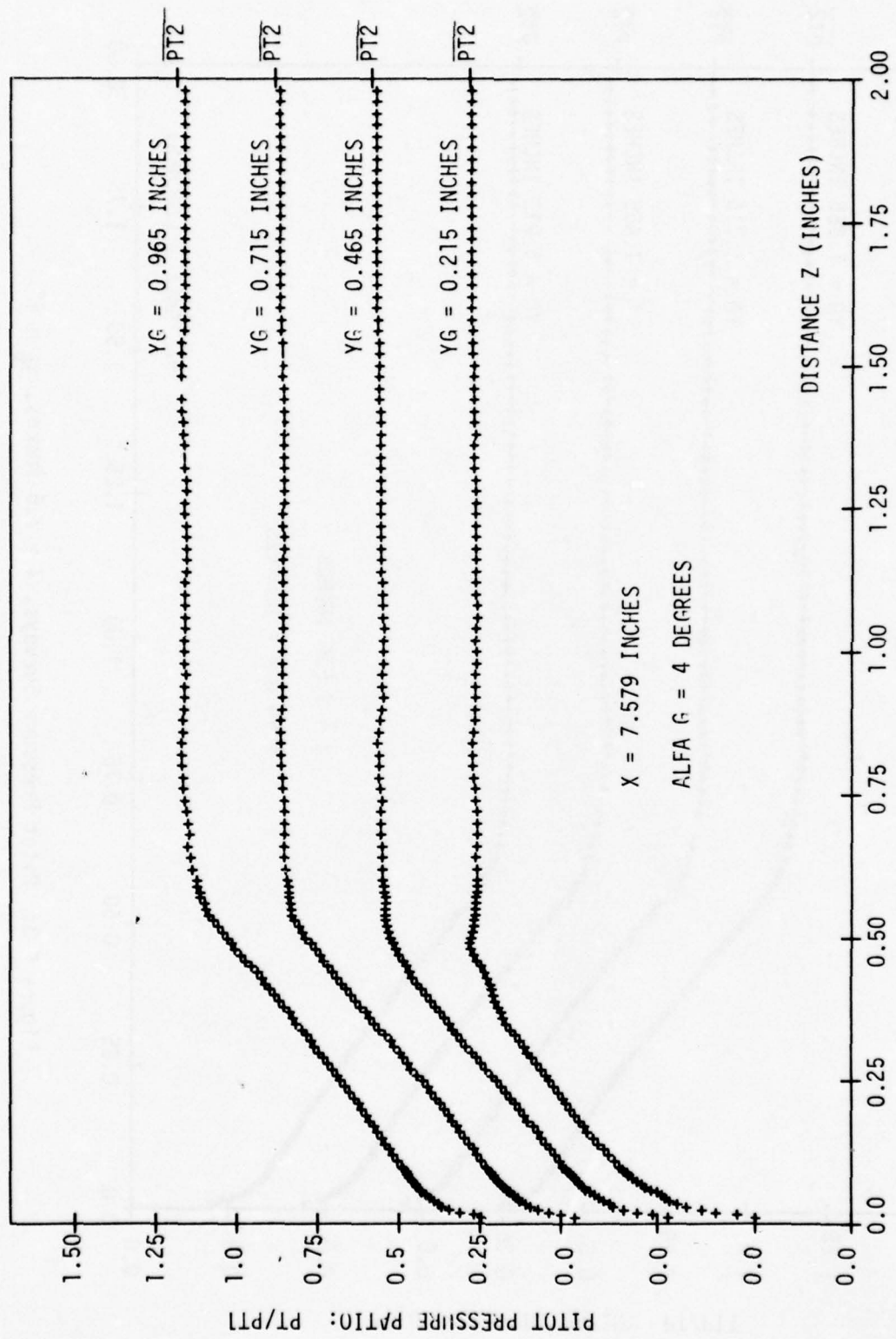


Figure F-2: Pitot Pressure Surveys, $X = 7.6$ inches, $\alpha_G = 4^\circ$.

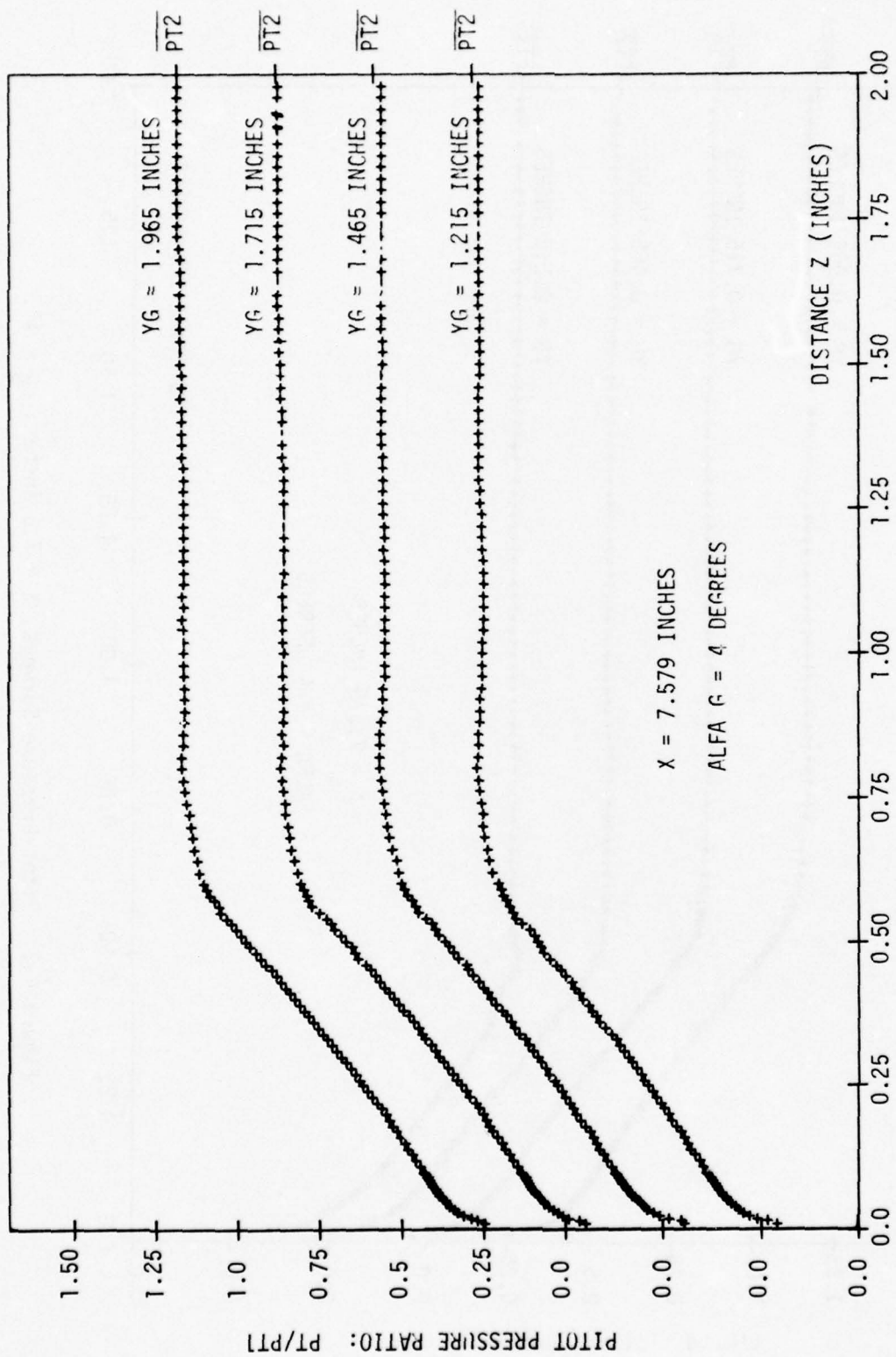


Figure F-3: Pitot Pressure Surveys, $X = 7.6$ inches, $\alpha_6 = 4^\circ$.

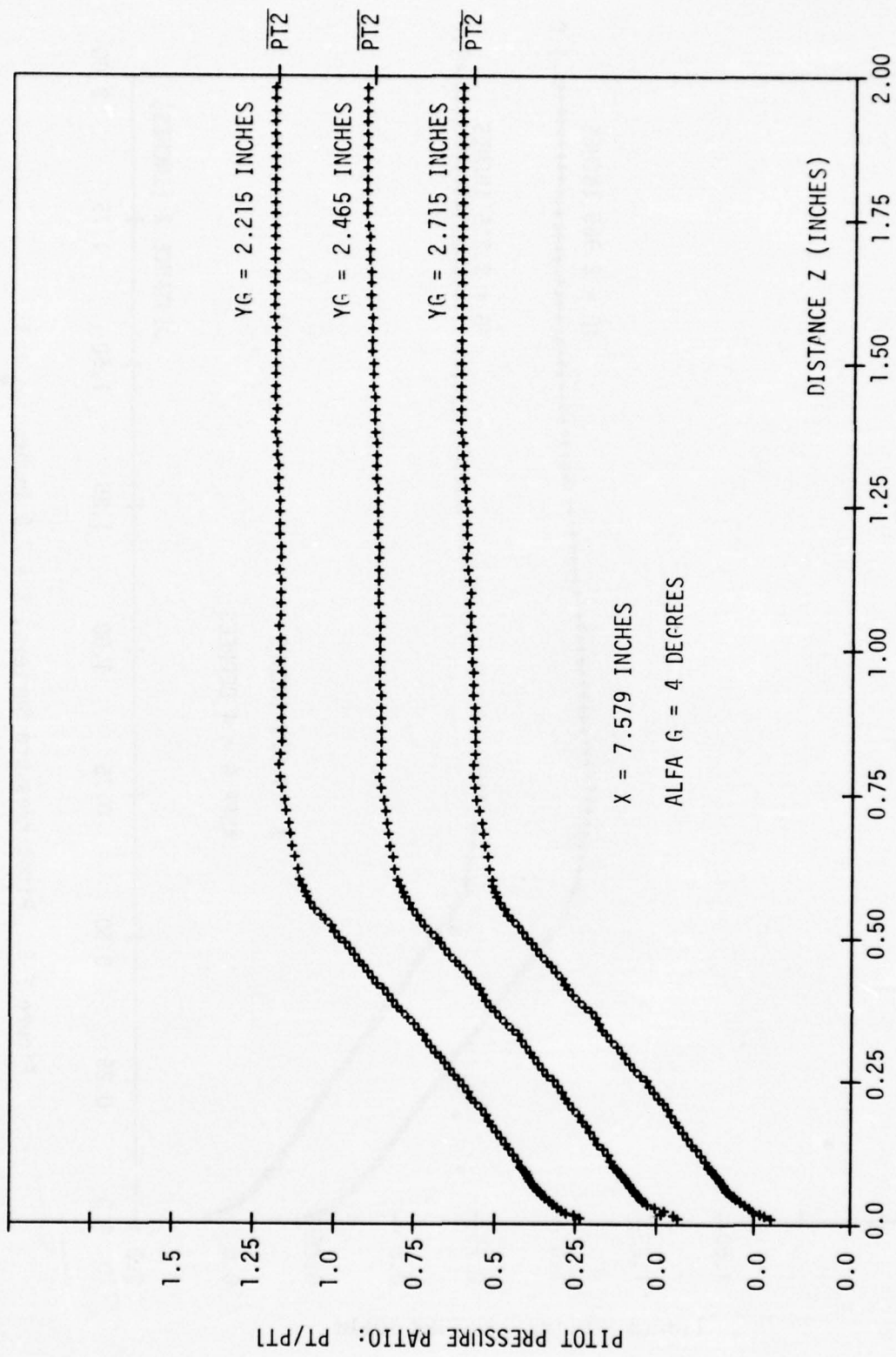


Figure F-4: Pitot Pressure Surveys, $X = 7.6$ inches, $\alpha_G = 4^\circ$.

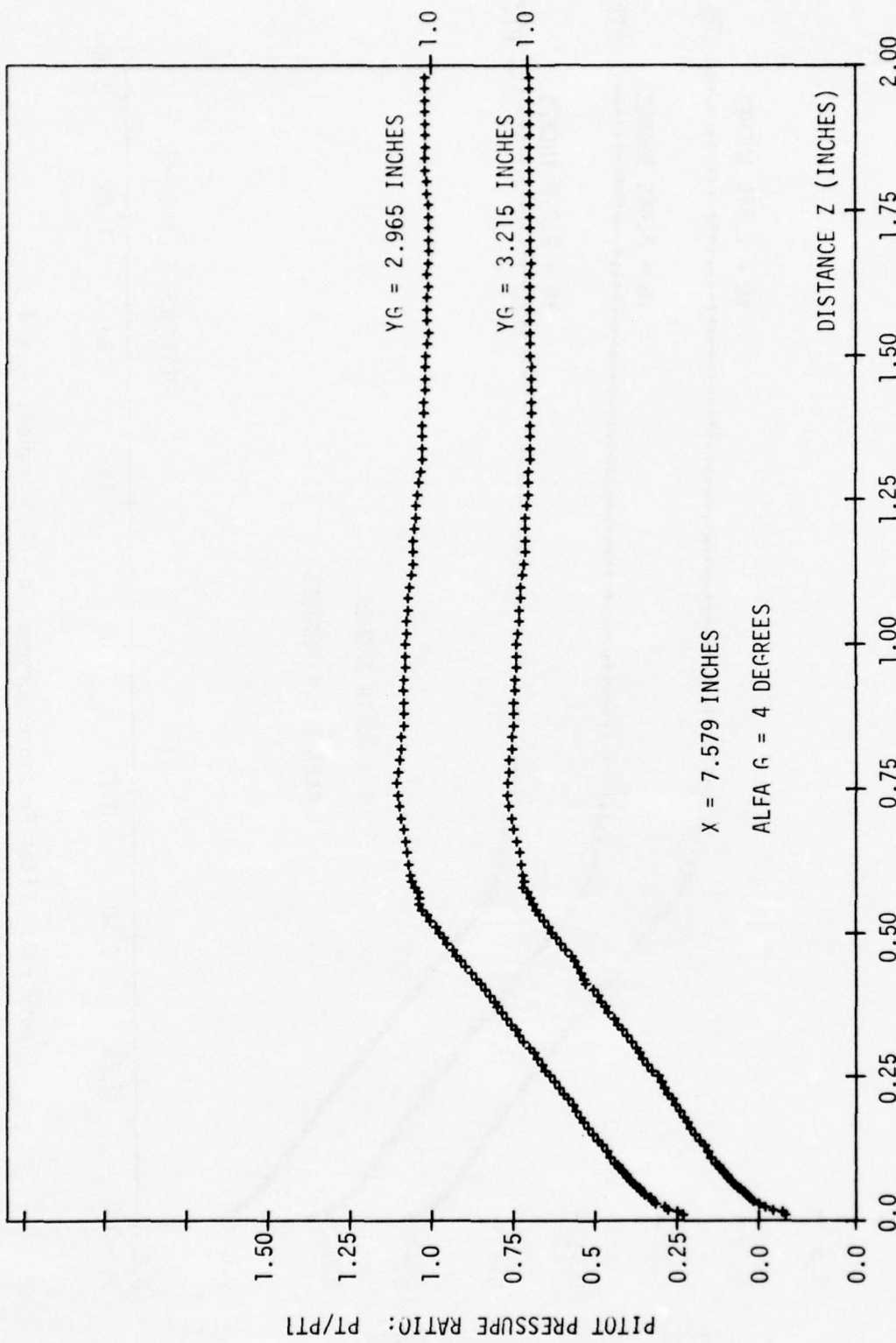


Figure F-5: Pitot Pressure Surveys, $X = 7.6$ inches, $\alpha_6 = 4^\circ$.

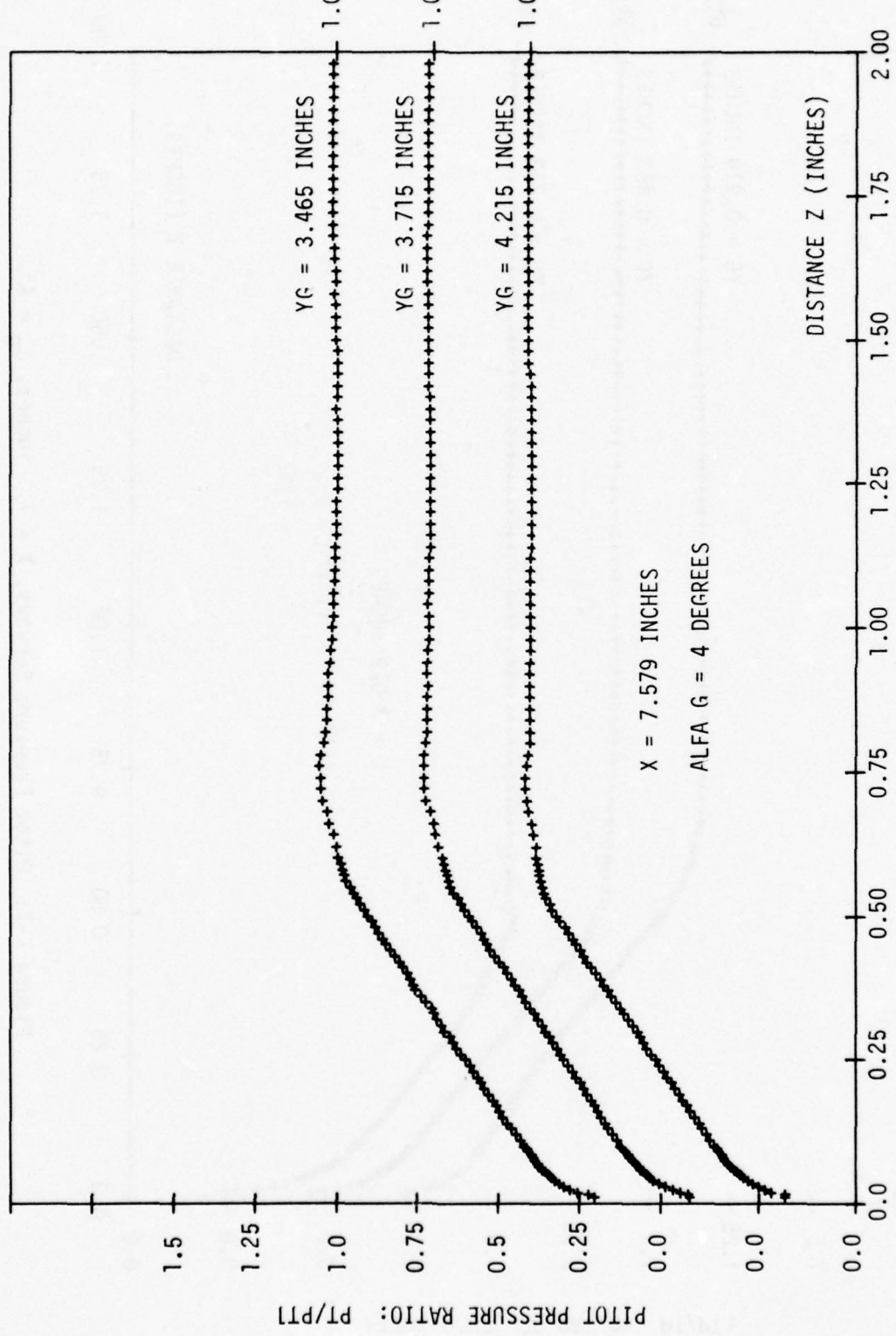


Figure F-6: Pitot Pressure Surveys, $X = 7.6$ inches, $\alpha_G = 4^\circ$.

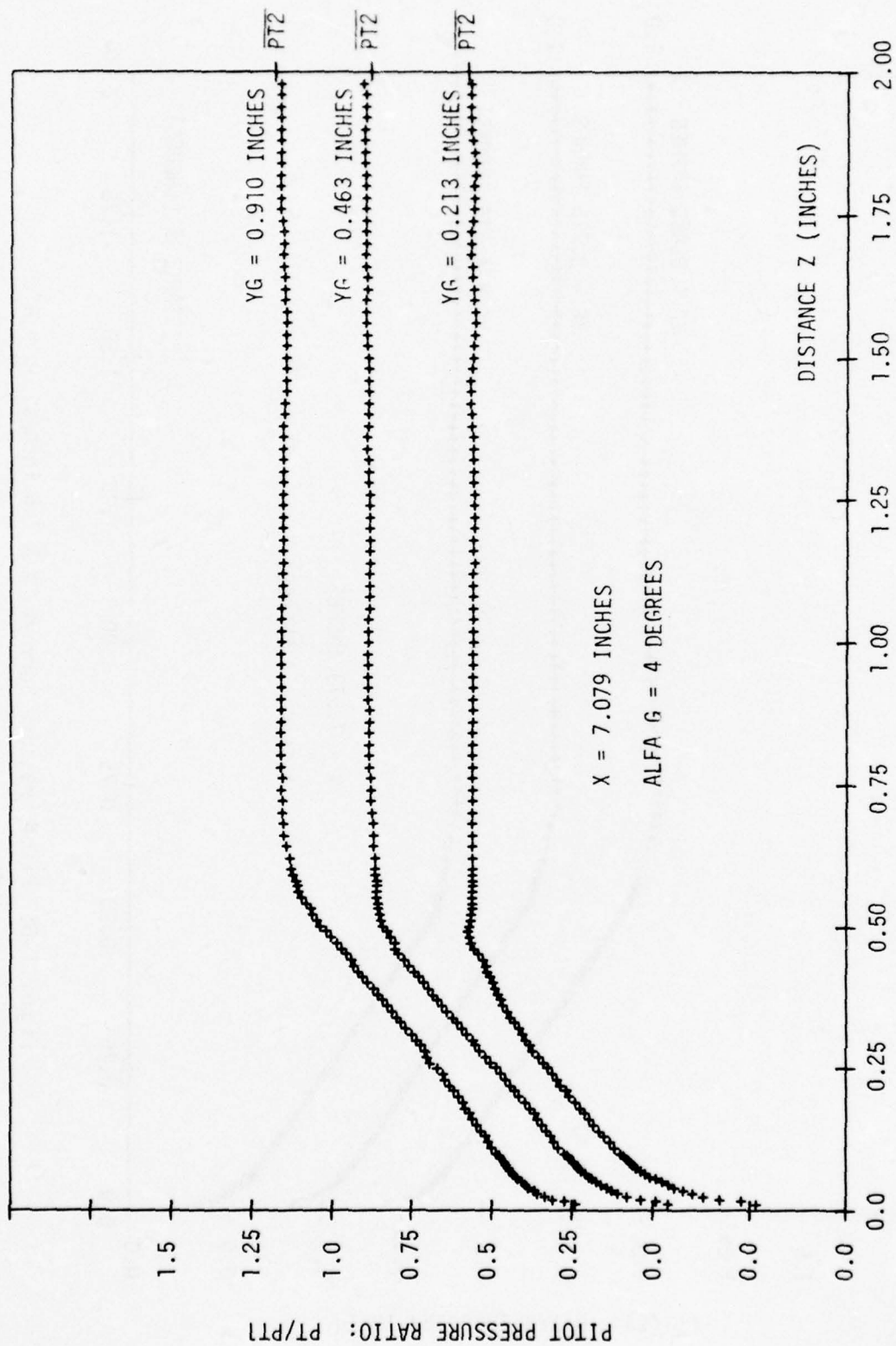


Figure F-7: Pitot Pressure Surveys, $X = 7.1$ inches, $\alpha_G = 4^\circ$.

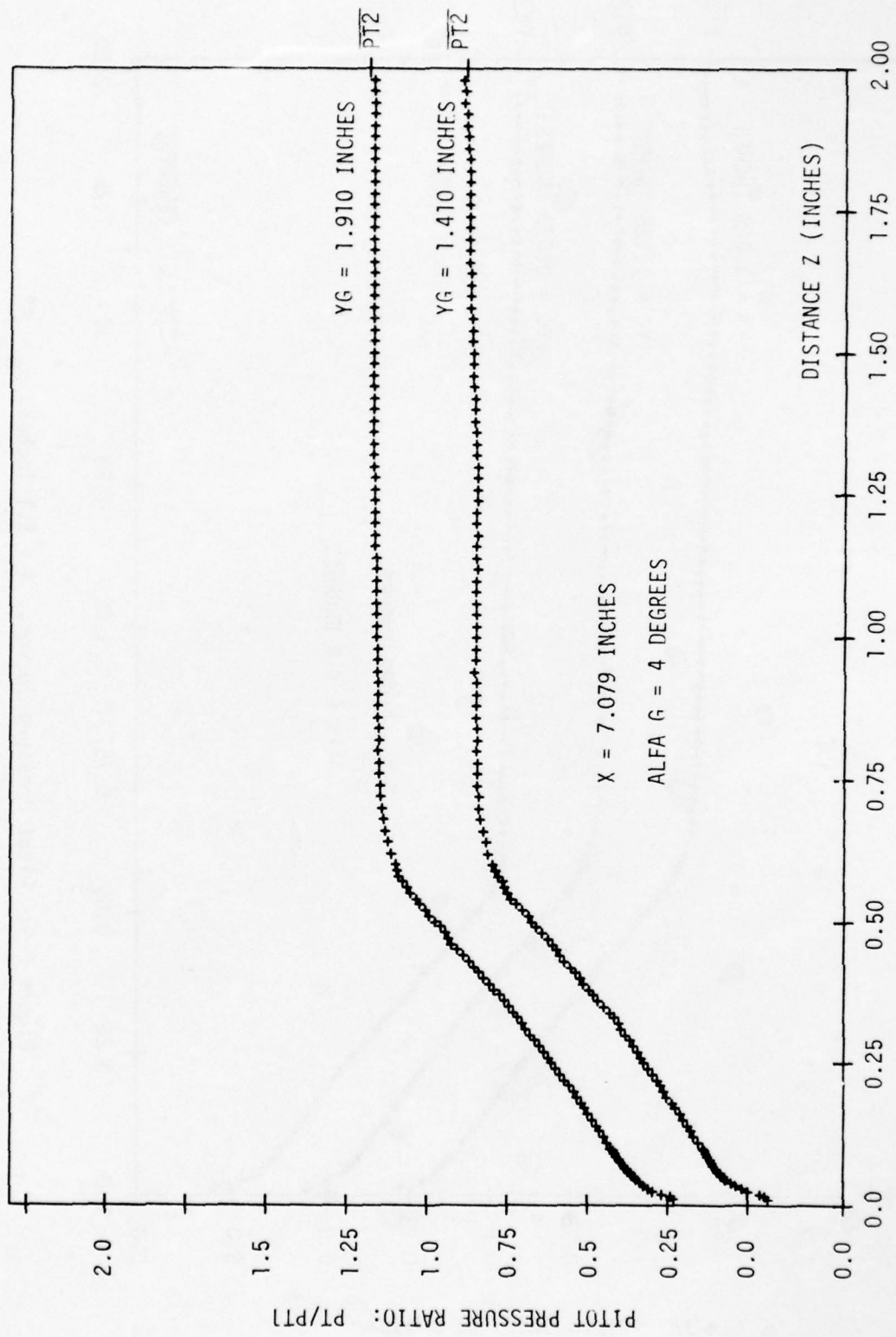


Figure F-8: Pitot Pressure Surveys, $X = 7.1$ inches, $\alpha_G = 4^\circ$

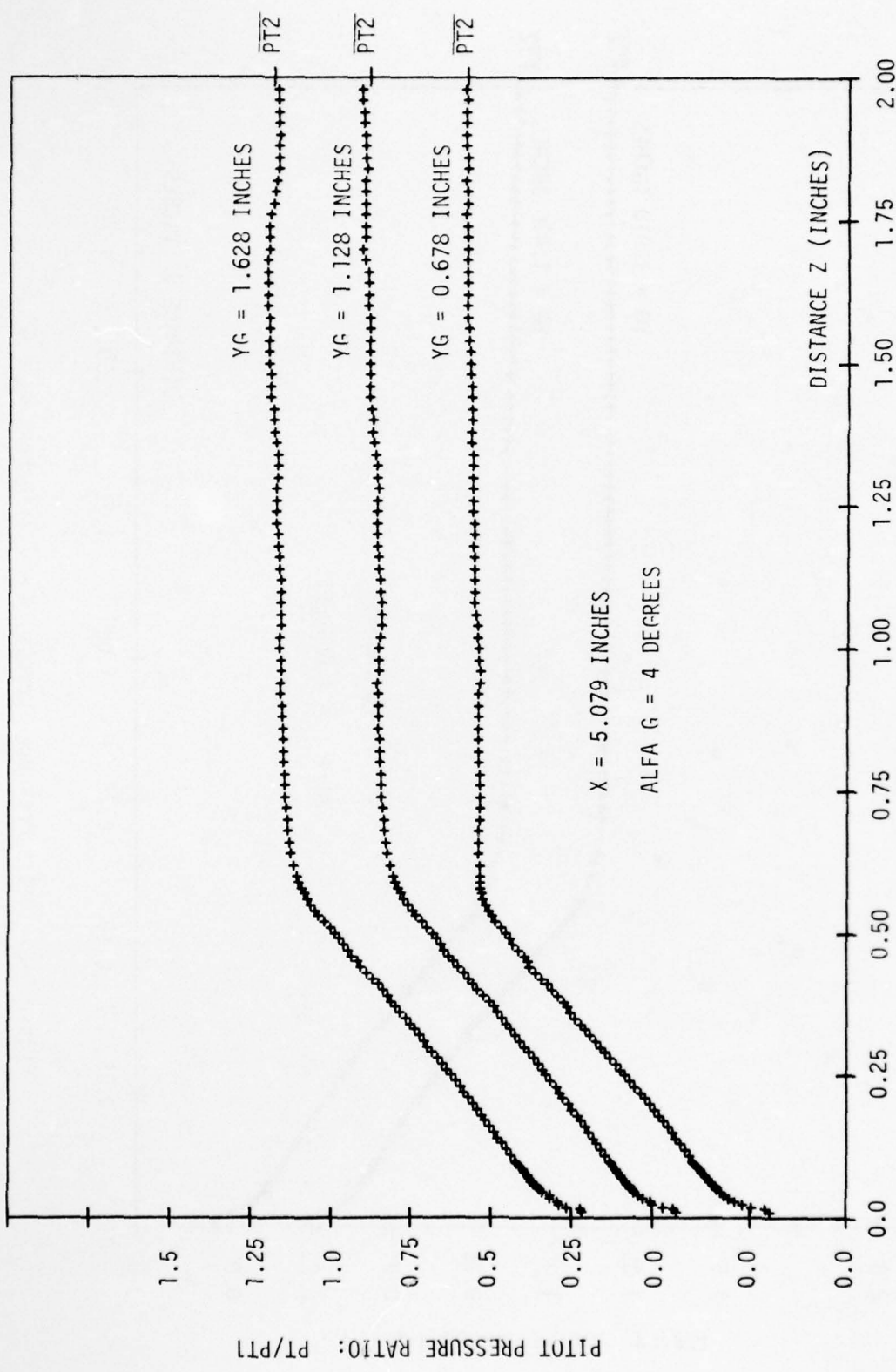


Figure F-9: Pitot Pressure Surveys, $X = 5.1$ inches, $\alpha_G = 4^\circ$.

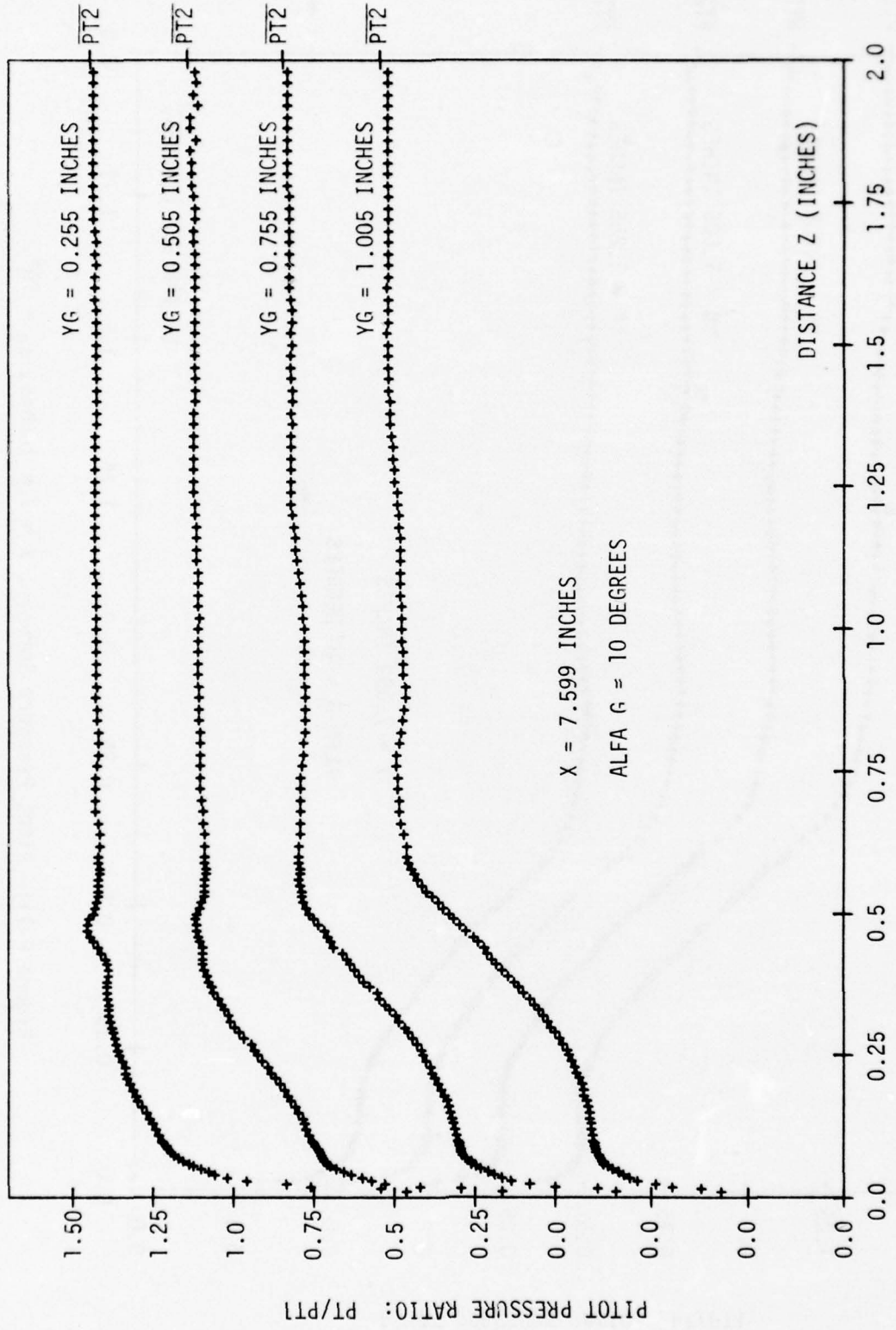


Figure F-10: Pitot Pressure Surveys, $X = 7.6$ inches, $\alpha_G = 10^\circ$.

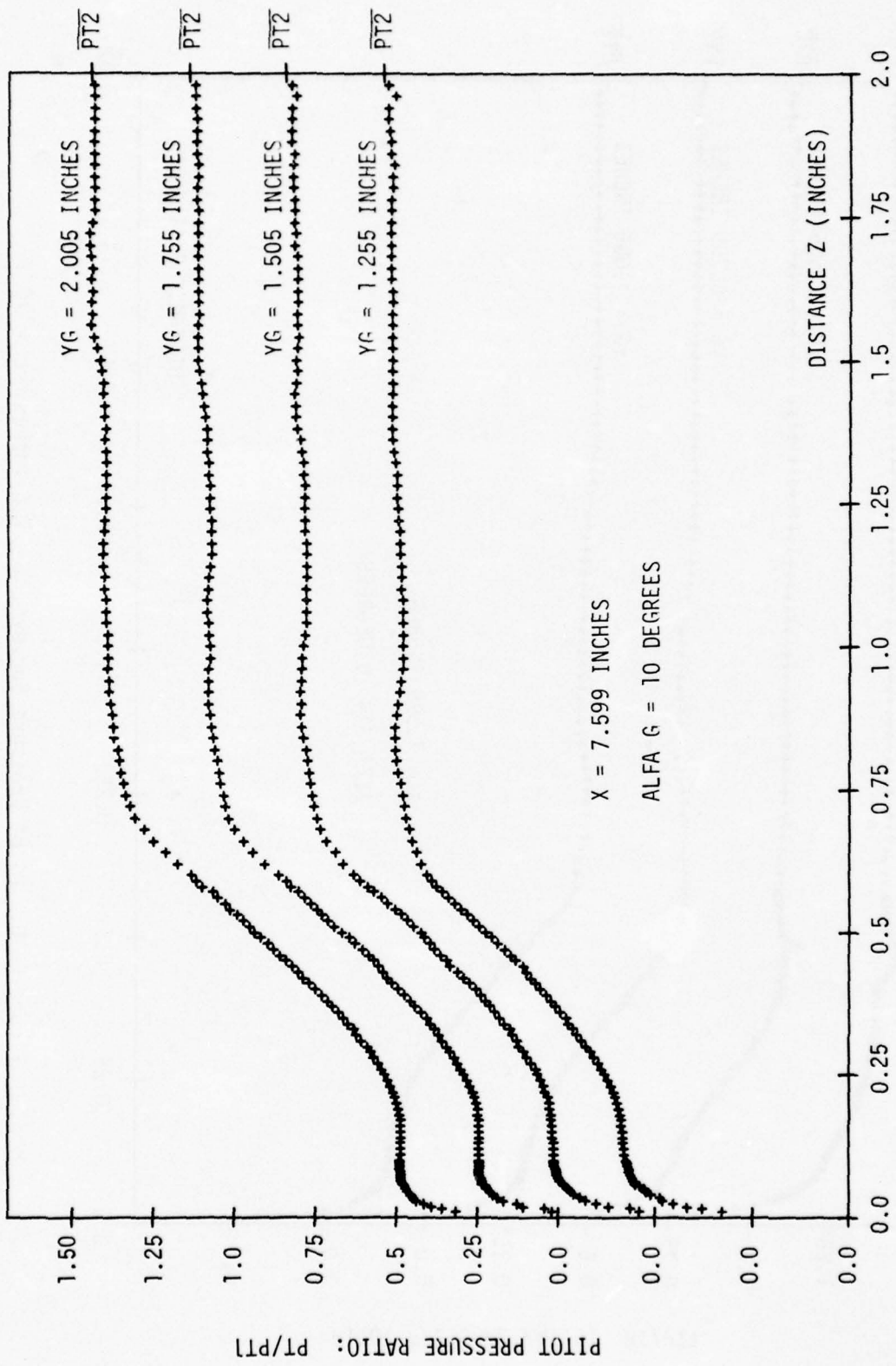


Figure F-11: Pitot Pressure Surveys, $X = 7.6$ inches, $\alpha_6 = 10^\circ$.

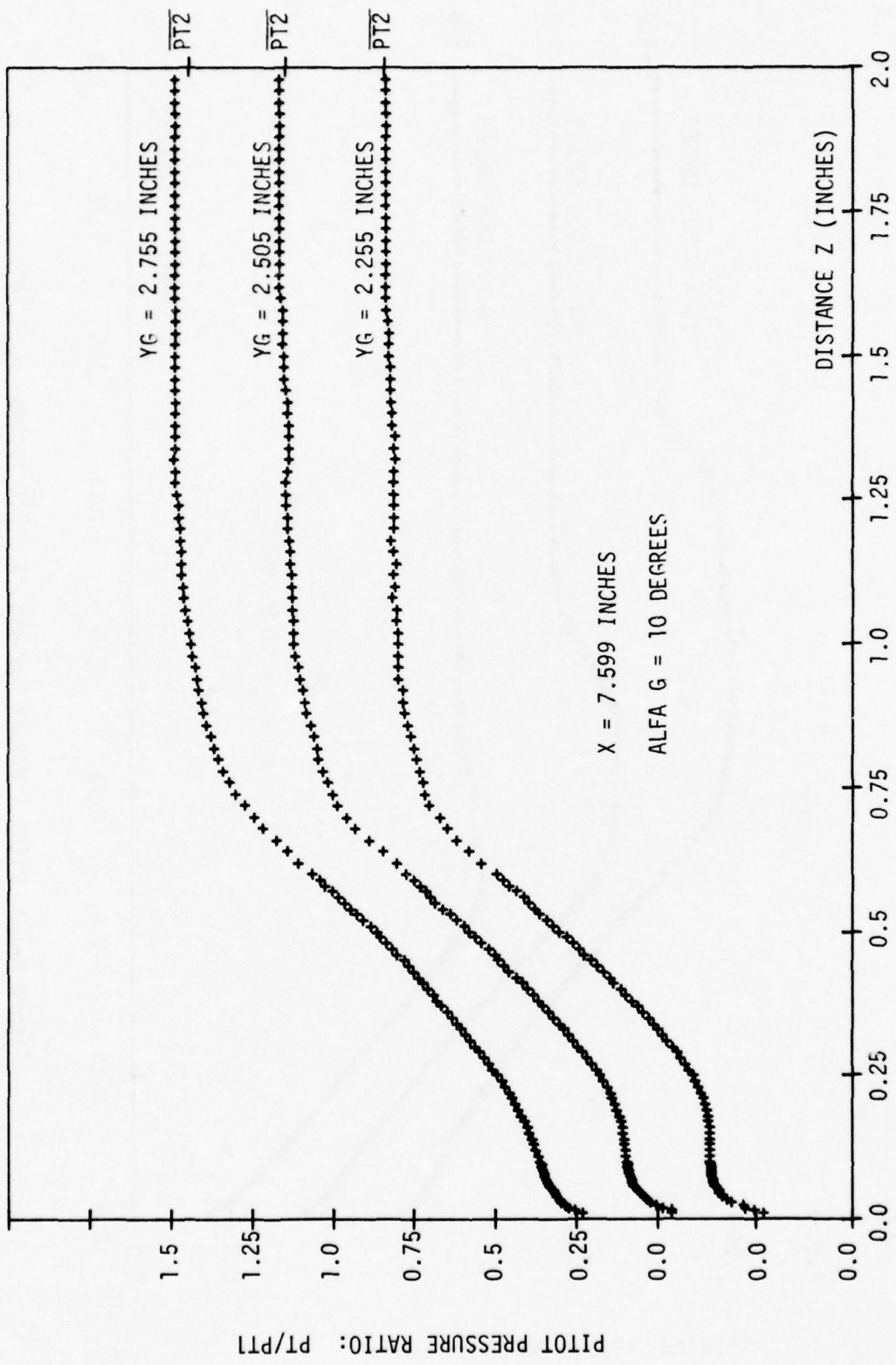


Figure F-12: Pitot Pressure Surveys, $X = 7.6$ inches, $\alpha_G = 10^\circ$.

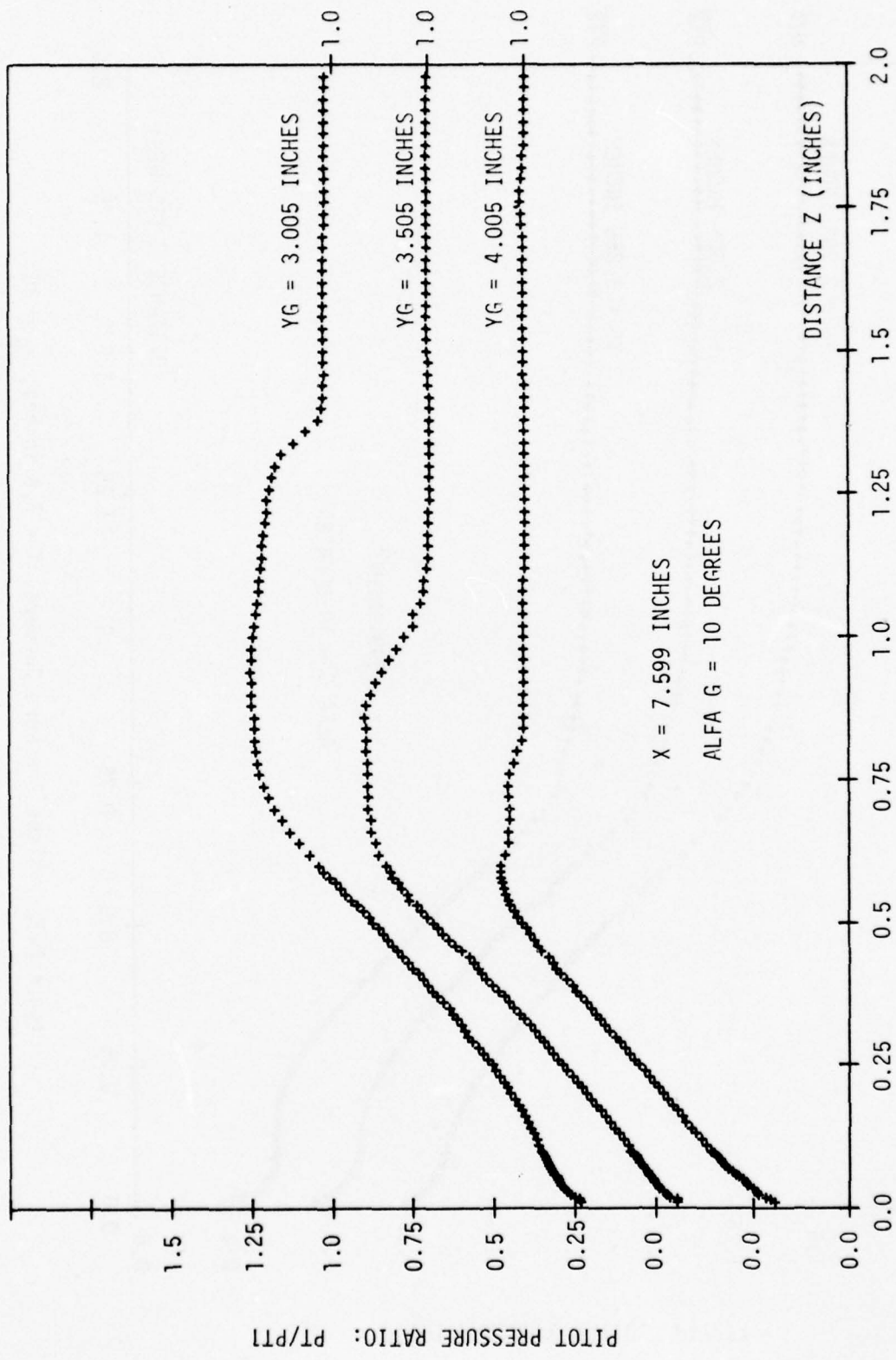


Figure F-13: Pitot Pressure Survey, $X = 7.6$ inches, $\alpha_G = 10^\circ$.

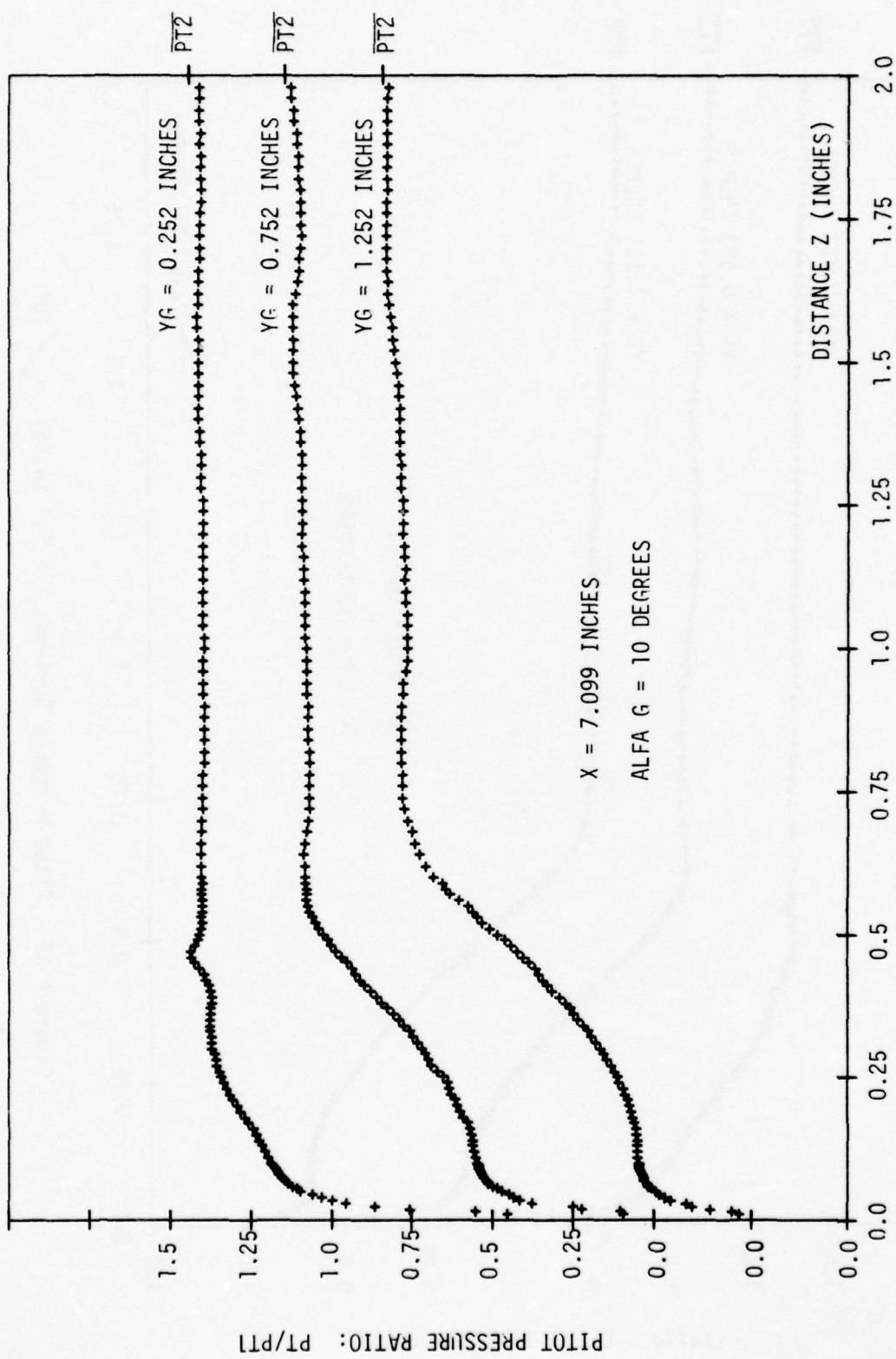


Figure F-14: Pitot Pressure Surveys, $X = 7.1$ inches, $\alpha_6 = 10^\circ$.

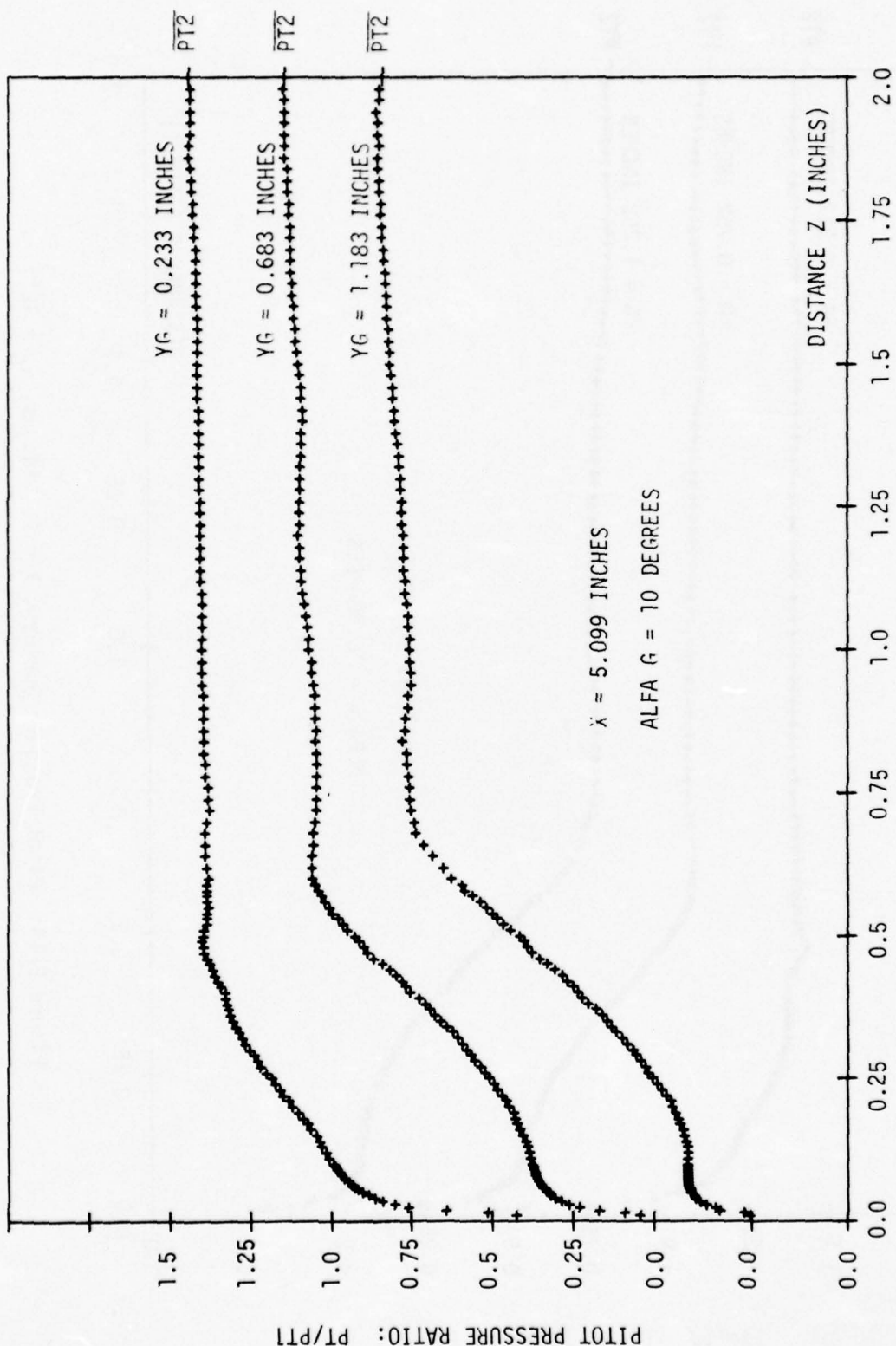


Figure F-15: Pitot Pressure Surveys, $X = 5.1$ inches, $\alpha_G = 10^\circ$.

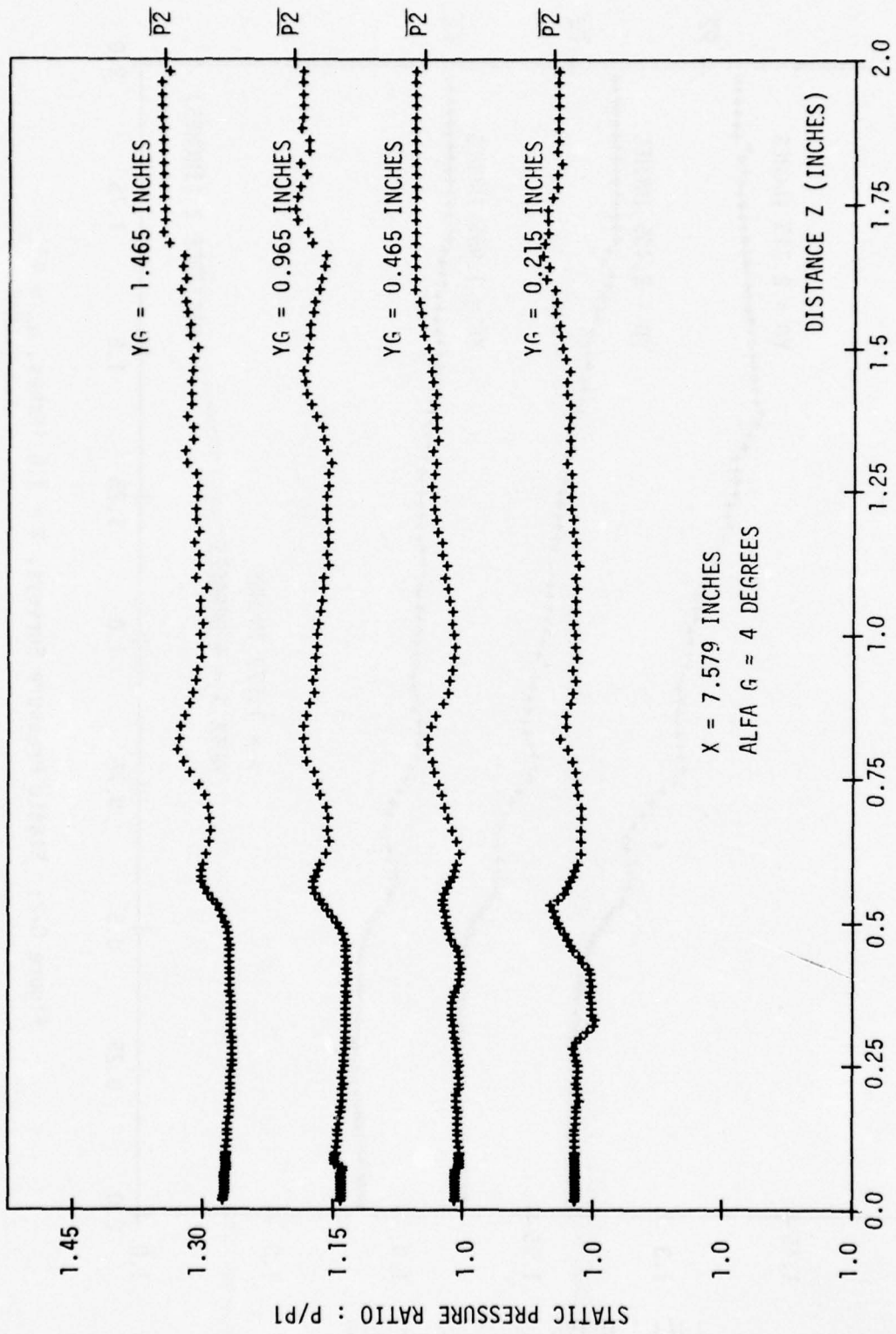


Figure 6-1: Static Pressure Surveys, $X = 7.6$ inches, $\alpha_G = 4^\circ$.

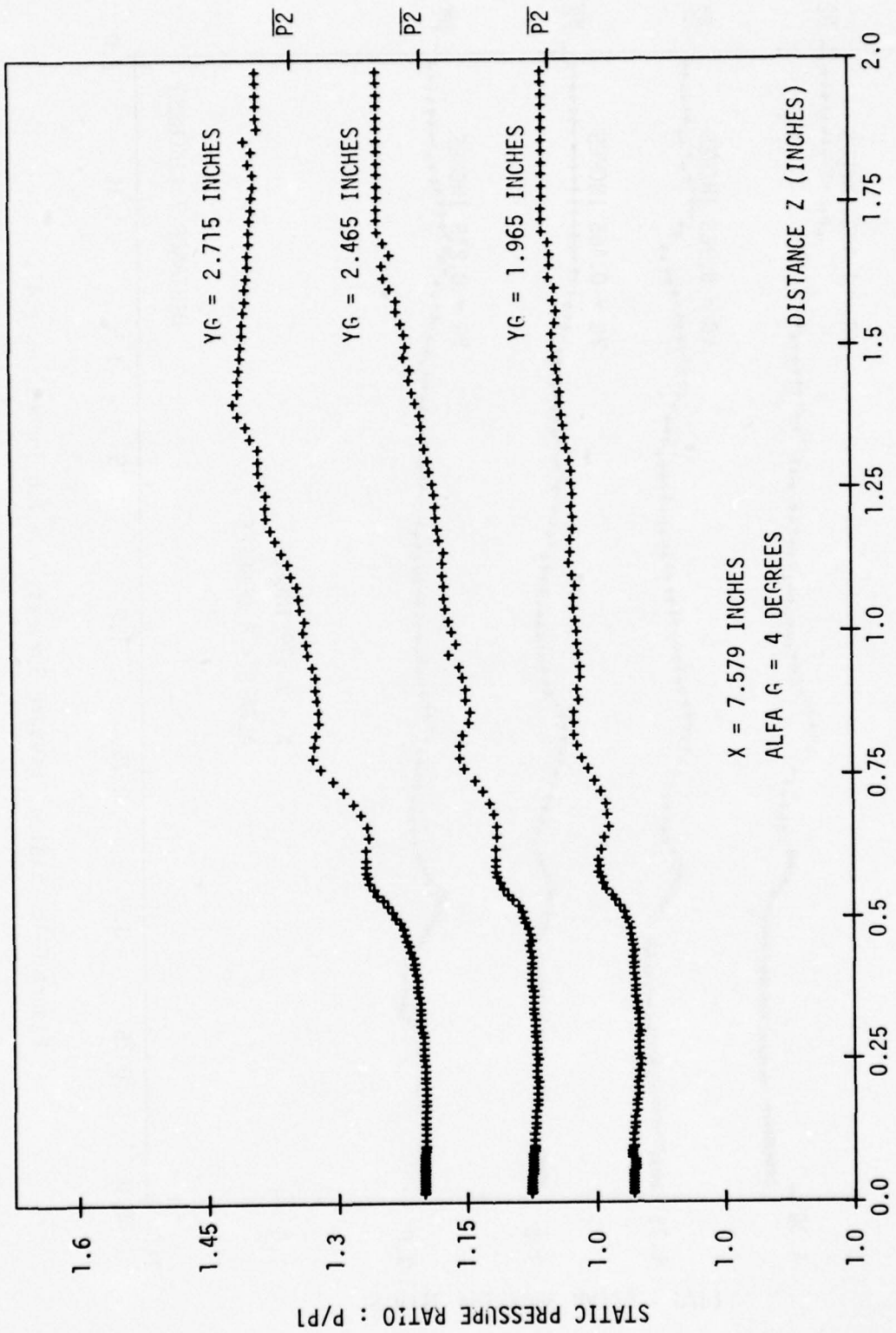


Figure 6-2: Static Pressure Surveys, $X = 7.6$ inches, $\alpha_G = 4^\circ$.

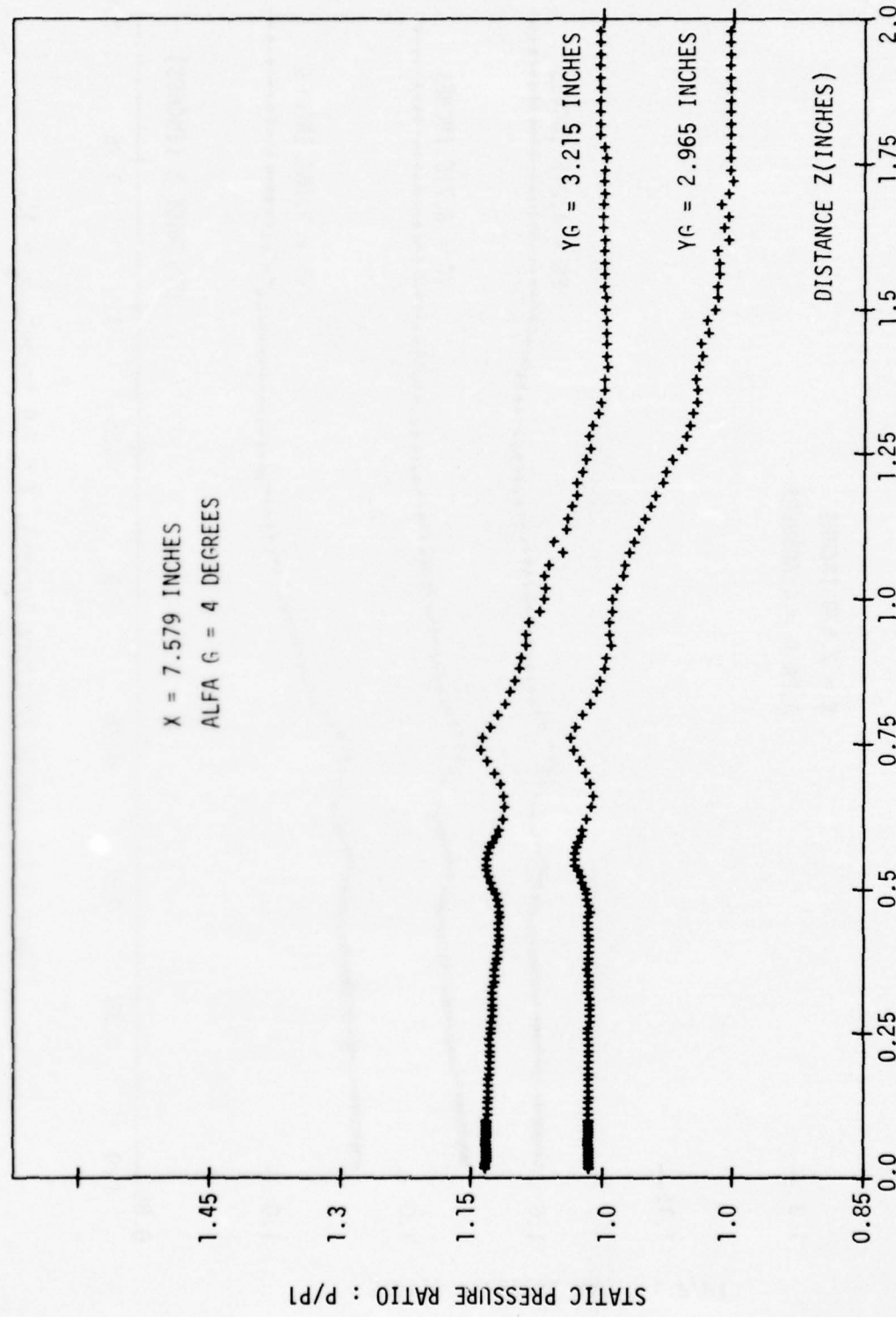


Figure 6-3: Static Pressure Surveys, $X = 7.6$ inches, $\alpha_G = 4^\circ$.

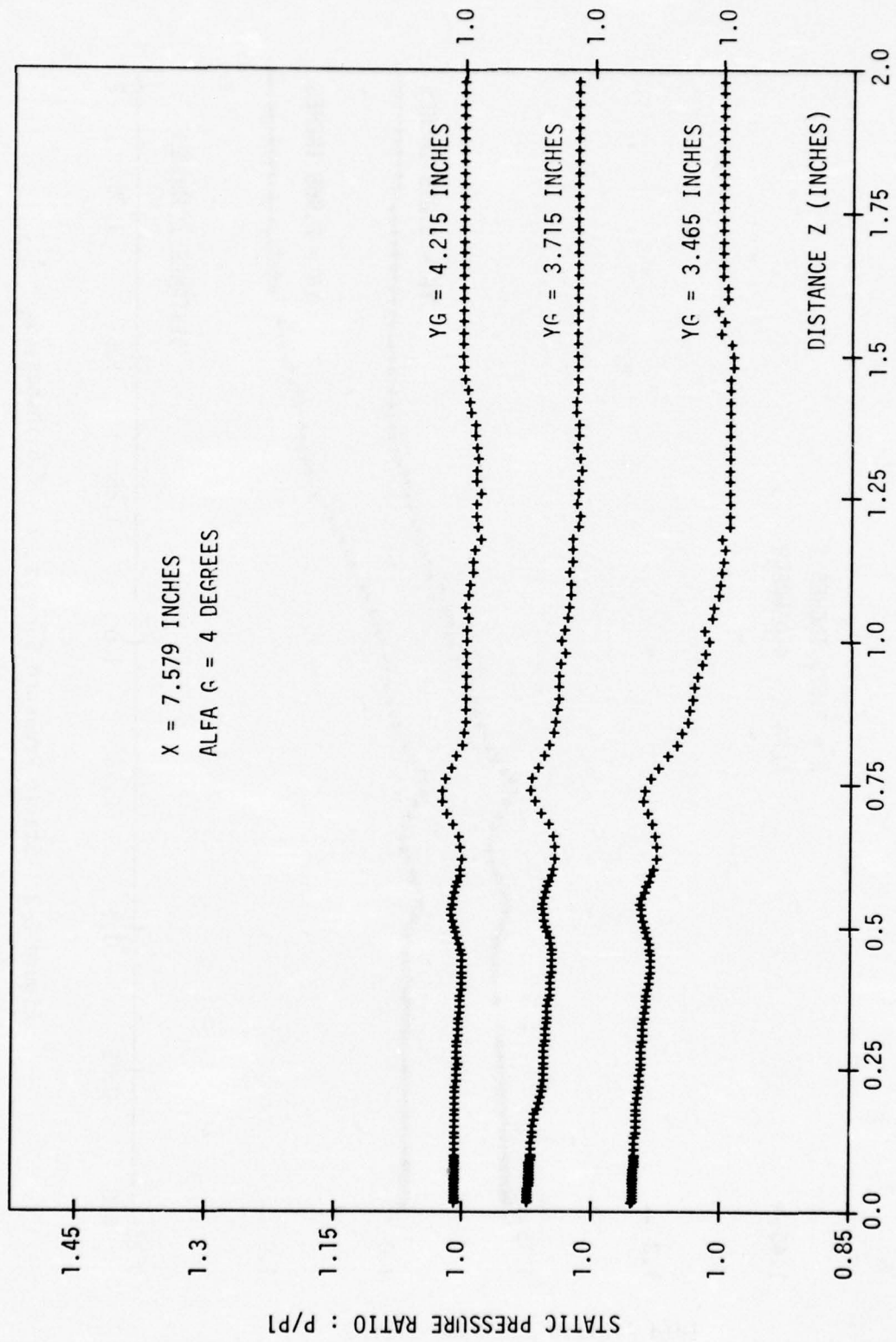


Figure 6-4: Static Pressure Surveys, $X = 7.6$ inches, $\alpha_G = 4^\circ$.

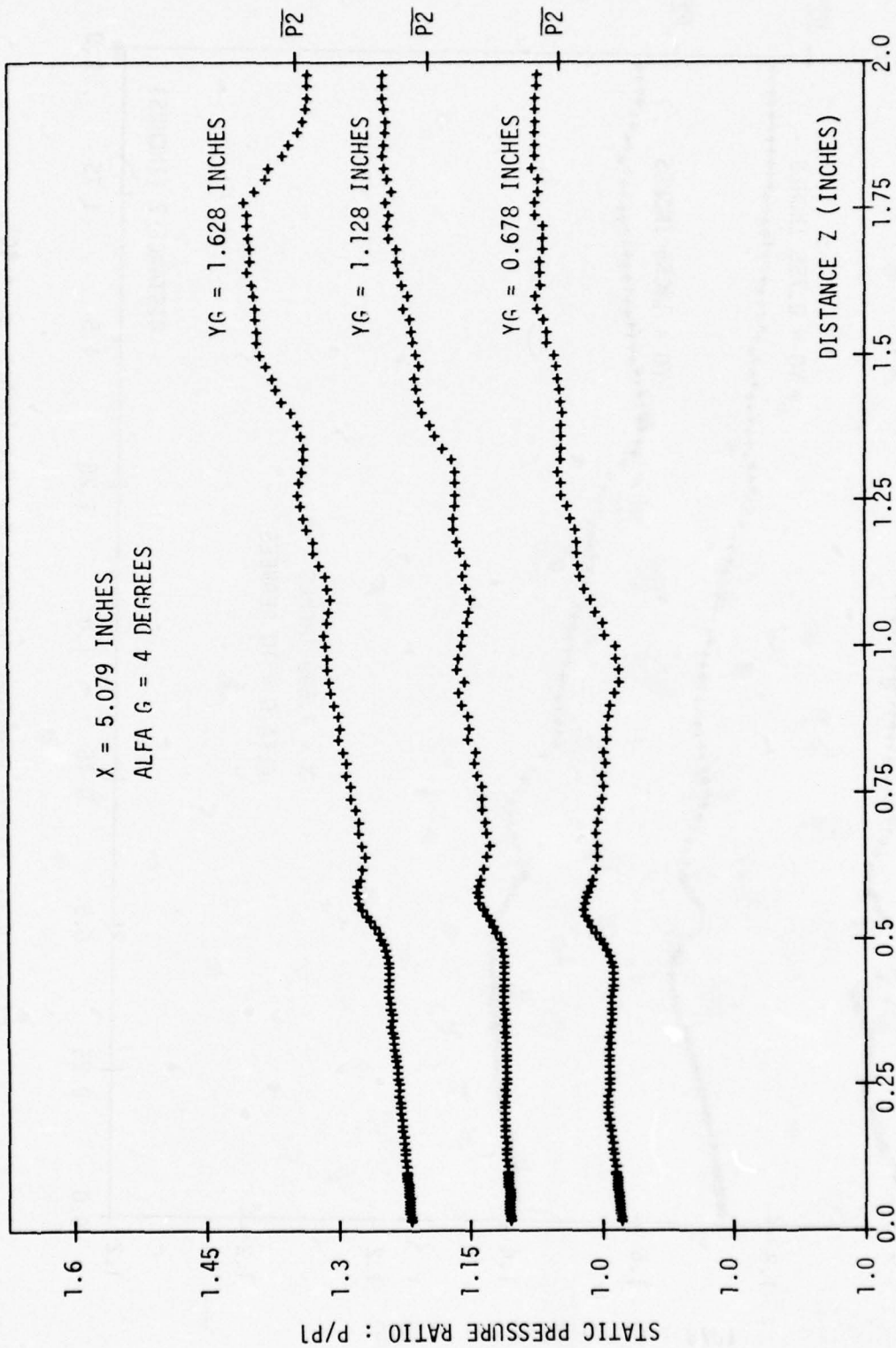


Figure 6-5: Static Pressure Surveys, $X = 5.1$ inches, $\alpha_G = 4^\circ$.

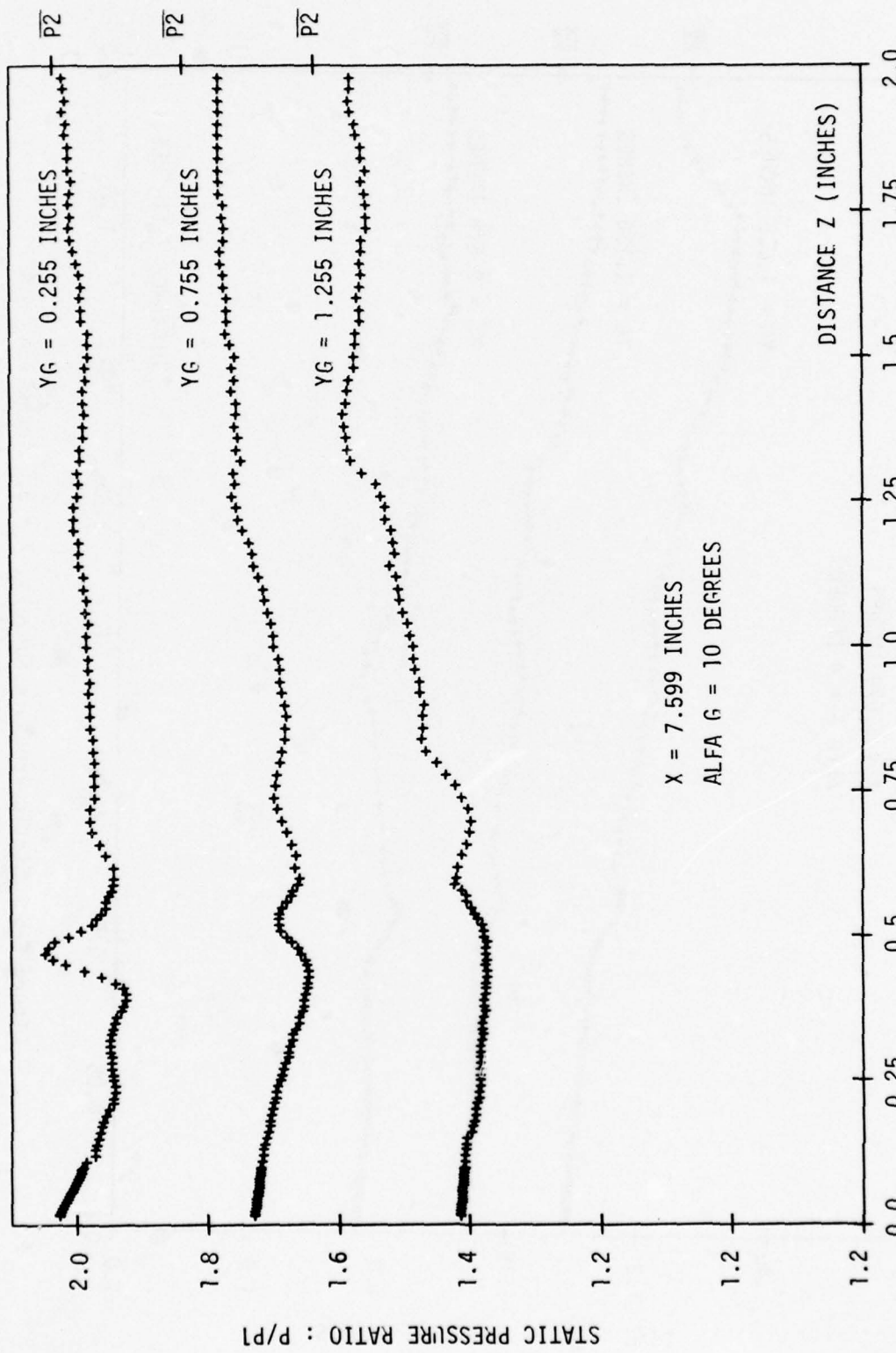


Figure 6-6: Static Pressure Surveys, $X = 7.6$ inches, $\alpha_G = 10^\circ$.

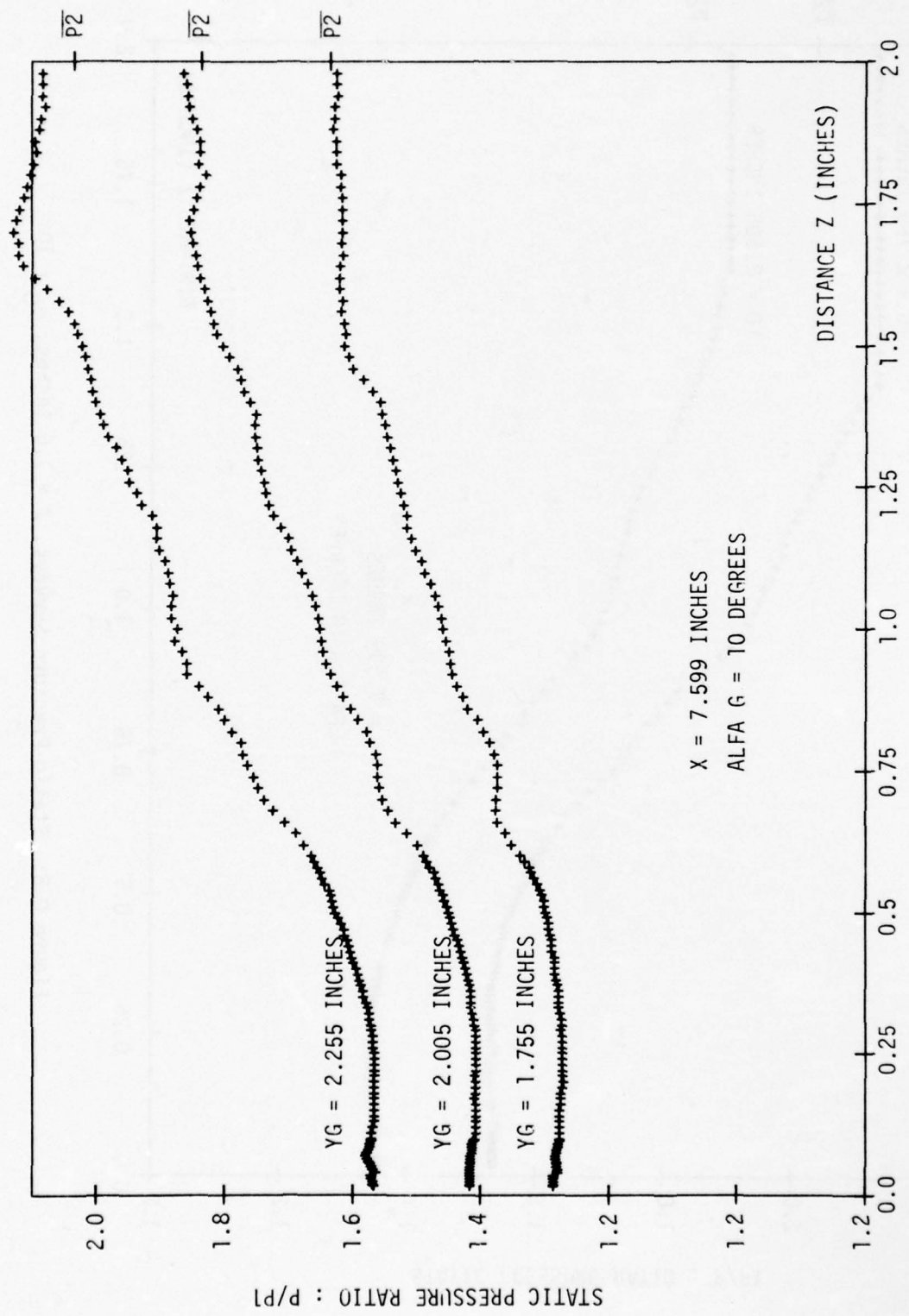


Figure 6-7: Static Pressure Surveys, $X = 7.6$ inches, $\alpha_G = 10^\circ$.

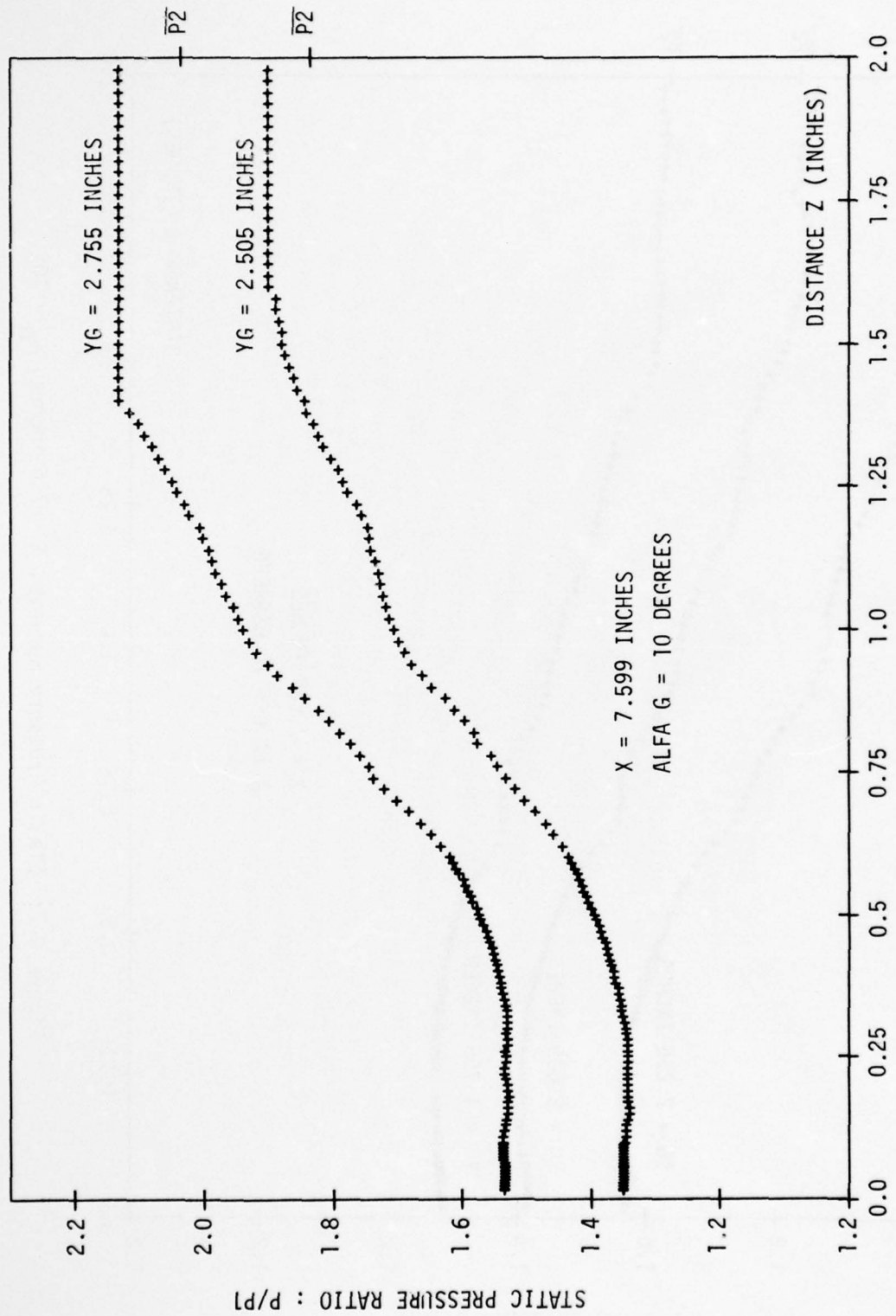


Figure 6-8: Static Pressure Surveys, $X = 7.6$ inches, $\alpha_G = 10^\circ$.

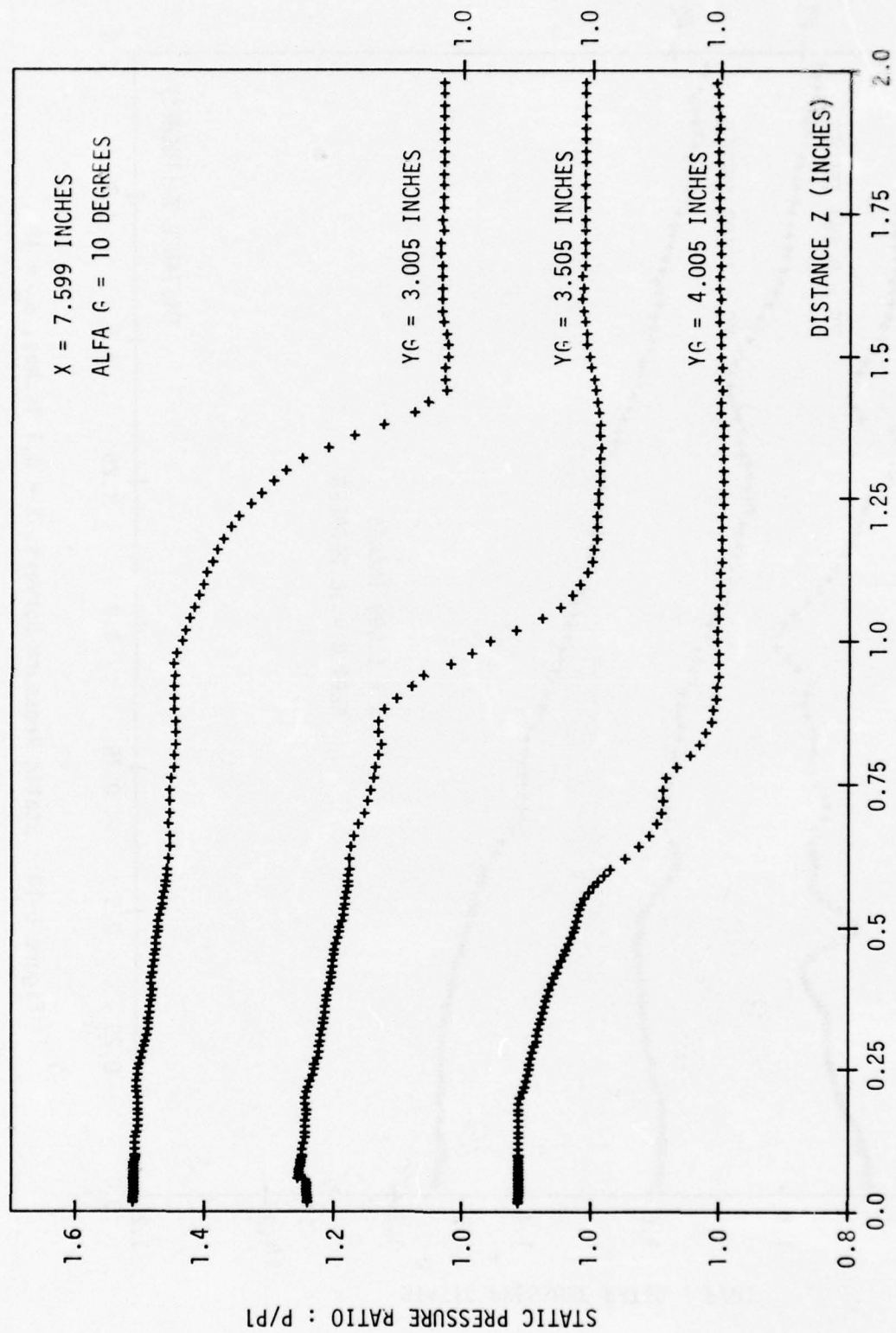


Figure 6-9: Static Pressure Surveys, $X = 7.6$ inches, $\alpha_G = 10^\circ$.

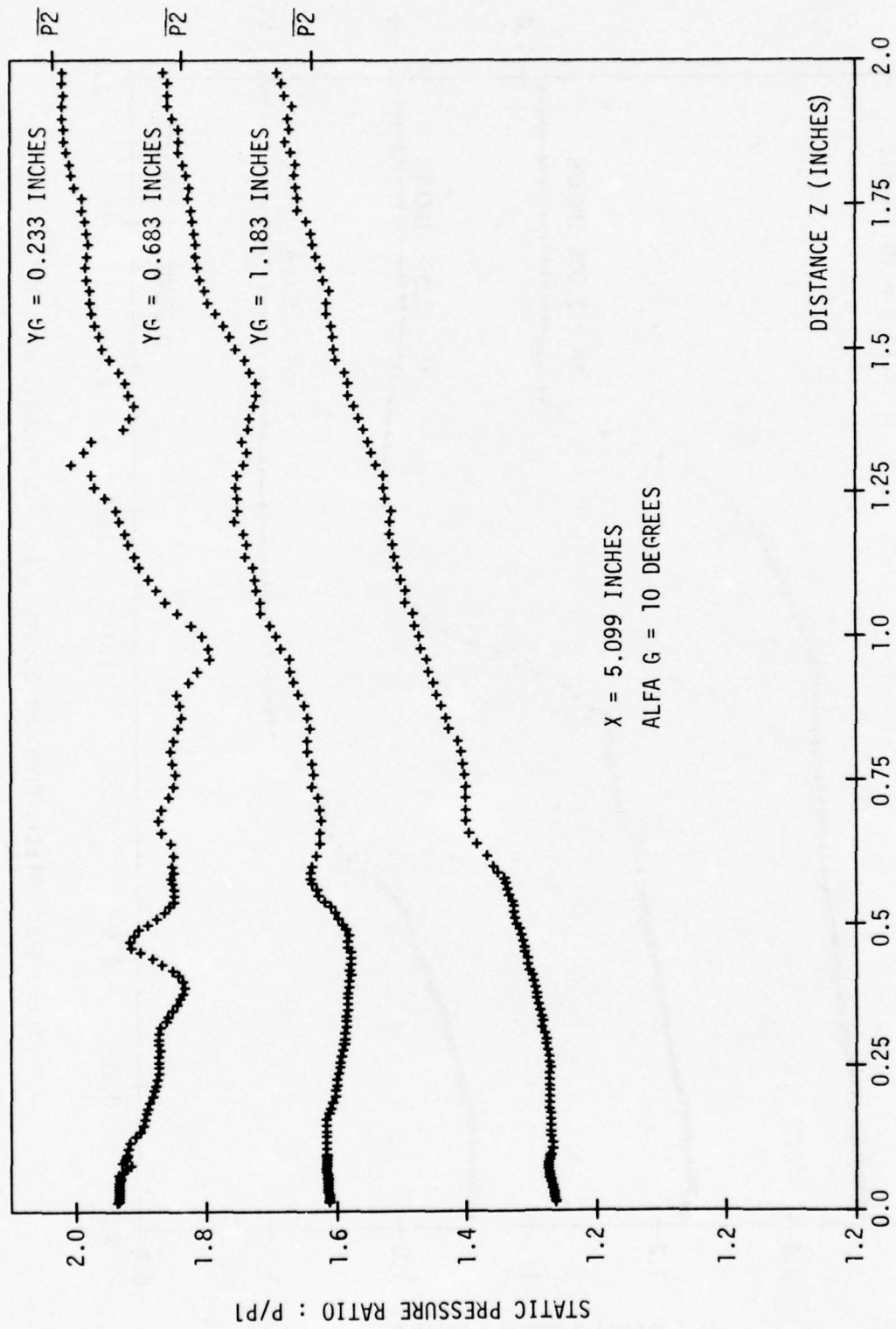


Figure 6-10: Static Pressure Surveys, $X = 5.1$ inches, $\alpha_G = 10^\circ$.

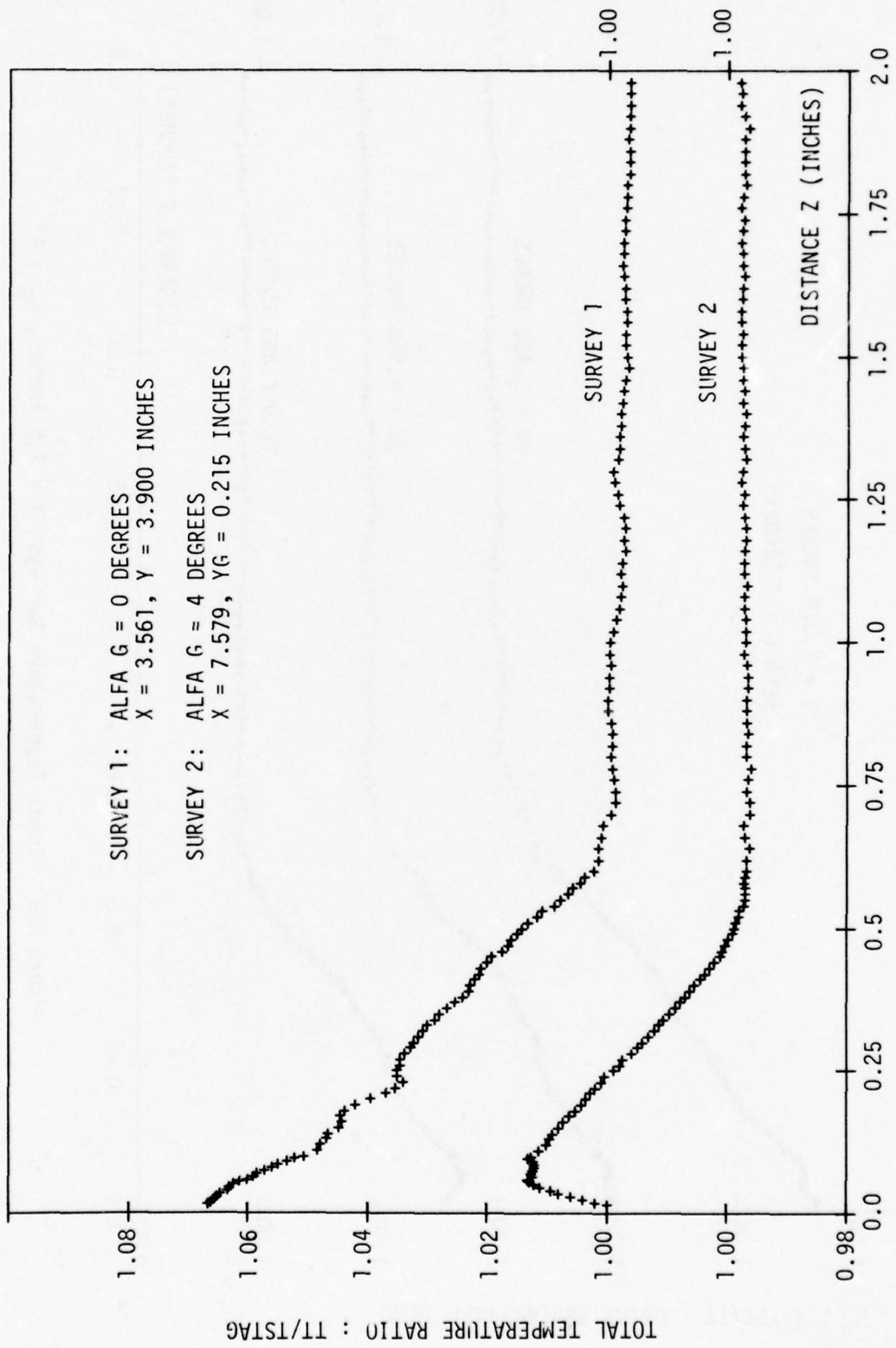


Figure H-1: Total Temperature Surveys, $\alpha_{\bar{G}} = 0^\circ$ and 4° .

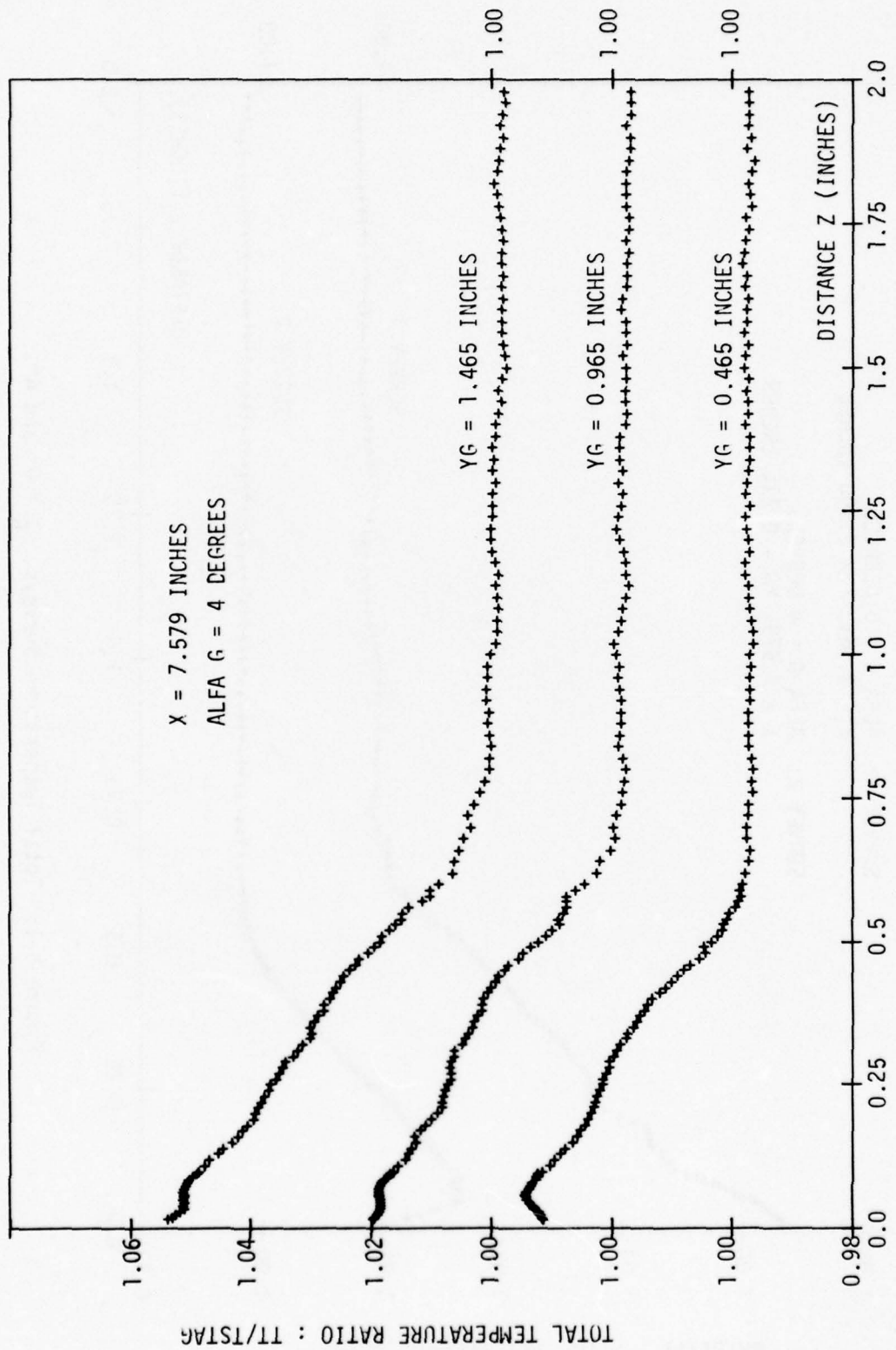


Figure H-2: Total Temperature Surveys, $X = 7.6$ inches, $\alpha_G = 4^\circ$.

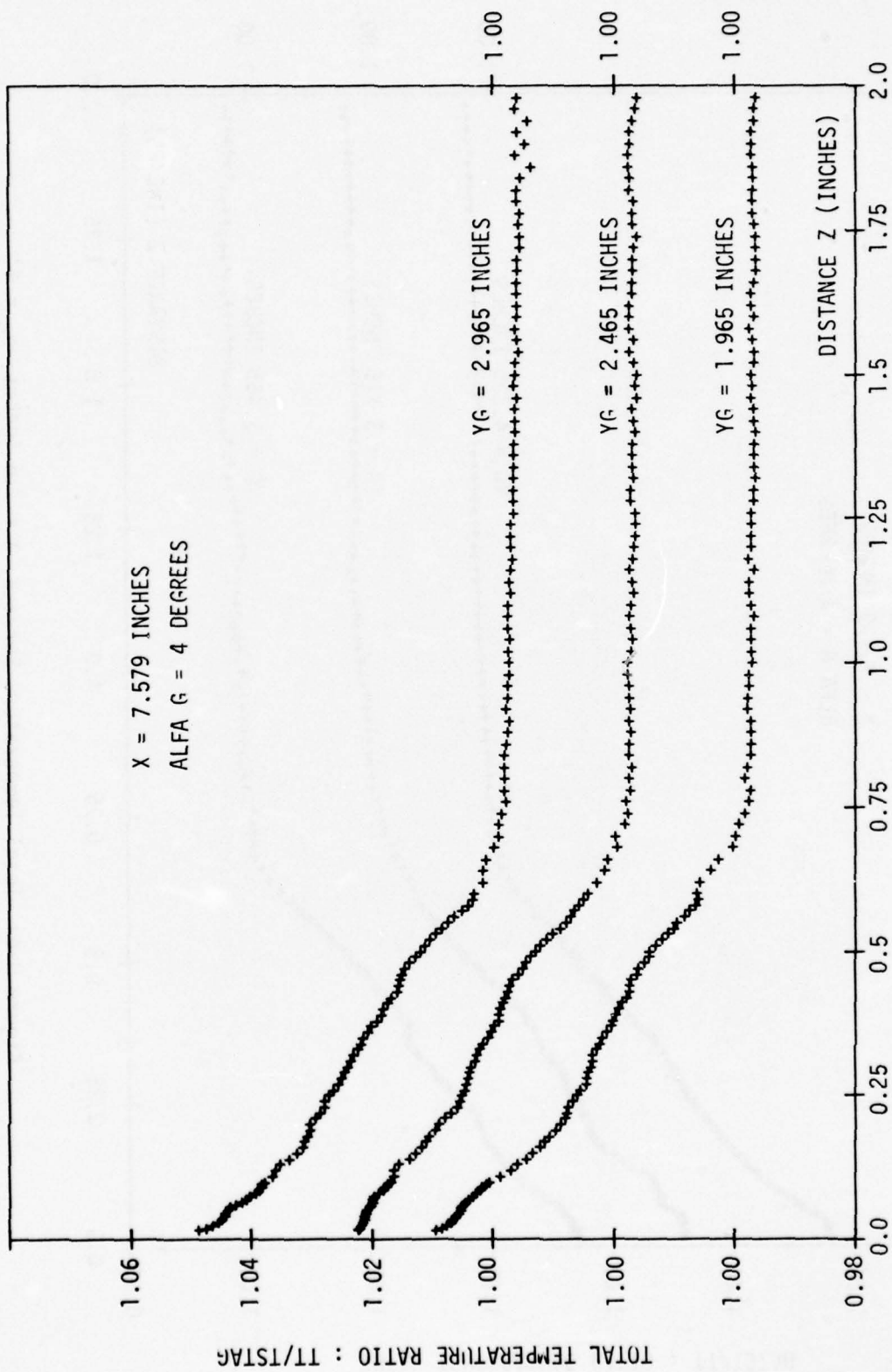


Figure H-3: Total Temperature Surveys, $X = 7.6$ inches, $\alpha_G = 4^\circ$.

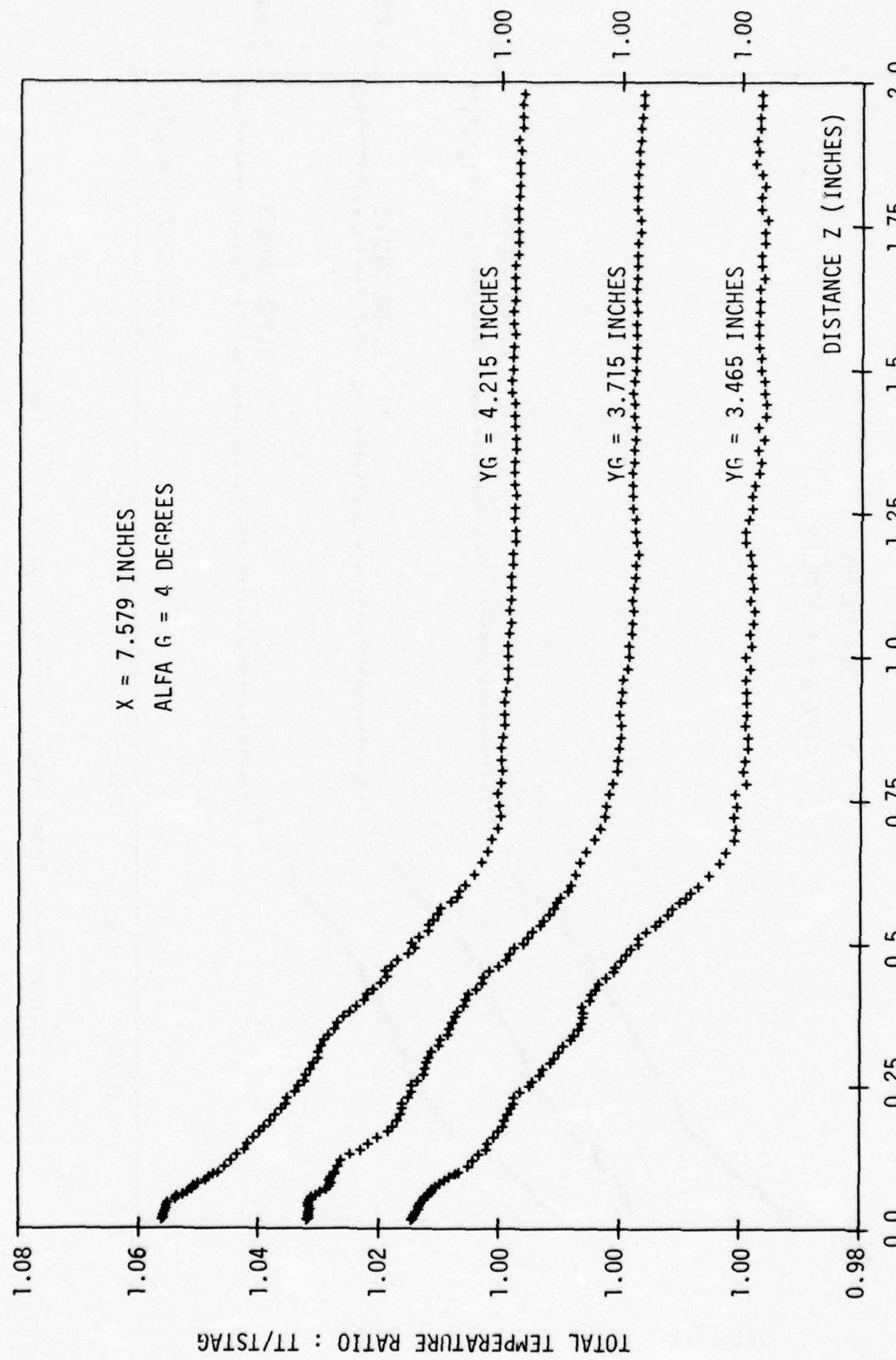


Figure H-4: Total Temperature Surveys, $X = 7.6$ inches, $\alpha_G = 4^\circ$.

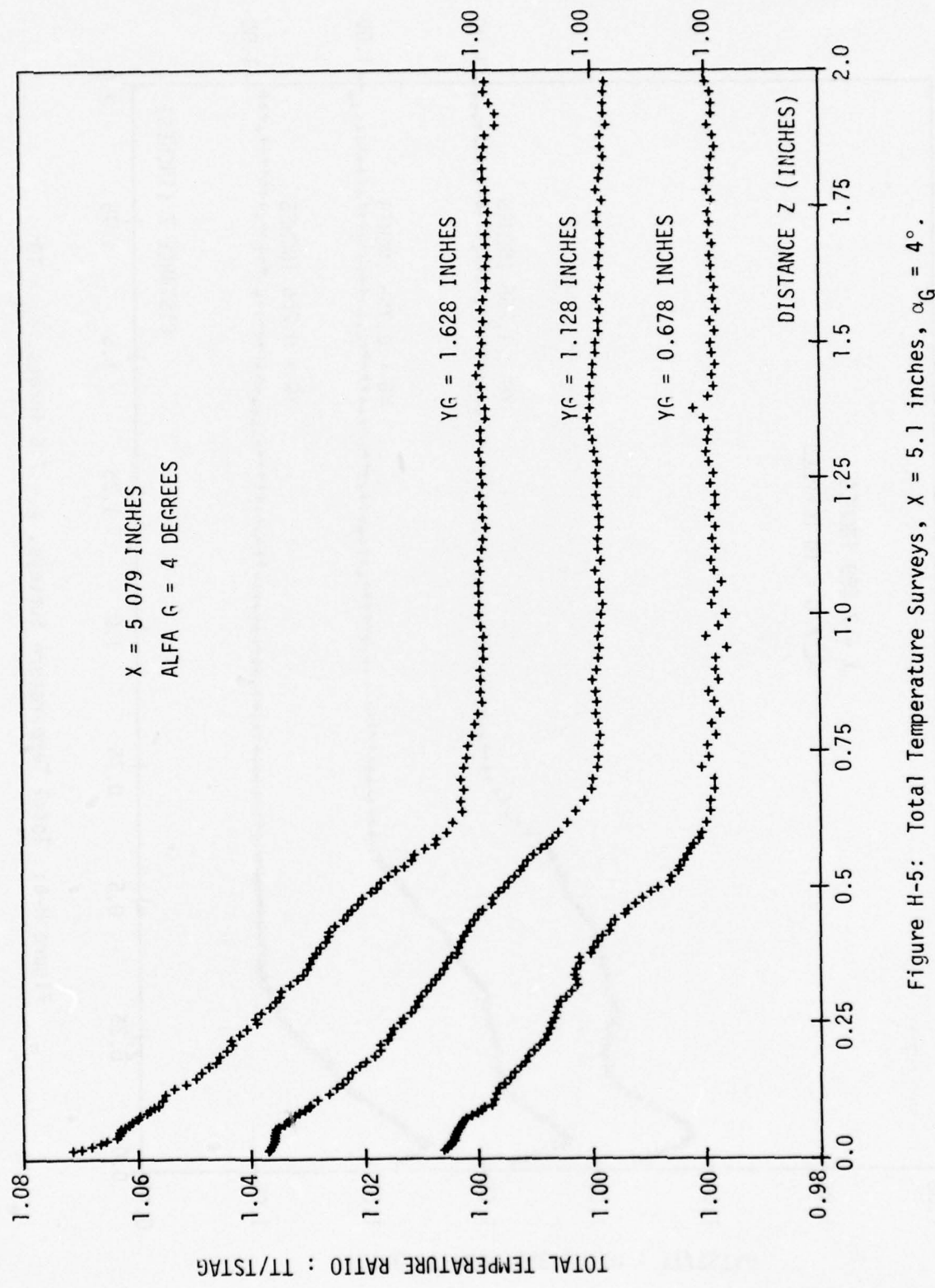


Figure H-5: Total Temperature Surveys, $X = 5.1$ inches, $\alpha_G = 4^\circ$.

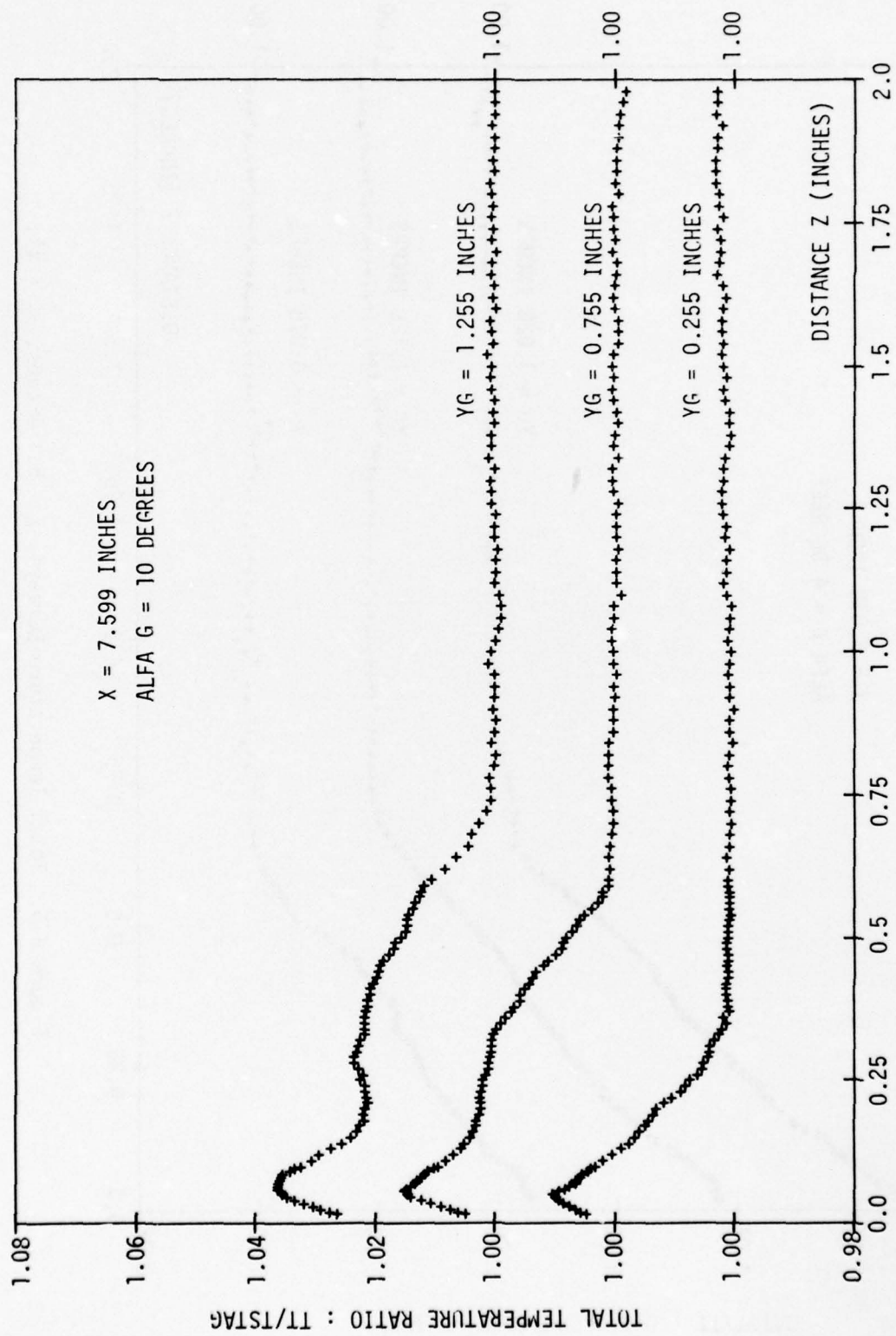


Figure H-6: Total Temperature Surveys, $X = 7.6$ inches, $\alpha_G = 10^\circ$.

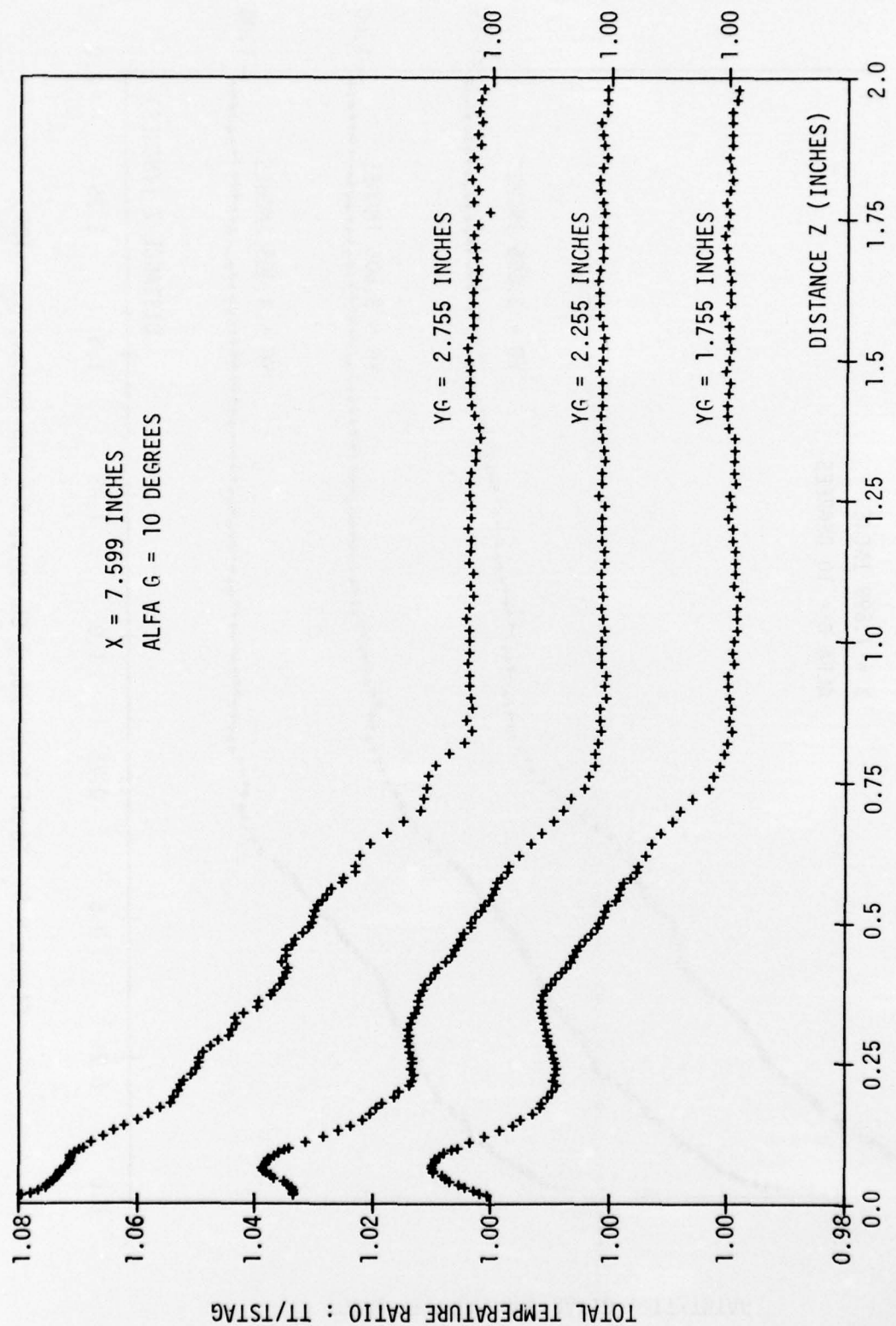


Figure H-7: Total Temperature Surveys, $X = 7.6$ inches, $\alpha_G = 10^\circ$.

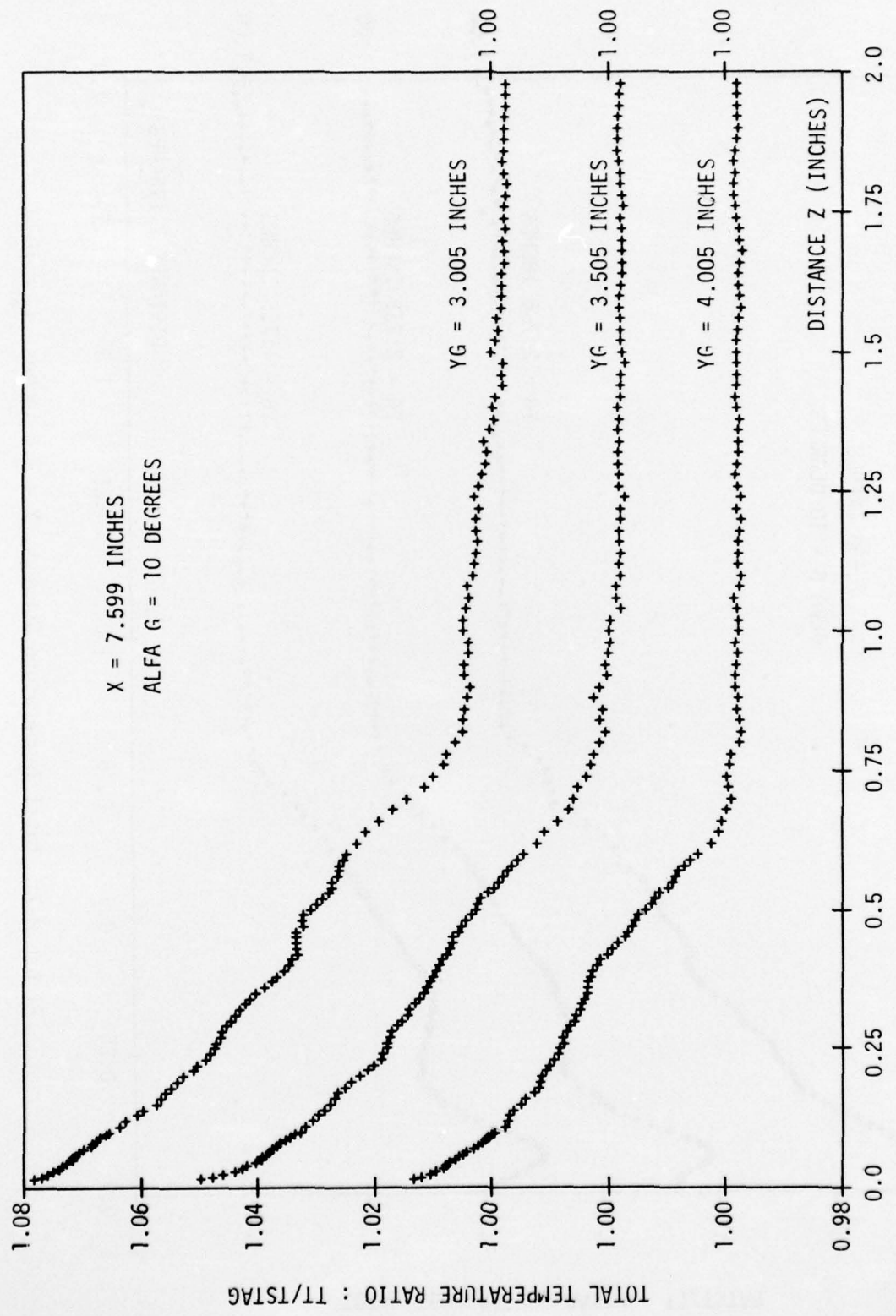


Figure H-8: Total Temperature Surveys, $X = 7.6$ inches, $\alpha_G = 10^\circ$.

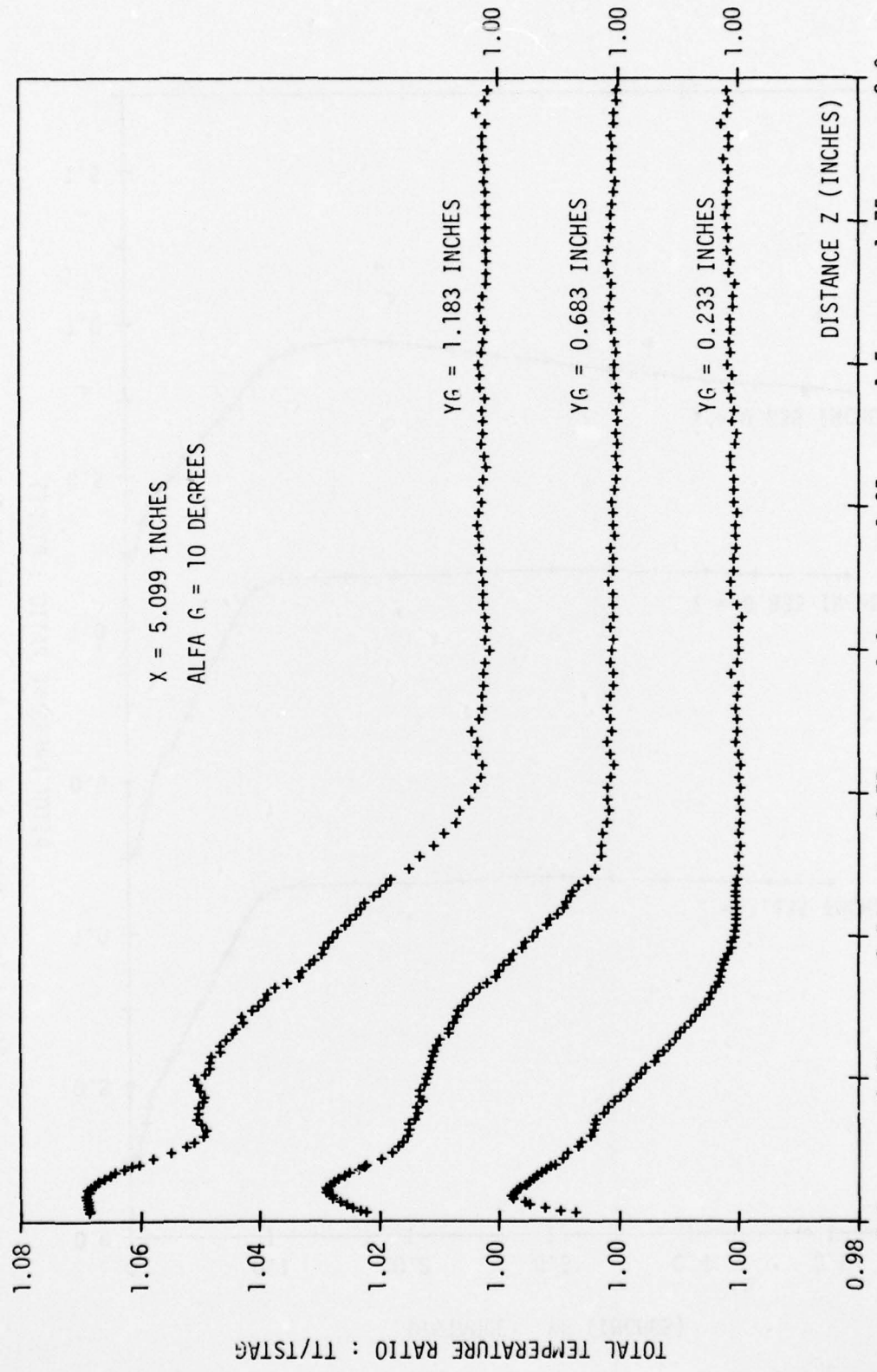


Figure H-9: Total Temperature Surveys, $X = 5.1$ inches, $\alpha_G = 10^\circ$.

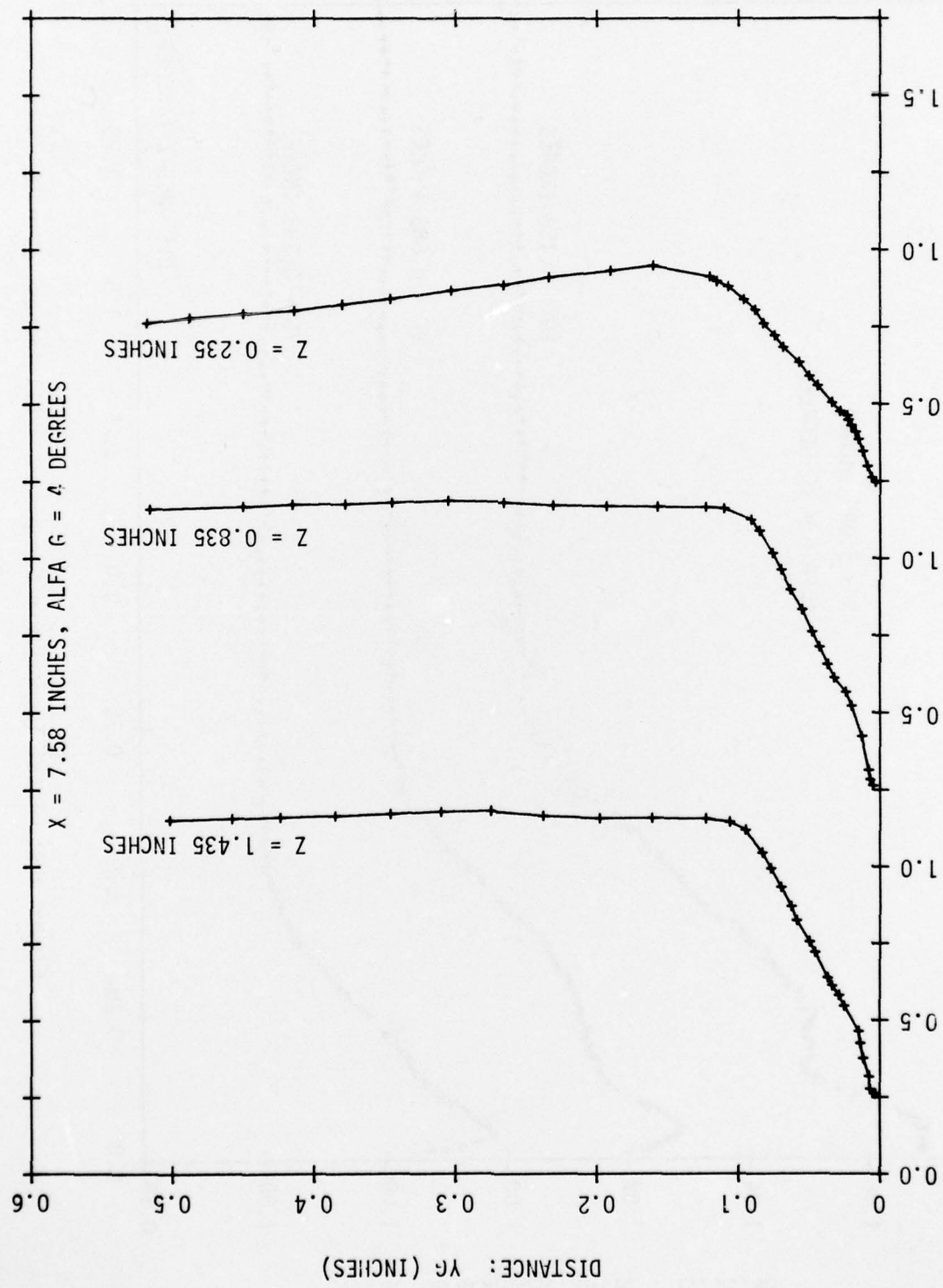


Figure I-1: Pitot Pressure Surveys, $X = 7.6$ inches, $\alpha_G = 4^\circ$.

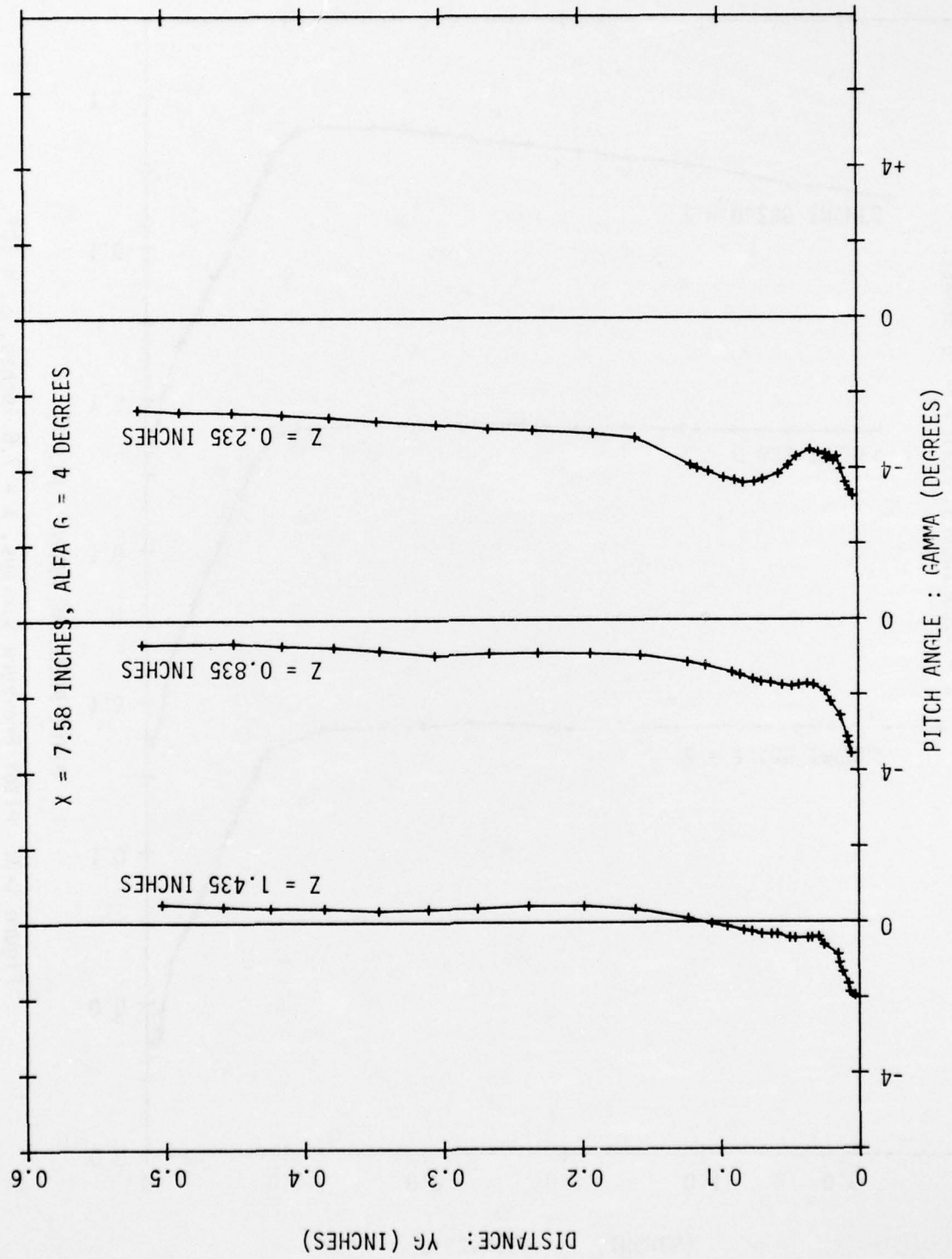


Figure I-2: Pitot Pressure Surveys, $X = 7.6$ inches, $\alpha_G = 4^\circ$.

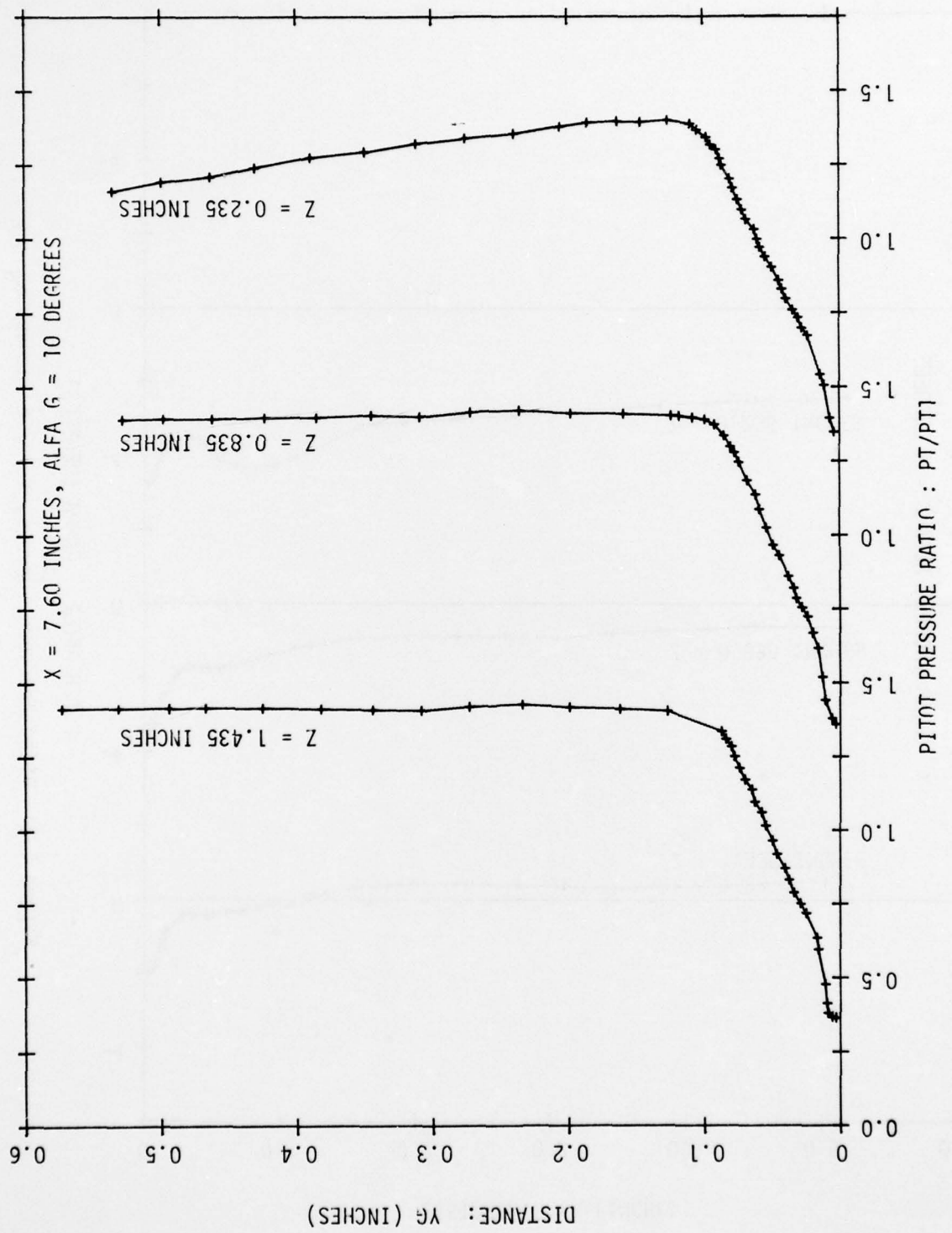


Figure 1-3: Pitot Pressure Surveys, $X = 7.6$ inches, $\alpha_G = 10^\circ$.

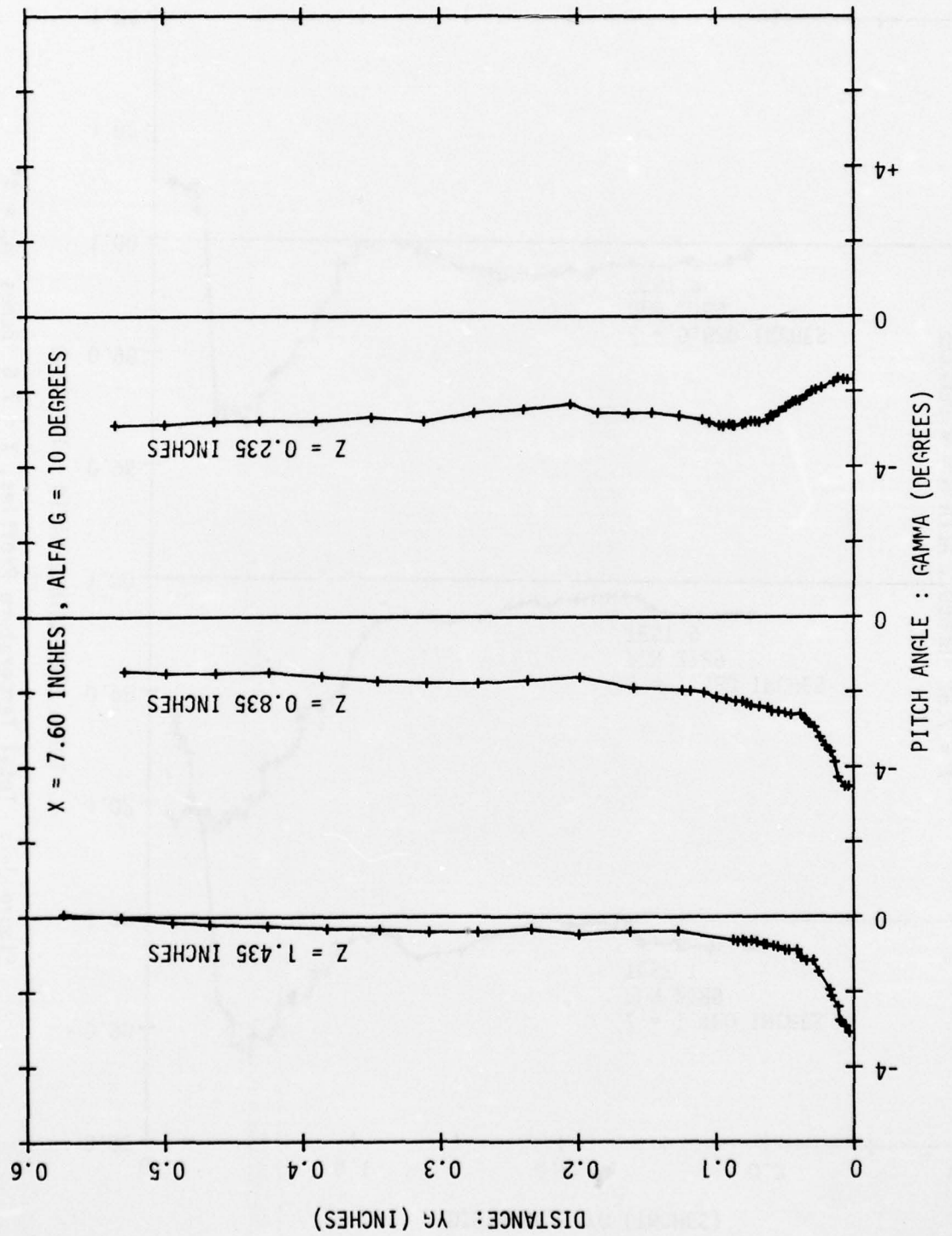


Figure I-4: Pitch Angle Surveys, $X = 7.6$ inches, $\alpha_G = 10^\circ$.

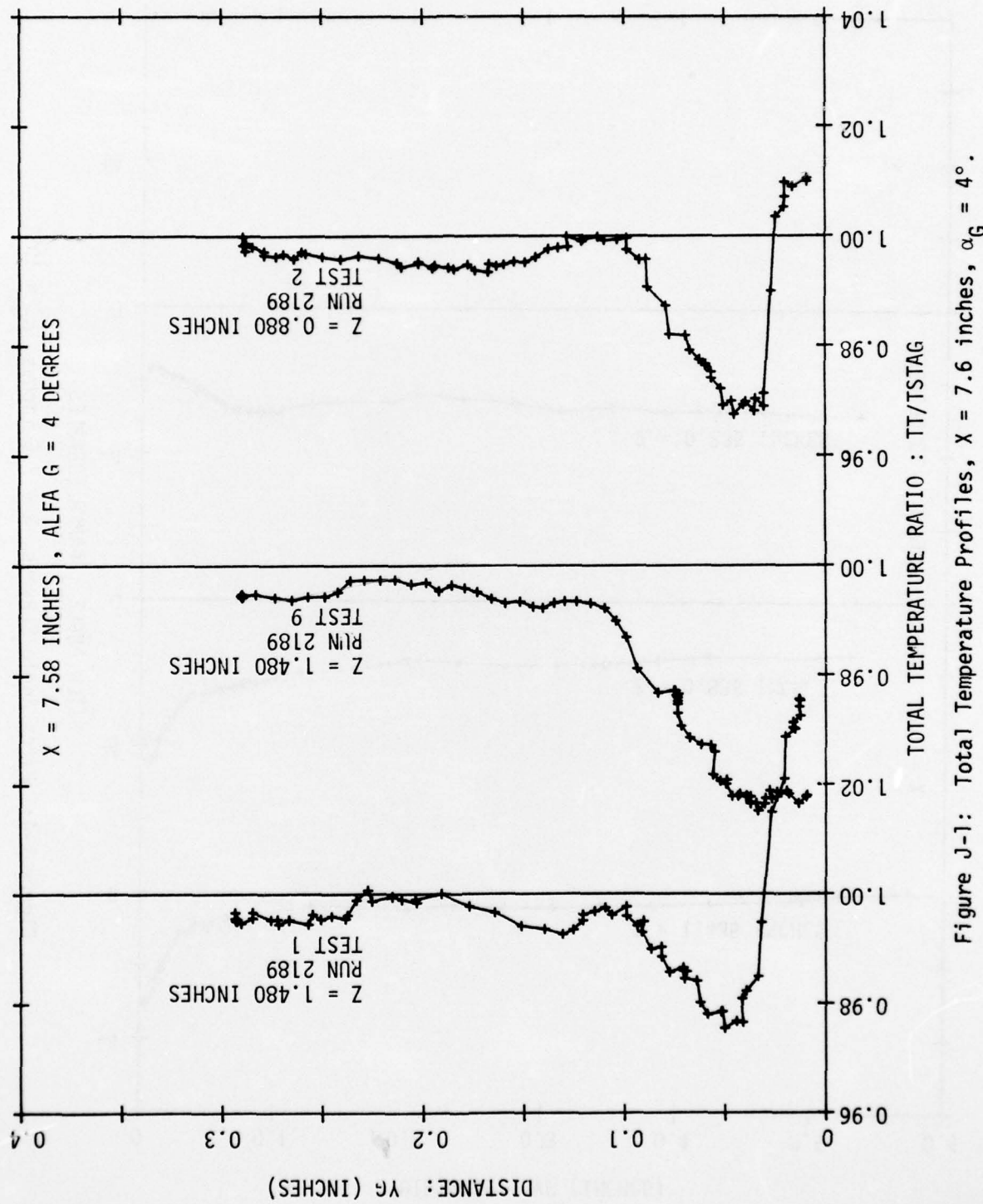


Figure J-1: Total Temperature Profiles, $X = 7.6$ inches, $\alpha_G = 4^\circ$.

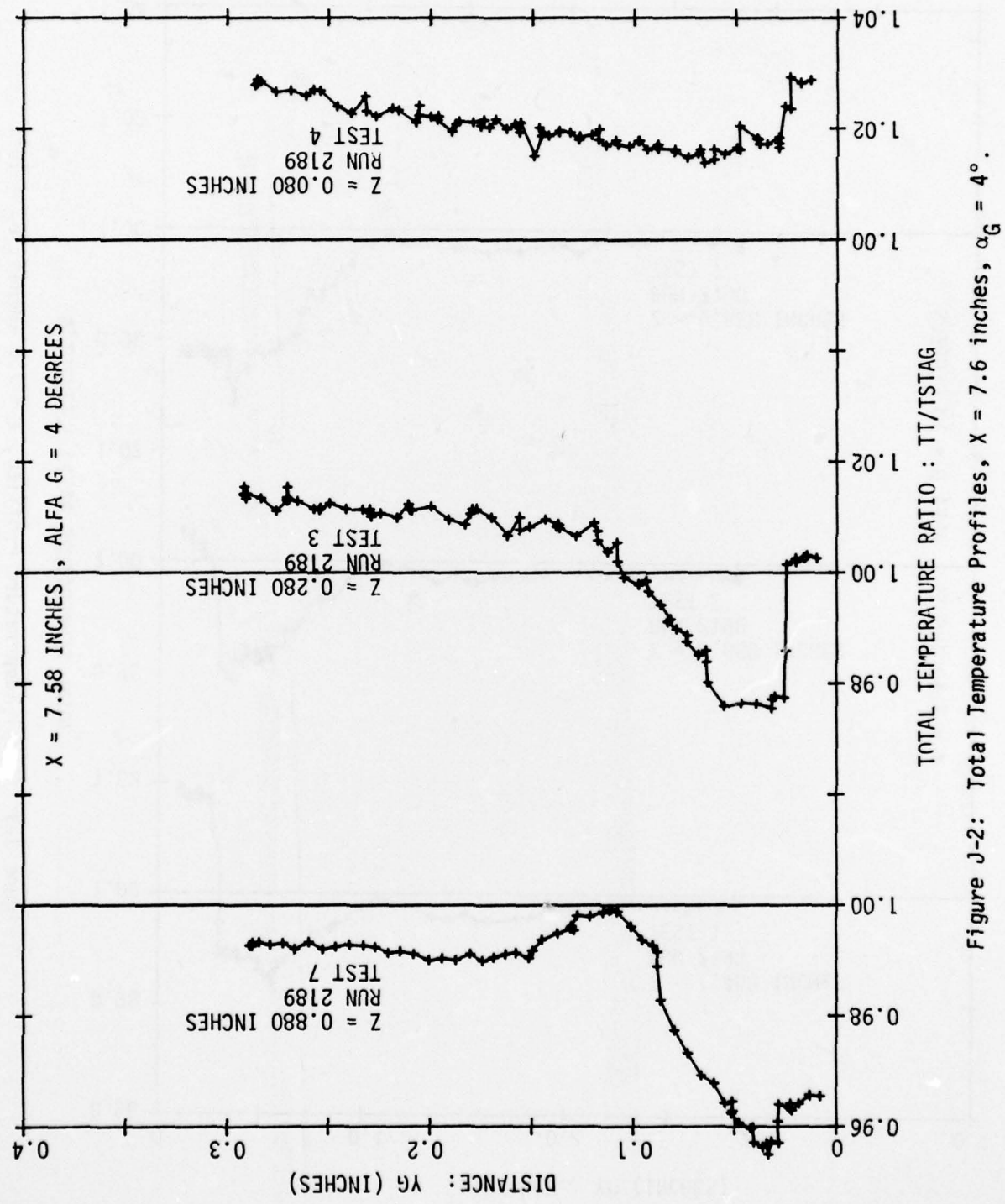


Figure J-2: Total Temperature Profiles, $X = 7.6$ inches, $\alpha_G = 4^\circ$.

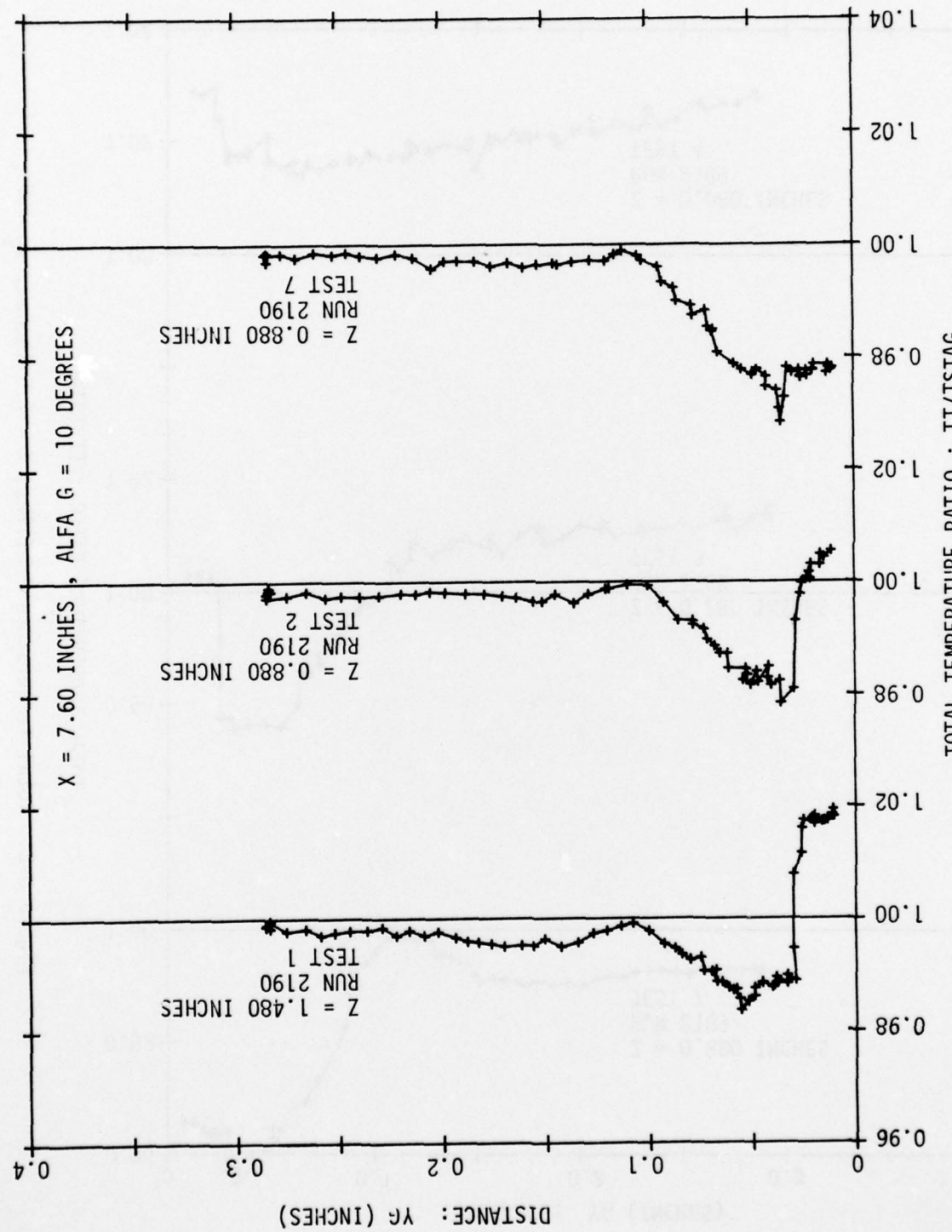


Figure J-3: Total Temperature Profiles, X = 7.6 inches, $\alpha_G = 10^\circ$.

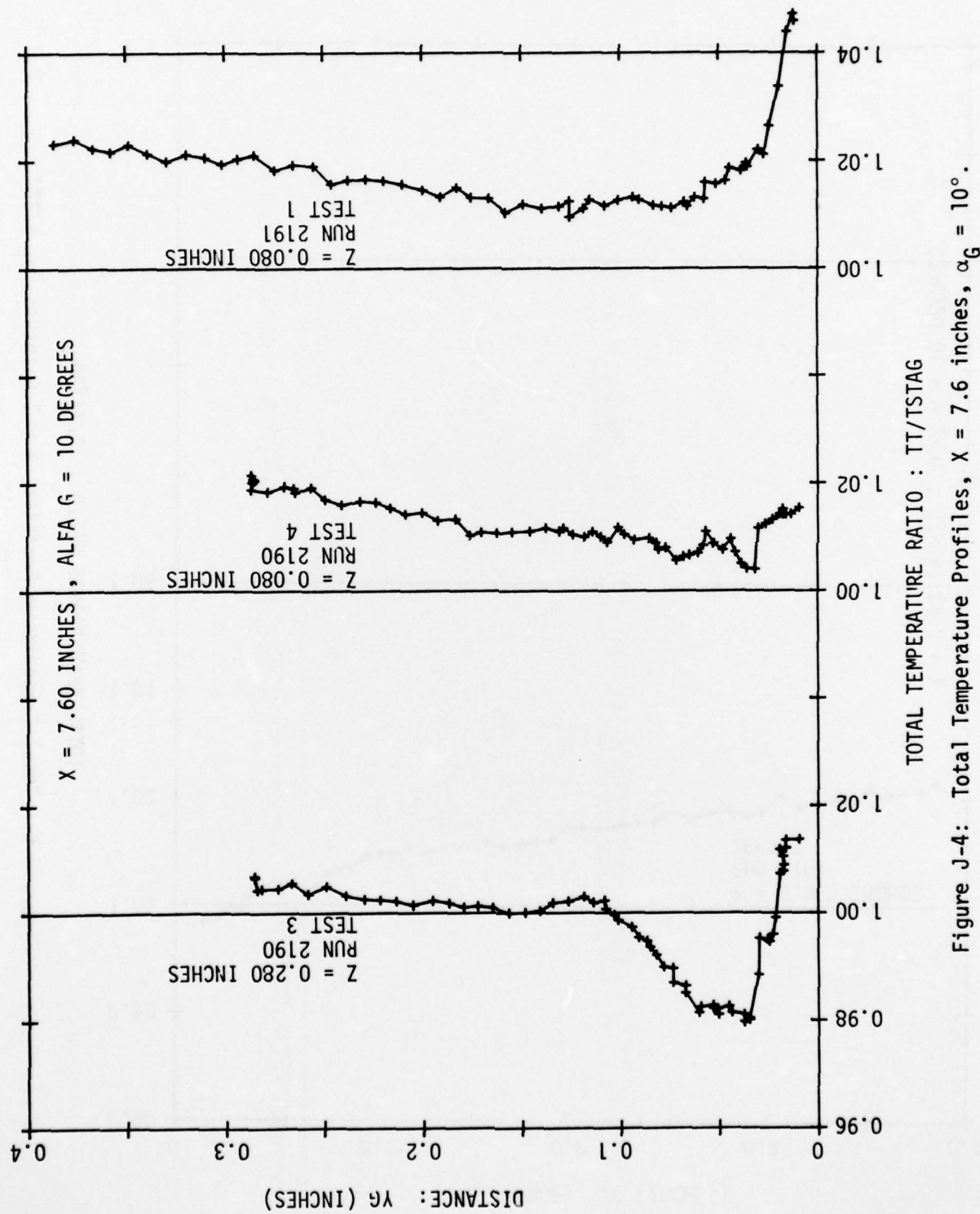


Figure J-4: Total Temperature Profiles, $X = 7.6$ inches, $\alpha_G = 10^\circ$.

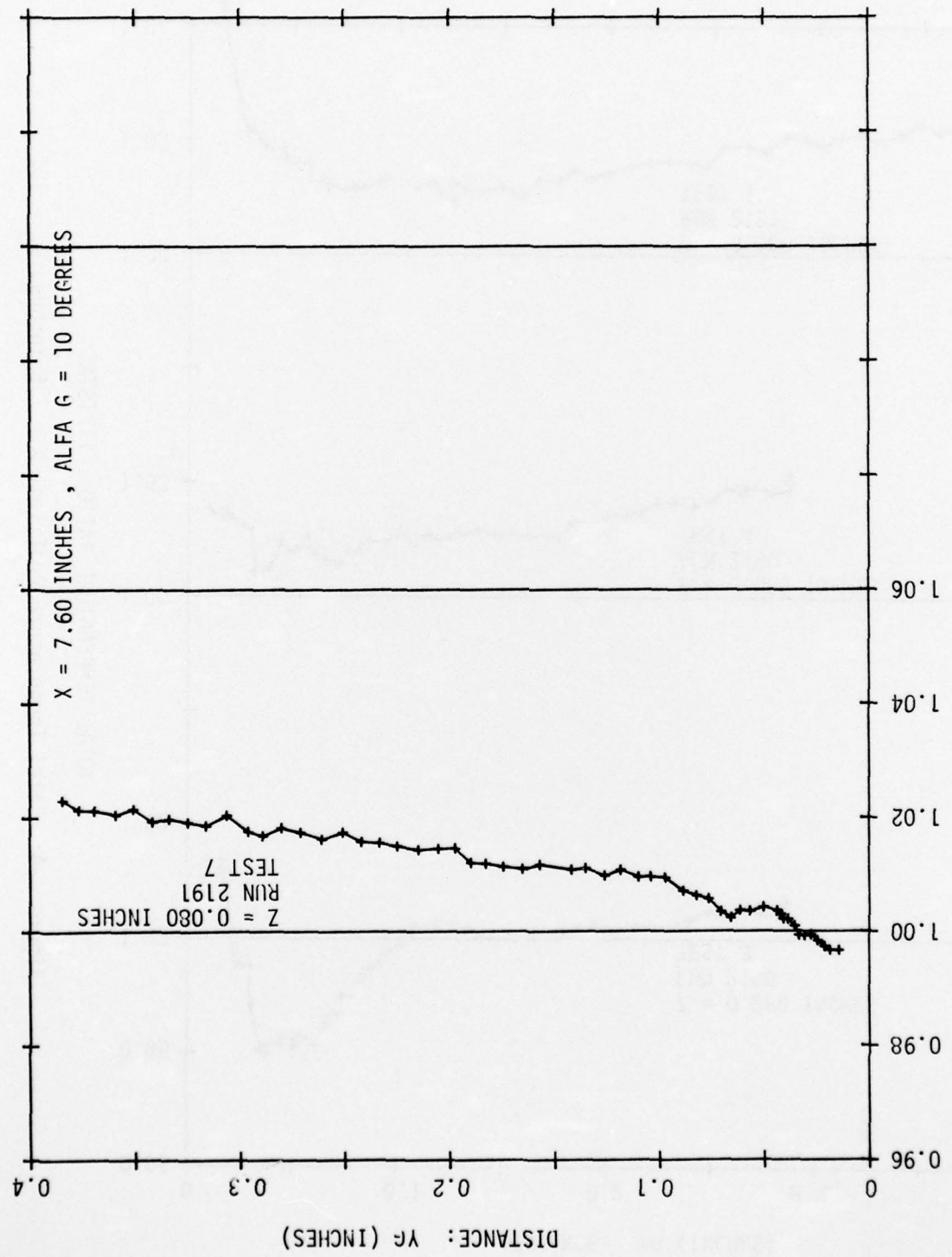


Figure J-5: Total Temperature Profiles, $X = 7.6$ inches, $\alpha_G = 10^\circ$.

REFERENCES

1. Hopkins, E. J. and Inouye, M., "An Evaluation of Theories for Predicting Turbulent Skin Friction and Heat Transfer on Flat Plates at Supersonic and Hypersonic Mach Numbers", AIAA Journal, Vol. 9, No. 6, June 1971.
2. Korkegi, R. H., "Survey of Viscous Interactions Associated with High Mach Number Flight", AIAA Journal, pp. 915-922, July 1972.
3. Neumann, R. D. and Token, K. H., "Prediction of Surface Phenomena Induced by Three-Dimensional Interactions on Planar Turbulent Boundary Layers", Paper No. 74-058, International Aeronautical Federation, XXV Congress, Amsterdam, The Netherlands, 30 Sept. - 5 Oct., 1974.
4. Oskam, B., Bogdonoff, S. M. and Vas, I. E., "Study of Three-Dimensional Flow Fields Generated by the Interaction of a Skewed Shock Wave with a Turbulent Boundary Layer", Technical Report AFFDL-TR-75-21, February 1975.
5. Oskam, B., Vas, I. E. and Bogdonoff, S. M., "Tabulated Data for Oblique Shock Wave/Turbulent Boundary Layer Interactions in Three-Dimensions at Mach 3", AFFDL-TR-76-48, Part II, January 1976.
6. Bogdonoff, S. M., "The Design, Construction, and Operation of the Princeton 4 by 8 inch Variable-Density Supersonic Tunnel", Princeton University, Technical Report TR-34, Project Squid, October 1951.
7. Vas, I. E. and Bogdonoff, S. M., "A Preliminary Report on the Princeton University High Reynolds Number 8" x 8" Supersonic Tunnel", Princeton University, Internal Memorandum 39, October 1971.
8. Peake, D. J. and Rainbird, W. J., "The Three-Dimensional Separation of a Turbulent Boundary Layer by a Skewed Shock Wave; and its Control by Tangential Air Injection", Paper 40, AGARD Conference Proceedings No. 168 on "Flow Separation", May 1975.
9. Franklin, R. E. and Wallace, J. M., "Absolute Measurements of Static-Hole Error Using Flush Transducers", J. Fluid Mech., Vol. 42, Part 1, pp. 33-48, 1970.
10. Reinecke, W. G., "The Measurement and Comparison with Theory of Heat Transfer from Similar Laminar Boundary Layers to Aerodynamic Bodies in Supersonic and Hypersonic Gas Streams", Princeton University, Report 569, October 1961.
11. Young, A. D. and Maas, J. N., "The Behaviour of a Pitot Tube in a Transverse Total-Pressure Gradient", R & M 1770, Sept. 1936, ARC, G.B.
12. Allen, J. M., "Pitot-Probe Displacement in a Supersonic Turbulent Boundary Layer", NASA-TN-D-6759, Langley Research Center, April 1972.

13. Johannesen, N. H. and Mair, W. A., "Experiments with Large Pitot Tubes in a Narrow Supersonic Wake", *Journal of the Aeronautical Sciences*, Vol. 19, No. 11, Nov. 1952, pp. 785-787.
14. Bannink, A. J. and Nebbeling, C., "Determination of the Position of a Shock Wave from Pitot Tube Experiments", *AIAA Journal*, Vol. 7, No. 4, April 1969, pp. 796-797.
15. Back, L. H. and Cuffel, R. F., "Static Pressure Measurements Near An Oblique Shock Wave", *AIAA Journal*, Vol. 9, No. 2, February 1971, pp. 345-347.
16. Norris, J. D., "Calibration of Conical Pressure Probes for Determination of Local Flow Conditions at Mach Numbers from 3 to 6", *NASA-TN-D-3076*, November 1965.
17. Norris, J. D. and Pierpoint, P. K., "Experimental Performance of a Conical Pressure Probe at Mach Numbers of 3.0, 4.5, and 6.0", *NASA-TN-D-3719*, December 1966.
18. Cronvich, L. L., "Pressure Distributions Over a Cylinder with Conical or Hemispherical Head at Supersonic Velocities", Rept. CM-528, APL, Johns Hopkins University, February 1949.
19. Vas, I. E., "Flow Field Measurements Using a Total Temperature Probe at Hypersonic Speeds", *AIAA Journal*, Vol. 10, No. 3, March 1972.
20. Dewey, C. F., "A Correlation of Convective Heat Transfer and Recovery Temperature Data for Cylinders in Compressible Flow", *Int. J. Heat Mass Transfer*, Vol. 8, pp. 245-252, 1965.
21. Stanbrook, A., "An Experimental Study of the Glancing Interaction Between a Shock Wave and a Turbulent Boundary Layer", *ARC-CP No. 555*, G.B. 1961.
22. McCabe, A., "The Three-Dimensional Interaction of a Shock Wave with a Turbulent Boundary Layer", *The Aeronautical Quarterly*, August 1966, pp. 231-252.
23. Lowrie, B. W., "Cross-Flows Produced by the Interaction of a Swept Shock Wave with a Turbulent Boundary Layer", Ph.D. Thesis, Univ. of Cambridge, 1965.
24. Token, K. H., "Heat Transfer Due to Shock Wave Turbulent Boundary Layer Interactions on High Speed Weapon Systems", *AFFDL-TR-74-77*, April 1974.
25. Peake, D. J., "The Three-Dimensional Interaction of a Swept Shock-Wave with a Turbulent Boundary Layer and the Effects of Air Injection on Separation", Ph.D. Thesis, Carleton University, Ottawa, 1975.